High-resolution x-ray scattering studies of charge ordering in highly correlated electron systems

Mohammad Ebrahim Ghazi

In the name of God

High-Resolution X-Ray Scattering Studies of Charge Ordering in Highly Correlated Electron Systems

Mohammad Ebrahim Ghazi

A thesis submitted in fulfilment of the requirements
for the degree of Doctor of Philosophy

University of Durham
Department of Physics
2002

To the memory of my father

who passed away during my Ph.D. study in Durham University

Abstract

Many important properties of transition metal oxides such as, copper oxide high-temperature superconductivity and colossal magnetoresistance (CMR) in manganites are due to strong electron-electron interactions, and hence these systems are called highly correlated systems. These materials are characterised by the coexistence of different kinds of order, including charge, orbital, and magnetic moment. This thesis contains high-resolution X-ray scattering studies of charge ordering in such systems namely the high-T_C copper oxides isostructural system, $La_{2-x}Sr_xNiO_4$ with various Sr concentrations (x = 0.33 – 0.2), and the CMR manganite system, $Nd_{1/2}Sr_{1/2}MnO_3$. It also includes a review of charge ordering in a large variety of transition metal oxides, such as ferrates, vanadates, cobaltates, nickelates, manganites, and cuprates systems, which have been reported to date in the scientific literature.

Using high-resolution synchrotron X-ray scattering, it has been demonstrated that the charge stripes exist in a series of single crystals of $La_{2-x}Sr_xNiO_4$ with Sr concentrations (x = 0.33 – 0.2) at low temperatures. Satellite reflections due to the charge ordering were found with the wavevector (2ε, 0, 1) below the charge ordering transition temperature, T_{CO}, where 2ε is the amount of separation from the corresponding Bragg peak. The charge stripes are shown to be two-dimensional in nature both by measurements of their correlation lengths and by measurement of the critical exponents of the charge stripe melting transition with an anomaly at x = 0.25. The results show by decreasing the hole concentration from the x = 0.33 to 0.2, the well-correlated charge stripes change to a glassy state at x = 0.25. The electronic transition into the charge stripe phase is second-order without any corresponding structural transition. Above the second-order transition critical scattering was observed due to fluctuations into the charge stripe phase.

In a single-crystal of $Nd_{1/2}Sr_{1/2}MnO_3$ a series of phase transitions were observed using high-resolution synchrotron X-ray scattering. Above the charge ordering transition temperature, T_{CO}, by measuring the peak profiles of Bragg reflections as a function of temperature, it was found that this crystal undergoes two transitions corresponding to the transition from a paramagnetic- to a ferromagnetic state at $T \approx$ 252 K, and the formation of a mixture of the antiferromagnetic and ferromagnetic phases below $T \approx$ 200 K. Below the charge ordering temperature, T_{CO} =162 K, additional satellite reflections with the wavevector, q = (1/2, 0, 0), were observed due to Jahn-Teller distortion of the MnO_6 octahedra caused by charge- and orbital ordering in sample. This transition was observed to be of first-order with a hysteresis width of 10 K. In addition, another very weak satellites with wavevector (1/2, 1, 1/2) were observed possibly due to spin ordering.

Acknowledgments

First of all, I would like to express my greatest and sincere appreciation to my supervisor, Dr. Peter D. Hatton to support throughout this thesis. Certainly without his kindness, guidance and great help, I would not have been able to complete this thesis.

I would like to express my appreciation to those who contributed to the completion of this thesis, Dr. C-H. Du, Mr. Stuart Wilkins, and Mr. Phil Spencer. I am also grateful to all members of the X-ray scattering and magnetism group in particular Prof. B. K. Tanner, Dr. Tom Hase, and other staff and technicians especially Mr. John Dobson. I also thank other academic staff for the postgraduate courses.

I gratefully acknowledge the help of a number of people who have collaborated with this work; Firstly, Prof. S-W. Cheong at Rutgers University and Bell Laboratories, and Drs P. Prabhakaran and A. Boothroyd at Oxford University for providing good quality single crystals. Secondly, many thanks to the members of the *XMaS* beamline at the ESRF, Dr. S. Brown, Dr. D. Mannix, Dr. P. Thompson, Dr. D. Paul, and Mrs S. Beaufoy, Prof. M. J. Cooper and Prof. W. G. Stirling and beamline 16.3 at the SRS, Dr. S. P. Collins and B. M. Murphy for their help and assistance during the my experiments.

I acknowledge the financial support from the Ministry of Science, Research and Technology of Iran, and also Shahrood University for giving me an opportunity to undertake this research.

Finally, I would like to express my greatest thanks to my wife for her patience especially during my experiments when I was out of UK, and her encouragement during my study, and to my nice sons, Mehran and Farzan. I also give great thanks to my lovely mother, who always supported me during the whole of my life and my wife's parents. This thesis is dedicated to them.

Declaration

This thesis has been conducted by myself and it has not been submitted in any previous application for a degree. The work contained in this thesis is my own unless otherwise stated. Part of results of this thesis have been published in:

1. 2-Dimensional Charge Stripes in $La_{5/3}Sr_{1/3}NiO_4$, *C-H. Du, M. E. Ghazi, Y. Su, I. Pape, P. D. Hatton, S. Brown, S-W. Cheong*, ESRF Science Highlights Annual Report 52-53, 1998/99.
2. Dynamical and Quenched Disorder of 2-Dimensional Charge Stripes in $La_{5/3}Sr_{1/3}NiO_4$, *M. E. Ghazi, C-H. Du, P. D. Hatton, S. Brown, and S-W. Cheong*, "Magnetic and Superconducting Materials" edited by M. Akhavan, J. Jensen, and K. Kitazawa, published by World Scientific Press, London, ISBN 981-02-4244-1; 2000
3. Synchrotron X-ray Scattering Studies of Charge and Spin Stripes in Manganites, *C-H. Du, Y. Su, M. E. Ghazi, P. D. Hatton, S. P. Collins, S. Brown, and S-W. Cheong*, "Magnetic and Superconducting Materials" edited by M. Akhavan, J. Jensen, and K. Kitazawa, published by World Scientific Press, London, ISBN 981-02-4244-1, 2000
4. Quenched Disordered 2-Dimensional Charge Stripes in $La_{5/3}Sr_{1/3}NiO_4$, *C-H. Du, M. E. Ghazi, Y. Su, I. Pape, P. D. Hatton, S. Brown, G. Stirling, M. J. Cooper, and S-W. Cheong*, Phys. Rev. Lett. 84, 3911-3914, 2000.
5. Critical Fluctuations and Quenched Disorder of two-Dimensional Charge Stripes in $La_{5/3}Sr_{1/3}NiO_4$, *P. D. Hatton, M. E. Ghazi, S. Brown, and S-W. Cheong*, International Journal of Modern Physics B 14, (29-31), 3488-3493, 2000.
6. Observations of Magnetic Domain Structures and Charge Ordering in Single-Crystal $Nd_{1/2}Sr_{1/2}MnO_3$ Using X-ray Scattering, *C-H. Du, M. E. Ghazi, P. D. Hatton, S. P. Collins, B. M. Murphy, T. Katsufuji, and S-W. Cheong*, (submitted to J. of Phys. Condens. Matter)

7. X-ray Scattering Studies of Charge Stripes in $La_{2-x}Sr_xNiO_4$ (x = 0.20 - 0.33), *P. D. Hatton, M. E. Ghazi, S. B. Wilkinson, P. D. Spencer, D. Mannix, T. d'Almeida, P. Prabhakaran, A. Boothroyd, and S-W. Cheong,* Physica B, 2002 (in print)
8. X-ray Scattering Studies of Charge Stripes in $La_{2-x}Sr_xNiO_4$ (x = 0.20 - 0.33), *P. D. Hatton, M. E. Ghazi, S. B. Wilkinson, P. D. Spencer, D. Mannix, T. d'Almeida, P. Prabhakaran, and A. Boothroyd,* International Journal of Modern Physics B, 2002 (in print)
9. Charge Stripe Melting Processes in $La_{2-x}Sr_xNiO_4$ (x = 0.275 and 0.3), *M. E. Ghazi, S. B. Wilkinson, P. D. Spencer, P. D. Hatton, D. Mannix, P. Prabhakaran, and A. Boothroyd* (in preparation)

Mohammad E. Ghazi

March 2002

Contents

Figures

Chapter 1

General view

1.1 Introduction

Transition metal oxides compounds show a variety of interesting phenomenon. Among them, colossal magnetoresistance (CMR), high-T_C superconductivity, and charge-, spin-, and orbital ordering have recently attracted much interest, and the later is the central focus of research. Charge-, spin-, and orbital ordering have been observed in a variety of transition metal oxides such as ferrates, vanadates, cobaltates, nickelates, manganites, and cuprate systems.

When charge carriers are doped into antiferromagnetic insulators, such as nickelates or cuprates, they tend to order in some directions and form the stripes. The carriers form the boundaries of antiferromagnetically ordered regions. The charge stripe phase undergoes a transition to the charge-disordered phase with melting of the charge stripes upon warming. In the manganite systems, especially for half-doped systems, the doped holes are localized at low temperatures due to the ordering of cations with different valence states on specific lattice sites. In the half-doped manganite, $Nd_{0.5}Sr_{0.5}MnO_3$ system, this ordering of Mn^{3+} and Mn^{4+} sublattices is accompanied with *CE*-type spin and e_g electron orbital ordering.

Many experimental techniques, including transport measurements, optical spectroscopy, NMR, neutron diffraction, electron microscopy and X-ray scattering have been employed to study the charge ordering phenomena in transition-metal oxides. Among these techniques, X-ray scattering is a uniquely direct tool for this purpose, because it directly probes the charge modulations. Nowadays, with third generation synchrotron sources, this technique has many advantages over other

techniques, being able to detect very weak satellites with very high wavevector resolution.

This thesis generally reports synchrotron X-ray scattering studies of charge ordering in a few transition metal oxides namely nickelates and manganites. However, laboratory-based X-ray scattering was also used for preliminary studies of the crystals. All the results presented in this thesis were obtained on single crystals with a series of different hole concentrations.

1.2 Thesis outline

The content of this thesis will be as follows:

Chapter 2 is a review of studies of charge-, spin-, and orbital ordering in transition metal oxides, such as ferrates, vanadates, cobaltates, nickelates, manganites, and cuprates systems, which have been reported to date in the scientific literature.

The theory of X-ray scattering based on kinematical scattering theory is presented in *Chapter 3*. In this chapter the concept of charge and magnetic scattering will be briefly explained. The theory of resonance scattering is also included in this chapter.

In *Chapter 4*, the experimental technique of X-ray scattering is introduced and explained. The chapter contains a brief discussion of X-ray sources, both laboratory and synchrotron radiation sources, including the beamlines 16.3 at the Synchrotron Radiation Source (SRS) in Daresbury and BM28 at the European Synchrotron radiation Facility (ESRF) in France. Finally in this chapter, the floating-zone method of crystal growth will be explained, as this was the method by which all the samples studied, were produced.

The experimental results obtained on studies of the charge stripe on single crystals of $La_{2-x}Sr_xNiO_4$ with Sr concentrations x = 0.33, 0.3 and 0.275 are explored in *Chapter 5*. At the end of this chapter the dependence of the charge ordering temperature and the charge stripe correlation length with hole concentration is explained. It was found

the charge stripes in these compounds is 2-dimensional and quasi long-range ordered with a maximum correlation length for the Sr concentration $x = 0.33$.

In *Chapter 6* the study of the charge stripes in nickelate systems is expanded to single crystals with lower Sr concentration $x = 0.25$ and 0.2. The measured correlation lengths showed that the correlation length decreases with decrease of the Sr concentration and the charge stripes exist in a glassy state. The charge ordering transition also decreases with decrease of the Sr concentration.

The results of the study of the magnetic domain structures above the charge ordering transition temperature and the microscopic phase separation scenario on a single crystal of $Nd_{0.5}Sr_{0.5}MnO_3$ are explored in *Chapter* 7. Then the results obtained on a study of Jahn-Teller distortion and spin ordering are given. Finally, by tuning the beam energy to the Mn *K*-edge, the behaviour of the intensity of the satellites corresponding to the distortion and spin ordering is introduced.

Chapter 8 is a summary of the results that were obtained in this thesis from synchrotron X-ray scattering studies of nickelate and manganite systems.

Chapter 2

Charge and spin ordering in transition metal oxides

2.1 Introduction

Materials with strong electron correlations exhibit many interesting physical phenomena such as high-T_C superconductivity and colossal magnetoresistance. The study of these and charge, spin, and orbital ordering is one of the liveliest areas of research in condensed matter physics.

Among these phenomena, charge ordering has attracted much interest due to its possible relationship with high-T_C superconductivity and colossal magnetoresistance. It has been now understood that the charge ordering arises primarily due to a combination of strong electron-electron correlation, exchange interactions, electron-phonon coupling, and the commensurability of the carrier concentration with the periodicity of the lattice [1, 2].

In this chapter, charge and spin ordering in transition metal oxides such as ferrates, nickelates, manganites, cuprates, cobaltates, and vanadates systems is reviewed with a special focus on the nickelates and manganites systems which are experimentally studied in this thesis.

2.2 Charge and spin ordering in ferrates, cobaltates, and vanadates

2.2.1 Ferrates

2.2.1.1 Fe_3O_4

Magnetite, Fe_3O_4, was the first material in which a charge ordering transition was proposed. This compound, which is a ferrimagnetic, undergoes a first-order metal-

insulator phase transition at T_V =120 K, the so-called Verwey transition [3]. This system has an inverse spinel structure of cubic symmetry (space group *Fd3m*) at room temperature [4]. The oxygen atoms form a face-centred-cubic structure and the iron atoms occupied two different positions; one third are located at the tetrahedral site, or *A* sites, and the remaining two thirds occupy the octahedral sites, or *B* sites. The Fe^{3+} ions occur on the *A* sublattice while the *B* sublattice contains a mixture of Fe^{3+} and Fe^{2+}, leading to the so-called inverse spinel structure [4]. This magnetite undergoes the ferrimagnetic transition with antiferromagnetic coupling between the tetrahedral site [Fe^{3+} $(t_{2g}^3 e_g^2, S = 5/2)$] and the octahedral site [Fe^{2+} $(t_{2g}^4 e_g^2, S = 2)$] at quite high temperatures (T = 858 K) and hence near T_V = 120 K the t_{2g} conduction electrons on the *B* sites are almost fully spin polarized. Verwey proposed the metal-insulator transition at T_V is due to the charge ordering in the sample, ordering of Fe^{3+} and Fe^{2+} ions on the octahedral sites (*B* sites) of the spinel structure.

The Verwey transition has been interpreted as an order-disorder transition of the Fe^{3+} and Fe^{2+} ions. Electron [5] and neutron [6] diffraction experiments revealed the existence of half-integer superlattice reflections (h, k, l+1/2), indicating a doubling of the unit cell along the c-axis. Charge ordering in the Fe_3O_4 system is complicated, with some short-range ordering present even above T_V. Yamada *et al.* by using electron microscopy suggested that unit cell of the low temperature phase should be twice as large as that proposed by Verwey and the ordering scheme should be more complicated than the Verwey order. The diffraction pattern showed the ordering phase below the low-temperature transition appears as finely divided stripes. They observed satellites at reciprocal lattice points with half-integer indexes such as (4, 0, 1/2), indicating doubling of the unit cell along the c-axis [5].

Optical conductivity measurements have also shown opening of a 0.14 eV optical gap below T_V [7] and also the d.c. conductivity abruptly increases by two orders of magnitude on heating through T_V [8].

Shirane *et al.* by using high-resolution neutron scattering suggested that the alternate Fe^{3+} and Fe^{2+} occur in the *ab* plane, in contrast to the Verwey model of the single modulation along the c-axis [9]. Rudee *et al.* studied a thin film sample of Fe_3O_4 by electron diffraction and claimed the observation of a new form of charge ordering at room temperature, which has a cubic, rather than a layered, structure [10]. This charge

ordering occurs on the tetrahedral sites, and is unrelated to the well known low-temperature ordering on octahedral sites below 120 K.

More recently Garcia *et al.* have studied Fe_3O_4 by x-ray resonant scattering at the iron *K*-edge of the (0, 0, 2) and (0, 0, 6) forbidden reflections [11]. They found that the energy and azimuthal angle dependence of the intensity of these reflections do not change above, and below, the transition temperature. So they concluded that no Fe^{3+} / Fe^{2+} charge ordering should occur in the low temperature phase, because the spectra are identical above and below the Verwey transition, both for the oriented and non-oriented crystal. The lack of contribution of the Fe atoms to the (4, 0, 1/2) reflection shows that the motion of the oxygen atoms drives the structural phase transition.

2.2.1.2 $La_{1-x}Sr_xFeO_3$

In single crystal $La_{1-x}Sr_xFeO_3$ $0.0 < x < 0.7$, the existence of charge ordering has been proved by transmission electron microscopy (TEM) [12]. In a $x = 0.3$ sample, this study revealed superlattice spots due to charge ordering (CO) below 150 K at (1/2, 0, 0) positions. A [001] zone-axis electron diffraction pattern of this compound is shown in Figure 2.1, which was obtained at 110 K. The Figure clearly shows the superlattice spots midway between the fundamental reflections. They proposed for $x < 0.4$ the valence states of the Fe ions are +3 or +4, so the charge ordering is ordering of Fe^{3+} and Fe^{4+} ions. Charge and spin ordering have also been observed in an $x = 0.67$ sample at 207 K accompanying charge disproportionation into nominally Fe^{3+} and Fe^{5+} sites, as well as antiferromagnetic spin ordering with a increase in electrical resistivity at T_{CO} [13]. The charge and spin ordered structure of this compound is shown in Figure 2.2.

Park *et al.* studied the $R_{1/3}Sr_{2/3}FeO_3$ systems with *R* = La, Pr, Nd, Sm, and Gd by TEM technique and found identical superlattice patterns when the La ions are replaced with Pr (T_{CO} = 182 K), and Nd (T_{CO} = 165 K) [14]. They could not find such super-structure spots for *R* = Sm and Gd, down to the lowest temperature of their TEM measurements (20 K). When the *R*-site ion was changed from *R* = La (La^{3+} = 1.22 Å) to a smaller-size *R* ion towards *R* = Gd (Gd^{3+} = 1.11 Å), the *p-d* hybridization interaction is decreased. This causes a decrease in T_{CO} and finally the

CO transition disappears for R = Sm (Sm^{3+} = 1.13 Å) and Gd. From this, it is anticipated that the Sm and Gd compounds do not undergo the CO transition in contrast with the larger (La, Pr, and Nd) ions. They suggested that strong *p-d* hybridization was realized for R = La, Pr, and Nd is necessary for stabilizing the charge-ordered state.

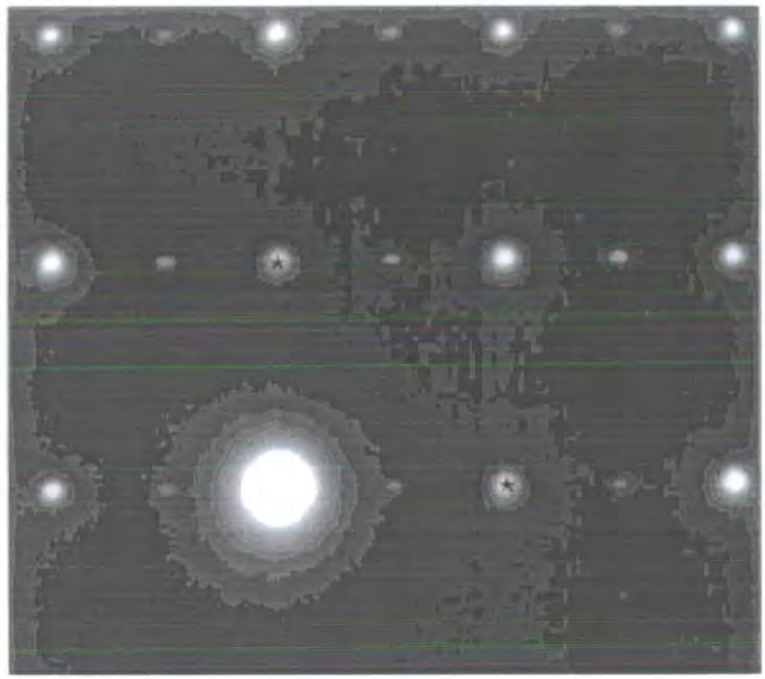

Figure 2.1 [001] zone-axis electron diffraction pattern of $La_{0.7}Sr_{0.3}FeO_3$ obtained at 110 K. (taken from Li *et al.* [12])

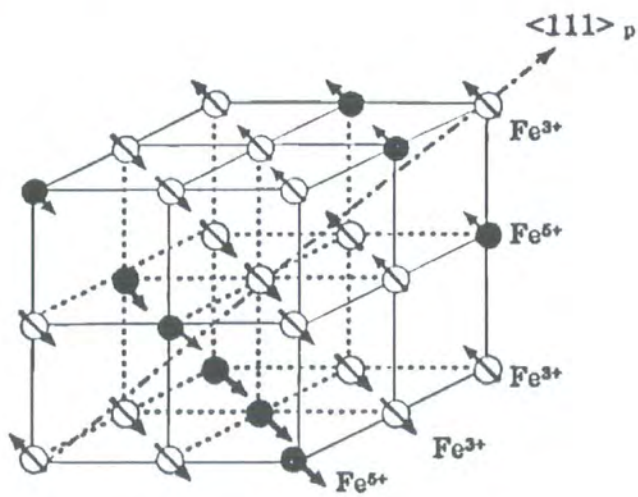

Figure 2.2 Charge and spin ordering in $La_{1/3}Sr_{2/3}FeO_3$. (taken from Battle *et al.* [13])

The temperature dependence of resistivity of the $R_{1/3}Sr_{2/3}FeO_3$ systems (R = La, Pr, Nd, Sm, and Gd) from these studies is shown in Figure 2.3. For the compounds which undergo transition to the charge ordered state, their resistivity curves show a jump at $T_{CO} = T_N$. These compounds undergo a phase change from a paramagnetic metallic state to an antiferromagnetic state at T_N that is accompanied with a charge-ordered state ($T_{CO} = T_N$). The charge-ordered state has been assigned to the ordering of magnetically different Fe^{3+} ($3d^5$) and Fe^{5+} ($3d^3$) ions with the ratio of 2:1.

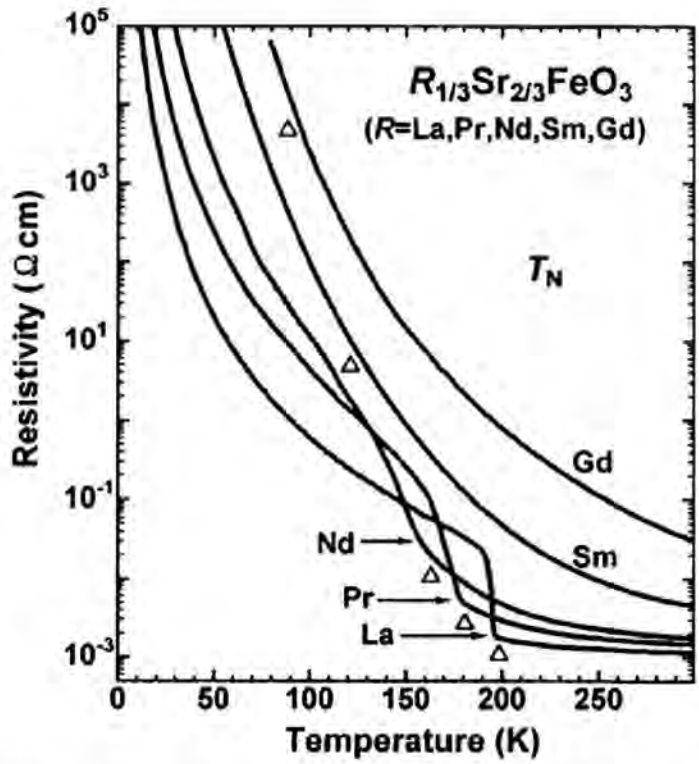

Figure 2.3 Resistivity as a function of temperature of $R_{1/3}Sr_{2/3}FeO_3$ (R = La, Pr, Nd, Sm, Gd). Open triangles indicate the critical temperature T_N for the antiferromagnetic phase transition. T_N for R = La, Pr, and Nd coincides with the charge ordering transition temperature T_{CO}. (taken from.Park *et al.* [14])

Kajimoto *et al.* have also studied single crystal $Nd_{1/3}Sr_{2/3}FeO_3$ using neutron diffraction [15]. The results of resistivity and magnetization measurements are shown in Figure 2.4. Both curves, the resistivity and spontaneous magnetization, show a considerable change at $T_N = T_{CO}$ =185 K due to the charge and spin ordering. By neutron diffraction they observed a series of reflections with modulation wave vectors $q = a^*(1/3, 1/3, 1/3)$ due to charge ordering, $q = a^*(1/6, 1/6, 1/6)$ and $q = a^*(1/2, 1/2, 1/2)$ due to the spin ordering, which is shown in Figure 2.5. Charge and

spin ordering transition temperature coincide with each other and this transition is first-order with the hysteresis width of 4 K. The charge and spin ordered states form a three-dimensional stripe order.

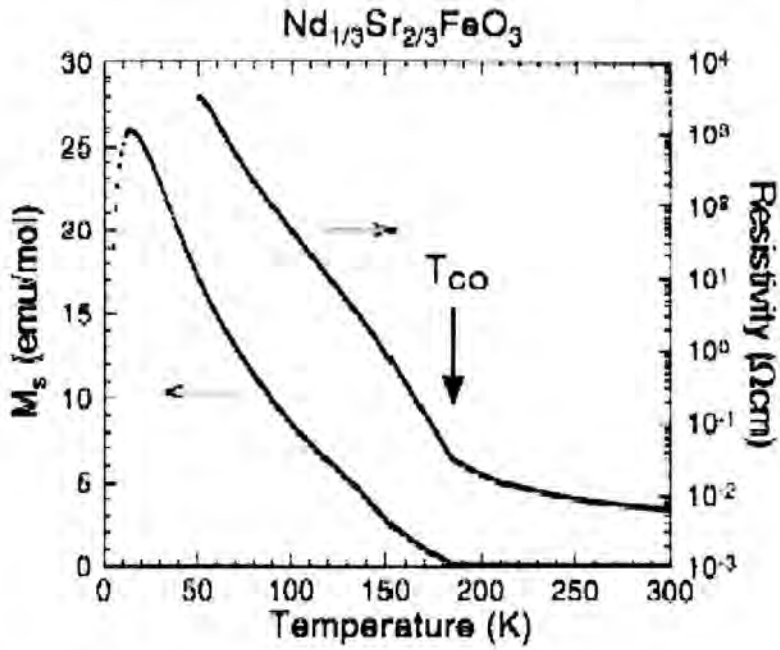

Figure 2.4 Resistivity and spontaneous magnetization as a function of temperature for $Nd_{1/3}Sr_{2/3}FeO_3$. (taken from Kajimoto *et al.* [15])

2.2.1.3 $LuFe_2O_4$

$LuFe_2O_4$ belongs to a class of layered materials with hexagonal double layers of Fe ions, which are sandwiched by thick blocks of other ions. They show 2-dimensional (2D) ferrimagnetic ordering at ~ 240 K where spin correlation remains short-range. Neutron diffraction measurements have revealed diffuse streaks extending along (h±1/3, h±1/3, l) lines in the temperature range 350 K< T < 500 K indicating a 2D ordering of the charge density wave (CDW) state within the Fe double layer [16]. With further decreases of temperature the system transforms itself from a two-dimensional CDW state to a 3D charge density wave state at ~ 330 K.

This system has also been studied in addition to neutron scattering by x-ray, and electron diffraction. The results indicate for T < 320 K, the 3D ordering is incommensurate and 2D ordered state exists in temperature range 320 < T < 500 K [17].

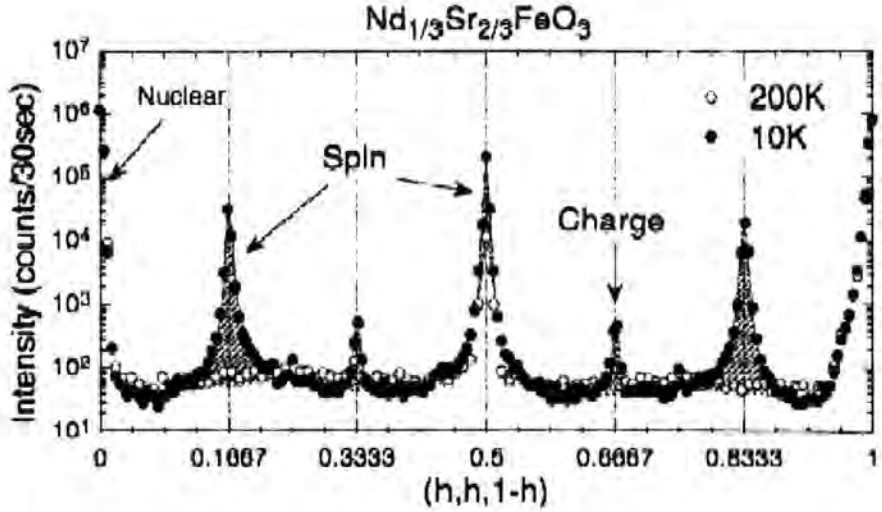

Figure 2.5 A profile of the line scan along the [11-1] direction at 200 K and 10 K. Shaded peaks represent the superlattice reflections due to spin and charge ordering. (taken from Kajimoto *et* al. [15])

2.2.2 Cobaltates

2.2.2.1 $YBaCo_2O_5$

This compound transforms from a paramagnetic (PM) state to a spin ordered antiferromagnetic (AFM) state at 330 K, which there is a cusp in magnetic susceptibility measurements [18]. This magnetic transition occurs simultaneously with a tetragonal to orthorhombic structural phase transition. Long range Co^{2+} and Co^{3+} charge ordering was detected below T_{CO} = 200 K by the appearance of (1/2, 0, 2), (1/2, 1, 2), (1/2, 1, 0), and (1/2, 1, 1) superlattice reflections, indicating a doubling of the unit cell along the *a*-axis.

2.2.2.2 $HoBaCo_2O_5$

Neutron powder diffraction measurements have shown this material first transforms from PM to AFM state at ~ 340 K, with appearance of additional satellites with wave vector (1/2, 1/2, 0) [19]. With further cooling of the sample, charge ordering of Co^{2+} and Co^{3+} ions occurs at T_{CO} ~ 210 K, with doubling of the unit cell along the *b*

direction, and change of space group symmetry. This transition is accompanied with an increase in the insulating behaviour of the system.

2.2.2.3 $La_{1.5}Sr_{0.5}CoO_4$

Zaliznyak *et al.* using elastic and quasi-elastic neutron scattering on a single crystal of $La_{1.5}Sr_{0.5}CoO_4$ found superlattice reflections due to the charge ordering of Co^{2+} and Co^{3+} ions and magnetic ordering [20]. The magnetic ordering peaks have a wave vector $q = (0.5+\varepsilon, 0, 1)$ which is slightly incommensurate $\varepsilon \approx 0.017$. They found that the stripes are better correlated within the layers, with diffuse scattering in the c^* direction. The magnetic peaks have a larger correlation length than the charge peaks (ξ_S / ξ_C ~ 79/26) both in plane and normal to these planes. They found the charge ordering transition temperature is more than 25 times higher than the characteristic energy scale of the cooperative spin fluctuations suggested charge ordering is independent of magnetic order.

Magnetoresistance (MR), but of a much smaller size those of the manganites, has also been observed in $La_{1-x}Sr_xCoO_3$ and $LnBaCo_2O_{5.4}$ (Ln = Eu, Gd) [21].

2.2.3 Vanadates

2.2.3.1 NaV_2O_5

The crystal structure of NaV_2O_5 consists of double chains of edge-sharing distorted tetragonal VO_5 pyramids running along the orthorhombic b-axis, which are linked together via common corners of the pyramids to form sheets. These in turn are stacked upon each other along c-axis with no direct V-O-V links. The Na atoms are located between these sheets. Konstantinovic *et al.* studied this material by Raman spectroscopy and argued that NaV_2O_5 undergoes a charge ordering phase transition at T_{CO} ~ 34 K. This phase transition is accompanied with redistribution of the charges, corresponding to a change of the vanadium ions valence, from uniform $V^{4.5+}$ to different V^{4+} and V^{5+} states [22].

^{23}Na and ^{51}V NMR measurements also showed that above T_{CO} ~ 34 K all the V sites are in an uniform state with the average oxidation of $V^{4.5+}$, but below this

temperature there are two inequivalents sets of V^{4+} and V^{5+}, an indication of charge ordering preceding the lattice distortion [23].

X-ray diffraction techniques using anomalous scattering near the vanadium *K* - absorption edge has been used to study charge ordering in NaV_2O_5 [24]. A dramatic energy dependence of the intensity of the superlattice reflection (15/2, 1/2, 1/4) was observed below $T_{CO} \sim 35$ K. The temperature dependence of the intensity of this peak at the vanadium *K*-absorption edge and below the edge is shown in Figure 2.6. The proposed charge ordering pattern is the fully charged zigzag-type ladder with the unit cell $2a \times 2b \times 4c$.

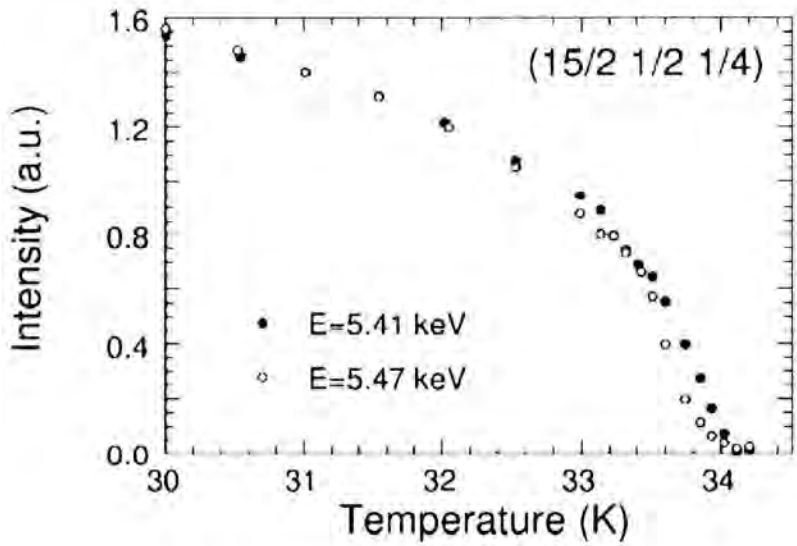

Figure 2.6 Intensity as a function of temperature at the vanadium *K*-absorption edge, and well below the edge. (taken from Nakao *et al.* [24])

More recently, Konstantinovic *et al.* published a polarized Raman study of NaV_2O_5 single crystal and concluded that the charge ordering does not have a static form below $T_{CO} \sim 34$ K and that true long-range charge ordering forms at $T \sim 0$ K [25].

2.3 Charge ordering in nickelates

2.3.1 Introduction

The nickelates have attracted much interest after the discovery of high-temperature superconductivity in the $La_{2-x}Sr_xCuO_4$ system. $La_{2-x}Sr_xNiO_4$, which is isostructural to

$La_{2-x}Sr_xCuO_4$ shows charge ordering at low temperature, has been chosen as a candidate for the study and understanding of any possible relationship between charge ordering and superconductivity.

The parent compounds, La_2NiO_4 and La_2CuO_4 are antiferromagnetic Mott insulators with the layered perovskite K_2NiF_4 structure [26, 27]. They are charge-transfer insulators, in which the charge-transfer band gap (i.e. the band gap between the unoccupied Cu/Ni 3d and occupied O 2p states) in La_2NiO_4 is about 3.5 eV twice as large as that one of in La_2CuO_4 [28, 29]. The coupling of spins within each Ni/CuO_2 planes is much stronger than that between spins in neighbouring planes [30]. They have a high degree of oxygen 2p character in the valence band and a transition metal 3d character in the conduction band [31].

La_2NiO_4 and La_2CuO_4 become metallic when a sufficient amount of holes are doped into the systems by the Sr^{2+} ion substitution for the La^{3+} ions. However, the critical hole concentrations, which are necessary for the insulator-metal transition, are considerably different between these two systems. In nickelates, metallic behaviour appears only around $x = 1$ [32], whereas $La_{2-x}Sr_xCuO_4$ becomes metallic and shows superconductivity for x as small as 0.05. In $La_{2-x}Sr_xNiO_4$ superconductivity has not been found for any value of x, suggesting that the doped hole carriers have considerably different behaviour between these two systems. The absence of bulk superconductivity in $La_{2-x}Sr_xNiO_4$ may be linked with smaller polaron size in this system [33]. La_2CuO_4 is a 3-dimensional long-range antiferromagnet. When holes are introduced into this system, the dimensionality changes to one of 2-dimensional short-range order, followed by an insulator-metal transition and superconductivity [34-36]. The difference in electrical and magnetic properties of these two systems has been attributed to the strong electron-lattice coupling in nickelates [37, 38] and the small mobility of the charge carriers in nickelates, because the holes have a greater 3d character compared to those in the cuprates [29].

2.3.2 Electrical and magnetic properties

Before moving on to describe the charge ordering in the nickelate $La_{2-x}Sr_xNiO_4$ system, it would be helpful to start with the general properties of this system. The temperature dependence of the resistivity, ρ, for different Sr concentrations is

displayed in Figure 2.7. The general trend of the resistivity is the same for all different stoichiometries and it increases at low temperatures, with the onset temperature depending on x (Sr concentration). The inset of the Figure shows the temperature derivative of the logarithmic resistivity with a clear indication of anomaly at x = 1/2 and 1/3.

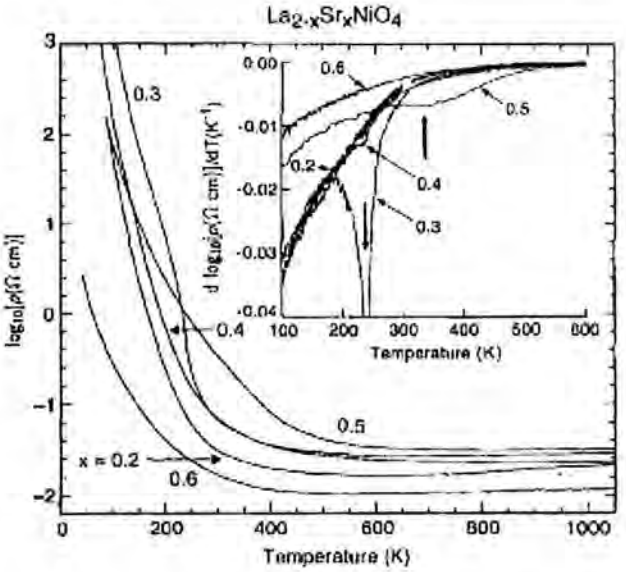

Figure 2.7 Logarithmic resistivity versus temperature for various Sr concentrations. The inset shows the temperature derivative of the logarithmic resistivity. (taken from Cheong *et al.*[39])

The normalized resistivity of $La_{1.67}M_{0.33}NiO_4$ (M = Ba, Sr, or Ca) as a function of temperature is shown in Figure 2.8 [40].

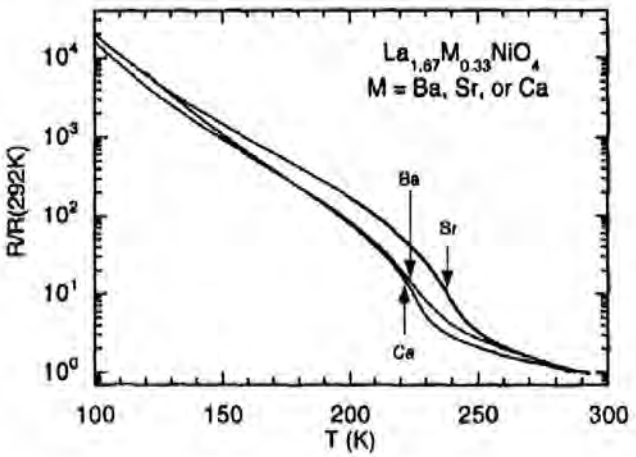

Figure 2.8 Normalized (room temperature) resistivity versus temperature of $La_{1.67}M_{0.33}NiO_4$ (M = Ba, Sr, or Ca). (taken from Han *et al.*[40])

The resistivity shows an abrupt increase at ~ 240 K, that is the charge ordering transition temperature. The charge ordering transition temperatures depend on the hole concentration and are approximately independent of the divalent ions (± 10 K). The ionic size of the dopant is not an important factor for the transition temperature, in contrast with the manganite systems. Han *et al.* suggested that the sudden increase of resistivity at T_{CO} shows that the holes in the polaronic states do not contribute to the conduction because they are frozen in the ordered state below T_{CO}. The temperature dependence of the sound velocity of $La_{2-x}Sr_xNiO_4$ (x = 0.25, 0.33, and 0.4) is shown in Figure 2.9 with a clear anomaly for x = 0.33 at ~ 240 K [41].

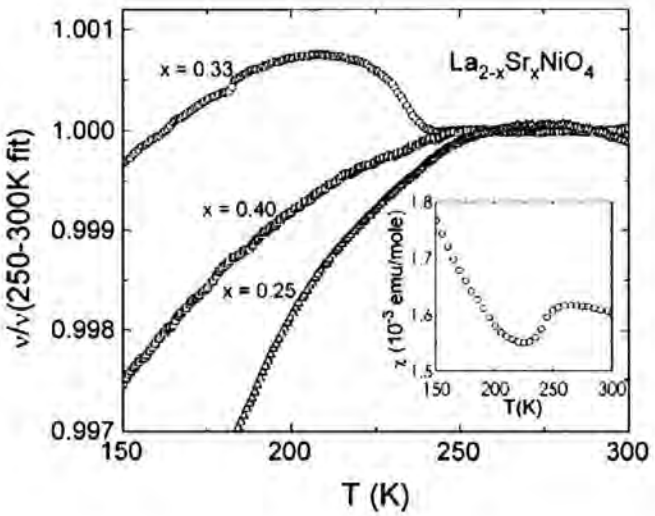

Figure 2.9 The sound velocity of $La_{2-x}Sr_xNiO_4$ for x = 0.25, 0.33, and 0.4. Inset: the susceptibility for x = 0.33. (taken from Ramirez *et al.* [41])

At the charge ordering transition temperature 240 K, the sound velocity, specific heat, resistivity, and magnetic susceptibility all show an obvious anomaly for x = 0.33, as displayed in Figure 2.10 [41]. In Figure 2.11 the temperature derivative of logarithmic resistivity and susceptibility of $La_{2-x}Sr_xNiO_4$ systems as a function of temperature is shown [39]. Again, for the hole concentration x = 0.33, the anomaly at ~ 240 K is very noticeable.

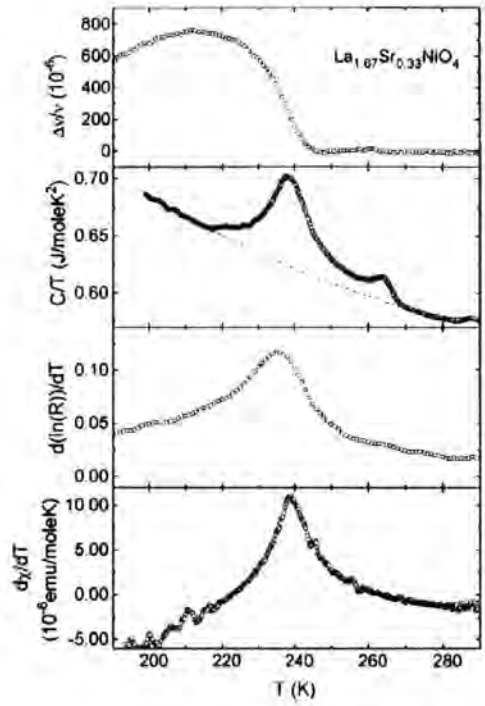

Figure 2.10 The sound velocity (normalised with a linear temperature dependence in the temperature range 250 K < T < 300 K), specific heat Cp/T, temperature derivatives of resistivity d ln ρ/dT, and magnetic susceptibility dχ/dT for $La_{1.67}Sr_{0.33}NiO4$. (taken from Ramirez *et* al. [41])

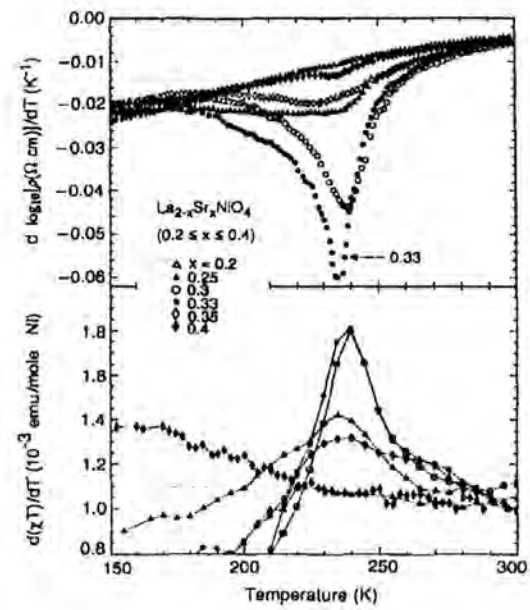

Figure 2.11 The temperature derivative of the logarithmic resistivity (upper panel) and susceptibility multiplied by temperature as a function of temperature (lower panel) for Sr concentration $0.2 \leq x \leq 0.4$. (taken from Cheong *et al.* [39])

2.3.3 Charge ordering

Hole doping in La_2NiO_4 systems can be achieved by two ways: 1- substitution of divalent ions such as Sr^{2+}, Ca^{2+} or Ba^{2+} for La^{3+} ions, 2- intercalation of excess oxygen. The doped holes in nickelates tend to order within the system at low temperature. These ordered holes act as domain walls in the NiO_2 planes, in which the Ni spins, are ordered antiferromagnetically within the domains. As the charge ordering in nickelates systems have a 2D nature, so it has a stripe-like form and is called a charge stripe. A schematic view of these charge stripes is shown in Figure 2.12.

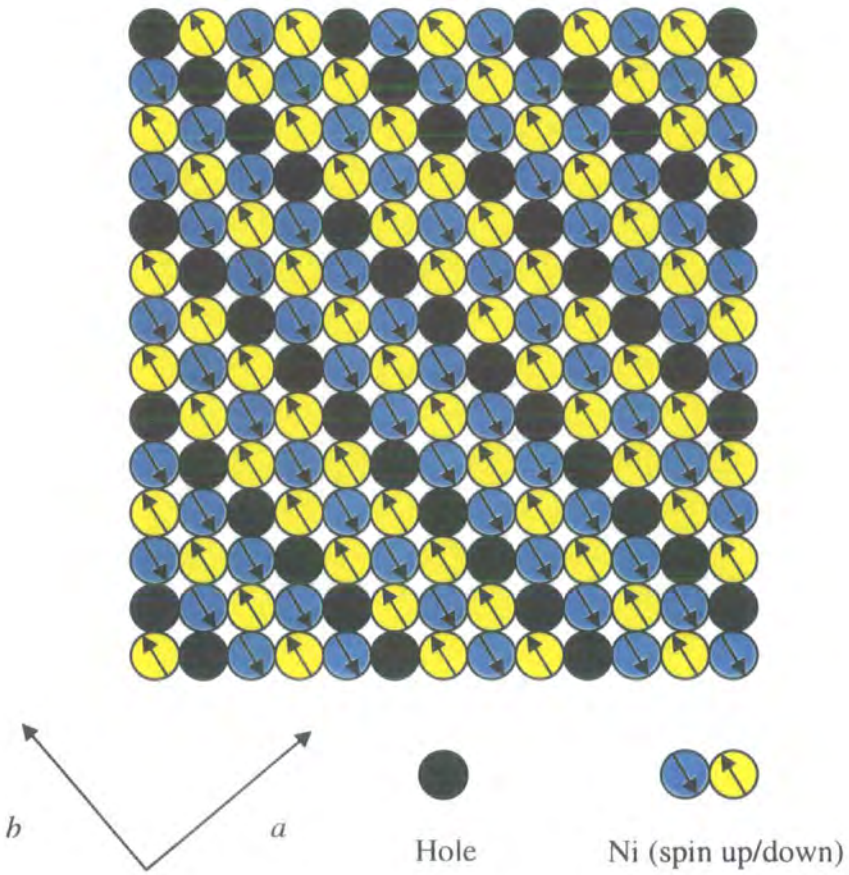

Figure 2.12 A schematic representation of the charge stripes in nickelate $La_{2-x}Sr_xNiO_4$. The coordinate axes are rotated 45°with respect to the Ni-Ni bond.

The existence of such charge and spin stripes in both $La_{2-x}Sr_xNiO_4$ and $La_2NiO_{4+\delta}$ systems have been proved by various methods including neutron [42-47], electron [2, 39], and x-ray scattering [48, 49] for x up to 0.5. The coexistence of superconductivity and stripe order has also been observed in $La_{1.6-x}Nd_{0.4}Sr_xCuO_4$ with x = 0.12, 0.15, and

0.2 [50, 51]. Neutron diffraction has been used in the study of the spin, as well as the charge-structure and the results of these measurements show that as the hole concentration is increased, 3D antiferromagnetic order is replaced by 2-dimensional correlation within the NiO_2 planes [30, 43-46, 52-55].

The incommensurability, ε, in the Sr doped nickelate is approximately linear in n_h up to 0.5, in sharp contrast with the $La_{2-x}Sr_xCuO_4$ [50, 56, 57]. There is a systematic deviation from the $\varepsilon \sim n_h$ law around $n_h = 1/3$, and this deviation strongly influences transport properties [58]. Charge and spin ordering temperatures reach a maximum at $n_h = 1/3$, and they decrease beyond $n_h = 1/3$. Both Sr and O doped nickelates show strong commensuration effects, that is the stripe spacing tends to lock in at a value commensurate with the lattice spacing [37, 43, 45, 54, 59]. Optical conductivity measurements on the $x = 1/3$ compound have shown the gradual opening of a charge gap up to ~ 0.26 eV below T_{CO}, indicating that such stripe ordering strongly affects the electronic structure of the compound [60] and that causes strong localization of hole carriers and binding of charges to the lattice [28].

Neutron scattering studies of the nickelate systems with different hole concentrations have revealed the correlation length of the stripes can be classified into the three regions as a function of n_h [55]. For $n_h \leq 1/4$, the correlation length is short, both within, and perpendicular to the NiO_2 planes, and the stripe order is essentially three-dimensional short-range order. For $n_h \geq 0.4$, on the other hand, the stripe order is well developed within the NiO_2 planes, but is less correlated between the NiO_2 planes, being quasi-2D long-range order. Near $n_h = 1/3$, the inverse correlation length shows a minimum, and the stripe order is quasi-3D long-range order, demonstrating the stability of the stripe order at $n_h = 1/3$. From this studies, Yoshizawa *et al.* concluded that in the stripe model, the hole density in a stripe n_{st} is always $n_{st} = 1$ for all ε when the $\varepsilon \sim n_h$ law holds. Here, the hole density in a stripe n_{st} is defined as n_{st} = [number of holes/Ni site]/[number of domain walls (DW)/Ni site] = n_h/ε. Because one hole exists per each Ni site, hole stripes are half filled. The deviation of ε from the $\varepsilon \sim n_h$ law indicates that the hole density deviates from 1 for both sides of $n_h = 1/3$. For $n_h \leq 1/3$, $n_{st} \leq 1$ and the carriers are expected to be electron-like, while for $n_h \geq 1/3$, $n_{st} \geq 1$ and the carriers are hole-like.

The stripes run along two equivalent diagonal directions e = (1, 1) or (1, -1) in the tetragonal unit cell with dimensions $a_t \times a_t$ in the basal plane, where a_t is the lattice parameter corresponding to the Ni-Ni spacing, compared to the cuprates which are horizontal. The stripe period perpendicular to the stripes for x = 1/3 is $3a_t/\sqrt{2}$ [61] and the average distance between domain walls in real space is $a/2\varepsilon$. On the basis of a Hartree-Fock study, the difference in the number of d electrons and the charge-transfer energy are essential factors for stabilization of vertical or diagonal charge stripes in cuprates and nickelates and it has been predicted that the diagonal charge stripes are stable in nickelates with a charge-transfer energy of $\Delta \sim 4$ eV [62].

In Sr-doped La_2NiO_4 (LSNO), the characteristic wave vector for the charge density modulation is $q_{CO} = (2\varepsilon, 0, 1)$ and $q_{SO} = (1+\varepsilon, 0, 0)$ for the spin density modulation. These wave vectors show only the dominant sinusoidal components of the charge and spin modulations. When the charge and spin modulations deviate from the sinusoidal, one expects appearance of the higher order superlattice reflections corresponding to higher Fourier components. Because the magnetic ordering is anti-phase in crossing the charge stripes, then for magnetic ordering only the odd harmonic satellites will appear. The relationship between charge and spin wave vectors indicates that the period of the spin structure in real space is twice that of the charge modulation. These results have also been predicted by Landau theory of coupled charge and spin-density-wave order [63]. The charge ordering state in nickelates is accompanied by spin ordering at lower temperature indicating that the magnetic order is driven by charge order. This idea, that the spin ordering is a sequence of charge ordering, has been predicted by analysing the stripes with Landau theory [63]. From this study Zacher *et al.* concluded that the driving force for the stripes is Coulomb-frustrated phase separation. The holes attempt to separate into hole-rich regions and hole-poor regions with antiferromagnetic spin order to minimize their kinetic energy. This phase separation is frustrated by long-range Coulomb interaction between the holes. The coexistence of charge and magnetic ordering implies that the interaction between the spin and charge ordering has an important role in physical properties of this system.

On the basis of magnetic susceptibility measurements [47, 64] and La nuclear magnetic resonance study (NMR), Yoshinari *et al.* have suggested that $La_{2-x}Sr_xNiO_4$ might

have spin stripes, which are glassy in character, displaying only very short-range correlations [61]. Anomalies in the charge-ordering correlation length have been observed in both the *ab* plane and *c*-axis [2, 48]. Resistivity measurements on a single crystal of $x = 1/3$ has shown a large anisotropy in the ratio of the *ab* plane and *c*-axis resistivity (about 500 at room temperature) and similar anomalies in both the *ab* plane and *c*-axis resistivity at T_{CO} [60]. Both *ab* plane and *c*-axis resistivity show a sharp increase at 240 K and the magnetic susceptibility drops slightly at this temperature. Anisotropy has also been seen in phonon thermal conductivity measurements on $x = 1/3$ single crystal in the *ab* plane and *c*-axis that shows the ratio of the height of the low-temperature-maxima $\kappa_c^{max}/\kappa_{ab}^{max} \approx 1.7$, with clear kinks near T_{SO} and T_{CO} [65]. From these measurements Hess *et al.* suggested the anisotropic behaviour of κ near T_{CO} suggests that the charge-ordering transition is of the static-dynamic type and not a static order-disorder transition.

So far, charge stripes in the nickelate is confirmed in the oxygen-doped $La_2NiO_{4+\delta}$ compounds with $\delta = 0.105$, 0.125, 0.133 and 2/15 [37, 43, 52, 66] and the Sr-doped $La_{2-x}Sr_xNiO_4$ compounds with $x = 0.135$, 0.20, 0.225, 0.275, 0.289, 1/3, and 0.39 [42, 45, 46, 49 44, 55] by neutron diffraction.

Lander *et al.* using neutron diffraction on $x = 0.2$ sample have observed a second-order transition from the high-temperature tetragonal (*I4/mmm*) phase to the low-temperature orthorhombic (*Bmab*) phase at ~ 120 K [47]. They saw a peak at ~17 K in susceptibility measurements and suggested an anisotropic spin glass state for the low temperature with a freezing temperature of ~ 17 K. X-ray diffraction studies on a sample with the same Sr but with excess oxygen between 0.001 and 0.003 has revealed this structural transition at ~ 100 K [67].

The first incommensurate magnetic correlations were found by Hayden *et al.* on a $La_{1.8}Sr_{0.2}NiO_{3.96\pm0.06}$ single crystal by neutron diffraction [30]. They observed four incommensurate satellites at $(1\pm\delta, 0, 1/2)$ and $(1, \pm\delta, 1/2)$ in reciprocal space. The measured magnetic correlation lengths were 8.7 Å and 17 Å parallel and perpendicular to modulation direction respectively. The first evidence of a charge/lattice modulation came from the electron diffraction results by Chen *et al.* on polycrystalline $La_{2-x}Sr_xNiO_{4+y}$ samples [2]. They observed superlattice reflections in an

electron diffraction pattern at wavevector $q = (1, \pm\delta, 0)$ with $\delta \approx 1/3$ for $0.2 < x < 0.4$ samples. The [001] zone-axis electron diffraction pattern for $x = 0.2$ sample at 93 K is shown in Figure 2.13 (a), in which fundamental spots are indexed with an orthorhombic cell ($a \approx b = 5.35$ Å, $c = 12.4$.Å) and a schematic view of the superlattice spots is also shown in (b).

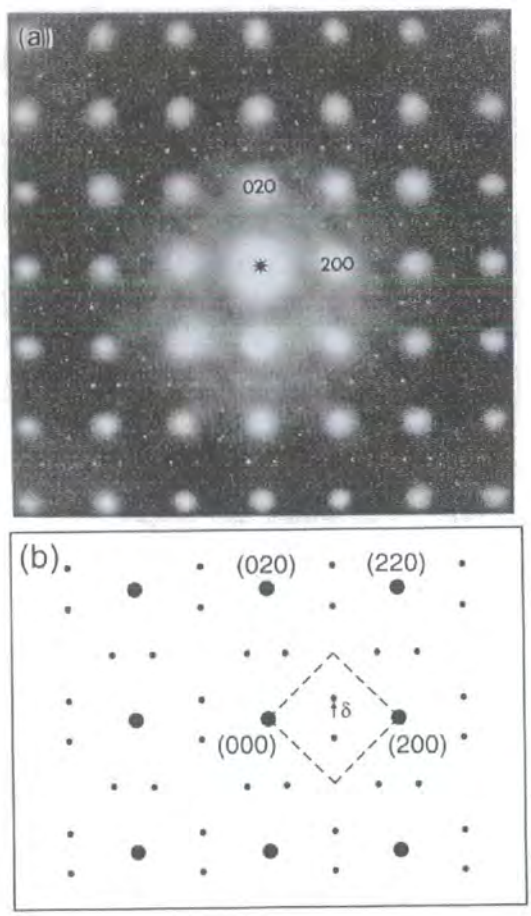

Figure 2.13 (a) The [001] zone-axis electron diffraction pattern for a $x = 0.2$ sample at 93 K. (b) A schematic view of the location superlattice spots in reciprocal space. (taken from Chen *et al.* [2])

The measured δ is twice as much as that of the δ measured by Hayden *et al.* for the magnetic reflections. These charge satellites were much sharper (~ 500 Å) than the magnetic correlations observed by neutron scattering, and they found that these superlattice modulations display quasi-2D order with a *c*-axis correlation length of 60 Å. They argued that these charge/lattice modulations arise from the ordering of self-localized holes due to the strong magnetic and phononic confinement, and

interpreted them in terms of polarons. They suggested that the ordering is restricted to special commensurate values of x such as 1/3 and 1/2.

In 1994, Cheong *et al.* measured the resistivity and magnetic susceptibility of a range of samples with different Sr concentrations [39]. They observed an increase of resistivity and a drop of susceptibility for an x = 1/3 sample below ~ 235 K and attributed this to the real-space ordering of the doped holes. They proposed the segregation of the hole carriers occurs for $0.2 \leq x \leq 0.4$ in such a way as to form mesoscopic domains.

In an oxygen over-doped sample $La_2NiO_{4+\delta}$ with $\delta = 0.125$ charge ordering as well as incommensurate magnetic ordering have been observed with strong temperature dependence of the incommensurability ε [43]. This combined ordering of charges and spins occur below 110 K and ε varying from 0.295 at 110 K to 0.271 at 10 K. The ordering involves sinusoidal modulations of the spin density and the Ni-O bond lengths within the NiO_2 planes. From this study, Tranquada *et al.* argued that the stripes could be viewed as hole-rich regions and stripes of antiferromagnetic spin ordering and the hole-rich regions acting as antiphase-domain boundaries.

Charge and spin ordering have also been observed by neutron diffraction on oxygen doped single crystal with δ = 2/15 [37]. In this sample charge stripes survive up to higher temperature, $T \approx 220$ K and the spin ordering satellites disappear at $T \approx 110.5$ K. Upon cooling the sample, the incommensurability is ε = 1/3 below the charge ordering temperature, and it jumps to ε = 0.295 at the magnetic ordering temperature. With further lowering of the temperature, ε decreases continuously. The authors suggested that the striped phase is O-centred at $T > T_{SO}$ and it changes to the Ni-centred stripe at low temperatures. The stripe models in this compound for ε = 1/3 that have been proposed by Tranquada *et al.* are shown in Figure 2.14 [66].

Further studies of the x = 0.2 and 0.135 single crystals by neutron scattering revealed the presence of charge and spin ordering satellites below ~ 150 K and ~ 100 K respectively, and only magnetic peaks for the x = 0.135 crystal [46]. In this neutron scattering studies, Sachan *et al.* observed magnetic peaks at $(1\pm\varepsilon, 0, l)$, for integer l and charge reflections at $(4-2\varepsilon, 0, l)$, with l odd. They mentioned that the incommensurability, ε, is almost exactly 1/4 for an x = 0.2 crystal and for an x =

0.135 sample it is $\varepsilon \approx 0.12$ with a magnetic transition temperature of ~ 65 K. They suggested the proper parameter for charactering the periodicity of the ordering and transition temperature is the net hole concentration that can be calculated as $n_h = x+2\delta$ and the incommensurability follows the $\varepsilon \approx n_h$ law.

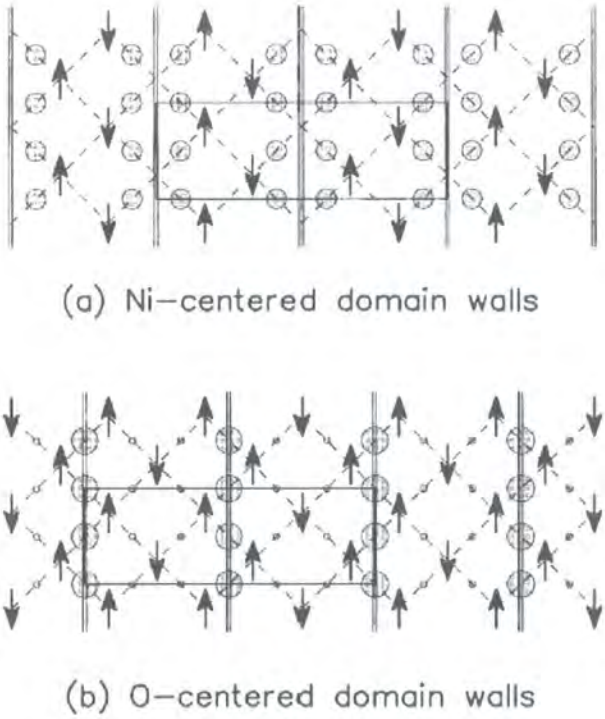

Figure 2.14 Stripe models for ε = 1/3. Arrows and shaded circles indicate Ni spins and holes respectively. Solid lines and double lines indicate the magnetic unit cell and positions of domain walls respectively. (a) Ni-centered domain walls and (b) O-centered domain walls. (taken from Tranquada *et al.* [66])

In 1996 and 1997 an $x = 0.225$ single crystal was studied by using neutron- and hard X-ray diffraction respectively [45, 49]. The neutron results show the magnetic peaks disappear at ~ 100 K and the charge order peaks vanish at ~ 150 K with the magnetic correlation length of 150 Å in an h-scan twice as large as the charge order correlation length at low temperature. The incommensurability was found to be temperature dependent, and at low temperature it is $\varepsilon \approx 0.275$. Their intensity profile, width, and incommensurability, ε, is displayed in Figure 2.15. Hard x-ray scattering results on the same sample are in agreement with that observed by neutron scattering and they

also observed scattering due to the spin correlations with an intensity of 10^{-8} of the corresponding Bragg peaks.

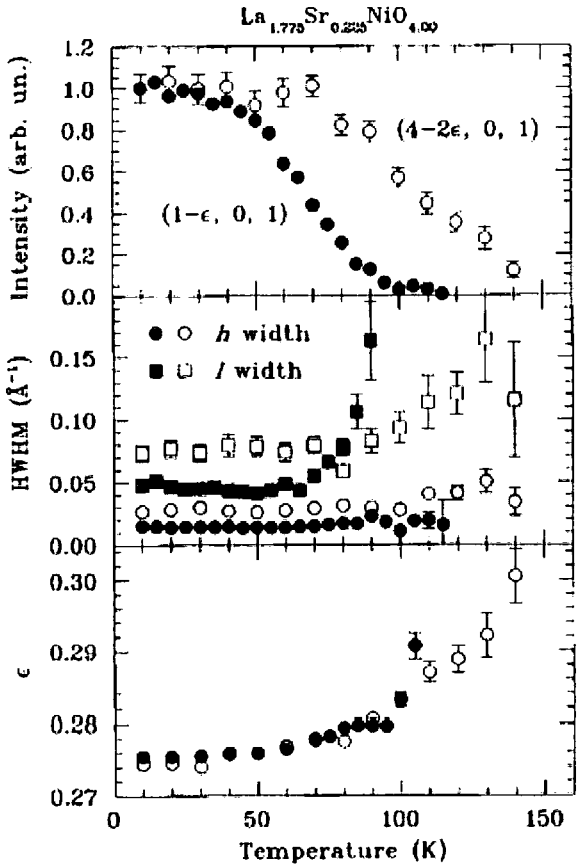

Figure 2.15 Intensity, peak width and incommensurability, ε, as a function of temperature. Solid and open symbols indicate magnetic- and charge-order. (taken from Tranquada *et al.* [45])

2.3.4 Charge ordering in x = 1/3 compound

The first neutron diffraction study on $La_{2-x}Sr_xNiO_4$ with x = 1/3, which is a special hole concentration with commensurate charge and spin ordering, was reported by Lee *et al.* [42]. According to their results the charge and spin ordering temperatures are ~ 239 K and ~ 190 K respectively. The measured in-plane charge order correlation length (350 Å) is about 3 times longer than the spin one and interpreted that the charge ordering is the driving force for spin ordering. From these measurements it was concluded that in temperature range 190 K < T < 240 K the quasi-2D charge stripes are in a glassy form with a short-range correlation length and the Sr ions may

play an important role in this intermediate temperature region. Their charge and spin ordering wave vectors are not consistent with other studies and also with our experiments (see chapter 5). In this compound ε does not show any temperature dependence in contrast with the considerable temperature dependence of ε when $\varepsilon <$ 1/3 or $\varepsilon >$ 1/3, indicating the stability of the ε = 1/3 modulation, probably due to the commensurability effect [42].

Recent neutron scattering studies of the charge and magnetic ordering in Sr doped nickelates with $0.289 \leq x \leq 0.5$ showed that the incommensurability, ε, is approximately linear with hole concentrations n_h up to 0.5 with a systematic deviations around n_h = 1/3 [55]. These results show the charge and spin ordering temperatures are maximum at n_h = 1/3 and decrease in both sides of the n_h = 1/3. Their results for incommensurability and transition temperatures are displayed in Figure 2.16.

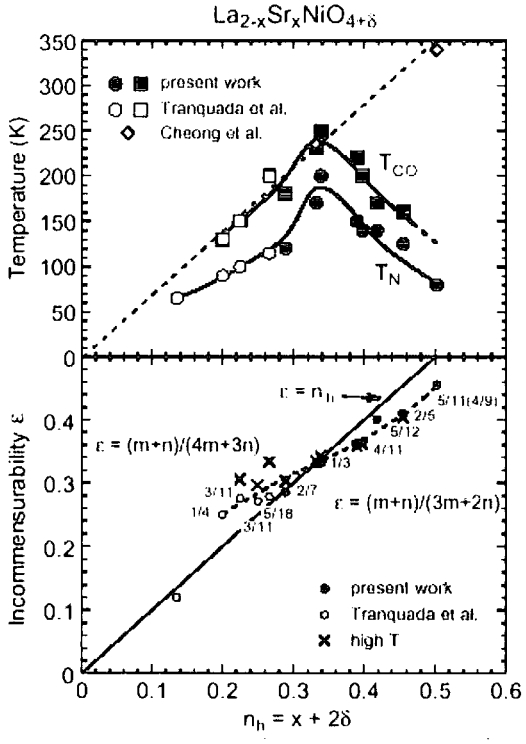

Figure 2.16 T_{CO}, T_{SO} and incommensurability, ε, as a function of the hole concentration n_h. (taken from Yoshizawa *et al.* [55])

The incommensurability, ε, is exactly 1/3 when n_h = 1/3, but when n_h deviates from 1/3, ε does not follow the n_h and tends to stick to 1/3. One can see $\varepsilon > n_h$ for $n_h <$ 1/3 and $\varepsilon < n_h$ when $n_h >$ 1/3. Yoshizawa *et al.* concluded that the stripe order is a

combination of the $\varepsilon = 1/3$ stripe order and $n_h = 1/2$ charge order within the 2D NiO_2 planes for $1/3 \leq n_h \leq 1/2$. In $n_h = 1/3$ because the charge and spin wavevectors coincide with each other, this coincidence with electron-lattice coupling maybe stabilize the charge stripes. They proposed quasi-3D long-range order for the $n_h = 1/3$ compound.

More recently Lee *et al.* by polarized neutron scattering have claimed that spins in the spin ordered phases are canted by an angle θ from the stripe direction [44]. This deviation angle for $x = 0.275$ is $\theta \sim 27°$ and for $x = 1/3$ is $\theta \sim 40°$. They found another phase transition with canted angle $\theta \sim 53°$ at $T < 50$ K for $x = 1/3$ and suggested this is due to the further localization of charge carriers. They found the in-plane spin correlation length, 300 Å, is three times larger than charge correlation length, 100 Å. The intensity profiles for $x = 0.275$ and $x = 1/3$ compounds are shown in Figure 2.17. As the graph shows, the spin- and charge-ordering transition temperatures for $x = 0.275$ are 155 K and 200 K respectively.

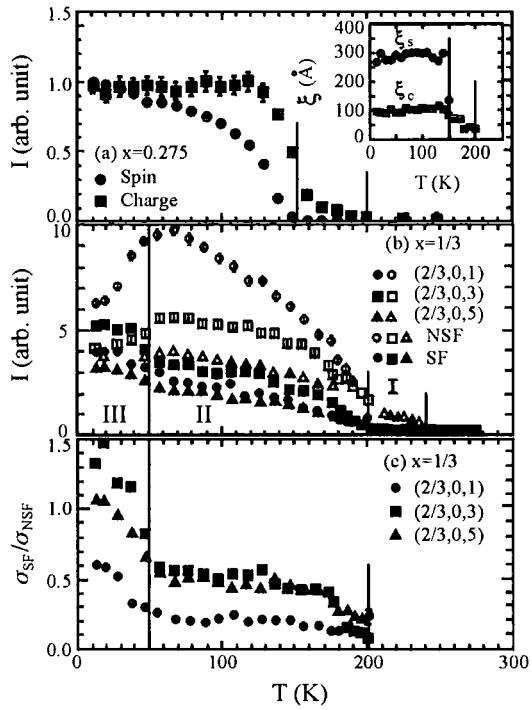

Figure 2.17 (Top) Temperature dependence of unpolarized elastic neutron scattering intensities of the charge and the spin peaks for $x = 0.275$. (Middle) non-spin flip (charge, open symbols) and spin flip (spin, filled symbols) scattering intensities at various superlattice reflections from $x = 1/3$ as a function of temperature. (bottom) Temperature dependence of the ratio of spin flip to non-spin flip scattering intensities after backgrounds were determined above the transition temperature and subtracted. (taken from Lee *et al.* [44])

An NMR study of x = 1/3 has revealed that magnetic order is suppressed by 30 K when detected on the μ-sec time scale of NMR compared to pico-second neutron scattering and attributed this suppression to the glassy character of stripe order [61]. Raman spectroscopy results have revealed that the magnetic order is driven by charge order and the existence of over-damped short-range AF correlations above T_{CO}, suggesting fluctuating stripes in the high-temperature phase [59]. Yamamoto *et al.* by Raman scattering suggested that the main effect on the spin correlation as well as the electronic structure, is the charge ordering transition [68]. It has been suggested that $La_{2-x}Sr_xNiO_4$ might have a spin glass ground state [47, 64], but such behaviour has not been confirmed by muon-spin-rotation measurements [31]. Some authors have suggested the appropriate parameter for controlling the magnetic transition temperature is not $n_h = x+2\delta$ but x itself [46, 69]. McQueeney *et al.* by theoretical and experimental studies have suggested for x = 1/3, that there maybe a mixed state of O- and Ni-centered stripe phases, and sensitivity to temperature, pressure and magnetic field [70].

Measurements of optical conductivity spectra in a sample of x = 1/3 have shown the opening of a charge gap below T_{CO}, that saturates at 0.26 eV, at low temperature (see Figure 2.18) [60]. The charge gap is approximately zero at ~ 240 K and then increases with decreasing temperature.

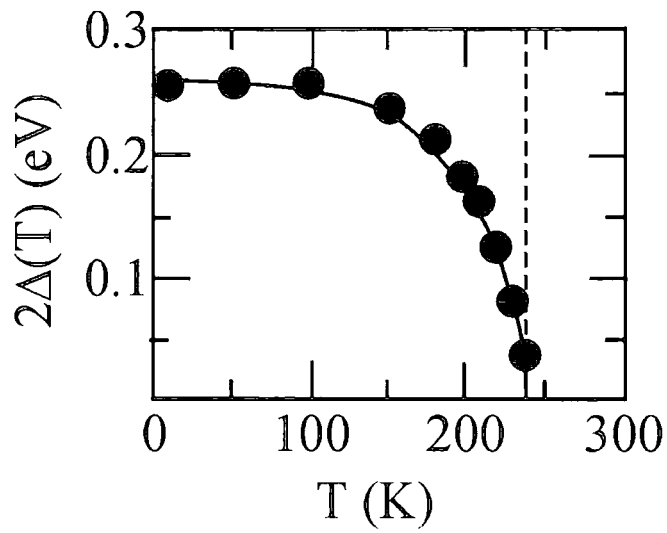

Figure 2.18 Temperature dependence of the magnitude of the energy gap. (taken from Katsufuji *et al.* [60])

Based on experiments on $La_{2-x}Sr_xNiO_4$ there is the suggestion that the charge ordering is a result of the formation of a small polaron lattice [2, 38]. Theoretical studies have shown that polaronic and/or stripe states are formed due to the competition between long-ranged Coulomb repulsion of the doped holes and short-ranged attractive interactions such as magnetic confinement effects or electron-lattice coupling [38, 71, 72]. The Hall coefficient (R_H) (see Figure 2.19) and thermoelectric power (S) measurements have revealed the sign of the R_H and S at $T < T_{CO}$ is negative for $x < 1/3$, whereas it is positive for $x > 1/3$ [58]. This indicates the change of the sign comes from a change of the character of the carriers from electron-like to hole-like carriers when x crosses the 1/3 point.

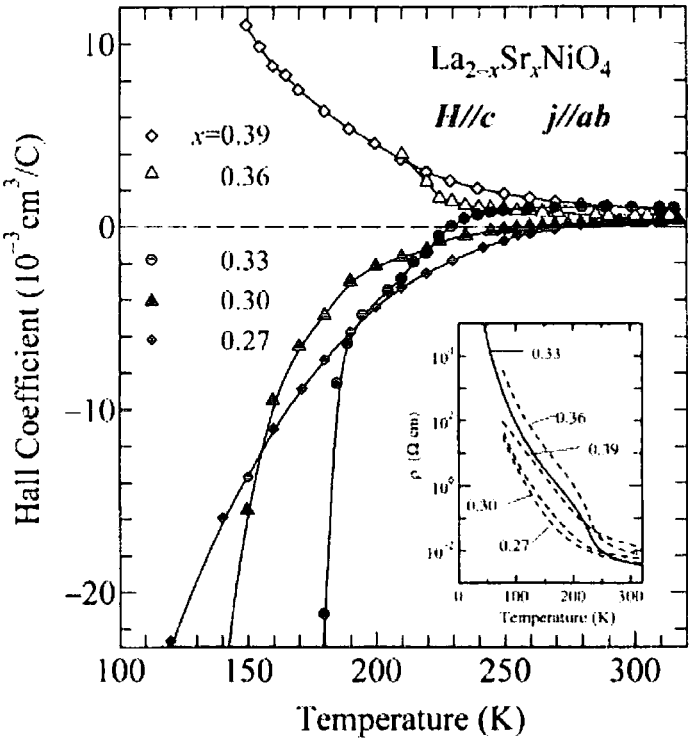

Figure 2.19 Temperature dependence of the in-plane Hall coefficient for $La_{2-x}Sr_xNiO_4$ crystals with various hole concentrations. The inset shows the temperature dependence of the in-plane resistivity. (taken from Katsufuji *et al.*[58])

One of the major questions in doped nickelates systems is: do the doped holes reside on metal sites or oxygen sites? According to oxygen 1s x-ray absorption spectroscopy (XAS) it has been suggested that the doped holes have primarily O 2p character [73]. But Tan *et al.* by Ni K-edge XAS measurements have found that the

doped holes also have a substantial amount of Ni d character and suggested a mixture of Ni 3d and O 2p character [74]. They believed a hole with a mixed character is probably more localized.

Zachar has argued about the disorder in stripes correlation and suggested that the stripes are disordered primarily by nontopological elastic deformations [75]. If the disorder is due to the topological defects, it should lead to the charge stripes correlation length being larger than spin stripes, i.e. $\xi_S/\xi_C < 1$ while predominant elastic deformation lead always to $\xi_S/\xi_C > 1$.

2.4 Charge, spin and orbital ordering in manganites

2.4.1 Introduction

The rare earth manganites $Ln_{1-x}A_xMnO_3$ (Ln = trivalent lanthanide; La, Pr, Nd, Y, Eu, Sm and A = divalent alkaline earth, such as Ca, Sr, Ba) have perovskite structure. The perovskite lattice structure of these materials is shown in Figure 2.20.

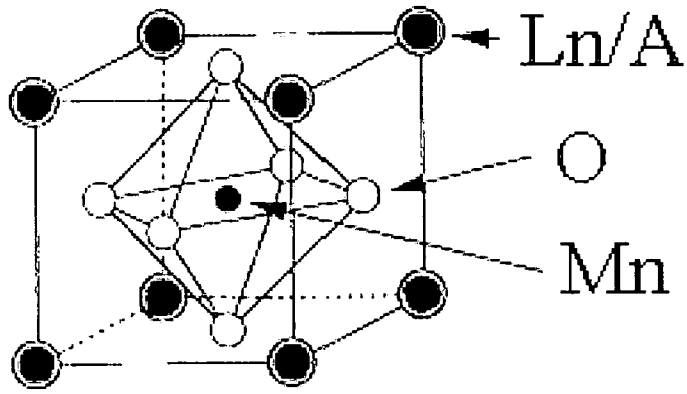

Figure 2.20 The perovskite structure of the manganites. (taken from Tokura [76])

Perovskites provide an ideal material for studying the physics of strongly correlated electronic systems, since they exemplify many basic interactions. Although studied in the 1950's, interest in the manganites has been renewed with the experimental

observation of a large magnetoresistance (MR) effect in $Nd_{0.5}Pb_{0.5}MnO_3$ by Kusters *et al.* [77] and in $La_{2/3}Ba_{1/3}MnO_3$ by Vonhelmolt *et al.* [78].

In manganites the doping level x controls the proportion of Mn atoms in the Mn^{4+} oxidation state. In addition to the discovery of colossal magnetoresistance (CMR) effect, which has potentially many technological applications, two very attractive phenomena exhibited by this system are the charge-order (CO) and the orbital-order (OO) states. Without hole doping, parent compounds such as $LaMnO_3$, $PrMnO_3$, $CaMnO_3$ and $NdMnO_3$ are all insulators at all temperatures.

Manganese has four electrons in the 3d state and is surrounded by the oxygen octahedron. These four electrons are spin aligned due to Hund's rule to minimize the electrostatic repulsions, which is believed to be large [79]. Electrostatic interaction between these four electrons and the neighbouring oxygen ions (crystal field) cause partial lifting of the degeneracy of the 3d orbitals, and they split it into two energy sublevels. Three of these electrons occupy the lower t_{2g} (triply degenerate) energy state and the remaining electron occupied a higher e_g (doubly degenerate) level. The t_{2g} orbitals point 45 degrees from the oxygen atoms, so their electrons, are viewed as localized electrons due to the weak hybridisation with O 2p states and forming the local spin ($S = 3/2$) even in the metallic state. The two e_g orbitals point directly to the oxygen atoms, are strongly hybridized with the oxygen p orbitals, which are responsible for conduction [80].

Changing the Mn valence by doping holes into the system, adds potentially mobile charge carriers, whereas smaller cations tend to induce insulating behaviour. When the Mn valence is in the intermediate region between Mn^{3+} and Mn^{4+}, different states can be seen, ferromagnetic (FM), antiferromagnetic (AFM), paramagnetic (PM) and CO state. In a FM state the electrons are mobile and the charge density on each Mn site is identical, the mobile electrons promote ferromagnetism by aligning the core spins on the Mn ions in a process called double exchange (DE) (see section 2.4.4). Alternatively the charge segregates preferentially between different sites of Mn^{3+} and Mn^{4+} valence, which is a CO state (insulator). Charge ordering was first observed by Wollan and Koehler [79].

In manganites with the perovskite structure, Coulomb repulsion, the effect of Jahn–Teller distortion on the e_g energy levels, lattice distortions arising from electron–

lattice interactions, and the double-exchange interaction play an important role in the many different states of the solid especially in the stability of the CO state. For example, in the FM state the dominant magnetic interaction is the ferromagnetic (FM) double exchange due to the strong Hund coupling of the itinerant e_g electrons with the t_{2g} ones. In the charge ordered phase, the dominant magnetic couplings are the superexchange interactions. These superexchange interactions are FM or AFM depending on which orbitals are involved in interaction [79, 81].

2.4.2 Colossal magnetoresistance

Colossal magnetoresistance (CMR) is a dramatic change in electrical conductivity of a particular family of manganites at some concentrations x, by application of an external magnetic field. This effect has generated a great motivation to the study of the manganite systems due to possibility of producing devices, especially in magnetic recording heads, which make use of this effect. The Curie temperature T_C decreases as the magnitude of the magnetoresistance effect increases and this affects the application of these materials in magnetic devices. CMR behaviour was first discovered in a compound with the perovskite structure, (La/Pb)MnO_3 [82]. The resistivity change observed in these materials is so large, compared to the giant magnetoresistance (GMR) observed in magnetic multilayers, that it was called colossal magnetoresistance (CMR).

Magnetoresistance MR is defined as:

$$MR = \left[\frac{\Delta\rho}{\rho(0)}\right] = \left[\frac{\rho(H) - \rho(0)}{\rho(0)}\right] \qquad [2.1]$$

where $\rho(H)$ and $\rho(0)$ are the resistance at high applied magnetic field (H), and at zero field respectively.

The CMR effect occurs in a small temperature region near the Curie temperature, showing that the spin alignment and the electrical transport are closely related. It is believed that a strong coupling of electrons to the lattice (favouring insulating behaviour) is one of the essential issues to explain the CMR effect. In this scenario, the electrons (or holes) are trapped by local lattice distortions, and these polarons, i.e. the localized holes and the surrounding lattice strain, inhibit the flow of current.

Another important interaction is the double-exchange interaction which favours the ferromagnetic metallic (FMM) state.

The results obtained on various compounds clearly show that the CMR effect results from the coexistence of two competing phases, a ferromagnetic metallic phase with an antiferromagnetic insulating phase (AFMI) [83]. Martin *et al.* by combining neutron diffraction, electron microscopy, and magneto-transport measurements to study the phase diagrams of the four $Ln_{1-x}A_xMnO_3$ series (Ln = Pr,Sm; A = Ca,Sr) concluded that the coexistence of ferromagnetism and metallicity is a very important factor for the appearance of CMR [84]. In hole doped regions, SmSr, PrSr, NdSr, and LaCa manganites, which have a larger $<r_A>$, should show CMR in the whole FMM range. In the electron-doped region, CMR will be obtained where FM and AFM are competing, i.e., for SmCa, PrCa, and LaCa manganites. Finally, the CMR effect can also appear at the boundary of the FM state, in the hole doped charge ordered state, provided that the latter is metastable such as PrCa manganites ($0.30 < x < 0.45$).

The phase diagram of the $La_{1-x}Ca_xMnO_3$ system is shown in Figure 2.21. CMR has been observed in the Ca concentration rang $0.2 < x < 0.5$.

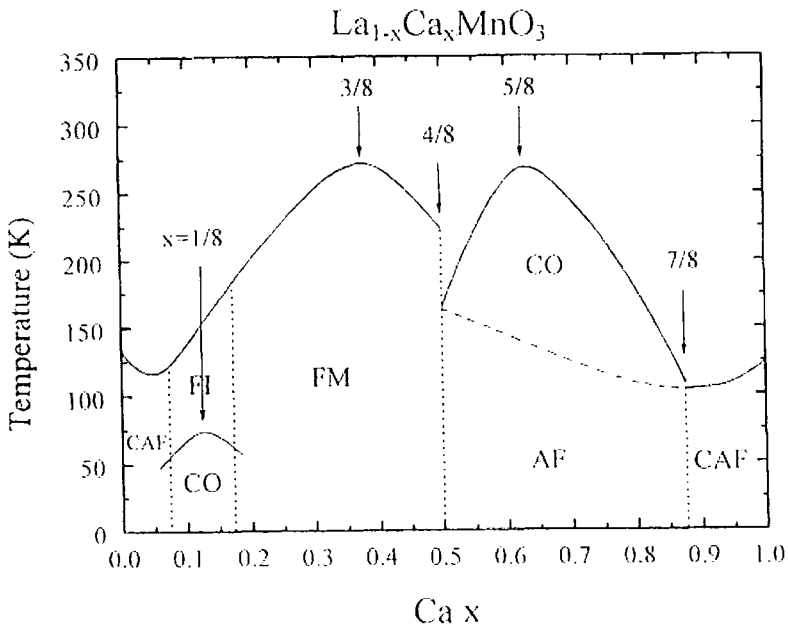

Figure 2.21 The phase diagram of $La_{1-x}Ca_xMnO_3$. (taken from Cheong *et al.* [85])

The $La_{1-x}Ca_xMnO_3$ system in doping rang $0.2 < x < 0.5$, exhibits a transition from PM to FM state with a sharp drop of the resistivity. CMR occurs as a result of rapid

change of the transition temperature in the presence of applied magnetic field. For $Pr_{1-x}Sr_xMnO_3$ this range is for Sr concentrations between 0.25 and 0.55 [84].

2.4.3 Charge, orbital, and spin ordering

Charge ordering is a phenomenon that has been observed in wide range of materials including manganite systems. Below a certain temperature T_{CO}, electronic carriers become localized onto specific sites and show long- or short-range order throughout the crystal structure depending on the composition, and concentration x. Historically, the occurrence of charge ordering in manganites was first observed by Wollan and Koehler [79] and later examined in neutron diffraction by Jirak *et al.* [86]. The competing interactions in the manganites showing CMR are the Jahn–Teller interaction favouring insulating behaviour, and the double exchange favouring the ferromagnetic metallic state. Charge ordering also competes with double exchange, and promotes insulating behaviour and antiferromagnetism. In $Ln_{1-x}A_xMnO_3$ charge ordering have been found in various ranges from $0.3 < x < 0.75$ depending on the *Ln* and *A* ions. It would be favoured with $x = 0.5$ for the presence of equal proportions of the Mn^{3+} and Mn^{4+} ions. With increasing x the average MnO_6 distortion decreases because the Mn^{4+} is not Jahn-Teller active. Long-range Coulomb repulsive interactions among conduction carriers might be responsible for the charge ordering [87-89]. However, the dominant long-range Coulomb interaction cannot account all the low temperature features and the on-site Coulomb interactions have also to be considered [90, 91].

Charge ordering with a stripe modulation is associated with a strong tendency towards microscopic electronic phase separation, when charge carriers are introduced into an AFM and insulating background. In Ca doped compounds, charge ordering has been observed in the Ca concentration range 0.5 - 0.875 where there is a transition from a PM state to a charge ordered state followed by AFM state (see Figure 2.21) [85]. The Curie temperature T_C is maximised at the commensurate value $x = 3/8$ and T_{CO} peaks at $x = 5/8$. Charge ordering has also observed at $x = 1/8$ where the system shows a transition from PM to FM state and then to a charge ordered

AFM state. These anomalies at the commensurate concentrations indicate that the electron-lattice coupling plays an important role in manganites.

The electronic phase diagram of the $La_{1-x}Sr_xMnO_3$ system, deduced from extensive magnetic and electrical measurements, is shown in Figure 2.22.

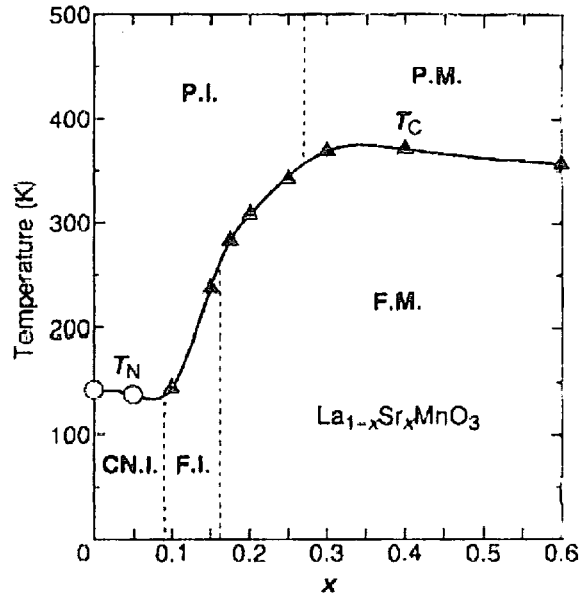

Figure 2.22 Electronic phase diagram of $La_{1-x}Sr_xMnO_3$. Open circles and filled triangle are the Neel (T_N) and Curie (T_C) temperatures, respectively. The abbreviations are paramagnetic insulator (*PI*), paramagnetic metal (*PM*), spin-canted insulator (*CNI*), ferromagnetic insulator (*FI*), and ferromagnetic metal (*FM*). (taken from Urushibara *et al.* [92])

Resistivity and neutron scattering measurements on $La_{1-x}Sr_xMnO_3$, x = 0.125, powder samples by Pinsard *et al.* have revealed that at T ~ 270 K orbital ordering appears due to a cooperative J-T effect [93]. At ~ 180 K, it becomes ferromagnetic and the orbital ordering is partially suppressed, and below 150 K the orbital ordering is completely suppressed.

Niemöller *et al.* have studied single crystals of $La_{1-x}Sr_xMnO_3$ with x = 0.125 and 0.15 by using high-energy X-ray scattering [94]. They found superlattice reflections associated with charge ordering at (h±0.25, k, 0) and (h, k±0.25, 0). The charge ordering transition temperatures are 150 K and 180 K respectively. In addition they found reflections at (h±0.5, k±0.5, l±0.5). They proposed these peaks originated from imperfect destructive interference of adjacent layers in the perovskite structure, due to the Sr doping which introduces distortions in the tilt pattern of the oxygen

octahedra. Fujishiro *et al.* have studied polycrystalline samples of $La_{1-x}Sr_xMnO_3$ in a wide range of the Sr concentration by measuring sound velocity, thermal expansion, magnetization, and electrical resistivity [95]. They observed anomalies in these measurements and suggested these are associated with charge ordering and concluded that the charge ordering occurs over a wide range of Sr concentration from $0.48 \leq x \leq 0.82$.

Neutron scattering results on a single crystal $x \approx 1/8$ showed the presence of superlattice reflections at (0, k, l±0.5) and (1, k, l±0.5), where k and l are even integers in the orthorhombic setting [96]. The satellite reflections appeared below T = 110 K, corresponding to the metal-insulator transition temperature. They interpreted these results as polaron ordering, due to the freezing of the hole configuration causing a lattice distortion below 110 K. In x = 0.1 and 0.15 samples, Yamada *et al.* found a polaron ordered phase by neutron scattering [97]. They suggested the polaron lattice has the tendency to lock into a commensurate structure, within a finite concentration range around x = 0.125. In $x \sim 0.12$ the transition from the ferromagnetic metallic state to the ferromagnetic insulating state occurs at T_{OO} = 145 K and ascribed to the transition between an orbital ordered state and an orbital disordered state [98]. In this study, Endoh *et al.* observed a resonance in energy scan through the orbital ordering peak at Mn K-edge.

Furthermore, the Mn^{3+} e_g orbitals ($3d_{z^2}$) and the associated lattice distortions (long Mn–O bonds) also develop long-range order, giving rise to orbital ordering. The Jahn-Teller distortion associated with Mn^{3+} cations results in orbital ordering [99]. The sensitivity of the X-ray scattering to orbital ordering in transition metal oxides is enhanced when the incident X-ray energy is tuned to the absorption edge. In experiments performed by Murakami *et al.* on $LaMnO_3$ and $La_{0.5}Sr_{1.5}MnO_4$, peaks corresponding to the orbital order were detected [100, 101]. The charge ordering transition accompanying simultaneous orbital ordering in $La_{0.5}Sr_{1.5}MnO_4$ at 217 K well above the magnetic phase transition temperature at 110 K. In $LaMnO_3$ the spins order at 140 K and the orbital ordered phase disappears at 780 K. These peaks show a strong enhancement at the Mn K-edge corresponding to the Mn 1s to 4p transitions. In both compounds, they also observed twofold symmetry in azimuthal angle dependence of the intensity of the orbital ordering reflection due to the anisotropic

electron density in the *ab* plane arising from the orbital ordering. In addition, Murakami *et al.* observed resonance at a charge order satellite in the related $La_{0.5}Sr_{1.5}MnO_4$ compound [101]. Nakamura *et al.* by using resonant X-ray scattering technique, detected a resonance enhanced signal at charge and orbital reflections in $Nd_{0.5}Sr_{0.5}MnO_3$. These resonances have been observed at energies corresponding to electric dipole transition from the Mn 1s state to a 4p state [102]. In $Pr_{1-x}Ca_xMnO_3$, x = 0.4 and 0.5, the enhancement of the intensity of the charge (0, 3, 0) and orbital (0, 1.5, 0) ordering reflections at the Mn *K*-edge have been observed [103]. The enhancements were at 6.555 keV, characteristic of dipole resonant scattering.

Historically, Wollan and Koehler investigated magnetic ordering first time in 1955, in a series of manganese perovskites of general formula $La_{1-2x}Ca_xMnO_3$ ($0.0 < x < 1$) by using neutron powder diffraction [79]. Theoretical work on this system was performed by Goodenough, who introduced super-exchange and double-exchange mechanisms [81].

The Mn-O-Mn superexchange interactions are ferromagnetic through a filled and an empty $3d_{z^2}$ orbital, but antiferromagnetic through two empty $3d_{z^2}$ orbitals. This, in turn, gives rise to complex magnetic ordering in the structures. At low temperatures, the rare earth manganites are antiferromagnetically ordered (AFM) with *CE*- or *A*-type ordering, but only the former occurs in the charge-ordered materials where the e_g electrons are localized (see Figures 2.29 and 7.8, for *A*-, *C*-, and *CE*-type ordering). The *CE*-type spin ordering is characterized by the ordering of Mn^{3+} and Mn^{4+} ions alternately. The type of charge and spin ordering depends on the radius of the *Ln* and *A* cations ($Ln_{1-x}A_xMnO_3$).

2.4.4 Mechanisms

One of the most important interactions which has been examined for magnetic and electronic properties of these materials is the double exchange (DE) mechanism [104, 105]. Double exchange requires a mixed-valence state of Mn^{3+} and Mn^{4+} cations and is responsible for ferromagnetism in manganites. It is a FM coupling between the local 3*d* electron (t_{2g} state) spin through kinetic exchange of the itinerant 3*d* electron (e_g state). Double exchange allows electron transfer between neighbouring Mn^{3+} and

Mn^{4+}, thereby delocalizing the e_g electron, if as suggested the spins of the d-electron on the ions are aligned parallel or nearly parallel. A schematic picture of these processes is shown in Figure 2.23.

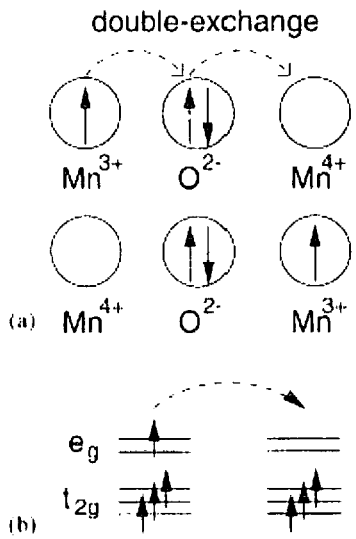

Figure 2.23 (a) A schematic picture of the double exchange mechanism, which involves two Mn ions and one O ion. (b) The mobility of e_g electrons improves if the localized spins are polarized. (taken from Dagotto *et al.* [106])

These two states Mn^{3+}-O-Mn^{4+} and Mn^{4+}-O-Mn^{3+} are degenerate [81]. So below the Curie temperature T_C, the e_g electron being free to hop between Mn^{3+} and Mn^{4+} via the oxygen orbitals due to DE. But when the Mn^{3+} and Mn^{4+} ions form an ordered state, the condition for DE is changed due to the non-degeneracy of these states. In the DE picture, localized carriers cannot induce FM coupling.

Another important interaction is the Jahn-Teller interaction. According to the well-known J-T theorem [107] an orbital degeneracy leads to instability of the system and to the modification of electronic and lattice structure. Ions with a strong J-T effect are Cu^{2+} (d^9, one hole in double degenerate e_g-orbital), low-spin Ni^{III} (d^7, one e_g-orbital), Mn^{3+} (d^4, one e_g-orbital), Cr^{2+} (d^4, one e_g-orbital). These ions are called strong J-T ions, because the orbital degeneracy involved is in orbitals with lobes directed towards the ligands, they have strong hybridization with the ligands, which will be strongly dependent on the cation-anion distance. In concentrated systems it leads to

structural phase transitions, cooprative J-T transitions, or orbital ordering lifting the orbital degeneracy.

Mn has four electrons in the 3d orbitals. These four electrons are all spin aligned due to the strong Hund's rule minimizing the electrostatic repulsions, which is believed to be large [79]. Electrostatic interactions between these four electrons and the crystal field of the neighbouring oxygen ions causes these five-fold degenerate atomic 3*d* levels to split into two energy sublevels. Three of the electrons occupy the lower t_{2g} (triply degenerate) energy state and the remaining electron occupies the higher e_g (doubly degenerate) level. This single electron is energetically unstable, and due to the well-known Jahn-Teller effect, the system reduces its energy by splitting the doublet state into another two energy levels (see Figure 2.24).

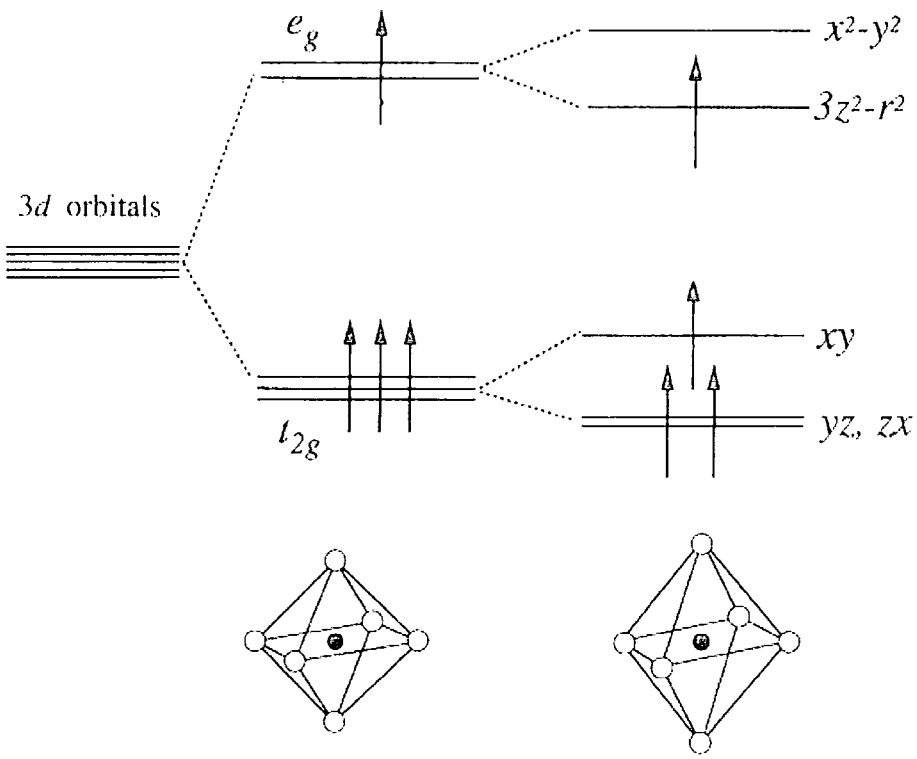

Figure 2.24 Splitting of five-fold degenerate atomic 3d levels due to the crystalline field and Jahn-Teller effect. (taken from Dagotto *et al.* [106])

The J-T interaction tends to lift the degeneracy of the occupied d electrons via the deformation of MnO_6 octahedron. By substitution of a divalent alkaline element, such as calcium or strontium, into some of the lanthanum sites, the Mn valence changes from all Mn^{3+} to some Mn^{3+} and Mn^{4+}, and creates holes in the e_g energy

state. Local distortion of the MnO_6 octahedra due to the Jahn-Teller effect plays a crucial role in the metal-insulator (MI) transition in the manganese oxides and in related materials [108-111]. The J-T distortion around the Mn^{3+} ions plays an important role in the insulating nature and anisotropic magnetic properties of these systems. There are two kinds of distortion in manganites. Tilting of MnO_6 octahedra arises from the mismatch of the ionic radii. The other distortion of the octahedral comes from the J-T effect due to the Mn^{3+} ion and causes long and short Mn-O bonds. This J-T distortion can split the e_g band and open a gap at the Fermi level. Hole doping reduces the J-T distortion and a certain number of the holes make the material metallic below T_C. The presence of Mn^{4+} has two essential roles in manganites. It provides the DE needed for FM and metallic behaviour, and it also helps to remove the J-T distortion of the Mn^{3+} ions and makes the structure closer to cubic.

The effective interaction between the orbitally non-degenerate localized t_{2g} orbitals is via super-exchange. This is virtual electron transfer between half-filled orbitals and is constrained by the Pauli exclusion principle to have a component of the transferred electron spin antiparallel to the spin of the t_{2g} configuration of the acceptor atom.

Millis *et al.* determined that DE alone could not explain all the experimental results in manganites, and an additional effect such as the J-T effect must be considered to reduce the electronic kinetic energy at the metal-insulator transition [108, 112]. Recent studies have revealed that the observed features is not due only to the DE interaction but also to other instabilities competing with the DE mechanism, such as antiferromagnetic superexchange, J-T, charge ordering (CO), orbital ordering interaction etc. [101]. Some of these competing interactions strongly couple with the lattice through the orbital degrees of freedom (or J-T) of the e_g electron on the Mn^{3+} ions [113]. In addition to the DE interactions as well as the J-T distortions, the ordering of the two-fold e_g orbitals of Mn ions plays an essential role to determine physical properties in the hole-doped manganites [114, 115]. For example, it was reported that the $d_{x^2-y^2}$ type orbital ordering leads to a metallic antiferromagnetic (AFM) state instead of either the metallic FM state or a so-called *CE*-type charge/spin ordered insulating state.

Interaction between charge carriers and vibrations of the crystal lattice (phonons) also plays a fundamental role in the electrical properties of the manganites. Vibration of the lighter oxygen ions, push the electrons towards the vacant state in the manganese ion and this strengthens the J-T effect, inducing a local distortion of the lattice. Such a distortion is known as a polaron and leads to self-trapping of the charge carriers. The strength of the electron- phonon coupling should depend on the bandwidth (or equivalently on the kinetic energy of the mobile carriers). The electron-phonon coupling should be stronger for narrower bandwidths, and enhancing the self-trapping effect, and leading to higher resistivity [116]. The electron-phonon interaction can arise from lattice distortions due to the different ionic size of Mn^{3+} and Mn^{4+} in general, and Jahn-Teller type distortions of the oxygen octahedra around Mn^{3+} in particular. Hotta *et al.* suggested that a purely J-T-phononic model is more effective than the purely Coulomb model for the theoretical investigation of manganites, although certainly both lead to very similar physics [117].

From experimental results it has been concluded that the correlation between polarons is essential to the formation of the charge-ordered state and the charge ordered state might be regarded also as long-range ordering of polarons [118].

2.4.5 Melting of the charge ordered state

When a charge ordered state melts in a magnetic field, the bulk electrical resistivity (ρ) changes substantially. This can arise either from changes in the mobility, μ, or in the free carrier density, n, due to closing of the energy gap in the density of state (DOS), or both. The sensitivity of the charge ordered state to an applied magnetic field depends on the average size of the *A*-site cations $\langle r_A \rangle$ (or Mn-O-Mn angle). The field required to melt the CO state varies with r_A. Manganites with smaller r_A remain charge ordered even upon application of high magnetic fields [119, 120].

The temperature dependence of the resistivity of $Nd_{0.5}Sr_{0.5}MnO_3$ crystals under applied magnetic field shows that the critical temperature of the CO transition is decreased by increasing the magnetic field [121]. It undergoes a metamagnetic transition and becomes ferromagnetic. The charge ordered AFM insulating state is totally extinguished over the whole temperature range by applying the field larger

than 7 T. This magnetic-field-induced destruction of the charge-ordered state can be an origin of the CMR effect.

For $Nd_{0.5}Ca_{0.5}MnO_3$ (r_A = 1.17 Å), a magnetic field of 6 T significantly affects the resistivity and makes it nearly metallic below T = 120 K. The magnetic field has however no effect on the resistivity of $Sm_{0.5}Ca_{0.5}MnO_3$ (r_A = 1.16 Å). The same is true of $Gd_{0.5}Ca_{0.5}MnO_3$ (r_A = 1.143 Å) and $Dy_{0.5}Ca_{0.5}MnO_3$ (r_A = 1.132 Å). It has already been shown that the resistivity of $Y_{0.5}Ca_{0.5}MnO_3$ (r_A = 1.127 Å) is not affected by a magnetic field of 6 T [122]. It appears that a r_A of 1.17 Å is a critical value below which magnetic fields (up to 6 T) have no effect on the charge-ordered manganites. The charge-ordered state in the manganites with r_A less than 1.17 Å is robust, being dominated by the cooperative Jahn–Teller effect [123]. The high T_{CO} values of 240 K and above, occur for $Ln_{0.5}Ca_{0.5}MnO_3$ with r_A less than 1.17 Å. T_{CO} becomes zero when r_A is greater than 1.24 Å. It is likely that the r_A values of 1.17 Å and 1.24 Å define two different regimes of charge ordering in the manganites.

The CO state can be transferred to the FM state even by substitution of ^{16}O with ^{18}O. This implies that the ground state energies of the two phases remain very close, despite large compositional changes. Substitution of Cr^{3+}, Ni^{3+} or Co^{3+} in place of Mn^{3+} also destroys the CO state in $Ln_{0.5}A_{0.5}MnO_3$. Vanitha *et al.* suggested that the electron jump between the transition metal ion with empty e_g orbitals, and the Mn^{3+} ion, may be the initial condition for the melting of the CO states in these materials [124]. They assumed that both Ni and Co are in the 3+ states. If they occur in the 2+ states there would be a proportionate conversion of Mn^{3+} to the Mn^{4+} state. With substitution of the Mn ion with Ru in $Nd_{0.5}Sr_{0.5}MnO_3$, T_C increases with the Ru content to well above the 300K, while the CO is destroyed [124].

2.4.6 x = 1/2 compounds

With 50% doping, there are an equal number of $Mn^{3+}$and Mn^{4+} ions and this can lead to charge, spin, and orbital ordering. However, the charge ordering is not restricted to this level of doping and charge ordering has been seen in other compositions. When the ratio of Mn^{3+} / Mn^{4+} = 1, the lattice is made up of an equal number of Jahn-Teller active (Mn^{3+}) and Jahn-Teller inactive (Mn^{4+}) ions.

$Ln_{0.5}A_{0.5}MnO_3$ (*Ln* = La, Pr, Nd, Sm: *A* = Sr, Ca) have been extensively studied and found to show interesting electronic and magnetic properties such as metal-insulator transition due to the DE interaction, CO transitions due to the long-rang Coulomb interaction among the carriers, and AFM transition due to the superexchange interaction, depending on the combination of *Ln* and *A* [1, 92, 125-130].

$La_{0.5}Ca_{0.5}MnO_3$ undergoes a FM transition at 225 K and then follows a first-order phase transition to a *CE*-type AFM charge ordered state at 135 K upon cooling [131, 132]. Electron diffraction patterns obtained in [001] zone-axis by Chen and Cheong together with their proposed schematic charge ordering is shown in Figure 2.25 [125].

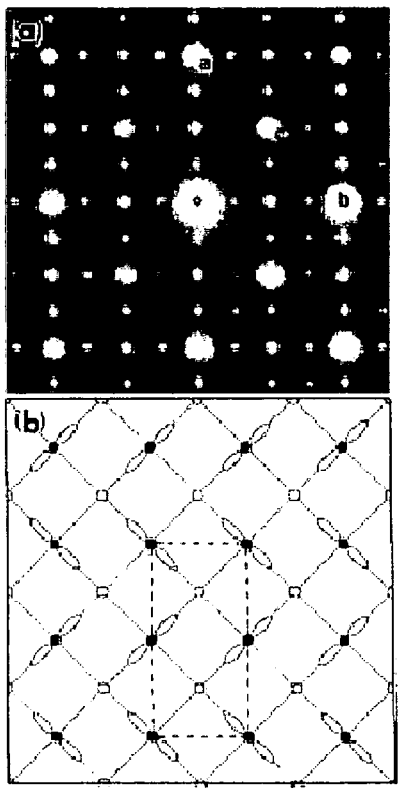

Figure 2.25 (a) [001] zone-axis electron diffraction pattern on $La_{0.5}Ca_{0.5}MnO_3$. (b) Schematic charge-ordering picture of Mn^{4+} (open circle) and Mn^{3+} (closed circle) ions. The doted line shows the orbital ordering unit cell. (taken from Chen *et al.* [125])

In the Figure sharp superlattice spots with wave vector $q = (2\pi/a)(1/2\text{-}\varepsilon, 0, 0)$ $\varepsilon = 0.013$ are clearly seen, in addition to the fundamental Bragg reflections. They found incommensurate (IC) charge ordering unusually exists in the FM phase and commensurate charge ordering is established at the AFM transition temperature. The coexistence of the commensurate long-range charge ordering with a quasi-orbital

ordered state has been suggested by X-ray and neutron powder diffraction measurements [133]. Mori *et al.* proposed the coexistence of FM and charge ordering is due to an inhomogeneous spatial mixture of IC charge ordered state and FM charge disordered microdomains with a size of 20-30 nm, and interpreted this as a microscopic electronic phase separation in the temperature range 220 – 135 K [134].

In the narrow-band manganites such as $La_{0.5}Ca_{0.5}MnO_3$ and $Nd_{0.5}Sr_{0.5}MnO_3$, the *CE*-type AFM phase is stabilized. In this structure, the t_{2g} spins form a ferromagnetic array along a zigzag 1-D path, the CO state appears with the checkerboard pattern, and the $(3x^2 - r^2)/(3y^2 - r^2)$-type orbital ordering is concomitant to this CO state. The origin of this complex spin-charge-orbital structure has been recently clarified on the basis of the topology of the zigzag structure [135]. Along the *z*-axis, the *CE*-pattern stacks with the same CO/OO structure, but the coupling of t_{2g} spins along the *z*-axis is antiferromagnetic.

$Nd_{0.5}Ca_{0.5}MnO_3$ is insulating over the whole temperature range 300 K - 4.2 K. It has a paramagnetic state for $T > 250$ K and charge ordering progressively establishes from $T_{CO} = 250$ K to $T_N = 160$ K [136-138]. In $Nd_{0.5}Ca_{0.5}MnO_3$, a significant broadening of the Bragg peaks has been found in the temperature region between the charge ordering transition and ferromagnetic ordering [136]. Chen and Cheong [125] have proposed that this can be related to a commensurate-to-incommensurate transition. Radaelli *et al.* speculated about the possibility of a distribution of lattice parameters which changes with temperature, or of the presence of several distinct phases, which are basically domains with different degrees of Jahn-Teller distorted MnO_6 octahedra [109]. The strain induced by this phenomenon could lead to anisotropic peak broadening in the *ab* plane. The electrical resistivity versus temperature of this compound is displayed in Figure 2.26. The discontinuity around 250 K is due to the charge ordering, which accompanies the first-order transition. Magnetic fields up to 7 T have a little effect on the resistivity [137]. Millange *et al.* after undertaking neutron scattering measurements, proposed the existence of two different charge-ordered phases. A charge-ordered phase with no long-range magnetic order, in the temperature range that the broadening of the Bragg peaks are observed, $T_N < T < T_{CO}$, and a long-rang *CE*-type AFM phase, which is accompanied with complete orbital ordering.

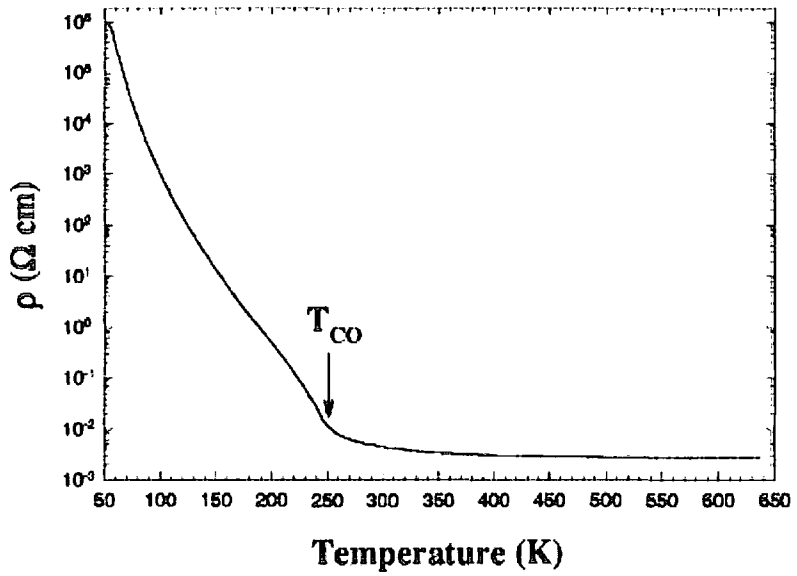

Figure 2.26 The electrical resistivity versus temperature for $Nd_{0.5}Ca_{0.5}MnO_3$. (taken from Millanage *et al.* [137])

$Pr_{0.5}Ca_{0.5}MnO_3$ shows a PM to an AFM transition at 180 K and does not show the FM metallic properties in the entire range of the Ca concentration, because it has a smaller one-electron bandwidth [139]. However, Kajimoto *et al.* reported that the FM spin fluctuations are developed for $T_N < T < T_{CO}$ [130]. Electron diffraction showed first incommensurate charge ordering establishes in the PM state at 260 K, and then a commensurate charge-ordered state occurs at the AFM transition temperature 180 K [139]. Recent neutron scattering results showed that the IC to commensurate (C) transition of the orbital ordering takes place in a bulk sample and changes the lattice structure and transport properties within the IC orbital ordered phase below the charge/orbital ordering temperature are related to the partial disordering of the orbital order [140].

$Bi_{0.5}Sr_{0.5}MnO_3$ shows charge and orbital ordering at room temperature [129, 141]. Neutron and synchrotron X-ray powder diffraction, magnetotransport, and magnetization measurements on $Bi_{0.5}Sr_{0.5}MnO_3$ showed that, the coexistence of two phases for the whole range of temperature 1.5 K < T < 300 K [129]. The majority phase presents charge and orbital order at least below 350 K, and *CE*-type AFM magnetic order at $T_N \approx 155$ K. The fact that magnetic fields higher than 45 T are not sufficient

to melt the charge-ordered state at 4 K indicates the stability of the charge ordered state in this compound.

The existence of the equal amounts of the Mn^{3+} and Mn^{4+} is not a pre-requisite for charge ordering. Neutron diffraction measurements on $Pr_{0.5}Sr_{0.5}MnO_3$ have revealed this compound undergoes a transition from a FM metal state to an *A*-type AFM structure at $T_N \sim 150$ K [115]. From these measurements, Kawano *et al.* could not find a clear sign of charge ordering. The sample's resistivity as a function of temperature shows an increase at T_N, but remains at a relatively low value down to 5 K. They proposed the absence of the *CE*-type charge ordering in this compound compared to $Nd_{0.5}Sr_{0.5}MnO_3$ is due to the wider one-electron bandwidth which enhances the itinerant character of e_g electrons.

$La_{0.5}Sr_{0.5}MnO_3$ shows a transition from a paramagnetic to a ferromagnetic metallic state at 340 K and remains metallic even down to low temperatures. So this compound does not show a charge-ordered state, which would be insulating. The charge ordered insulating phase in $Nd_{0.5}Sr_{0.5}MnO_3$ is considered to be stabilized by the larger $GdFeO_3$-type distortion (smaller Mn-O-Mn bonding angle) than in $La_{0.5}Sr_{0.5}MnO_3$, arising from the difference between the ionic radii of the atoms at the *A*-sites [142].

2.4.7 Effect of bandwidth (*W*) and tolerance factor (*f*)

The three localized electrons in the 3d orbitals of the manganese ions in the t_{2g} state are located at the bottom of the 3d band. The electron in the e_g state of manganese ions is shared with the oxygen ions and forms a higher energy band. The width of this energy band (*W*) depends on the amount by which the manganese and oxygen orbitals overlap, and it has a large effect on the motion of charge carriers. Another important parameter in the perovskite structure is the band filling (doping level). These two parameters control the kinetic energy of the conduction electrons and they have a major effect on the metal-insulator transition and also the competing magnetic interactions, i.e., FM versus AFM in the perovskite manganites. Modifying the chemical composition of the manganites can change the band filling and bandwidth.

In an ideal perovskite the Mn-O-Mn angle is 180° and the manganese-oxygen orbitals overlap is maximised. However, in real systems such as $Nd_{0.5}Sr_{0.5}MnO_3$ this is much reduced, and the Mn-O-Mn angle is only 166.13°. With substitution of Nd for La, the Mn-O-Mn angle in $La_{0.5}Sr_{0.5}MnO_3$ is 176.73° [143]. This increases the overlap between the orbitals and makes the band wider. Maximizing the kinetic energy of the conduction electrons stabilizes the FM metallic state. $Nd_{0.5}Sr_{0.5}MnO_3$ has an orthorhombic (*Imma*) structure and displays a charge- and *CE*-type AFM spin-ordered state at $T_N = T_{CO}$. $La_{0.5}Sr_{0.5}MnO_3$, with wider W remains a ferromagnetic metal below T_C = 340 K. $Pr_{0.5}Sr_{0.5}MnO_3$ exhibits a layered *A*-type AFM ordering. It has been suggested that suppression of *CE*-type charge ordering may be due to a wider one-electron bandwidth, leading to a strong enhancement of the itinerant character of e_g electrons [115]. With the increase of W, the DE mechanism may allow metallic conductivity within FM layers in the *A*-type AFM structure through gain of kinetic energy for the e_g electrons. With the increase of W the *CE*-type charge ordering is progressively suppressed, and the layered *A*-type AFM phase can be favoured, before the FM metallic state is established [115]. On the other hand, decreasing W will encourage carrier localization, which will stabilize both orbital- and charge-ordered states. It has been widely established that the CO transition is governed by the bandwidth of the e_g electrons [119, 144]. This bandwidth is controlled by the mean *A*-site cationic radius $\langle r_A \rangle$, a low r_A reducing the e_g bandwidth, favouring charge- and orbital-ordered states.

Another factor that has been used for prediction of electrical and magnetic properties of the manganites system is the tolerance factor f, which is defined as:

$$f = \left[\frac{(r_A + r_O)}{\sqrt{2}(r_{Mn} + r_O)} \right] \qquad [2.2]$$

where r_A is the average ionic radius of the *A*-site cations ($Ln^{3+}$and A^{2+}), r_O is the ionic radius of O^{2-}, and r_{Mn} is the average ionic radius of $Mn^{3+}$and Mn^{4+}. This factor is closely correlated with the rotation of the MnO_6 octahedron. The rotation of the MnO_6 octahedron makes the angle Mn-O-Mn deviate from 180°. A tolerance factor f = 1.0 characterizes an unstrained, cubic system, while a $f > 1$ or $f < 1$ represents a strain that is typically relaxed by distortion of the structure away from its ideal cubic

form. With decreasing f, the Mn-O-Mn bond angles decreases from 180° and this decrease in turn decreases the spatial overlap of the Mn e_g and O 2p orbitals, and consequently, the bandwidth W is reduced. Therefore the e_g electrons tend to transfer from the itinerant state to the localized state, and this leads to an increase in T_{CO} [123, 145]. For example, $La_{0.5}Sr_{0.5}MnO_3$ with $\langle r_A \rangle$ = 1.26 Å becomes ferromagnetic, and undergoes an insulator-metal transition around T_C, but $Nd_{0.5}Sr_{0.5}MnO_3$ with a slightly smaller $\langle r_A \rangle$ = 1.236 Å transforms to a charge-ordered, antiferromagnetic state at 160 K. The charge ordering transition temperature T_{CO} is 250 K in $Nd_{0.5}Ca_{0.5}MnO_3$ ($\langle r_A \rangle$ = 1.17 Å) and it is an insulator at all temperatures. FM and charge ordering in the manganites strongly depend on the average radius of the A-site cations [120, 123]. Figure 2.27 shows the variation of the charge ordering and FM transition temperatures as a function of radius of the A-site cations.

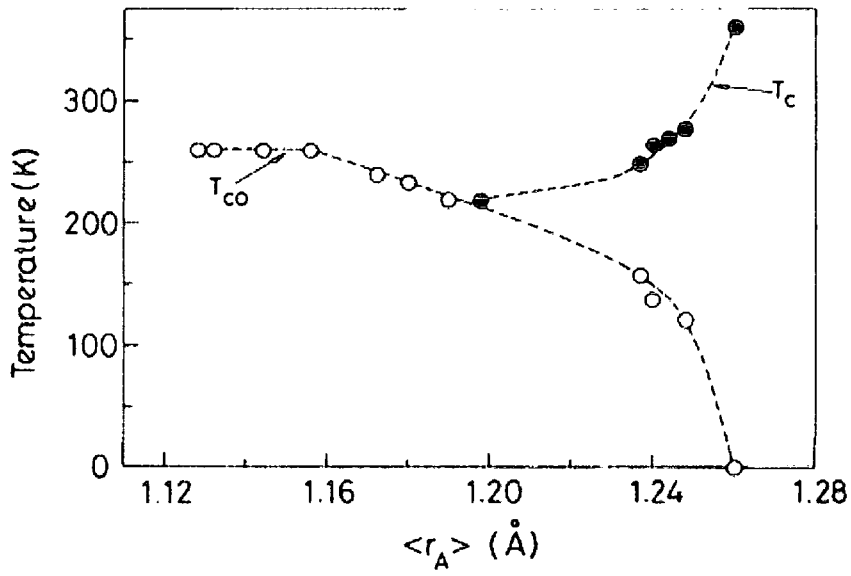

Figure 2.27 The variation of the charge-ordering transition temperature, T_{CO}, and the ferromagnetic transition temperature, T_C, with the average radius of the A-site cation. (taken from Arulraj et al. [120])

This phenomenon is easily explained by the fact that the Mn-O-Mn bond angle is significantly affected by the size of the A-site cations and, consequently, the e_g bandwidth is strongly dependent on r_A. Charge ordering has a strong effect on resistivity of manganites and usually the resistivity shows a huge increase at T_{CO} and due to this highly insulating behaviour, it opposes the appearance of a ferromagnetic

metallic (FMM) state. By applying a magnetic field, the highly insulating charge-ordered state transforms to the FM highly metallic state, and the resistivity jumps several orders which gives rise to the CMR effect. Arulraj *et al.* suggested an important factor determining the magnitude of the charge-ordering temperature and its dependence on r_A is likely to be the strain, resulting from the size mismatch between the *A*-site cations [120].

2.4.8 $Nd_{1-x}Sr_xMnO_3$

Charge ordering in this system is restricted to only a narrow range of the Sr concentration around x = 1/2. The phase diagram of $Nd_{1-x}Sr_xMnO_3$ as a function of Sr concentration is displayed in Figure 2.28 [146].

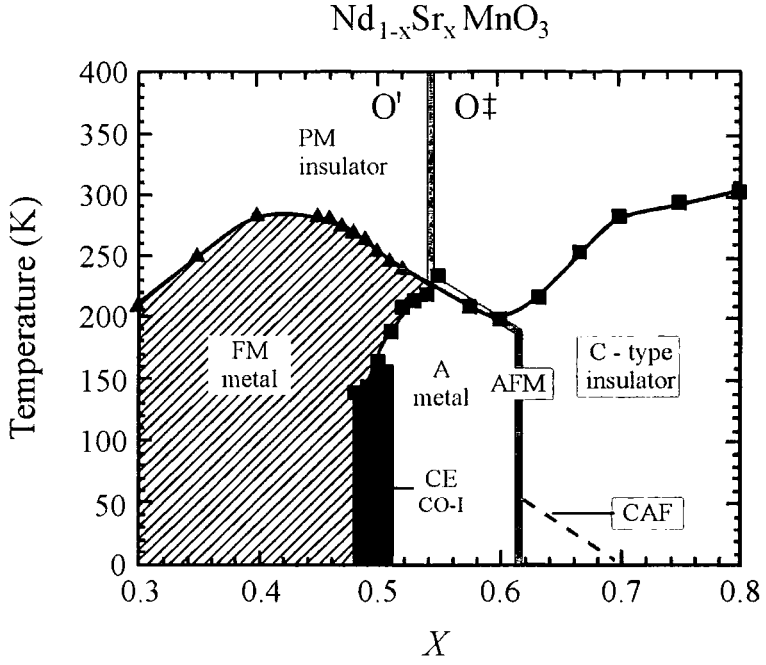

Figure 2.28 The phase diagram of $Nd_{1-x}Sr_xMnO_3$. PM: paramagnetic insulating, FM: ferromagnetic, AFM: antiferromagnetic, CE: *CE*-type charge/spin order, A: *A*-type antiferromagnetic, C: *C*-type antiferromagnetic, CAF: canted antiferromagnetic order. (taken from Kajimoto *et al.* [146])

It has a rich phase diagram with many different magnetic structures. $Nd_{1-x}Sr_xMnO_3$ is a PM insulator at high temperatures and it shows different magnetic transitions depending on x. At low doping, the ground state spin ordering is a FM metallic state and with increasing x it changes to charge ordered *CE*-type AFM state. With further

Sr doping a metallic *A*-type AFM state occurs, followed by an insulating *C*-type AFM. A schematic picture of the spin ordering in each of the various antiferromagnetic phases is shown in Figure 2.29 (left side).

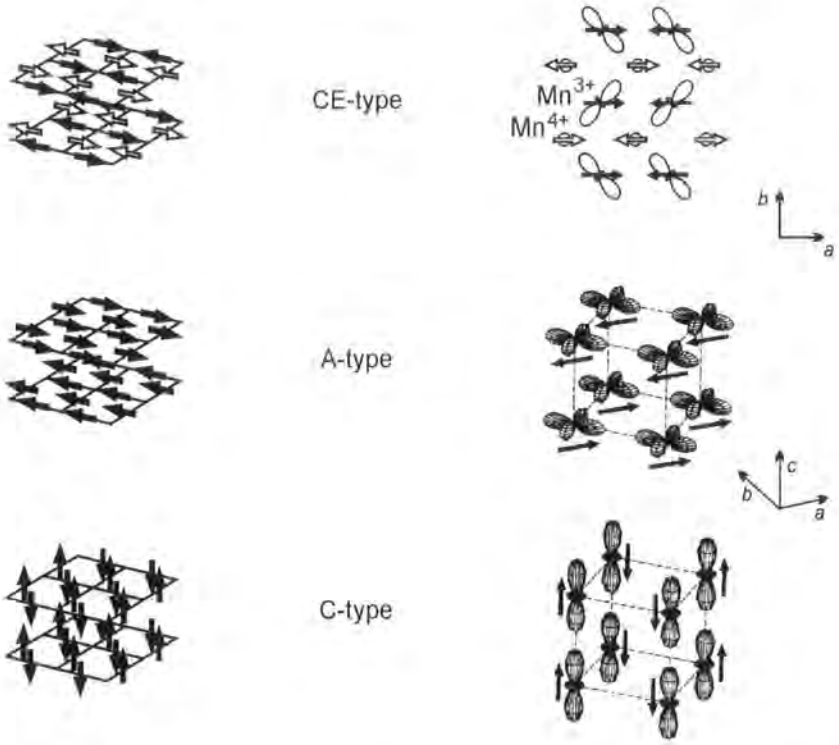

Figure 2.29 The spins (left) and orbitals (right) ordering in *CE*-, *A*-, and *C*-type AFM states. (taken from Kajimoto et al. [146])

The *CE*-type spin ordering (top left-hand side) is characterized by the antiferromagnetic ordering of the Mn^{3+} and Mn^{4+} ions, in both the *ab* plane and along the *c*-axis. The *CE*-type spin/charge ordering is only stable around $x = 1/2$ and it coexists with the *A*-type AFM state in the $x = 1/2$ and $x = 0.51$ samples. The coexistence of these two states has been interpreted as due to the orbital-order induced phase segregation between the insulating charge-ordered state and the metallic orbital-ordered state [146]. The charge-ordered distribution of Mn^{3+} / Mn^{4+} in the *CE*-type AFM state can occur only in the presence of localized e_g electrons. In *A*-type ordering (middle left-hand side), the spins are ordered ferromagnetically in the *ab* plane but antiferromagneticaly along the *c*-axis. The spin alignment is ferromagnetically along the *c*-axis in the *C*-type spin ordering (bottom left), but neighbouring spins in the *ab* plane have an AFM coupling. In *CE*- and *A*-type spin ordering, the magnetic moments are aligned in the *ab* planes, while they are along

the *c*-axis in the *C*-type magnetic ordering. Each of these spin ordered states has a corresponding orbital-ordered state (see Figure 2.29 (right side)). The results of X-ray and neutron scattering measurements show that there is an intense competition between FM metallic state, *A*-type AFM state, and the charge ordered *CE*-type AFM state near $x = 0.5$ [147].

2.4.9 $Nd_{0.5}Sr_{0.5}MnO_3$

This compound shows a transition from paramagnetic to ferromagnetic state at $T_C \sim$ 250 K. The ferromagnetic state is, however, unstable at low temperatures and transition to an insulating state is observed upon cooling below T_C at ~160 K. The insulating state is a charge ordered state (CO) where there is a real space ordering of Mn^{3+} and Mn^{4+} ions in alternate sublattices. The CO transition is accompanied by spin and $d_{3x^2-r^2} / d_{3y^2-r^2}$ orbital ordering, the spins are ordered in a *CE*-type antiferromagnetic state [126]. The transition is first-order, showing hysteresis, and is associated with large lattice distortions due to the smaller *A*-site cations and Jahn-Teller distortion of the Mn^{3+} ions [126, 136, 148].

$Nd_{0.5}Sr_{0.5}MnO_3$ at room temperature has an orthorhombic unit cell with space group *Imma*, which corresponds to a distortion from the ideal cubic perovskite structure caused by tilting of the octahedral about [101] [149]. In *Imma* symmetry, the Mn-O-Mn angle in the *ac* plane is closer to 180° than along the *b*-direction (long-axis). This anisotropy increases the spatial overlap of Mn e_g and O 2p orbitals, and hence the one-electron bandwidth, *W*.

In this system Mn ions are surrounded by six oxygen ions, whereas the Nd or Sr ions occupy the body centre position of the pesudio-cubic lattice of the MnO_6 octahedra. The Mn sites are occupied by the Mn^{3+} and Mn^{4+} with ratio 1:1[150]. The charge ordering phase transition is suppressed by application of a magnetic field and the FM region is extended to lower temperatures. Above 7 T the charge ordered antiferromagnetic insulating state totally disappears and compound transfers to a FM state [121]. Woodward *et al.* suggested that the Coulomb energy, which accompanies formation of an ordered Mn^{3+} / Mn^{4+} distribution, is essential in stabilizing the *CE*-type AFM state [147].

As in $Nd_{0.5}Sr_{0.5}MnO_3$, T_N is equal to T_{CO} implying that both AFM superexchange and Coulomb contributions are necessary to stabilise the *CE*-type AFM state competing with the other states (FM and *A*-type AFM) [123]. The *CE*-type AFM has been proposed as the ground state of this compound and other half doped perovskite manganites. Anomalies associated with charge ordering have also been observed in resistivity and magnetisation measurements [126]. The temperature dependence of the resistivity, lattice parameters, and magnetisation is displayed in Figure 2.30.

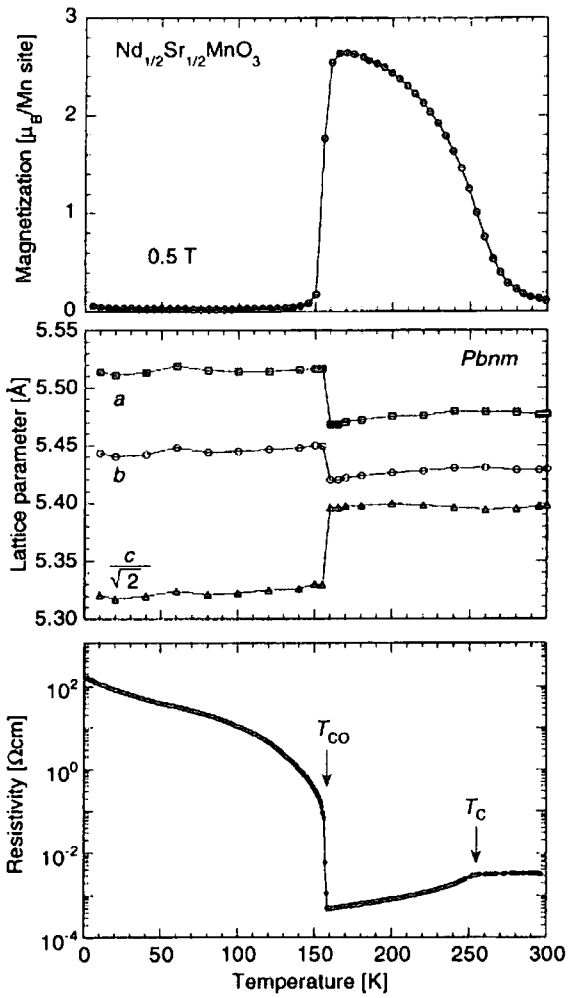

Figure 2.30 The temperature dependence of the magnetization (top), resistivity (middle), and lattice parameters (bottom) of $Nd_{0.5}Sr_{0.5}MnO_3$. (taken from Tokura *et al.* [151])

The magnetization (top panel) starts to increase at ~ 255 K due to the transition from a PM state to a FM state and it drops abruptly at ~ 160 K and the FM state disappears to form an AFM state. The lattice parameters (middle panel) also display

a considerable change at ~ 160 K due to the first-order transition to the charge ordered state. The resistivity shows a decrease at T_C (bottom panel) due to the reduced magnetic scattering of the charge carriers in the FM phase, in which the spins are ordered. At T_{CO}, where this compound shows a first order transition from a FM metallic state to charge ordered AFM insulating state, the resistivity jumps by more than two orders of magnitude.

Vacuum tunneling measurements show that a gap of 250 meV opens up below T_{CO}, suggesting that a gap in the density of states at E_F is necessary for the stability of the charge ordered state [152]. The charge-ordering gap as a function of temperature is displayed in Figure 2.31. The width of the gap reduces first on applying a magnetic field and then, for high enough magnetic field, the charge ordering gap collapses [127]. The magnetic field at which the charge ordering gap collapses depends on the ratio of T / T_{CO}.

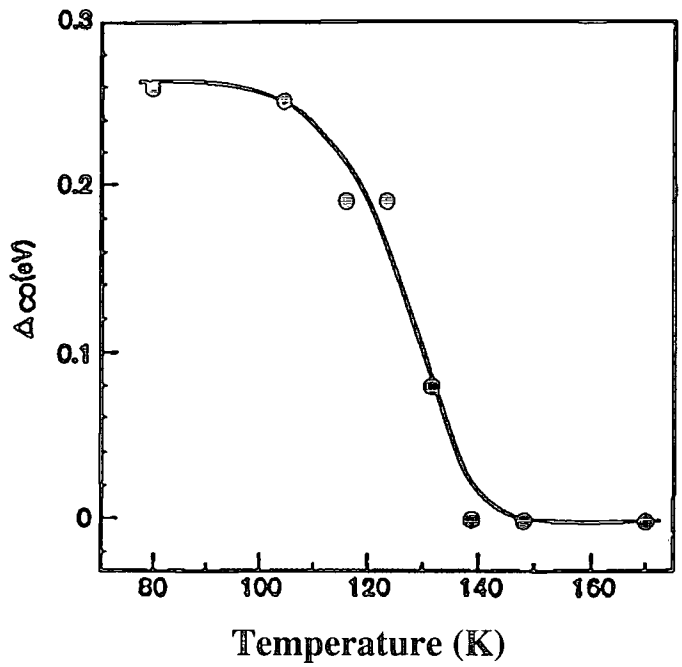

Figure 2.31 The variation of the charge-ordering gap in $Nd_{0.5}Sr_{0.5}MnO_3$ with temperature. (taken from Biswas *et al.* [152])

There is a competition between the *A*-type AFM state and the *CE*-type AFM state (stabilized by a 1:1 ratio of Mn^{3+} / Mn^{4+} charge ordering). In $Nd_{0.5}Sr_{0.5}MnO_3$, the results of the experiments show the coexistence of two or more phases at low temperature. The coexistence of the CO and FM has been suggested in optical

conductivity measurements [153]. Yoshizawa *et al.* have proposed the coexistence of the FM and *A*-type AFM states by observation of very weak magnetic Bragg peaks below 200 K [154].

Woodward *et al.* by using X-ray and neutron diffraction investigations concluded that 25% of the FM phase transforms to the *A*-type AFM phase in the temperature range 220-160 K, and it does not transform to the *CE*-type AFM phase. Then most of the remaining FM phase transforms to the *CE*-type AFM phase between 150 K and 100 K and about 15% of the FM phase is still present at 15 K [147]. From these studies $Nd_{0.5}Sr_{0.5}MnO_3$ phase separates into three macroscopic phases at low temperatures. These are the FMM high temperature phase (*Imma*), the orbitally ordered AFM (*A*-type) phase (*Imma*) and the charge-and orbitally ordered AFM (*CE*-type) low temperature phase (*P21/m*).

Ritter *et al.* observed the phase segregation at low temperature, which contains two different crystallographic structures and three magnetic phases: orthorhombic (*Imma*) ferromagnetic, orthorhombic (*Imma*) *A*-type antiferromagnetic, and monoclinic ($P2_1/m$) *CE*-type antiferromagnetic phases [155]. The incommensurate charge ordering (with $\varepsilon = 0.1$) in the FMM phase of $Nd_{0.5}Sr_{0.5}MnO_3$ has been observed by transmission electron microscopy [156]. From this study, Fukumoto *et al.* interpreted the fine mixture of the CO micro-domains in the FMM phase results from the microscopic-scale phase separation.

Application of a magnetic field can melt the charge ordered state. Kuwahara *et al.* first observed the several orders of magnitude decrease in resistivity under application of magnetic field [126]. They interpreted the results of a decrease in resistivity as melting of the charge ordered state under the applied magnetic field. The results of these measurements, resistivity versus magnetic field at various temperatures, is shown in Figure 2.32. The Figure clearly shows the field-induced melting of the charge ordered state.

It has been found that the replacing ^{18}O for ^{16}O can enhance the charge ordering temperature and in $Nd_{0.5}Sr_{0.5}MnO_3$ this increase in the charge ordering temperature is ~ 21 K [157]. Recent synchrotron X-ray scattering revealed the presence of an anisotropic short-range correlated structure distortion in the PM insulator phase and

metallic FM phase [158]. They argued that the observed correlation indicates the presence of local layered orbital ordering in the PM and FM phases.

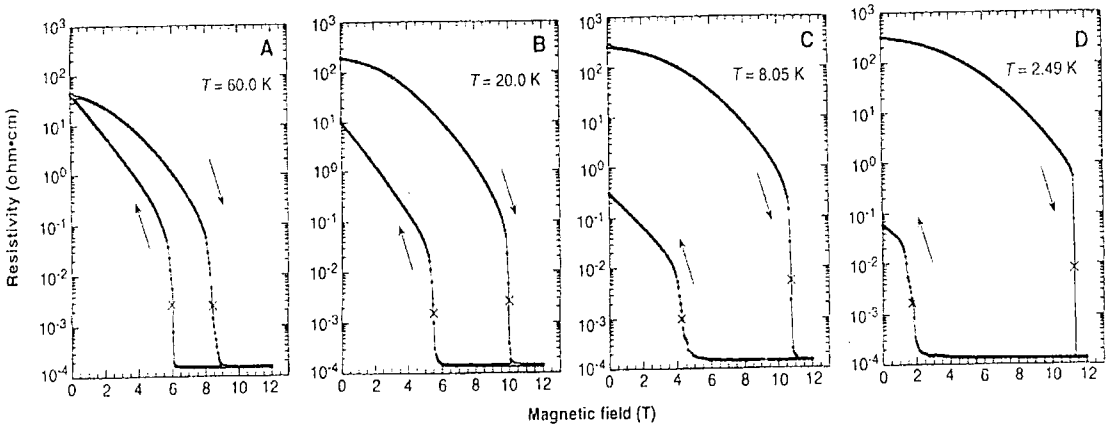

Figure 2.32 Resistivity as a function of magnetic field at various temperatures. (taken from Kuwahara *et al.* [126])

These recent studies suggest that the ground states of manganites tend to be intrinsically inhomogeneous due to the presence of strong tendencies toward phase separations, involving FMM, charge ordered AFM and orbital ordered insulating domains, and should be considered in theoretical work to describe the perovskite manganites.

2.5 Charge ordering in cuprates

2.5.1 Introduction

Superconductivity in layered copper-oxides compounds was found about 15 years ago. This discovery was a great surprise because these materials are insulators in their non-superconducting states. The parent compound La_2CuO_4 is an antiferromagnetic Mott insulator, as a result of strong electron-electron interaction within the K_2NiF_4 structure. Superconductivity can be achieved electronically by doping of holes into the parent compound system. One of the major ideas and intriguing subjects in doped-copper oxides is the concept of the stripe phase, which many theorists and experimentalist have studied. Many efforts have also been expended on the isostructural $La_{2-x}Sr_xNiO_4$ systems, which show static charge and spin stripes, to find any possible relationship between the stripes and

superconductivity. A stripe phase is an ordered array of doped holes that concentrate on the domain walls of the hole-poor antiferromagnetic regions, and run in a specific direction. Nowadays, the interplay between charge and spin correlations, and the relationship between the stripes and superconductivity, is an active area of research in copper-oxide high temperature superconductors.

So far in this chapter, the striped/ordered phase of many transition metal oxides has been explained. The stripes seen in nickelates, manganites and other compounds are static features. By contrast, those that show up in members of the superconductor $La_{2-x}Sr_xCuO_4$ family are believed to be dynamic stripes, which fluctuate in time and position. Until now the only static stripes reported in the cuprates were in materials containing neodymium and this discovery has added a new feature to high-temperature superconductivity.

2.5.2 $La_{2-x-y}Nd_ySr_xCuO_4$

Static charge and spin stripes have been observed in $La_{2-x}Sr_xCuO_4$ system with partial substitution of Nd for La ions. Nd has the same valence, but a smaller ionic radius (Nd^{3+} = 1.15 Å) than the La (La^{3+} = 1.22 Å) and induces a change in the low temperature tilt pattern of the CuO_6 octahedra, from that of the low-temperature orthorhombic (LTO) phase to a low-temperature tetragonal (LTT) phase, with strong suppression of T_C at $x \sim 1/8$ [159].

Tranquada *et al.* performed a neutron scattering study on a single crystal of $La_{1.48}Nd_{0.4}Sr_{0.12}CuO_4$, and found this compound undergoes a phase transition from the low-temperature orthorhombic phase (LTO) to a low-temperature tetragonal phase (LTT) at ~ 70 K [57]. They observed charge ordering satellites at $(2\pm2\varepsilon, 0, 0)$ and magnetic ordering satellites at $(1/2\pm\varepsilon, 1/2, 0)$ with $\varepsilon = 0.118 \pm 0.001$, with the charge and spin order peaks appear at ~ 60 K and at ~ 50 K respectively. These measurements showed the magnetic peaks have an in-plane correlation length of ~ 170 Å with a very weak correlation along the out-of-plane direction, indicating the 2D nature of the ordering. The temperature dependence of the intensity of the charge and magnetic peaks is shown in Figure 2.33. They concluded that the ordering is driven by the charge rather than the spin, and is consistent with stripe-phase order, in

which the holes order in domain walls that separate antiferromagnetic antiphase domains. In their measurement there were a few degrees difference between the charge order and the structural transition, but a later experiment showed they are coincident [160].

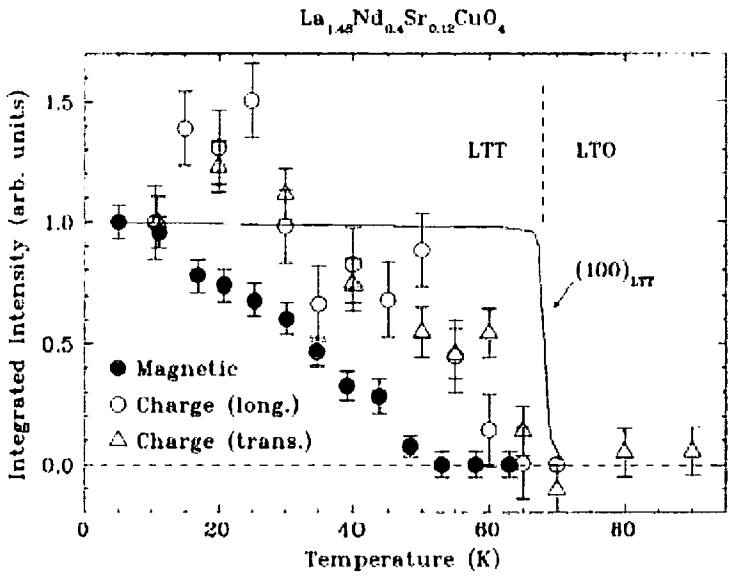

Figure 2.33 Temperature dependence of the intensities of the magnetic- (1/2-ε, 1/2, 0) and charge- (2+2ε, 0, 0) order peaks. (taken from Tranquada *et al.* [57])

Tranquada *et al.* re-examined an $x = 0.12$ sample, and measurements of the width of an elastic magnetic peak showed that the width saturates below 30 K, corresponding to a spin-spin correlation length of 200 Å, and it increases above 30 K, interpreted as critical scattering from slowly fluctuating spins [161]. Inelastic scattering measurements showed that incommensurate spin excitations survive at, and above 50 K. High-energy X-ray scattering was also used to investigate the charge ordering in the $x = 0.12$ sample, and confirmed the existence of the satellites due to the charge ordering [160]. The width of the these charge order peaks were four time greater than magnetic peak found by neutron scattering [57]. High-energy X-ray diffraction has also been employed in a study of a $La_{1.45}Nd_{0.4}Sr_{0.15}CuO_4$ crystal, and the superstructure reflections due to the ordering of holes into stripes, have been observed with an ordering temperature of 62(5) K [162]. These reflections have been observed in a sample, which is a superconductor at low temperatures ($T_C \sim 10$ K), and from the

study of the charge and magnetic reflections, they concluded that the spin ordering is driven by the charge ordering.

Results of recent electrical resistivity measurements parallel to CuO_2 planes on $La_{1.6-x}Nd_{0.4}Sr_xCuO_4$ samples with various Sr concentrations is shown in Figure 2.34 [163].

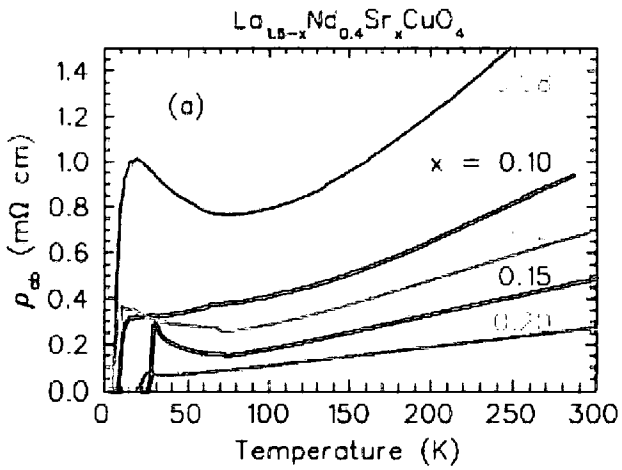

Figure 2.34 In-plane resistivity versus temperature measured on single crystals of $La_{1.6-x}Nd_{0.4}Sr_xCuO_4$ with several different Sr concentrations. (taken from Ichikawa *et al.* [163])

This graph shows the upturn point in resistivity in all samples, and superconductivity at low temperature, with some differences in the low temperature behaviour of x = 0.1 sample. Ichikawa *et al.* also performed neutron diffraction and found charge- and spin-ordering reflections in this compound, but the resistivity of this compound does not show increase at the charge ordering temperature, in contrast with other samples which show charge and spin ordering. The highest spin- and charge-ordering temperatures occur at $x \sim 1/8$, where the superconductivity is most greatly depressed. They concluded that local magnetic order and not charge order is responsible for the anomalous suppression of superconductivity at $x \sim 1/8$. Charge ordering is compatible with superconductivity as long as the spin correlation remains purely dynamic.

Zero-field-cooled susceptibility measurements have also shown a local coexistence of superconductivity and stripe order in x = 0.12, 0.15, and 0.2 [50]. From these studies it can be concluded when the Nd is introduced into the $La_{2-x}Sr_xCuO_4$ system, it suppressed the superconductivity completely, or to a lower temperature, and is accompanied with static charge and spin stripes.

2.5.3 $La_{2-x}Sr_xCuO_4$

$La_{2-x}Sr_xCuO_4$ is a unique system for which the chemical composition can be varied over a wide range, with subsequently different electronic properties. With increasing Sr concentration, the system changes from an antiferromagnetic insulator state to a superconductor with a maximum T_C for $x \approx 0.15$, and then to a "normal" metal. Figure 2.35 shows the critical temperature (T_C) as a function of x, as obtained from a.c. susceptibility measurements [164]. The dotted vertical line shows the position of the orthorhombic to tetragonal phase transition, and there is no discontinuity in T_C at this transition boundary. T_C reaches a maximum around $x = 0.15$ and then rapidly decreases. The anomaly at $x \approx 0.12$, and the suppression of T_C is clear in the graph. From these studies, Radaelli *et al.* concluded that bulk superconductivity exists in both the orthorhombic and tetragonal phases.

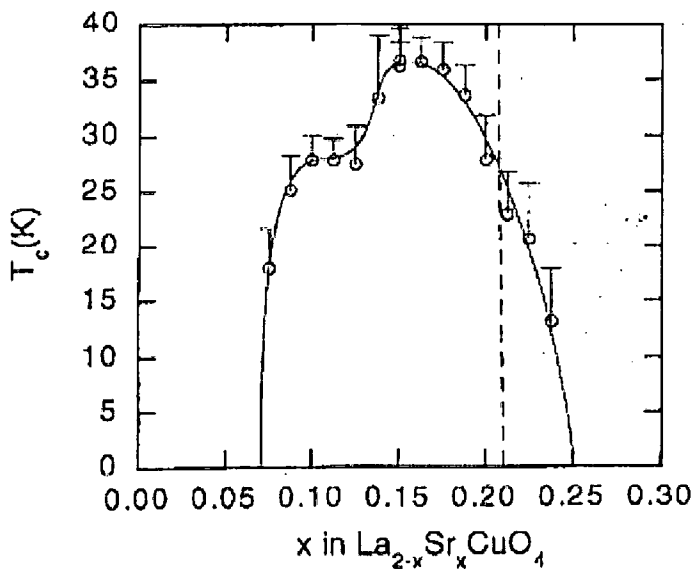

Figure 2.35 Onset (top of the error bars) and midpoint (open circle) critical temperature as a function of x, from a.c. susceptibility measurements. (taken from Radaelli *et al.* [164])

Inelastic neutron scattering measurements by Cheong *et al.* provided the first evidence for incommensurate magnetic fluctuations in $La_{2-x}Sr_xCuO_4$ with $x = 0.075$ and $x = 0.14$ [35].

Koyama *et al.* used electron diffraction on $La_{2-x}M_xCuO_4$ (M = Ba, and Sr) samples and observed that the LTO to LTT structural phase transition is restricted only

around the particular concentration of $x = 0.125$ for Ba doping and $x = 0.115$ for Sr doping [165]. They suggested the charge localization caused by a charge density wave (CDW) must be the physical origin of the T_C suppression in these compounds around $x = 0.12$.

In $La_{1.88}Sr_{0.12}CuO_4$ an incommensurate peak has been observed by neutron elastic scattering, evidence for static spin order [166]. In this sample the onset temperature of superconductivity is 31.5 K [167]. In these studies Suzuki *et al.* have performed neutron diffraction, NMR, and ultrasonic measurements on a single crystal of $La_{1.88}Sr_{0.12}CuO_4$. With neutron scattering, they observed magnetic superlattice peaks at $(1/2\pm\varepsilon, 1/2, 0)$ and $(1/2, 1/2\pm\varepsilon, 0)$ with $\varepsilon = 0.126$ which are symmetrically located around the (1/2, 1/2, 0) reciprocal point. They interpreted the existence of these peaks as evidence of modulated antiferromagnetic long-range order below $T_N = 45$ K in the orthorhombic phase. In this compound in contrast with $La_{2-x}Ba_xCuO_4$, the structural phase transition from LTO to LTT has not been observed and the structural transition to the LTO phase occurs at 240 K [168]. Kimura *et al.* used neutron diffraction on the same Sr concentration single crystal and found the incommensurate elastic magnetic peaks at $(1/2-\varepsilon, 1/2+\eta, 0)$ and $(1/2+\varepsilon', (1/2-\eta', 0)$, $\varepsilon = 0.115$, $\varepsilon' = 0.121$, $\eta = 0.007$ and $\eta' = 0.006$ which is the tilt angle between the incommensurate wave vector and the Cu-O-Cu direction [167]. The static magnetic peaks have a correlation length of over 200 Å. Elastic magnetic peaks are observed at the same IC positions as those of the magnetic inelastic peaks. Static spin-stripe order was also observed in $x = 0.05$ compound which also does not show a LTO to LTT phase transition [169].

The observation of superconductivity in both LTT and LTO phases belies the idea that the crystal symmetry is important for superconductivity. In contrary the structural properties of the CuO_2 planes may have an important role in controlling the electronic properties of $La_{2-x}Sr_xCuO_4$ system. Spin and charge ordering have also observed in simple copper oxide CuO by electron microscopy [170]. Phonon thermal conductivity (k_{ph}) measurements by Baberski *et al.* on the $La_{2-x}Sr_xCuO_4$ system have demonstrated that it is always strongly suppressed whenever the system shows superconductivity [171]. In contrast, such suppression is absent in non-superconducting compounds. They have given an explanation of this observation in terms of stripe

correlations, and concluded the existence of dynamic stripe correlations is of importance for superconductivity in these compounds.

More recent neutron scattering results on $La_{1.976}Sr_{0.024}CuO_4$ revealed that a short-range static one-dimensional spin modulation exists below ~ 40 K [172]. They found elastic magnetic peaks at the IC positions (1, $\pm\varepsilon$, 0) and (0, 1$\pm\varepsilon$, 0), with $\varepsilon \sim 0.023$ in the orthorhombic notation. These magnetic stripes run along diagonal directions, the same as in the nickelates. The magnetic correlation length in this non-superconducting compound is much smaller than in the superconducting state x = 0.12 compound [167] and is almost two-dimensional. Matsuda *et al.* have provided a phase diagram of the incommensurability as a function of hole concentration from their study, and other results, which is shown in Figure 2.36.

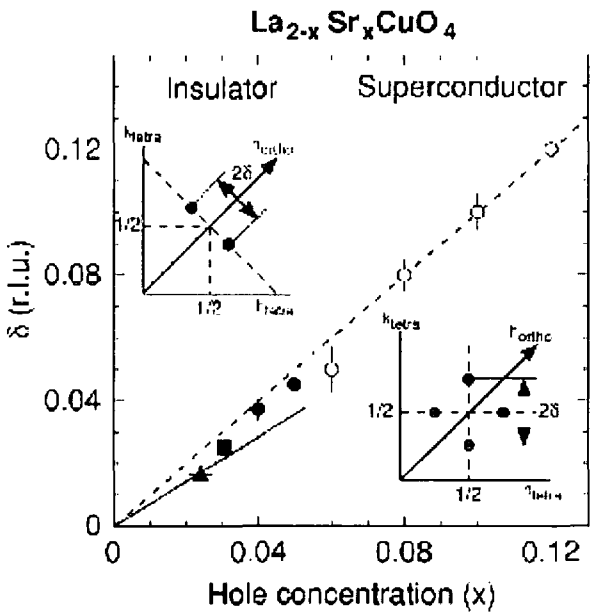

Figure 2.36 Incommensurability (tetragonal units) as a function of hole concentration x. The insets show the configuration of the IC peaks in the insulting phase (diagonal stripe) and the superconducting phase (collinear stripe). (taken from Matsuda *et al.* [172])

The interesting feature is the static magnetic spin modulation change from diagonal to collinear at x = 0.055 which is also the position of the insulator to superconductor transition. In the insulating phase the stripes run diagonally as in the $La_{2-x}Sr_xNiO_4$ system, that is an insulator. The static spin in-plane correlation length decreases when the hole concentration increases within the insulating phase. The graph shows the splitting of the IC peaks, δ, follows the linear relation $\delta = x$, apart from below x =

0.04. They interpreted this in the context of the stripe model, as the hole concentration is decreased, the hole concentration increases gradually from ~ 0.5 hole/Cu at $x = 0.12$ to 1 hole/Cu at $x = 0.024$.

Yamada *et al.* by using low energy neutron scattering on a broad range samples with hole concentration up to $x = 0.25$, suggested that the saturation of T_C occurs as a result of the saturations of the doped O ($2P$)-type carrier number and the decrease of T_C in the overdoped region is caused by the shortening of the dynamical coherence length of the incommensurate spin fluctuations [56]. From these studies it might be suggested that fluctuating form of stripes in the cuprates is necessary for high-temperature superconductivity and superconductivity and static magnetic order (fixed stripes) can coexist.

2.6 References

[1] Y. Tomioka, A. Asamitsu, H. Kuwahara, *et al.*, Physical Review B **53**, R1689 (1996).

[2] C. H. Chen, S. W. Cheong, and A. S. Cooper, Physical Review Letters **71**, 2461 (1993).

[3] J. Verwey, P. W. Haayman, and F. C. Romeijin, J. Chem. Phys. **15**, 181 (1947).

[4] Z. Zhang and S. Satpathy, Physical Review B **44**, 13319 (1991).

[5] T. Yamada, K. Suzuki, and S. Chikazumi, Applied Physics Letters **13**, 172 (1968).

[6] J. Samuelson, E. J. Bleeker, L. Dobrzynski, *et al.*, Appl. Phys. **39**, 1114 (1968).

[7] S. K. Park, T. Ishikawa, and Y. Tokura, Physical Review B **58**, 3717 (1998).

[8] P. A. Miles, W. B. Westphal, and A. von Hippel, Rev. Mod. Phys. **29**, 279 (1957).

[9] G. Shirane, S. Chikazumi, J. Akimitsu, *et al.*, J. Of Physical society of Japan **39**, 949 (1975).

[10] M. L. Rudee, D. J. Smith, and D. T. Margulies, Physical Review B **59**, R11633 (1999).

[11] J. Garcia, G. Subias, M. G. Proietti, *et al.*, Physical Review B **6305**, 4110 (2001).

[12] J. Q. Li, Y. Matsui, S. K. Park, *et al.*, Physical Review Letters **79**, 297 (1997).

[13] P. D. Battle, T. C. Gibb, and P. Lightfoot, Journal of Solid State Chemistry **84**, 271 (1990).

[14] S. K. Park, T. Ishikawa, Y. Tokura, *et al.*, Physical Review B **60**, 10788 (1999).

[15] R. Kajimoto, Y. Oohara, M. Kubota, *et al.*, Journal of Physics and Chemistry of Solids **62**, 321 (2001).

[16] N. Ikeda, Y. Yamada, S. Nohdo, *et al.*, Physica B **241**, 820 (1997).

[17] Y. Yamada, K. Kitsuda, S. Nohdo, *et al.*, Physical Review B **62**, 12167 (2000).

[18] T. Vogt, P. M. Woodward, P. Karen, *et al.*, Physical Review Letters **84**, 2969 (2000).

[19] E. Suard, F. Fauth, V. Caignaert, *et al.*, Physical Review B **61**, 11871 (2000).

[20] I. A. Zaliznyak, J. P. Hill, J. M. Tranquada, *et al.*, Physical Review Letters **85**, 4353 (2000).

[21] C. Martin, A. Maignan, D. Peloquin, *et al.*, Applied Physics Letters **71**, 1421 (1997).

[22] M. J. Konstantinovic, Z. V. Popovic, A. N. Vasil'ev, *et al.*, Solid State Communications **112**, 397 (1999).

[23] Y. Fagot-Revurat, M. Mehring, and R. K. Kremer, Physical Review Letters **84**, 4176 (2000).

[24] H. Nakao, K. Ohwada, N. Takesue, *et al.*, Physical Review Letters **85**, 4349 (2000).

[25] M. J. Konstantinovic, M. Isobe, and Y. Ueda, Physical Review B **6310**, 0303 (2001).

[26] G. Aeppli and D. J. Buttrey, Phys. Rev. Lett **61**, 203 (1988).

[27] D. Vaknin, S. K. Sinha, D. E. Moncton, *et al.*, Phys. Rev. Lett. **58**, 2802 (1987).

[28] T. Ido, K. Magoshi, H. Eisaki, *et al.*, Physical Review B-Condensed Matter **44**, 12094 (1991).

[29] V. I. Anisimov, M. A. Korotin, J. Zaanen, *et al.*, Physical Review Letters **68**, 345 (1992).

[30] S. M. Hayden, G. H. Lander, J. Zarestky, *et al.*, Physical Review Letters **68**, 1061 (1992).

[31] T. Jestadt, K. H. Chow, S. J. Blundell, *et al.*, Physical Review B-Condensed Matter **59**, 3775 (1999).

[32] R. J. Cava, B. Batlogg, T. T. Palstra, *et al.*, Physical Review B-Condensed Matter **43**, 1229 (1991).

[33] X. X. Bi and P. C. Eklund, Physical Review Letters **70**, 2625 (1993).

[34] T. R. Thurston, R. J. Birgeneau, M. A. Kastner, *et al.*, Physical Review B **40**, 4585 (1989).

[35] S. W. Cheong, G. Aeppli, T. E. Mason, *et al.*, Physical Review Letters **67**, 1791 (1991).

[36] H. Takagi, T. Ido, S. Ishibashi, *et al.*, Physical Review B **40**, 2254 (1989).

[37] P. Wochner, J. M. Tranquada, D. J. Buttrey, *et al.*, Physical Review B **57**, 1066 (1998).

[38] J. Zaanen and P. B. Littlewood, Physical Review B **50**, 7222 (1994).

[39] S. W. Cheong, H. Y. Hwang, C. H. Chen, *et al.*, Physical Review B-Condensed Matter **49**, 7088 (1994).

[40] S. H. Han, M. B. Maple, Z. Fisk, *et al.*, Physical Review B-Condensed Matter **52**, 1347 (1995).

[41] A. P. Ramirez, P. L. Gammel, S. W. Cheong, *et al.*, Physical Review Letters **76**, 447 (1996).

[42] S. H. Lee and S. W. Cheong, Physical Review Letters **79**, 2514 (1997).

[43] J. M. Tranquada, D. J. Buttrey, V. Sachan, *et al.*, Physical Review Letters **73**, 1003 (1994).

[44] S. H. Lee, S. W. Cheong, K. Yamada, *et al.*, Physical Review B **6306**, 0405 (2001).

[45] J. M. Tranquada, D. J. Buttrey, and V. Sachan, Physical Review B-Condensed Matter **54**, 12318 (1996).

[46] V. Sachan, D. J. Buttrey, J. M. Tranquada, *et al.*, Physical Review B **51**, 12742 (1995).

[47] G. H. Lander, P. J. Brown, C. Stassis, *et al.*, Physical Review B-Condensed Matter **43**, 448 (1991).

[48] C. H. Du, M. E. Ghazi, Y. Su, *et al.*, Physical Review Letters **84**, 3911 (2000).

[49] A. Vigliante, M. vonZimmermann, J. R. Schneider, *et al.*, Physical Review B-Condensed Matter **56**, 8248 (1997).

[50] J. M. Tranquada, J. D. Axe, N. Ichikawa, *et al.*, Physical Review Letters **78**, 338 (1997).

[51] J. E. Ostenson, S. Budko, M. Breitwisch, *et al.*, Physical Review B **56**, 2820 (1997).

[52] J. M. Tranquada, Y. Kong, J. E. Lorenzo, *et al.*, Physical Review B **50**, 6340 (1994).

[53] J. M. Tranquada, J. E. Lorenzo, D. J. Buttrey, *et al.*, Physical Review B **52**, 3581 (1995).

[54] J. M. Tranquada, P. Wochner, and D. J. Buttrey, Physical Review Letters **79**, 2133 (1997).

[55] H. Yoshizawa, T. Kakeshita, R. Kajimoto, *et al.*, Physical Review B **61**, R854 (2000).

[56] K. Yamada, C. H. Lee, K. Kurahashi, *et al.*, Physical Review B **57**, 6165 (1998).

[57] J. M. Tranquada, J. D. Axe, N. Ichikawa, *et al.*, Physical Review B **54**, 7489 (1996).

[58] T. Katsufuji, T. Tanabe, T. Ishikawa, *et al.*, Physical Review B-Condensed Matter **60**, R5097 (1999).

[59] G. Blumberg, M. V. Klein, and S. W. Cheong, Physical Review Letters **80**, 564 (1998).

[60] T. Katsufuji, T. Tanabe, T. Ishikawa, *et al.*, Physical Review B-Condensed Matter **54**, 14230 (1996).

[61] K. Yoshinari, P. C. Hammel, and S. W. Cheong, Physical Review Letters **82**, 3536 (1999).

[62] T. Mizokawa and A. Fujimori, Physical Review B-Condensed Matter **56**, 11920 (1997).

[63] O. Zachar, S. A. Kivelson, and V. J. Emery, Physical Review B **57**, 1422 (1998).

[64] T. Strangfeld, K. Westerholt, and H. Bach, Physica C **183**, 1 (1991).

[65] C. Hess, B. Buchner, M. Hucker, *et al.*, Physical Review B-Condensed Matter **59**, R10397 (1999).

[66] J. M. Tranquada, P. Wochner, A. R. Moodenbaugh, *et al.*, Physical Review B **55**, R6113 (1997).

[67] S. A. Hoffman, C. Venkatraman, S. N. Ehrlich, *et al.*, Physical Review B-Condensed Matter **43**, 7852 (1991).

[68] K. Yamamoto, T. Katsufuji, T. Tanabe, *et al.*, Physical Review Letters **80**, 1493 (1998).

[69] K. H. Chow, P. A. Pattenden, S. J. Blundell, *et al.*, Physical Review B **53**, 14725 (1996).

[70] R. J. McQueeney, A. R. Bishop, Y. S. Yi, *et al.*, Journal of Physics-Condensed Matter **12**, L317 (2000).

[71] Y. S. Yi, Z. G. Yu, A. R. Bishop, *et al.*, Physical Review B-Condensed Matter **58**, 503 (1998).

[72] K. Yonemitsu, A. R. Bishop, and J. Lorenzana, Physical Review B **47**, 12059 (1993).

[73] P. Kuiper, J. Vanelp, G. A. Sawatzky, *et al.*, Physical Review B **44**, 4570 (1991).

[74] Z. Q. Tan, S. M. Heald, S. W. Cheong, *et al.*, Physical Review B-Condensed Matter **47**, 12365 (1993).

[75] O. Zachar, Physical Review B **62**, 13836 (2000).

[76] Y. Tokura, in *Colossal magnetoresistive oxides*, edited by Y. Tokura (Gordon and Breach Science publishers, Vol. 2, p. 1.

[77] R. M. Kusters, J. Singleton, D. A. Keen, *et al.*, Physica B **155**, 362 (1989).

[78] R. Vonhelmolt, J. Wecker, B. Holzapfel, *et al.*, Physical Review Letters **71**, 2331 (1993).

[79] E. O. Wollan and W. C. Koehler, Phys. Rev. **100**, 545 (1955).

[80] D. S. Dessau and Z.-X. Shen, in *Colossal magnetoresistive oxides*, edited by Y. Tokura (Gordon and Breach Science publishers, 2000), Vol. 2, p. 149.

[81] J. B. Goodenough, Phys. Rev. **100**, 564 (1955).

[82] C. W. Searle and S. T. Wang, Can. J. Phys. **47**, 2703 (1969).

[83] M. Uhera, S. Mori, C. H. Chen, *et al.*, Nature **399**, 560 (1999).

[84] C. Martin, A. Maignan, M. Hervieu, *et al.*, Physical Review B **60**, 12191 (1999).

[85] S.-W. Cheong, in *Colossal magnetoresistive oxides*, edited by Y. Tokura (Gordon and Breach Science publishers, 2000), Vol. 2, p. 237.

[86] Z. Jirak, S. Krupicka, Z. Simsa, *et al.*, Journal of Magnetism and Magnetic Materials **53**, 153 (1985).

[87] V. I. Anisimov, I. S. Elfimov, M. A. Korotin, *et al.*, Physical Review B **55**, 15494 (1997).

[88] S. K. Mishra, R. Pandit, and S. Satpathy, Physical Review B **56**, 2316 (1997).

[89] L. Sheng and C. S. Ting, Physical Review B **57**, 5265 (1997).

[90] L. F. Feiner and A. M. Oles, Physical Review B **59**, 3295 (1999).

[91] J. van den Brink, P. Horsch, F. Mack, *et al.*, Physical Review B **59**, 6795 (1999).

92 A. Urushibara, Y. Moritomo, T. Arima, *et al.*, Physical Review B **51**, 14103 (1995).

93 L. Pinsard, J. RodriguezCarvajal, A. H. Moudden, *et al.*, Physica B **234**, 856 (1997).

94 T. Niemoller, M. von Zimmermann, S. Uhlenbruck, *et al.*, European Physical Journal B **8**, 5 (1999).

95 H. Fujishiro, T. Fukase, and M. Ikebe, Journal of the Physical Society of Japan **67**, 2582 (1998).

96 Y. Yamada, J. Suzuki, K. Oikawa, *et al.*, Physical Review B **62**, 11600 (2000).

97 Y. Yamada, O. Hino, S. Nohdo, *et al.*, Physical Review Letters **77**, 904 (1996).

98 Y. Endoh, K. Hirota, S. Ishihara, *et al.*, Physical Review Letters **82**, 4328 (1999).

99 J. F. Mitchell, D. N. Argyriou, and J. D. Jorgensen, in *Colossal magnetoresistive oxides*, edited by Y. Tokura (Gordon and Breach Science publishers, 2000), Vol. 2, p. 187.

100 Y. Murakami, J. P. Hill, D. Gibbs, *et al.*, Physical Review Letters **81**, 582 (1998).

101 Y. Murakami, H. Kawada, H. Kawata, *et al.*, Physical Review Letters **80**, 1932 (1998).

102 K. Nakamura, T. Arima, A. Nakazawa, *et al.*, Physical Review B-Condensed Matter **60**, 2425 (1999).

103 J. P. H. Zimmermann M. v, Doon Gibbs, M.Blume, D. casa, B. Kimer, Y. Murakami, Y. tomioka, and Y. Tokura, Rev. Lett. **83**, 4872 (1999).

104 C. Zener, Physical Review **82**, 403 (1951).

105 P. G. Degennes, Physical Review **118**, 141 (1960).

106 E. Dagotto, T. Hotta, and A. Moreo, Physics Reports **344**, 1 (2001).

107 H. A. Jahn and E. Teller, Proc. Roy. Soc. London, A **161**, 220 (1937).

108 A. J. Millis, P. B. Littlewood, and B. I. Shraiman, Physical Review Letters **74**, 5144 (1995).

109 P. G. Radaelli, D. E. Cox, M. Marezio, *et al.*, Physical Review Letters **75**, 4488 (1995).

110 K. H. Kim, J. Y. Gu, H. S. Choi, *et al.*, Physical Review Letters **77**, 1877 (1996).

111 P. Dai, J. D. Zhang, H. A. Mook, *et al.*, Physical Review B **54**, R3694 (1996).

112 A. J. Millis, B. I. Shraiman, and R. Mueller, Physical Review Letters **77**, 175 (1996).

113 T. Kimura, Y. Tomioka, A. Asamitsu, *et al.*, Physical Review Letters **81**, 5920 (1998).

114 R. Maezono, S. Ishihara, and N. Nagaosa, Physical Review B **57**, R13993 (1998).

115 H. Kawano, R. Kajimoto, H. Yoshizawa, *et al.*, Physical Review Letters **78**, 4253 (1997).

116 J. Fontcuberta, Physiscs World **February**, 33 (1999).

117 T. Hotta, A. L. Malvezzi, and E. Dagotto, Physical Review B **62**, 9432 (2000).

[118] S. Shimomura, N. Wakabayashi, H. Kuwahara, *et al.*, Physical Review Letters **83**, 4389 (1999).

[119] C. N. R. Rao, A. Arulraj, P. N. Santosh, *et al.*, Chemistry of Materials **10**, 2714 (1998).

[120] A. Arulraj, P. N. Santhosh, R. S. Gopalan, *et al.*, Journal of Physics-Condensed Matter **10**, 8497 (1998).

[121] Y. Tokura, H. Kuwahara, Y. Moritomo, *et al.*, Physical Review Letters **76**, 3184 (1996).

[122] A. Arulraj, R. Gundakaram, A. Biswas, *et al.*, Journal of Physics-Condensed Matter **10**, 4447 (1998).

[123] N. Kumar and C. N. R. Rao, Journal of Solid State Chemistry **129**, 363 (1997).

[124] P. V. Vanitha, R. S. Singh, S. Natarajan, *et al.*, Solid State Communications **109**, 135 (1999).

[125] C. H. Chen and S. W. Cheong, Physical Review Letters **76**, 4042 (1996).

[126] H. Kuwahara, Y. Tomioka, A. Asamitsu, *et al.*, Science **270**, 961 (1995).

[127] A. Biswas, A. Arulraj, A. K. Raychaudhuri, *et al.*, Journal of Physics-Condensed Matter **12**, L101 (2000).

[128] A. Chainani, H. Kumigashira, T. Takahashi, *et al.*, Physical Review B-Condensed Matter **56**, R15513 (1997).

[129] C. Frontera, J. L. Garcia-Munoz, A. Llobet, *et al.*, Journal of Physics-Condensed Matter **13**, 1071 (2001).

[130] R. Kajimoto, T. Kakeshita, Y. Oohara, *et al.*, Physical Review B-Condensed Matter **58**, R11837 (1998).

[131] A. P. Ramirez, P. Schiffer, S. W. Cheong, *et al.*, Physical Review Letters **76**, 3188 (1996).

[132] P. Schiffer, A. P. Ramirez, W. Bao, *et al.*, Physical Review Letters **75**, 3336 (1995).

[133] P. G. Radaelli, D. E. Cox, M. Marezio, *et al.*, Physical Review B-Condensed Matter **55**, 3015 (1997).

[134] S. Mori, C. H. Chen, and S. W. Cheong, Physical Review Letters **81**, 3972 (1998).

[135] T. Hotta, Y. Takada, H. Koizumi, *et al.*, Physical Review Letters **84**, 2477 (2000).

[136] T. Vogt, A. K. Cheetham, R. Mahendiran, *et al.*, Physical Review B **54**, 15303 (1996).

[137] F. Millange, S. de Brion, and G. Chouteau, Physical Review B **62**, 5619 (2000).

[138] C. Frontera, J. L. Garcia-Munoz, A. Llobet, *et al.*, Physical Review B **62**, 3002 (2000).

[139] S. Mori, T. Katsufuji, N. Yamamoto, *et al.*, Physical Review B-Condensed Matter **59**, 13573 (1999).

[140] R. Kajimoto, H. Yoshizawa, Y. Tomioka, *et al.*, Physical Review B **6321**, 2407 (2001).

[141] J. L. Garcia-Munoz, C. Frontera, M. A. G. Aranda, *et al.*, Physical Review B **6305**, 4415 (2001).

142 H. Kuwahara, Y. Moritomo, Y. Tomioka, *et al.*, Physical Review B **56**, 9386 (1997).

143 A. Llobet, C. Ritter, C. Frontera, *et al.*, Journal of Magnetism and Magnetic Materials **197**, 549 (1999).

144 J. Fontcuberta, B. Martinez, A. Seffar, *et al.*, Physical Review Letters **76**, 1122 (1996).

145 T. Terai, T. Sasaki, T. Kakeshita, *et al.*, Physical Review B **61**, 3488 (2000).

146 R. Kajimoto, H. Yoshizawa, H. Kawano, *et al.*, Physical Review B-Condensed Matter **60**, 9506 (1999).

147 P. M. Woodward, D. E. Cox, T. Vogt, *et al.*, Chemistry of Materials **11**, 3528 (1999).

148 M. R. Lees, J. Barratt, G. Balakrishnan, *et al.*, Physical Review B **52**, 14303 (1995).

149 V. Caignaert, F. Millange, M. Hervieu, *et al.*, Solid State Communications **99**, 173 (1996).

150 Y. Tomioka, A. Asamitsu, Y. Moritomo, *et al.*, Physical Review Letters **74**, 5108 (1995).

151 Y. Tokura and Y. Tomioka, Journal of Magnetism and Magnetic Materials **200**, 1 (1999).

152 A. Biswas, A. K. Raychaudhuri, R. Mahendiran, *et al.*, Journal of Physics-Condensed Matter **9**, L355 (1997).

153 J. H. Jung, H. J. Lee, T. W. Noh, *et al.*, Physical Review B **62**, 481 (2000).

154 H. Yoshizawa, R. Kajimoto, H. Kawano, *et al.*, Materials Science and Engineering B-Solid State Materials For Advanced Technology **63**, 125 (1999).

155 C. Ritter, R. Mahendiran, M. R. Ibarra, *et al.*, Physical Review B **61**, R9229 (2000).

156 N. Fukumoto, S. Mori, N. Yamamoto, *et al.*, Physical Review B-Condensed Matter **60**, 12963 (1999).

157 R. Mahesh and M. Itoh, Journal of Solid State Chemistry **144**, 232 (1999).

158 V. Kiryukhin, B. G. Kim, T. Katsufuji, *et al.*, Physical Review B **6314**, 4406 (2001).

159 M. K. Crawford, R. L. Harlow, E. M. McCarron, *et al.*, Physical Review B **44**, 7749 (1991).

160 M. Von Zimmermann, A. Vigliante, T. Niemoller, *et al.*, Europhysics Letters **41**, 629 (1998).

161 J. M. Tranquada, N. Ichikawa, and S. Uchida, Physical Review B-Condensed Matter **59**, 14712 (1999).

162 T. Niemoller, N. Ichikawa, T. Frello, *et al.*, European Physical Journal B **12**, 509 (1999).

163 N. Ichikawa, S. Uchida, J. M. Tranquada, *et al.*, Physical Review Letters **85**, 1738 (2000).

164 P. G. Radaelli, D. G. Hinks, A. W. Mitchell, *et al.*, Physical Review B **49**, 4163 (1994).

165 Y. Koyama, Y. Wakabayashi, K. Ito, *et al.*, Physical Review B **51**, 9045 (1995).

166 T. Suzuki, T. Goto, K. Chiba, *et al.*, Physical Review B **57**, R3229 (1998).

167 H. Kimura, H. Matsushita, K. Hirota, *et al.*, Physical Review B **61**, 14366 (2000).

168 Y. Maeno, A. Odagawa, N. Kakehi, *et al.*, Physica C **173**, 322 (1991).

169 S. Wakimoto, R. J. Birgeneau, M. A. Kastner, *et al.*, Physical Review B **61**, 3699 (2000).

170 X. G. Zheng, C. N. Xu, Y. Tomokiyo, *et al.*, Physical Review Letters **85**, 5170 (2000).

171 O. Baberski, A. Lang, O. Maldonado, *et al.*, Europhysics Letters **44**, 335 (1998).

172 M. Matsuda, M. Fujita, K. Yamada, *et al.*, Physical Review B **62**, 9148 (2000).

Chapter 3

A brief introduction to the theory of X-ray scattering

3.1 Introduction

X-rays are electromagnetic waves with wavelengths in the region of an Angstrom. The German physicist Röentgen discovered X-rays in 1895, and since that time it is a valuable probe to extracting the structure of mater. Max von Läue discovered the diffraction of X-rays by crystals in 1912. Von Läue showed that the phenomenon could be described in term of diffraction from a three-dimensional grating. In 1913, W. L. Bragg noticed the similarity of diffraction to ordinary reflection and deduced a simple equation treating diffraction as reflection from planes in the lattice. In the 1970s, it was realised that the synchrotron radiation emitted from charged particles is a more intense and useful source of X-ray. Third generation synchrotron sources are $\sim 10^{12}$ times brighter than the early laboratory-based sources and this makes synchrotron X-rays a vital probe for the exploration of very weak superlattice peaks. Nowadays, synchrotron X-ray scattering is widely used in the study of both charge and magnetism.

3.2 Charge scattering

X-rays from conventional generators are unpolarized, that is the electric and magnetic vectors, associated with a given photon, have a random orientation with respect to the orientations of the electric and magnetic vectors of other photons. In the classical theory of X-ray scattering, when the X-ray photons collide with matter, the oscillating electric field of the incident photon exerts a force on the electric charge, which then causes the charged particles of the object to oscillate with the same frequency as the incident radiation. This process is known as elastic scattering.

In a quantum mechanical description, the X-ray photon has a momentum of $\hbar k$ and energy $\hbar\omega$, which may be transferred to the electron. This process is known as the Compton effect. In scattering process even in elastic scattering, the momentum may be transferred with definition:

$$\hbar Q = \hbar k - \hbar k' \qquad [3.1]$$

where $\hbar k$ and $\hbar k'$ are the initial and final momentums of the photon respectively. The vector, Q, is known as the wavevector transfer or scattering vector.

3.2.1 Kinematical theory of scattering

The kinematical theory treats the scattering from each volume element in the sample as being independent of that of other volume elements. If the interference from multiple reflections is ignored, the kinematical theory is a good approximation for the studies of highly imperfect crystals.

The theory is based on the assumption that the total diffracted radiation is a very small portion of the incident beam and every X-ray photon only scatters within the sample volume once. The source of radiation and the detector are far from the sample and so it can be assumed that the incident beam is a plane wave front and the scattered rays travel along parallel paths. It is also assumed that the scattering is coherent over a mosaic block and the small energy loss due to the exchange of energy between photon and nuclei is also ignored.

Real macroscopic crystals are often imperfect, and may be considered as small perfect blocks that are each slightly misaligned relative to one another. The crystal is then said to be mosaic, as it is composed of a mosaic of small blocks. These mosaic blocks are typically about 10^3 Å in diameter. A crystal with such mosaic character is considered imperfect because the internal periodicity is not exact and long-range. Each block is small and can be considered that the diffracted beam before being re-scattered exits the block. In this case the kinematical approximation applies. As the block size becomes larger this approximation breaks down, and instead it is necessary to allow for multiple scattering effects. If a truly collimated monochromatic beam of X-ray is scattered from a infinite perfect crystal, the Bragg

condition would be satisfied only at discrete 2θ values. However, because radiation is not exactly monochromatic and most crystals exhibit a mosaic spread, the spots really occur over a small range of 2θ values. Diffraction from an imperfect crystal is said to be kinematic because the mosaic nature of the crystal allows a large volume of the crystal to be involved in the diffraction process. Kinematic diffraction theory can only explain single scattering events and cannot explain the reduced intensities seen in crystals affected by multiple scattering events. For study of perfect crystals we should use the dynamical theory because the interaction between the X-ray and the crystal becomes strong, and the primary and the diffracted beams interfere with each other inside the crystal, and dispersion occurs.

3.2.1.1 Bragg's law

According to the model of Bragg, X-ray diffraction can be viewed as a process that is similar to the reflection from planes of atoms in a crystal. The crystal plane acts as a partial reflector of X-rays. The incident and diffracted rays are in the same plane as the normal to the crystal planes and defines the scattering plane. In Figure 3.1 consider two atoms A and D are situated on two adjacent crystal planes, which are separated by a distance d, the interplane spacing. The parallel X-rays beam falls on the crystal planes at an angle θ and the scattered X-rays emerge with an angle of reflection also of θ.

Bragg proposed that constructive interference between the scattered rays would occur only when the path length difference between the rays diffracting from parallel crystal planes be an integral number of wavelengths ($n\lambda$). When the crystal planes are separated by a distance d, from Figure 3.1, the path length difference between two rays from two adjacent planes containing atoms A and D is:

$$BD + DC = 2d\sin\theta \qquad [3.2]$$

Thus constructive interference occurs when the following relation holds:

$$n\lambda = 2d\sin\theta \qquad [3.3]$$

This relation was first formulated by W. L. Bragg and is known as Bragg's Law. n is called the order of reflection and it may take any integer value. Thus for a given d spacing and wavelength, the first-order peak will occur at a particular θ value. Similarly, the θ values for the second and higher order peaks can be predicted.

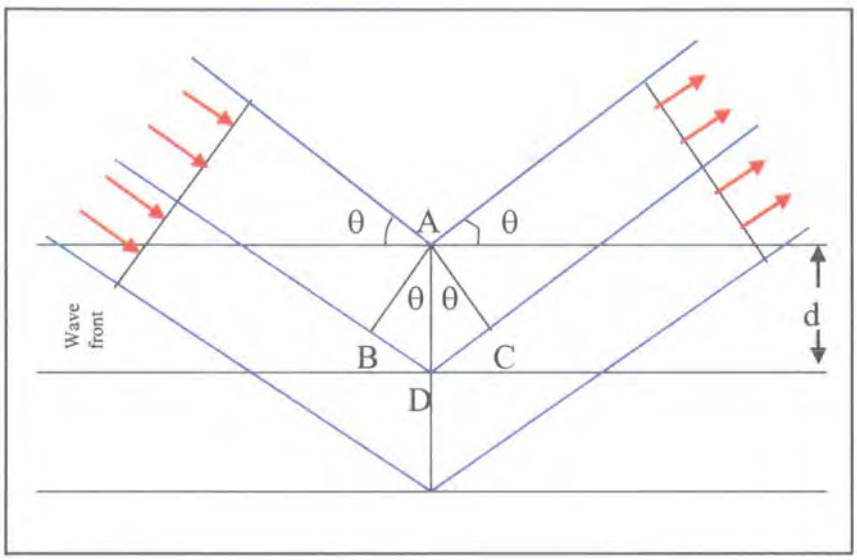

Figure 3.1 A schematic representation of diffraction of X-rays by the crystal planes.

The above derivation assumes that phase differences between wavelets scattered at different points depend only on path length differences. It is assumed that there is no intrinsic phase change between the incident and scattered beams or that this phase change is constant for all scattering events.

3.2.1.2 Ewald sphere

From the real space unit cell, the reciprocal lattice positions can be determined, which can be found in any X-ray scattering and crystallography textbook [1, 2]. Conversely, from the reciprocal lattice vectors, the dimensions of the unit cell parameters can be determined. The reciprocal lattice is a property of the crystal. Therefore, a rotation of the crystal will cause a similar rotation of the reciprocal lattice. A very useful way of representing the criterion for the Bragg law is by the sphere of reflection that was originally proposed by P. P. Ewald (Ewald sphere). The advantage of this description, the Ewald construction, is that it allows the observer to

calculate which Bragg peaks will be measurable if the orientation of the crystal with respect to the incident beam is known.

In the Ewald construction a circle with radius $1/\lambda$ is drawn centred at the crystal. A schematic representation of this construction in 2-dimensions is shown in Figure 3.2.

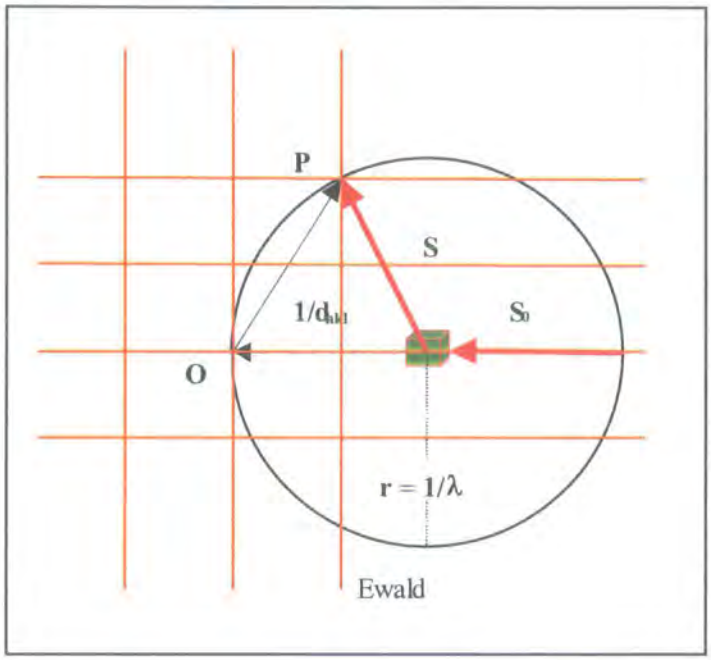

Figure 3.2 A schematic representation of the Ewald construction. S_0 and S denote the incident and scattered beams.

In 3-dimensions the circle becomes a sphere, the Ewald sphere. The direction of the primary beam is shown by vector S_0. The vector S which connects the centre of the sphere to the point P is diffracted beam. The reciprocal lattice is then drawn on the same scale as the circle (or sphere) with its origin located $1/\lambda$ from the centre of the circle on the left-hand side of the incident beam (O). The diffraction maxima (diffraction spots) occur only when the 3 Laue equations, or equivalent, the Bragg equation in vector form, are satisfied. Any reciprocal lattice point, which falls on the surface of the sphere, represents a set of planes (hkl), for which the Bragg law is satisfied. Now, by rotating the crystal about its origin, the reciprocal lattice is also rotated, and various reciprocal lattice points can be brought into coincidence with the surface of the Ewald circle (sphere). In this condition the reciprocal lattice point is in the reflecting position and the corresponding reflection can be observed.

Ewald's construction and Bragg's Law tell us that for a given wavelength constructive interference occurs when a set of crystal lattice planes separated by a spacing of d make a correct angle θ with respect to the incident beam. A diffracted beam can be measured at an angle 2θ from the incident beam. The scattering vector is perpendicular to the crystal lattice planes, and has a length inversely related to the spacing between the planes d. From Figure 3.2, it is evident that:

$$|S - S_0| = 1/d_{hkl} = 2\sin\theta/\lambda \qquad [3.4]$$

where 2θ is the angle between the incident and scattered beam. This equation can be rewritten as:

$$2d_{hkl}\sin\theta = \lambda \qquad [3.5]$$

which is Bragg's law. So Bragg's law for a set of planes (*hkl*) is simply the condition that the reciprocal lattice point (*hkl*) falls on the surface of the sphere.

3.2.1.3 Scattering by a free electron

Suppose a free electron with electric charge e and mass m is at the origin of coordinate system O in Figure 3.3. It is interesting to determine the intensity of scattered radiation at a point P in the $y-x$ plane, which is at a distance $\boldsymbol{r}$ from the electron at the origin. Suppose an electromagnetic wave with frequency ν and electric field $\vec{E}(\vec{r},t)$ interacts with the electron at O. The electric field of the incident wave can be described by equation:

$$\vec{E}(\vec{r},t) = \vec{E}_0 \exp[i(\omega t - \vec{k}.\vec{r})] \qquad [3.6]$$

where $\vec{E}_0$ is a constant vector, which describes the amplitude of the electric wave. In this equation k and ω are the wavevector and angular velocity of the incident beam.

The field exerts a periodic force $e\vec{E}(\vec{r},t)$ on the electron and therefore the electron will undergo oscillatory motion with acceleration $\vec{a} = \frac{e\vec{E}(\vec{r},t)}{m}$ and frequency ν.

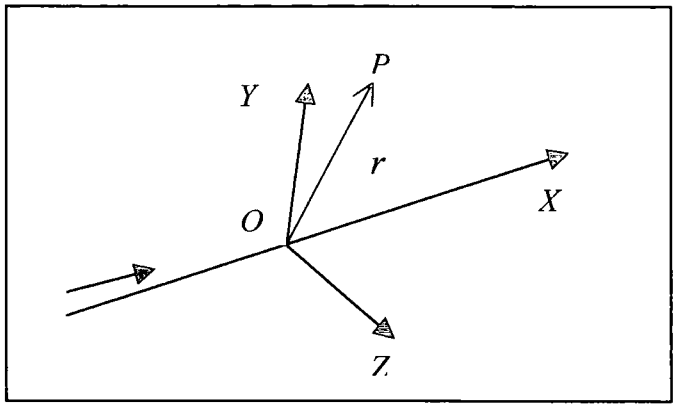

Figure 3.3 Coherent scattering of X-rays by a single electron located at the origin *O*. *P* is the observation point.

According to the classical theory of electromagnetism a charged particle in accelerated motion is a source of electromagnetic radiation. The electric field of the scattered radiation at the observation point *P* defined by vector *r* is:

$$E_{rad}(\vec{r},t) = -\vec{E}_{0rad}\exp[i(\omega t - \vec{k}.\vec{r})] \qquad [3.7]$$

where the minus sign is due to the phase shift between the incident and re-emitted radiation. $\left|\vec{E}_{orad}\right|$, the amplitude of the scattered radiation, as proposed by J. J. Thomson, is:

$$\left|\vec{E}_{0rad}\right| = \left|\vec{E}_0\right|\left(\frac{e^2}{4\pi\varepsilon_0 rmc^2}\right)\sin\varphi \qquad [3.8]$$

where φ is the angle between the direction of acceleration of electron and the scattered beam. The term sin φ is a polarization term. The decrease of $\left|\vec{E}_{orad}\right|$ with r has its origins in the fact that the scattering of radiation is in all directions. The constant factor:

$$r_0 = \left(\frac{e^2}{4\pi\varepsilon_0 mc^2}\right) = 2.82\times10^{-5}\,\text{Å} \qquad [3.9]$$

is known as the Thomson scattering length. In term of intensity, Equation [3.7] becomes:

$$I = I_0\left(\frac{e^2}{4\pi\varepsilon_0 rmc^2}\right)^2 \sin^2\varphi \qquad [3.10]$$

where I is the intensity of scattered radiation and I_0 is the intensity of incident radiation. Suppose the direction of propagation of the incident beam is along the x-axis, then we consider the components of the incident radiation polarised along the z– and y–axes. If the primary beam is completely polarized along the z-axis, then:

$$I = I_0\left(\frac{e^2}{4\pi\varepsilon_0 rmc^2}\right)^2 \qquad [3.11]$$

and with $\vec{E}(\vec{r},t)$ along the y-axis then:

$$I = I_0\left(\frac{e^2}{4\pi\varepsilon_0 rmc^2}\right)^2 \cos^2 2\theta \qquad [3.12]$$

where 2θ is the angle between the primary beam and the direction of scattering. The total scattering at P, if the primary beam is not polarized, can be written as [2]:

$$I = I_0\left(\frac{e^2}{4\pi\varepsilon_0 rmc^2}\right)^2 [1+\cos^2 2\theta]/2 \qquad [3.13]$$

This is the Thomson equation for the scattering of an X-ray beam by a single electron. The equation shows that the scattered intensity decreases as the inverse square of the distance from the scattering electron. The factor:

$$P = [1+\cos^2 2\theta]/2 \qquad [3.14]$$

is called the polarization factor which depends on the X-ray source. For synchrotron radiation in the vertical scattering plane, $P \approx 1$ and with horizontal scattering plane, the polarization factor is $\cos^2 2\theta$. When un-polarized sources are used, the P from Equation [3.14] has to be used.

The scattering is coherent, according to Thomson, because there is a well-defined phase relation between the incident radiation and the scattered one, for the electron α = 180°. The factor m^{-2} in Equation [3.13] ensures that scattering from the nucleus can be ignored because the lightest nucleus, the proton is 1837 times heavier than electron.

3.2.1.4 Scattering by an atom (Scattering factor)

The function that describes the scattering of X-rays by an atom is called the form factor, or atomic scattering factor, *f*. To a first approximation, these scattering functions are determined assuming that the electron density of each atom is discrete and spherically symmetric. At zero scattering angle, the value for a scattering function of a given atom has a value equal to the number of electrons in the atom (*Z*). As the scattering angle is increased, the value of the scattering function decreases. The decrease in scattering function with increasing scattering angle is because X-ray photons hitting different parts of the electron cloud of an atom are less likely to scatter in phase with one another as the scattering angle is increased. Scattering functions in diffraction analyses are always calculated from quantum mechanical theory. The assumption of spherically symmetric scattering functions can be a poor approximation for heavy atoms with considerable number of *d*- and *f*-type valence electrons.

The electron density of the atom, $\rho(r)$, is considered to be the sum of the distribution $\rho_j(r)$ attributed to individual electrons as:

$$\rho(\vec{r}) = \sum_{j=1}^{N} \rho_j(\vec{r})\delta(\vec{r} - \vec{r}_j) \qquad [3.15]$$

where $\rho_j(r)$ is the electron density associated with the electron centred at $r = r_j$. The atomic scattering factor can be written as the Fourier transform of this electron density:

$$f(\vec{s}) = \int \rho(\vec{r}) \exp(2\pi i \vec{s}.\vec{r}) d\vec{r} \qquad [3.16]$$

$f(\vec{s})$ is a measure of the scattering power of the atom. The value of f involves the number and distribution of atomic electrons. The integral is over the electron concentration associated with a single atom. A geometrical interpretation of scattering vector $\vec{s} = \vec{S} - \vec{S}_0$ is shown in Figure 3.4, where $\vec{S}$ and $\vec{S}_0$ are vectors along the direction of the incident and scattered beam and:

$$|\vec{s}| = (4\pi / \lambda)\sin\theta \qquad [3.17]$$

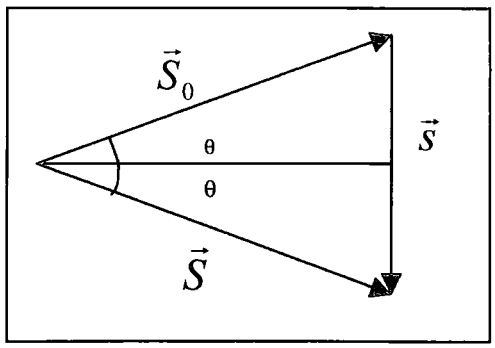

Figure 3.4 A schematic representation of the scattering vector *S*.

3.2.1.5 Scattering by an unit cell (Structure factor)

Since the crystal is made of a repeating of the fundamental unit cell, so it is enough to consider the way in which the arrangement of atoms within a single unit cell affects the diffracted intensity. The resultant wave scattered by all the atoms of the unit cell is called the structure factor. It describes how the atom arrangement affects the scattered beam.

If there are N atoms in the unit cell, the structure factor is the resultant of N waves scattered from these N atoms in the direction of the reflection (hkl). Each of these waves has amplitude proportional to f_j, the scattering factor of the j^{th} atom and a phase factor with respect to the origin of the unit cell. Then the total structure factor for a given (hkl) reflection from one unit cell in the crystal will be [3]:

$$F_{hkl}(\vec{s}) = \sum_{j=1}^{N} f_j(\vec{s})\exp(2\pi i\vec{s}.\vec{r}_j) \qquad [3.18]$$

where the summation is over all the N atoms within the unit cell. The quantity F_{hkl}, which depends on the configuration of the atoms in unit cell, is called the structure factor and h, k, and l are referred to as the indices of the reflection. Since F_{hkl} is a Fourier transform of the electron density, the electron density can also be obtained by the inverse Fourier transform of the set of structure factor for a crystal.

$$\rho(\vec{r}) = 1/v \int F_{hkl}(\vec{s}) \exp(-2\pi i \vec{s}.\vec{r}) d\vec{s} \qquad [3.19]$$

The electron density in direct space and the structure factors in reciprocal space are transforms of each other.

F_{hkl} can be divided into a real and imaginary part and written as:

$$F_{hkl} = A_{hkl} + iB_{hkl} \qquad [3.20]$$

where real and imaginary parts are:

$$A_{hkl} = \sum_{j=1}^{N} f_j \cos(2\pi \vec{s}.\vec{r}_j) \qquad [3.21]$$

$$B_{hkl} = \sum_{j=1}^{N} f_j \sin(2\pi \vec{s}.\vec{r}_j) \qquad [3.22]$$

The intensity of diffracted beam by all the atoms of the unit cell is proportional to $|F_{hkl}|^2$, the square of the amplitude of the resultant beam. It can be calculated by multiplying the F_{hkl} by its complex conjugate:

$$I_{hkl} = |F_{hkl}|^2 = A^2{}_{hkl} + B^2{}_{hkl} \qquad [3.23]$$

$$I_{hkl} = \sum_{i=1}^{N} \sum_{j=1}^{N} f_i f_j \cos[2\pi \vec{s}.(\vec{r}_i - \vec{r}_j)] \qquad [3.24]$$

It clearly shows the intensity depends only on the interatomic vector and not the actual atomic coordinates. Therefore it shows the choice of the origin of the unit cell is arbitrary.

For a crystal with a centrosymmetric unit cell and the centre of symmetry as origin, the structure factor is real:

$$F_{hkl} = \sum_{j=1}^{N} f_j \cos(2\pi \vec{s}.\vec{r}_j) \qquad [3.25]$$

For calculating the structure factor, usually the positions of atoms in the unit cell are expressed in terms of fractional coordinates and the scattering vector in reciprocal space. Then, the structure factor from Equation [3.18] can be written as:

$$F_{hkl} = \sum_{j=1}^{N} f_j \exp\left[2\pi i(hx_j + ky_j + lz_j)\right] \qquad [3.26]$$

and for centrosymmetric structure:

$$F_{hkl} = \sum_{j=1}^{N} f_j \cos\left[2\pi(hx_j + ky_j + lz_j)\right] \qquad [3.27]$$

and in this case the intensity, Equation [3.24], can be written as:

$$I_{hkl} = \sum_{i=1}^{N}\sum_{j=1}^{N} f_i f_j \cos\left\{2\pi\left[h(x_i - x_j) + k(y_i - y_j) + l(z_i - z_j)\right]\right\} \qquad [3.28]$$

Equations [3.26] and [3.27] can be used to calculate the structure factors when the atomic coordinates (x, y, z) are known for particular indices of reflection (hkl).

3.2.1.6 Scattering from a crystalline lattice

A crystalline material is constructed by periodic arrays of a basic structure unit known as the unit cell. The position of the atom in the crystal may then be written as $R_n + r_j$, where R_n specifies the origin of the unit cell in the crystal and r_j is the position of the atom related to that origin. Therefore the scattering amplitude for a crystalline material that is periodic in space can be divided by two terms and may be written as:

$$f^{crys}(\vec{s}) = \sum_{r_j} f_j(\vec{s}) e^{2\pi i \vec{s}.\vec{r}_j} \sum_{R_n} e^{2\pi i \vec{s}.\vec{R}_n} \qquad [3.29]$$

where the first term is the unit cell structure factor, and the second term, the lattice sum, is a sum over all unit cells in the crystal. The sum of the second part becomes of order N when:

$$\vec{s}.\vec{R}_n = 2\pi \times \text{integer} \quad [3.30]$$

where $\vec{R}_n$ is:

$$\vec{R}_n = n_1\hat{a}_1 + n_2\hat{a}_2 + n_3\hat{a}_3 \quad [3.31]$$

and a_1, a_2, a_3 are the basis vectors of the lattice. Any lattice site in the reciprocal lattice can be written as:

$$G = h\hat{a}^* + k\hat{b}^* + l\hat{c}^* \quad [3.32]$$

where a^*, b^*, and c^* are the basis vectors of reciprocal space. From relationship between the basis vectors in real and reciprocal space; the dot product of G and R_n becomes:

$$\vec{G}.\vec{R}_n = 2\pi \times \text{integer} \quad [3.33]$$

So:

$$\vec{s} = \vec{G} \quad [3.34]$$

This proves that $F^{crys}(s)$ is non-vanishing if, and only if, s coincides with a reciprocal lattice vector. This is the Laue condition for diffraction and is completely equivalent to Bragg's law and this equivalently follows from the relationship between points in reciprocal space and planes in the direct lattice. In diffraction experiments it is the square of the structure factor, the intensity, that is of interest. It can be shown that the contribution from the lattice sum when the number of unit cells in all three dimensions is large, is given by [4]:

$$\left|S_N(s)\right|^2 \rightarrow Nv_c^*\delta(\vec{s} - \vec{G}) \quad [3.35]$$

where v_c^* is the volume of the unit cell in reciprocal space. The variation of the temperature affects the intensity of the scattered beam. By increasing the temperature, the structure factor reduces due to the increasing of the apparent size of the atom. To include the temperature effect, the structure factor should be multiplied by a Debye-Waller factor:

$$\exp(-1/2Q^2\langle u_Q^2\rangle) \quad [3.36]$$

where $\langle u_Q^2 \rangle$ is the mean square displacement of an atom. By increasing the temperature, the atoms vibrate about their equilibrium positions and this gives rise to thermal diffuse scattering, which increases the background.

There are some factors that limit the accuracy of the experimental results on imperfect crystals:

1. Extinction, which means the exchange of energy between the incident and scattered beams.
2. Multiple reflection due to the exchange of energy between more than two beams in the crystal. It occurs when several reciprocal lattice points are simultaneously located on the sphere of reflection.
3. Absorption of the x-ray beam in the crystal by photoelectric processes, and incoherent Compton scattering.
4. Thermal diffuse scattering, which is related to the lack of translation symmetry induced by the thermal vibrations in the crystal.

The use of smaller crystals and very short wavelength beams will reduce the absorption, extinction and multiple reflection effects.

3.3 Magnetic scattering

3.3.1 Non-resonance magnetic scattering

In recent years there has been a rapid increase in the use of X-ray scattering techniques for the study of magnetism, largely due to the unique properties of synchrotron radiation, including the high flux, the possibility for tuning the beam energy, and the well-defined polarization of the beam. Most X-ray scattering by matter occurs due to scattering by electronic charge. One can also observe another type of scattering, namely by the electron's spin, which is very weak and is called X-ray magnetic scattering. In magnetic scattering one has to take into account the interaction between the photon and the spin on the electron. Magnetism originates from two parts, electronic spin and orbiting currents. In fully occupied orbitals,

because a pair of electrons occupies every orbital, the total spin and orbital momentum is zero. So magnetism can only occur if there are electrons in incompletely filled orbitals. In scattering the magnetic scattering is always dominated by strong non-magnetic, Thomson scattering (or charge scattering). Purely magnetic reflections will arise in scattering from samples in which the magnetic order does not coincide with the chemical order, as in antiferromagnets. The occurrence of antiferromagnetic ordering lowers the symmetry of a crystal, and this enlarges the unit cell. This generally produces some superstructure reflections in the X-ray scattering due to the photon-spin interaction. In ferro- and ferrimagnetic samples, in which the magnetic diffraction is superposed on Thomson diffraction, there are some methods to separate their contribution to the scattering. Polarization of the incident and secondary photons beams can be used to discriminate magnetic from Thomson scattering.

Magnetic scattering can be used in the study of the magnetic structure of matter by utilizing the polarized character of synchrotron radiation. The interaction is dependent on the direction and size of the magnetic moments, and their arrangement relative to the polarization of the incident beam. The interaction of X-rays with magnetization can be divided into two categories depending on the photon energy. When the photon energy is much higher than the absorption edge of magnetic elements, the characteristic atomic energy is neglected, and this leads to normal non-resonance magnetic X-ray scattering. When the photon energy is tuned close to the absorption edge, resonant scattering occurs. In this section non-resonance magnetic scattering will briefly be explained and the later will be explained in section 3.3.2.

Non-resonance magnetic scattering corresponds to the early predictions by Gell-Mann *et al.* [5], who developed the theory using both classical physics and quantum mechanics and Platzman *et al.* [6]. They showed that in the photon scattering cross section from electrons there exists a spin dependent correction to the classical Thomson term.

The interaction between photon and electron can be described by the following Hamiltonian proposed by Blume [7]:

$$H = \frac{e^2}{2mc^2}\sum_i A^2(r_i) - \frac{e}{mc}\sum_i P_i.A(r_i) - \frac{e\hbar}{mc}\sum_i s_i.\nabla \times A(r_i) - \frac{e^2\hbar}{2(mc^2)^2}\sum_i s_i.\left(\frac{\partial A(r_i)}{\partial t} \times A(r_i)\right) \quad [3.37]$$

The sum is over i the number of electrons in the sample. A_i is the vector potential of the electromagnetic field at the position r_i of the i^{th} electron. The first term is proportional to A^2, which is independent of spin and orbital configuration, is responsible for the normal charge scattering or Thomson scattering. The second term, which is linear in A, depends on the electron momentum and contributes to the scattering from orbital moments. This term also contributes to photon absorption, emission and resonance (anomalous) scattering processes. This term involved the energy denominator and when the photon energy is near to the one of the excitation energies in the sample, the denominator becomes very small and causes resonant scattering. The third and fourth terms contain the photon-spin coupling.

The cross section for X-ray scattering by including the interaction of photons field with magnetisation density, contains terms in addition of those for normal charge scattering, which depend on the Fourier transforms of the spin and the orbital angular momentum densities, $S(Q)$ and $L(Q)$ respectively. For X-ray energies near to that of an absorption edge there are resonant terms which can enhance the cross section for magnetic scattering. The non-resonance interaction between photons and spin and orbital momentum densities arises from relativistic interactions.

Defining the spin form factor $S(Q)$ and orbital form factor $L(Q)$ as the Fourier transforms of the spin and orbital angular momentum densities [8], the scattering amplitude per atom when the photon energy is far from any absorption edge can be written as:

$$f(Q) = f^{charge}(Q) + f^{mag.}_{non-reso.}(Q) \quad [3.38]$$

The charge and non-resonance magnetic amplitude can be written as [9-11]:

$$f^{charge}(Q) = r_0 \rho(Q) \hat{e}.\hat{e}' \quad [3.39]$$

$$f^{mag.}_{non-reso.}(Q) = i\frac{\hbar\omega}{mc^2} r_0 [A.L(Q)/2 + B.S(Q)] \quad [3.40]$$

The imaginary factor i shows the magnetic scattering is 90° out of phase with respect to the charge scattering. $\rho(Q)$ is the Fourier transform of the electric charge density and $\hat{e}$ and $\hat{e}'$ are the incident and final photon polarization vectors respectively. This equation has a pre-factor $\frac{\hbar\omega}{mc^2}$, which, for typical x-ray energies for scattering $\hbar\omega \approx 10\,\text{keV}$, is of order of 1/50 less than charge scattering. The intensity of the magnetic peak scales with square of this factor. In addition only the electrons from incomplete shells contribute to the intensity. The ratio of the magnetic to charge cross sections for the (1/2, 1/2, 1/2) magnetic satellite in NiO was found to be ~ 10^{-8} [12].

The quantities A and B are complex vectors which contain the wave vectors and polarization states of the incident and scattered photons [8]. Because these two vectors are formally different, the spin momentum μ_S and the orbital momentum μ_L contribute differently to $f^{mag.}$ and can be distinguished experimentally. The polarization vectors A and B are given by:

$$A = \frac{K^2}{2k^2}\begin{pmatrix} 0 & -(\hat{k}_i + \hat{k}_f) \\ \hat{k}_i + \hat{k}_f & 2\hat{k}_i \times \hat{k}_f \end{pmatrix} \quad [3.41]$$

$$B = \begin{pmatrix} \hat{k}_i \times \hat{k}_f & K^2/(2k^2)\hat{k}_i \\ K^2/(2k^2)\hat{k}_f & \hat{k}_i + \hat{k}_f \end{pmatrix} \quad [3.42]$$

The polarization dependence of the matrices A and B show that the diagonal elements give σ - σ and π - π scattering and the off-diagonal elements give σ - π and π - σ scattering. As the matrix A couples with the orbital part, so the σ - σ scattering can come only from spin scattering. As Equation [3.40] shows in X-ray scattering the spin and orbital terms both contribute separately to the scattering amplitude. This is in contrast to neutron scattering in which both terms are mixed. Thus X-ray scattering affords a method of separating the individual contributions of spin and orbital scattering. The orbital scattering contains the vector product of $\hat{e}$ and $\hat{e}'$, the

unit polarization vectors of the scattered and primary photon beams respectively, which means that in contrast to the charge and spin scattering, the orbital scattering in the un-rotated channel vanishes [12]. Langridge *et al.* used the non-resonant magnetic X-ray scattering to separate contributions from spin and orbital moments in the antiferromagnetic compound UAs [13].

The polarisation analysis of the scattered beam can be measured by means of the polarisation analyser. It uses this fact that for horizontal scattering, the transverse component varies with angle and at 90° becomes zero [12]. Different linear polarisation states can be selected by rotating the analyser crystal about the X-ray beam direction.

3.3.2 Resonant Scattering

Nowadays, resonant X-ray magnetic scattering has become a widely used tool for investigations of magnetic systems. The earliest resonance enhancement of the scattered intensity was observed by Namikawa *et al.*, at the *K*-edge of ferromagnetic Ni more than 15 years ago [14]. At the L_{III}-edge of holmium metal a very significant 50-fold intensity gain was observed by Gibbs *et al.* [15]. This was the first measurement of resonance magnetic diffraction from an antiferromagnetic material. The resonant enhancement of the scattered intensity was also observed at the L_{III}-edge of Dy [16], at the M_{IV}-edge of U in UAs [17] [18], and the *M*-edge energy of the NpAs [19]. These resonant enhancements result from electronic multipole transitions with the sensivity to the magnetization arising from exchange effects [10]. At the *L*-edges of rare earth elements these enhancements may amount to a factor between $10^1$and 10^2 but at the *M*-edges of the actinides it is more like 10^4-10^6. On the other hand at the *K*-edges of transition elements it is less than a factor of 2 [20].

Recently there has been an increasing effort to use the resonance X-ray scattering to study of the charge, spin, and orbital ordering in $La_{0.5}Sr_{1.5}MnO_3$ [21], $LaMnO_3$ [22], $La_{0.88}Sr_{0.12}MnO_3$ [23], $Pr_{1-x}Ca_xMnO_3$ x = 0.25, 0.4, 0.5 [24], V_2O_3 [25], and $Nd_{0.5}Sr_{0.5}MnO_3$ [26].

Tuning the photon energy to an absorption edge of a magnetic element in a crystal always produces significant changes in the scattering cross-section, usually described

under the name of anomalous dispersion, and represented by adding energy-dependent real and imaginary terms to the scattering factor. The atomic-scattering factor near the edge energy depends on the X-ray energy (E) and it is generally represented by:

$$f(Q,\omega) = f_0(Q) + f'(\omega) + if''(\omega) + f_{spin} \qquad [3.43]$$

In this equation f_0, f' and f'' are the Thomson scattering factor, the real and imaginary parts of anomalous scattering factor, respectively. f' and f'' are the contributions from processes of dispersion and absorption of X-ray. The imaginary term f'' can be directly deduced from the absorption measurements and then f' can be calculated from the Kramers-Kroning transformation of f''. The resonance scattering enters the cross section through f' and f'', and is the contribution arising from $P.A$ term in Equation [3.37]. When the incident X-ray energy is in the vicinity of the absorption edge of a constituent element in the crystal, these parameters in the atomic form factor f of the relevant type of atoms are strongly modified, which in turn modifies the structure factors.

The incident absorbed photon excites an electron to a higher lying level. The electron then decays back to the same state it started from by emitting a photon of the same energy as the incident one. This type of process, emission via some intermediate state, requires second order perturbation theory to describe it, and the resonant behaviour then arises from the energy denominator. Resonant X-ray diffraction is a method sensitive to the local properties of the crystal, such as anisotropy of the local atomic environment or atomic moments orientation. The enhancement of the scattered X-ray intensity occurs when the energy of the incident photons approaches the value required to excite an inner-shell electron into an empty state of the valance shell, and is closely related to anomalous dispersion [27]. The local environment of the edge atom strongly affects these valence shells, and therefore the atomic scattering amplitude depends on the local crystal field, the atomic magnetic moment and other factors that influence the electronic states. If the degeneracy of the valence-electron states is broken, the susceptibility of the crystal becomes anisotropic near the absorption edge. Then the anisotropic properties of the susceptibility tensor, leads to

excitement of the forbidden magnetic reflections. When the incident X-ray energy is close to the absorption edge of the material concerned, this phenomenon is known as resonance magnetic scattering. The resonant enhancement of the magnetic signal (XRES) originates in electric multipole transitions involving an electron excited to a spin-polarised state near the Fermi level [10]. The X-ray magnetic resonant scattering technique gives information on the spin state of magnetic materials. Stronger resonant enhancement occurs when the scattering involves a low-order electronic multipole transition (E1, electric dipole (much stronger) or E2, electric quadrupole) between a core level and either an unfilled atomic shell, or a narrow band [10].

The enhancement of the scattering amplitude can be used to detect weak magnetic signals. The scattering near the absorption edge is affected by the details of chemical environment. It can also be used to distinguish different magnetic elements in the unit cell or several valence states of the same ion, by tuning the photon energy from one edge to others. The chemical shift of the absorption edge is due to the variation in binding energy with the electrostatic potential in the core region, and to electronic-state-dependent differences between the spectroscopic transitions to bound unoccupied levels. For example, in study of charge ordering in manganites, since the edge energy E_A of Mn^{4+} will be slightly different from that of Mn^{3+}, an anomaly of the peak intensity near E_A is expected, which is attributed to the anomalous scattering term.

By contrast with the non-resonant magnetic X-ray scattering, which originates from magnetic coupling, the resonant magnetic X-ray scattering and the dichroism can be analysed in term of electric multiple transitions between an atomic core level and either an un-filled atomic shell or a narrow electronic band. The resonant magnetic scattering amplitude for electric dipole transitions which usually dominates in resonant magnetic cross section, can be written as [10]:

$$f_{res.}^{mag.}(E) = 3\lambda/8\pi\{e'_f \cdot e_i[F_{11} + F_{1-1}] - i(e'_f \times e_i) \cdot Z_j[F_{11} - F_{1-1}] + (e'_f \cdot Z_j)(e_i \cdot Z_j)[2F_{10} - F_{11} - F_{1-1}]\} \quad [3.44]$$

In this Equation $E = \hbar\omega$ is the photon energy, and e_i and e_f are the polarization vectors of the primary and secondary beam, implicitly contained in the vectors A and

B for the non-resonant magnetic scattering (Equations [3.41] and [3.42]). The quantity Z_j represents the magnetization direction defined by the local moment on site j. The coefficients F_{lm} contain matrix elements, which couple the ground state to the excited magnetic levels, and a resonant energy denominator for dipole transition with a change in magnetic quantum number m. The strength of the resonance is determined by the factor F_{lm}. The first term is independent of the quantization direction, corresponds to the classical anomalous scattering and can be thought of as a correction to the charge scattering. Its polarization dependence is given by $e'_f \cdot e_i$ and it only contributes for $\sigma - \sigma'$ and $\pi - \pi'$ scattering. The second term is linear in Z, and leads to magnetic scattering at the same reciprocal lattice points as non-resonant magnetic scattering which is also linear. The polarization dependence of this term is given by $e'_f \times e_i$. For σ-polarised incident radiation, which is usual in synchrotron X-ray scattering, the dipole transition rotates the magnetic scattering polarisation from σ - π, and this factor reduces to $K' \cdot Z$. So, if the magnetic moment is perpendicular to the scattering plane, no resonance magnetic scattering will be observed. The strength of this term depends on the difference between $F_{1\,1}$ and $F_{1\,-1}$. The third term is quadratic in Z and it will give second harmonic magnetic Bragg peaks and the plane of polarization is partially rotated in the scattering process.

Resonant X-ray scattering has also been used to study the orbital ordering. Resonance X-ray scattering is sensitive to the occupancy of electronic orbitals because it probes the symmetry of vacant electronic states through resonant multipole electric transitions. The variation of the orbital resonant scattering cross section with the direction of the incident polarization (azimuthal angle ψ) reflects the spatial symmetry of ordered orbitals. Unfortunately under normal conditions the core electrons of atoms control X-ray scattering and the sensitivity to the valence electron distribution is usually very low. However, Murakami *et al.*, have demonstrated this possibility by the use of X-ray energies corresponding to K-absorption edges of Mn in $La_{0.5}Sr_{1.5}MnO_3$ [21]. By turning the photon energy to the edge, it can greatly enhance the sensitivity of X-ray scattering cross sections to the valence electron distribution making a direct observation of orbital ordering. In the above mentioned K-edge experiments the direct transitions to the d states are not dipole allowed and therefore

involve weak quadrupole transitions. They concluded that the anisotropy of the atomic scattering factor is the origin of the forbidden reflection at the orbital superlattice reflection point.

3.4 References

[1] L. V. Azaroff, *Elements of X-Ray Crystallography* (McGraw-Hill, 1968).

[2] B. D. Cullity, *Elements Of X-ray Diffraction* (Addison-Wesley Publishing Company, 1978).

[3] M. M. Woolfson, *An Introduction To X-ray Crystallography* (Cambridge University Press, 1997).

[4] J. Als-Nielsen and D. McMorrow, *Elements of Modern X-Ray Physics* (John wiley & Sons, 2001).

[5] M. Gell-Mann and M. L. Golberger, Physics Review **96**, 1433 (1954).

[6] P. M. Platzman and N. Tzoar, Physics Review B **2**, 3536 (1970).

[7] M. Blume, Journal of Applied Physics **57**, 3615 (1985).

[8] M. Blume and D. Gibbs, Physical Review B **37**, 1779 (1988).

[9] D. Laundy, Radiation Physics and Chemistry **56**, 151 (1999).

[10] P. Hannon, G. T. Trammel, M. Blume, *et al.*, Physical Review Letters **61**, 1254 (1988).

[11] D. Gibbs, G. Grubel, D. R. Harshman, *et al.*, Physical Review B **43**, 5663 (1991).

[12] S. W. Lovesey and S. P. Collins, *X-ray Scattering and Absorption by magnetic Materials* (Clarendon Press. Oxford, 1996).

[13] S. Langridge, G. H. Lander, N. Bernhoeft, *et al.*, Physical Review B **55**, 6392 (1997).

[14] K. Namikawa, M. Ando, T. Nakajima, *et al.*, Journal of the Physical Society of Japan **54**, 4099 (1985).

[15] D. Gibbs, D. R. Harshman, E. D. Isaacs, *et al.*, Physical Review Letters **61**, 1241 (1988).

[16] E. D. Isaacs, D. B. McWhan, D. P. Siddons, *et al.*, Physical Review B **40**, 9336 (1989).

[17] E. D. Isaacs, D. B. McWhan, C. Peters, *et al.*, Physical Review Letters **62**, 1671 (1989).

[18] D. B. McWhan, C. Vettier, E. D. Isaacs, *et al.*, Physical Review B **42**, 6007 (1990).

[19] S. Langridge, W. G. Stirling, G. H. Lander, *et al.*, Physical Review B **49**, 12010 (1994).

[20] M. J. Cooper and W. G. Stirling, Radiation Physics and Chemistry **56**, 85 (1999).

[21] Y. Murakami, H. Kawada, H. Kawata, *et al.*, Physical Review Letters **80**, 1932 (1998).

[22] Y. Murakami, J. P. Hill, D. Gibbs, *et al.*, Physical Review Letters **81**, 582 (1998).

[23] Y. Endoh, K. Hirota, S. Ishihara, *et al.*, Physical Review Letters **82**, 4328 (1999).

[24] J. P. H. Zimmermann M. v, Doon Gibbs, M.Blume, D. casa, B. Kimer, Y. Murakami, Y. tomioka, and Y. Tokura, Physical Review Letters **83**, 4872 (1999).

[25] L. Paolasini, C. Vettier, F. de Bergevin, *et al.*, Physical Review Letters **82**, 4719 (1999).

[26] K. Nakamura, T. Arima, A. Nakazawa, *et al.*, Physical Review B-Condensed Matter **60**, 2425 (1999).

[27] E. N. Ovchinnikova and V. E. Dmitrienko, Acta Crystallographica Section a **56**, 2 (2000).

Chapter 4

Experimental equipment and techniques

4.1 Introduction

After the discovery of X-rays in 1895 by Roentgen and the invention of X-ray generators, X-rays have become a powerful probe for the study of materials. In this chapter, the generation of X-rays by laboratory-based generators and synchrotron radiation will be explained. Then the Durham X-ray laboratory diffractometer, D^3 system, will be introduced. This follows with a brief introduction about the beamlines 16.3 at SRS and BM28 at ESRF, where the experiments described in this thesis were performed. After that, double- and triple-crystal scattering geometry will be described. Finally, the floating-zone method of crystal growth will be described, the method by which the samples studied in this research were grown.

4.2 X-ray sources

The choice of source of radiation to be used in X-ray diffraction is an important factor. There are two kinds of X-ray sources that are commonly used in X-ray scattering experiments, laboratory sources and synchrotron radiation. In laboratory-based experiments, there are two types of X-ray generators, which commonly have been used, a sealed X-ray tube and a rotating anode. Nowadays, much interest has focused on synchrotron radiation sources and improvement of this kind of source is a subject of considerable research.

4.2.1 Laboratory X-ray sources

For several years the only source for producing X-rays was a hot-cathode tube. It was invented by W. D. Coolidge in 1913 and this type of generator is still used in many

laboratories today. In this device, electrons from a heated filament are accelerated through a potential difference V towards an anode, which is made of copper, molybdenum, cobalt or some other material. Each of these target materials has a different characteristic wavelength of emitted X-rays. The accelerated electrons impact on the anode and some of the kinetic energy of the electrons is converted into electromagnetic radiation in the form of X-rays. Most of the energy, is however, converted into heat, which has to be rapidly dissipated to avoid melting of the metallic target. The spectrum of X-rays generated from electrons impinging on a metal anode has two distinct components. When the accelerating potential V is low, there is a continuous spectrum, which comes from the electrons being decelerated and eventually stopped in the metal. This is known as Bremsstrahlung radiation and has a maximum energy that corresponds to the high voltages applied to the tube. The tube is constructed as a permanently sealed unit. In order to keep the anode from melting, it is made hollow and is cooled internally with circulating chilled water. The maximum power of such a device is limited by number of factors, including the cooling efficiency.

If the accelerating potential increased, then the impacting electrons can eject inner core electrons from the target element to the valence state and the X-rays will be produced by filling the core hole from other levels. This gives rise in addition to Bremsstrahlung, to characteristic radiation with a wavelength given by:

$$\lambda = \frac{hc}{E_1 - E_2} \qquad \textbf{[4.1]}$$

where h is Plank's constant, E_1 and E_2 are the energy levels of the shell electron. The characteristic lines are labelled K, L, M, etc. depending on the level from which the electron fills the core hole created by the impacting electrons.

It is also possible to produce a more powerful X-ray generator, by using a rotating anode target. In a rotating anode, the target has a cylindrical shape, which rotates about its vertical axis. The heat created by the electron's beam is spread out over a larger area compared with the fixed anode in a conventional X-ray tube. The heat is removed by circulating cooled water within the anode. In the rotating anode, the anode is changeable, and can be changed with different targets to produce different

wavelengths. In both type of X-ray sources, the radiation is emitted through beryllium windows. Beryllium is used as a window because of its low atomic number, and hence low absorption.

The major problem in using the normal X-rays sources are firstly that most of the energy of the electrons is converted to heat and secondly that only a small fraction of the produced X-ray can be used for experiment because the source emits radiation in a large solid angle.

The characteristic lines of the X-rays produced by these sources, are superimposed upon the continuous Bremsstrahlung radiation. For most X-ray scattering experiments, a monochromatic beam is required, and not the white radiation produced by X-ray sources. This can be achieved by using a single crystal monochromator. The beam is diffracted from a single crystal according to Bragg's law and only a very narrow band of wavelength appears after scattering from the monochromator crystal.

4.2.1.1 D^3 system

Recently Durham physics X-ray scattering laboratory has developed a Bede plc D^3 system. The X-ray source is a rotating anode with an electron beam spot size of 3 mm × 300 μm on a copper target. Generally the X-rays produced by laboratory-based system emerge over a wide solid angle and the use of a beam conditioner reduces the beam intensity. In this system, crossed parabolic mirrors have been used as beam conditioning optics. These mirrors collimate the beam into a relatively small spot size ~ 1 mm^2 in cross section at the sample position 500 mm from the second mirror. The system can be used in double- and triple-axis scattering geometry. A four-circle diffractometer allows measurements in all three directions in reciprocal space. The diffractometer has a facility to move the sample along the *x*-, *y*-, and *z*-direction to align the sample. The movement of the sample is fully computer controlled. This system uses a miniature size cryostat, and temperatures down to 90 K are possible using high-pressure Ar gas. Scintillation and solid-state germanium detectors are used as detector system. A view of the D^3 system is shown in Figure 4.1.

Figure 4.1 A representation of the D^3 system.

4.2.2 Synchrotron sources

Synchrotron radiation was observed for the first time in 1947 at a 70 MeV synchrotron at General Electric Laboratories in USA. Only in the 1960's was it recognised for its exceptional properties, especially in the X-ray range. In the 1970's it was realized that the synchrotron radiation emitted from charged particle, circulating in storage rings constructed for high-energy nuclear physics experiments was potentially a much more intense and useful source of X-rays and synchrotron centres were built for academic research.

The first second generation storage ring was built in Tokyo and then the high-energy storage ring, the SRS, in the UK at Daresbury in 1980. At Daresbury electrons are circulated at an energy of 2 GeV. In a synchrotron the electrons are emitted by an electron gun and then accelerated in a linear accelerator (LINAC) using pulsed electric fields. The electrons are then transferred into a circular accelerator (booster synchrotron), where their energy is further increased using radio-frequency cavities. They are then injected into the storage ring where they circulate at constant energy for many hours. For example, the revolution of electrons in the storage ring at the ESRF is 350000 revolutions per/sec. When electrons travelling at high speed are

forced to change direction by a magnetic field, they emit light called synchrotron radiation. It is necessary to pass the electrons through the radio-frequency cavity in the storage ring to compensate for the energy losses due to the emitted synchrotron radiation. In all parts of synchrotron, the electrons travel in a vacuum chamber. The quality of the vacuum is a determining factor for the lifetime of the beam. In the storage ring the electrons are grouped into bunches according to the operation of the machine. This bunch frequency means that the emitted X-rays can be pulsed at different frequencies.

The ESRF storage ring circulates electrons at an energy of 6 GeV and a current of 200 mA. The circumferences of the synchrotron and storage ring are 300 m and 844 m respectively with a booster synchrotron functioning at 10 MHz. Figure 4.2 shows a schematic representation of the ESRF synchrotron including the beamlines.

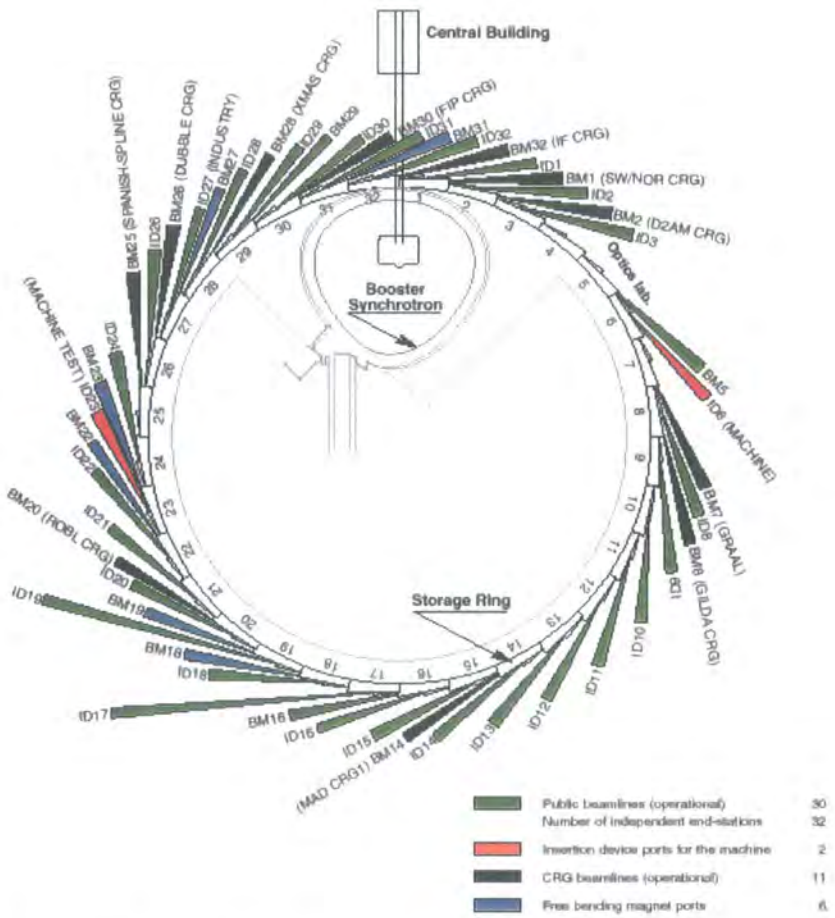

Figure 4. 2 A schematic view of ESRF synchrotron with beamlines.

Inside a storage ring, synchrotron radiation is produced by bending magnets, which are needed to keep the electrons beam to form a circle. As the beam passes through each magnet, the electrons are deviated and emit synchrotron radiation in a forward direction. At the corners of the storage ring, dipole magnets are used to provide a central force to bend the trajectory of the electrons (see Figure 4.3). When the electrons are deviated in a magnetic field of a bending magnet, X-rays will be produced at the deflecting point at a tangent to the orbit of the electron's trajectory. The radiation emitted is fan shaped.

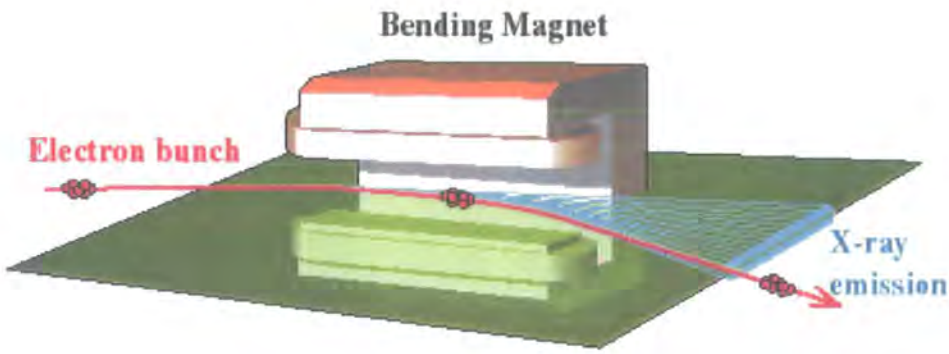

Figure 4. 3 A schematic view of a bending magnet. (taken from ESRF [3])

In the third generation of synchrotron sources, the beam characteristics were significantly improved by the use of insertion devices in the straight sections between the bending magnets. One of these inserting devises is a wiggler, which is made up of a series of dipole magnets of alternating polarity. Another important device is an undulator. These devices produce a spatially alternating magnetic field, which causes an undulation of the electron trajectory, and a large increase in intensity and coherence. In the undulators the deviations are weaker, so the light cones from the different bends overlap and the brilliance is increased. In a wiggler the amplitude of the oscillations is rather large, and the radiation from different wigglers add incoherently, whereas in undulators, the small-amplitude oscillations from the passage of a single electron produces a coherent addition of the radiation from each oscillation.

Figure 4.4 shows a schematic view of an insertion device. Wigglers and undulators are made up of a succession of small magnets with alternating polarity. The light

cones emitted at each bend superimpose, consequently increasing the light intensity. In wigglers the intensity increases proportionally with the number of magnets, and the energy spectrum is continuous. Using a multipole wiggler with n poles produces n times the flux from a dipole magnet, radiating into the same solid angle. Undulators have more magnets and the light cones from different bends overlap and interfere with each other and the wavelength spectrum is modified (the wavelength is discontinuous). At certain wavelengths it provides very high-intensity peaks.

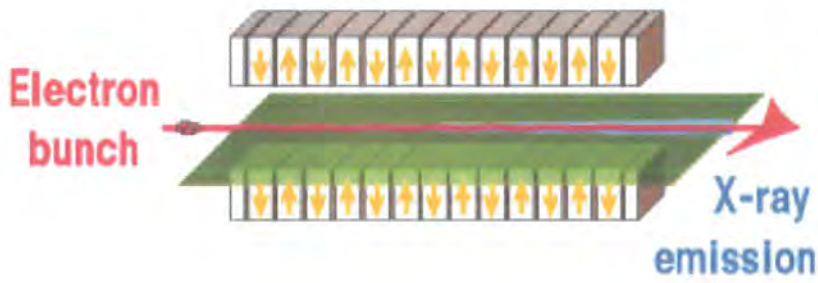

Figure 4. 4 A schematic view of an insertion device. (taken from ESRF [3])

A quality of the X-ray beam is the brilliance, which allows for comparison of the quality of the X-ray beams from different sources. This parameter is defined as:

$$\text{Brilliance} = \frac{\text{photons/second}}{(\text{mrad - collimation of beam})^2\,(\text{mm - source area})^2\,(0.1\%\ \text{bandwidth})}$$

The third generation synchrotron sources, are approximately 10^{12} times brighter than the early lab-based sources.

Synchrotron radiation produces X-rays in a wide range of energy. A single crystal monochromator can be used to produce monochromatic radiation. Further decrease of the monochromated beam bandwidth can be obtained by using a pair of monochromating crystals.

Synchrotron based X-ray scattering has several advantages compared to neutron diffraction. Firstly, it has a higher spatial resolution. With the current high-brightness synchrotron sources, it is possible to investigate ordering phenomena with correlation lengths extending over micron length scales with high accuracy. Secondly, photon beams from a synchrotron source have a high degree of linear polarization while

neutron beams are generally unpolarized. By linear polarization analysis of the diffracted beam, it is possible to distinguish between charge and magnetic diffraction. It can also provide information on the magnetic structure, and the relative contributions from spin and orbital scattering. Thirdly, because of the much higher intensities, much smaller crystals can be studied.

4.2.2.1 Beamline 16.3 (SRS)

Station 16.3 has situated on the central beamline of Wiggler 16 (a 6 Tesla superconducting wavelength-shifter) at the 2 GeV Synchrotron Radiation Source (SRS) at Daresbury and has the highest critical energy of any of the SRS stations. Beamline 16.3 is a high-resolution and high-energy single-crystal diffraction facility. A broad range of photon energies from 5 keV to above 50 keV are accessible with a maximum flux of ~ 1.2×10^{10} at around 15 keV [4]. The white X-ray beam is monochromated by either one or two channel-cut Si (111) and Si (311) single crystals. The first crystal is water-cooled to prevent thermal effects due to the absorption of incident radiation power. The polarization of the beam is tuneable from nearly linear to elliptical. The beamline is equipped with a triple-axis modified Huber cradle diffractometer that is shown in Figure 4.5. The diffractometer can translated horizontally and perpendicular to the beam direction. All motions and rotations of the diffractometer are computer controlled using PINCER software, developed at Daresbury.

4.2.2.2 Beamline BM28 (ESRF)

Beamline BM28 (*XMaS*) is a British CRG situated on a bending magnet at the ESRF. The *XMaS* beam line has been designed to perform single crystal diffraction over an energy range of 3 to 15 keV. The optic part of the beam line consists of a double-crystal Si (111) monochromator followed by a toroidal mirror, delivering a monochromated and focused beam both in horizontal and vertical directions. The first monochromator crystal is water-cooled to avoid the thermal effect arising from absorption of the incident synchrotron radiation power. The mirror is made from

single crystal silicon and to enhance the mirror reflectivity, its surface has been coated with a thin layer of rhodium. The mirror has a sectored cylindrical cross-section and focuses the beam to a small spot onto the sample surface.

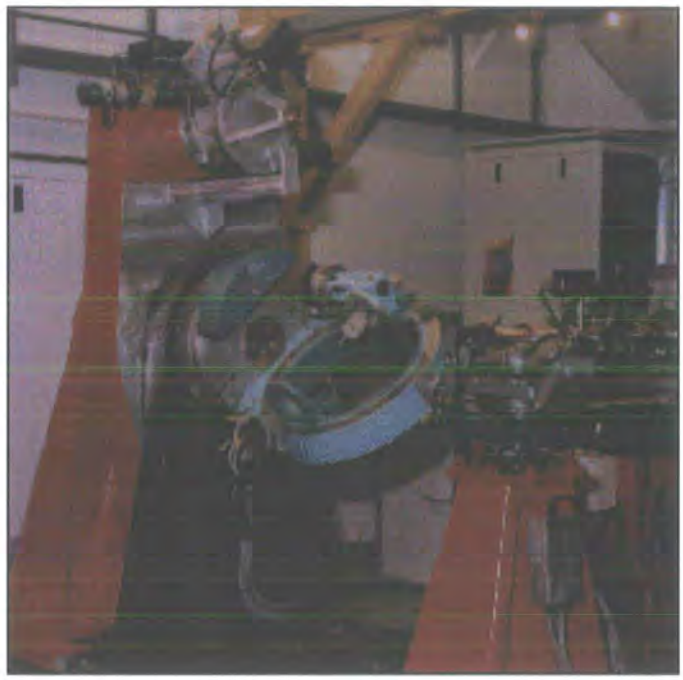

Figure 4. 5 A view of diffractometer situated at beamline 16.3 at SRS.

The beamline is equipped with a four-circle, 11-axis Huber diffractometer as shown in Figure 4.6. The four circles are the number of rotation motions available and in the instrument shown three of these are associated with the crystal and one with the detector. The plane containing the incident and diffracted beam is normally vertical. The four circles are normally divided into the crystal orienter, which contains the phi (ϕ) and chi (χ) circle, and the base which contains omega (ω) and 2 theta (2θ). The detector is mounted on the (2θ) circle, the angle between the detector and the direct beam can be set to any desired value.

Nowadays all single crystal diffractometers are computer controlled. They can determine the orientation of the crystal, move the crystal and records the diffracted photons. In *XMaS*, which uses SPEC software, orientation matrices may be defined in (phi, chi, omega, 2 theta) four-circle-scattering geometries. Once a number of reflections have been described in terms of measured setting angles, these are used to

define two matrices conventionally called U and B [5]. The matrix B used quantities related to the direct and reciprocal cell constants to convert reflection indices to parameters (in $Å^{-1}$) in reciprocal space, while U relates these reciprocal space coordinates to the coordinate system of the diffractometer to give values that can be manipulated in fairly standard ways by relations about the various setting axes.

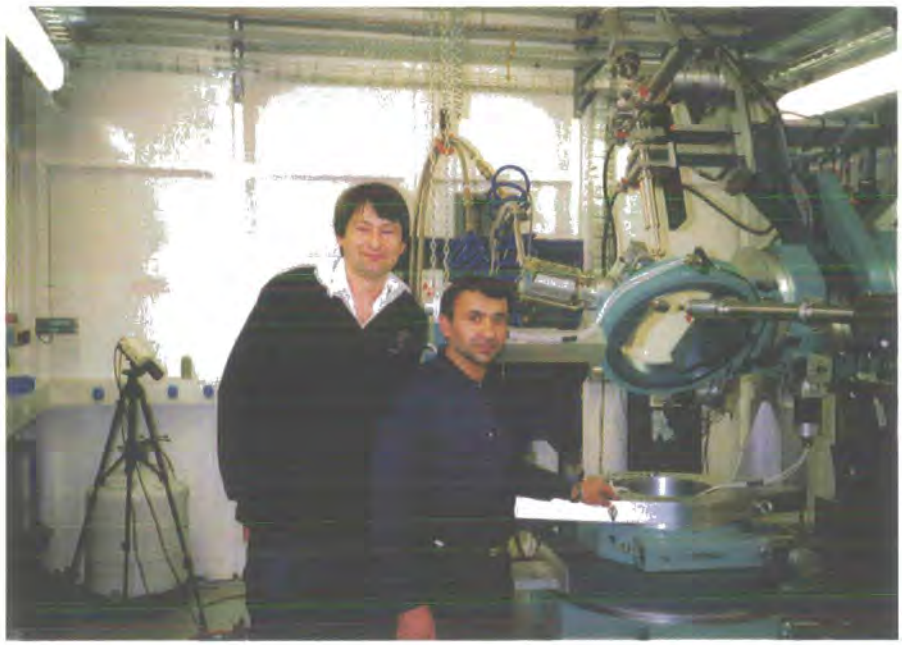

Figure 4.6 A presentation of the diffractometer situated on the *XMaS* beamline at ESRF.

All metallic parts around the sample circles are of non-magnetic material. The diffractometer carries a goniometer on the phi circle to hold and adjust the sample and a cryostat which can be operated from ~10 K to 300 K. Figure 4.7 shows a view of the cryostat. The beamline is equipped with a NaI scintillator and a Ge solid state detector. A view of the evacuated scattered beam tube, analyser crystal stage and detector at BM28 is shown in Figure 4.8.

The *XMaS* beamline is built on the soft part of a bending magnet (critical energy 9.8 keV). The beamline uses a 0.4 T section as its source point. The degree of linear polarization depends critically on the vertical primary slits opening. It is 99.5 % in the plane of the electron ring, but it changes quickly with vertically opening of the

primary slits. Unfocused monochromatic, white beam and focused monochromatic beam, can all be used for experiments.

Figure 4.7 A view of evacuated incoming photon tube, sample holder and cryostat at BM28.

Figure 4.8 A view of evacuated scattered beam tube, analyser crystal stage and detector in BM28.

4.3 Diffraction geometry

An important factor in X-ray scattering experiments is the configuration of the instruments which are employed. Typically either two-axis geometry or triple-axis geometry (employing the use of an inserted crystal analyser) is used depending on the resolution required. Whilst triple-axis geometry generally has the higher resolution, this can only be achieved with a loss of intensity.

4.3.1 Double-axis X-ray scattering geometry

A schematic representation of double-axis geometry is shown in Figure 4.9. In double-axis geometry, the first axis refers to the beam conditioner and the second one is for the sample. In this geometry, the X-rays after being monochromated by suitable set of crystals, impact upon the crystal. By use of the various axes that are available on the diffractometer, the crystal can be aligned and centred at the scattering condition by a combination of motions and rotations. The intensity of the scattered beam is measured by a suitable positioning of the detector. In double-axis geometry, the resolution can be increased by using a slit in front of the detector. It can also limit the diffracted beam divergence before the beam reaches the detector.

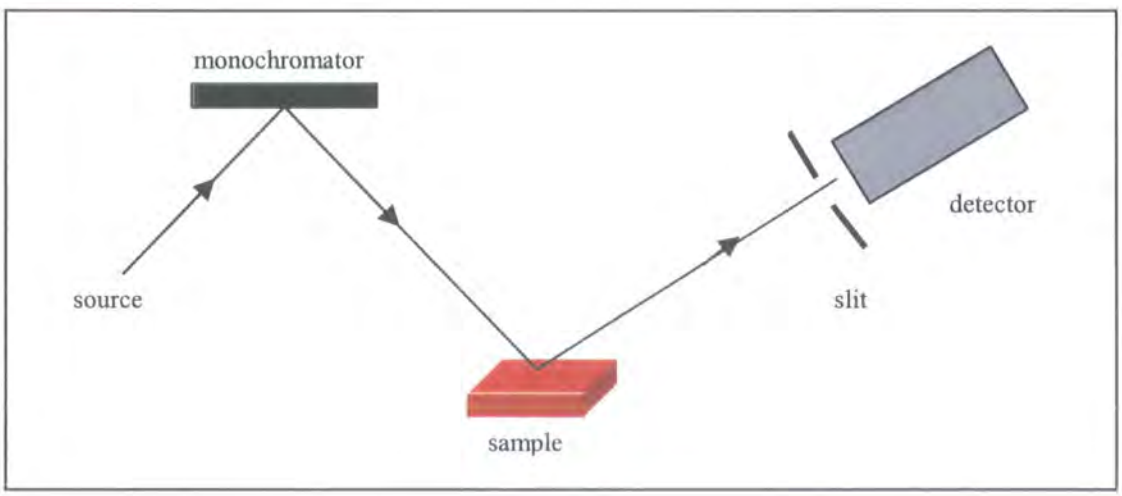

Figure 4.9 A schematic view of the double-axis X-ray scattering geometry in (+ -) setting.

4.3.2 Triple-axis X-ray scattering geometry

A schematic representation of triple-axis geometry is shown in Figure 4.10. In this geometry another crystal (an analyser crystal) is placed on the detector arm between the sample and detector and defines the third axis of the instrument. The first crystal (monochromator) collimates the incident beam. The second crystal is the sample and the third one (analyser) is used to analyse the angular spectrum of the scattered radiation from the sample and reduce the background.

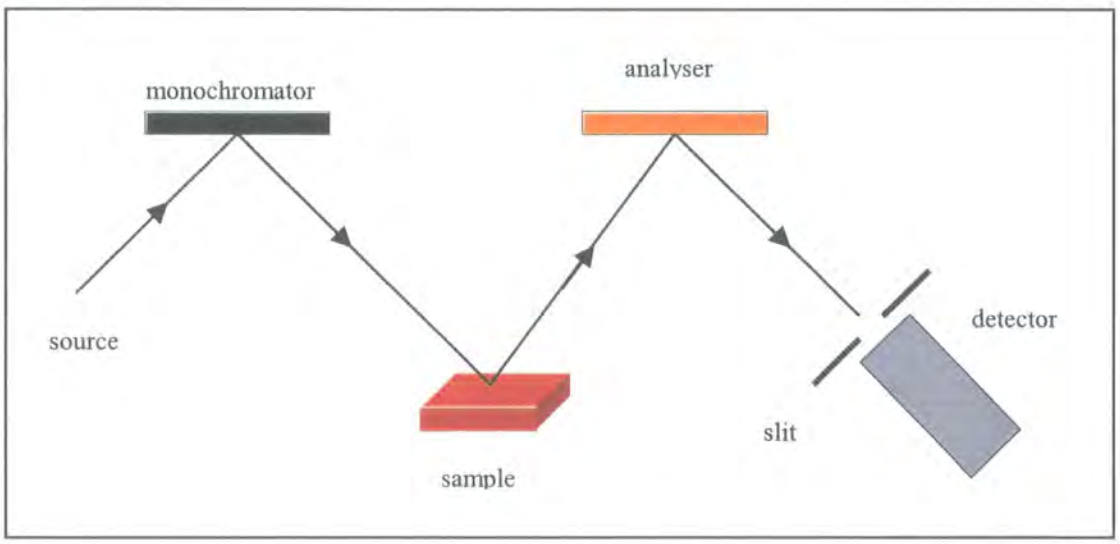

Figure 4. 10 A schematic representation of the triple-axis X-ray scattering geometry in (+ - +) setting.

4.4 Crystal growth

All crystals, which were used for experiments described in this thesis were grown by the floating-zone technique. In the following section the technique will be explained briefly.

4.4.1 Floating-zone technique

The floating-zone method is extensively used for growth of single, high purity crystals. It is zone melting in a vertical configuration. A schematic view of the floating-zone apparatus is shown in Figure 4.11.

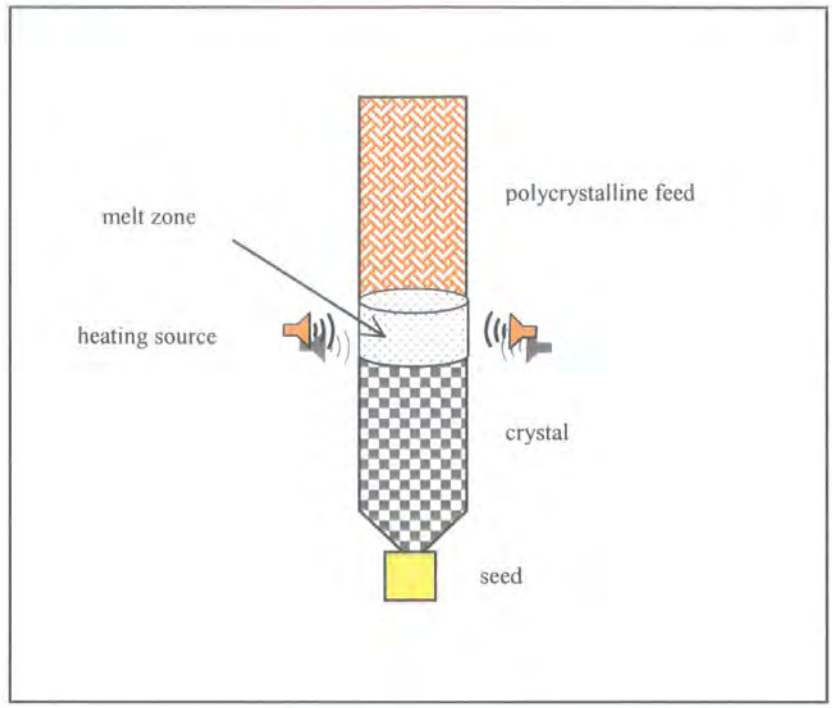

Figure 4. 11 A schematic view of a floating-zone apparatus.

The advantage of this method is the elimination of the melt container, which reduces contamination. Materials which decompose before melting or undergo a phase transition between the melting point and room temperature, cannot be grown from the melt. Gravitational forces limit the zone length and crystal diameter [6]. In this method, the main sources of heating are electron beam, optical heating, and radio frequency (r.f.) heating. Laser beams or focused high intensity light sources are used in optical heating. Choosing the heating sources for the growth of a crystal depends on the properties of the crystal. The r.f. source is used in growing silicon single crystal, with a specially shaped coil. Electron beam heating is often used for refractory metals, contamination of the zone by material sputtered from the cathode can be reduced by the use of a magnet to focus the electron beam. Optical techniques are commonly used for refractory non-conducting oxides. The purity of the single crystal is determined mainly by the purity of the polycrystalline starting material and by the cleanliness of the growth chamber, including that of the gas atmosphere.

All the crystals were used in this research were grown by this technique. The starting materials were different for $Nd_{0.5}Sr_{0.5}MnO_3$ and $La_{2-x}Sr_xNiO_4$ (x = 0.2 – 0.33). The raw materials were weighted to a proper ratio, mixed and stirred with acetone or ethanol. The mixture was heated for a period of times, which depends on the compounds. A feed rod was formed to a cylindrical shape by applying a suitable hydrostatic pressure and heated again in air. For example, the starting materials for the growth of $La_{2-x}Sr_xNiO_4$ single crystals were La_2O_3, $SrCO_3$ and NiO, heated in air at 1200-1300 °C for 72 hours. Then the feed rods of 12 mm diameter and 100 mm in length were sintered in air at 1400-1500 °C for 6-12 hours. Crystal growth was performed by using the floating-zone furnace equipped with four 1.5 kW halogen incandescent lamps and elliptic focusing mirrors, which is shown in Figure 4. 12.

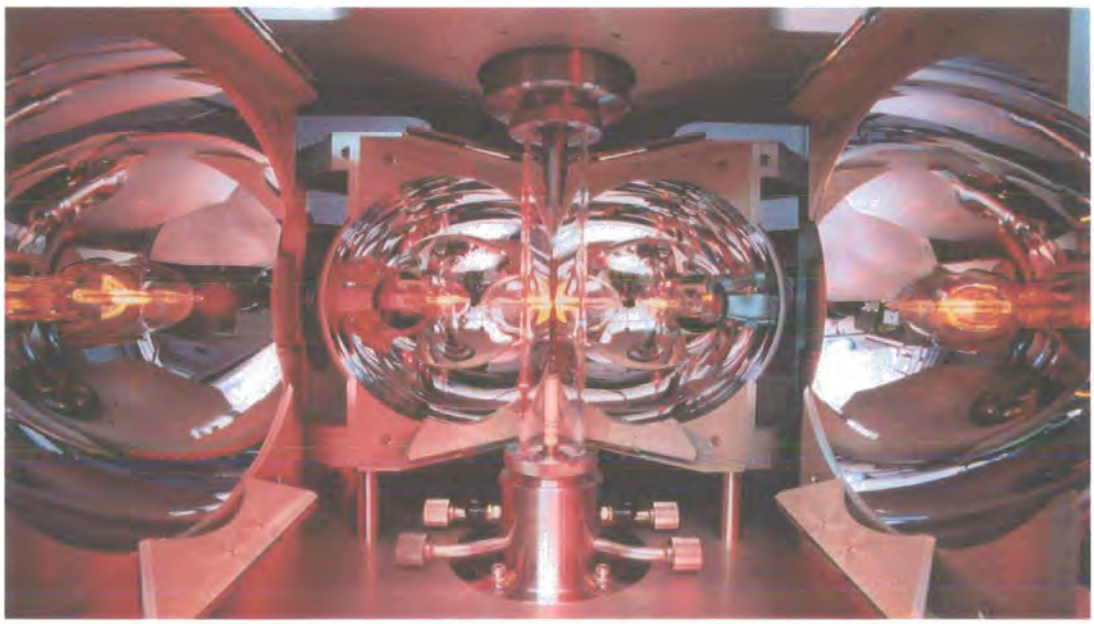

Figure 4. 12 The floating-zone furnace equipped with four 1.5 kW halogen incandescent lamps and elliptic focusing mirrors situated at Oxford University.

During the floating zone process a melt zone is established between the lower seed material and upper feed material by applying localised heating. This floating zone is moved along the rod in such a way that the crystal is growing on the seed and simultaneously melting the feed material above the floating zone. In this method the seed and feed rods are rotated in opposite directions at a proper rate and also the melted zone is vertically scanned.

I gratefully acknowledge Prof. S-W. Cheong at Rutgers University and Bell Laboratories, who grew the $Nd_{0.5}Sr_{0.5}MnO_3$ and $La_{1.67}Sr_{0.33}NiO_4$ crystals and Drs P Prabhakaran and A. Boothroyd at Oxford University for growing $La_{2-x}Sr_xNiO_4$ (x = 0.3 – 0.2) crystals.

4.5 References

[1] B. D. Cullity, *Elements Of X-ray Diffraction* (Addison-Wesley Publishing Company, 1978).

[2] G. H. Stout and L. H. Jensen, *X-ray Structure Determination* (John Wiley & Sons, 1989).

[3] http://www.esrf.fr/

[4] S. P. Collins, R. J. Cernik, B. Fell, *et al.*, J. Synchrotron Rad. **5**, 1263 (1998).

[5] W. R. Busing and H. A. Levy, Acta. Cryst. A **22**, 457 (1967).

[6] W. Bardsley, D. T. J. Hurie, and J. B. Mullin, *Crystal Growth: A Tutorial Approach* (North-Holland Publishing Company, 1979).

Chapter 5

Experimental results on $La_{2-x}Sr_xNiO_4$ (x = 0.275 – 0.33) displaying quasi long-range order

5.1 Introduction

To examine the ordering process of the doped holes in more detail using high-resolution X-ray scattering, a systematic study of the temperature dependence of the charge stripe superlattice peaks was carried out in samples with the hole concentrations x = 0.2 - 0.33. The results of this will be explored in this and next chapters. To date, most of the experiments carried out on charge ordering in nickelates have been performed by using neutron diffraction techniques. But neutrons do not scatter from charge directly, and they can only detect the nuclear displacements associated with the charge ordering modulation. In this thesis X-ray scattering techniques have been used to study the charge ordering because X-rays directly interact with the charges, scattered from them, allowing a more direct probe.

Using high-resolution X-ray scattering, the charge ordering in $La_{2-x}Sr_xNiO_4$ systems with n_h = 1/3, 0.3, and 0.275 has been studied in detail. As the charge ordering in these nickelate systems is 2-dimensional, it has been termed "*charge stripes*". The superlattice peaks occurring due to the formation of these charge stripes in these samples were found at low temperatures, below the charge ordering transition temperatures T_{CO}. These peaks are separated from the fundamental Bragg reflections with a wavevector q = (2ε, 0, 1). The commensurability follows approximately the $\varepsilon = n_h$ law with $n_h = x+2\delta$, where δ is the amount of excess oxygen from stoichiometry. The transition into the charge ordered phase is second-order in all three samples and above this transition critical scattering was observed due to the critical fluctuations into the charge stripe phase. By measuring the correlation lengths in all three principal directions in reciprocal space (H, K, and L) using triple crystal geometry, it has been found that the charge stripes are two dimensional in nature in all these three

compounds. The correlation length of the charge stripes decreases with reduction of the hole concentration n_h from x = 1/3 to x = 0.275.

5.2 Charge stripes in $La_{5/3}Sr_{1/3}NiO_4$

5.2.1 Introduction

Among the nickelates systems, $La_{5/3}Sr_{1/3}NiO_4$ has attracted much interest because the static stripe order is more stable in this compound compared to others with different hole concentrations. This behaviour has been attributed to the commensurability effect [1]. Electron-diffraction and neutron scattering measurements on $La_{5/3}Sr_{1/3}NiO_4$ have confirmed that the charge ordering (CO) occurs at $T_{CO} \approx 240$K and the spins order antiferromagnetically (SO) at $T_{SO} \approx 190$K [1-3].

In this compound, the charge ordering peaks with wavevector $q_{CO} = (2\varepsilon, 0, 1)$ and spin ordering satellites with wavevector $q_{SO} = (1\pm\varepsilon, 0, 0)$ exactly coincide at the same wavevector in reciprocal space (Figure 5.1), and it has been argued that this coincidence enhances the stability of the charge stripes in this system and the related effect on resistivity [4].

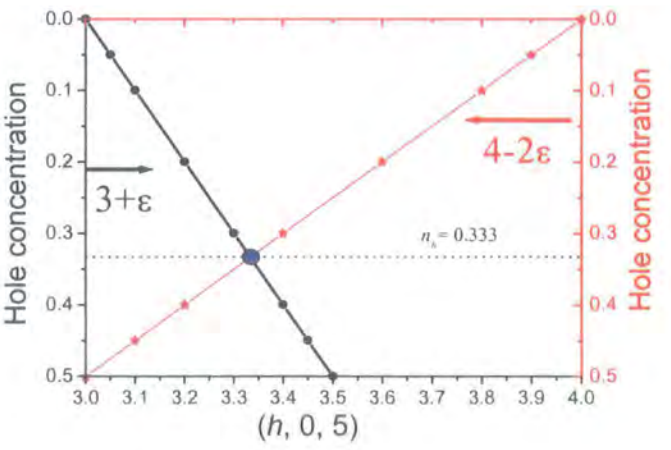

Figure 5.1 A schematic representation of shift of the spin and charge ordering satellites from Bragg reflections (3, 0, 5) and (4, 0, 5) as a function of n_h.

Anomalies associated with such charge ordering in resistivity and magnetic susceptibility in the $x = 1/3$ compound are stronger than those with other Sr doping levels [4]. The phase transition into the charge stripe phase is second order and the average crystal structure remains the same in the whole temperature range [5]. The charge stripes run along diagonal directions in NiO_2 planes, although there is a discrepancy about whether the charge stripes are site-centred or bond-centred. Zhengquan *et al.* have suggested that maybe the best way to describe the doped holes is as a mixture of Ni 3d and O 2p character [6].

5.2.2 Experimental details

The single crystal sample of $La_{5/3}Sr_{1/3}NiO_4$ was grown at Bell Laboratories using the floating-zone method (see section 4.4) and had been previously characterized by neutron scattering [1]. The crystal was cut into small pieces, and one of them was polished to get a shiny and even surface with an area of ~ 2×1 mm^2 using 1 mm^2 diamond paste.

The crystal was first aligned and studied using an in-house diffractometer at Durham, which is a four-circle Huber diffractometer mounted on a rotating anode X-ray source. The synchrotron experiments were performed on the beam lines 16.3 at Synchrotron Radiation Source (SRS) (Daresbury in UK) and *XMaS* (BM28) at the European Synchrotron Radiation Facility (ESRF) (Grenoble in France). In both beam lines, the incident X-ray was selected using a Si (111) monochromator, and also most of the high-order contamination was rejected at BM28 by the use of a focusing mirror. A Ge (111) single bounce analyser was used to reduce the background and increase the wave vector resolution. The sample was mounted on a Displex closed-circle cryostat with the [111] direction perpendicular to the sample surface. All the measurements were performed in the ($h0l$) zone of reciprocal space. The use of the multicircle diffractometer allows measurements of the scattering to be performed along the principal axes H, K, and L in reciprocal space. The crystal has a tetragonal structure with the *I4/mmm* symmetry [5]. For convenience we indexed reflections in orthorhombic lattice units with $a_o \sim b_o = \sqrt{2}\, a_t = 5.4145$ Å and $c = 12.715$ Å where o and t stand for orthorhombic and tetragonal respectively. No realignment of the

crystal was undertaken during measurements because $La_{5/3}Sr_{1/3}NiO_4$ does not display any structural phase transition at low temperatures which was clarified by measuring the Bragg reflections (4, 2, 4), (3, 3, 3) and (4, 0, 6). The full width at half maximum (FWHM) of the Bragg reflection (4, 2, 4) along the longitudinal and transverse directions as a function of temperature is shown in Figure 5.2. The width of the charge-ordering peak (4.66, 0, 5) over a reduced temperature region is also displayed in Figure 5.2. The width is in reciprocal lattice unites, which means to convert it to $Å^{-1}$ it should multiply by $2\pi / d$, where d is the real space lattice parameter in the specified direction.

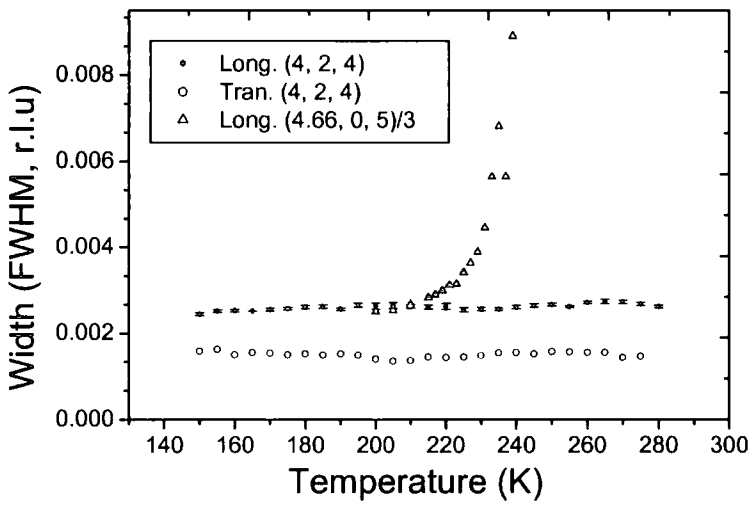

Figure 5.2 Width of the Bragg reflection (4, 2, 4) as a function of temperature. The width of the charge ordering reflection (4.66, 0, 5) is also shown over a reduced temperature region around the charge ordering transition.

The width of the Bragg reflection does not show any anomaly with temperature, even in the region of the charge ordering transition temperature. The experimental resolution function was determined to be as $\xi^{-1}_H \sim 0.0015$ $Å^{-1}$, $\xi^{-1}_K \sim 0.0015$ $Å^{-1}$, and $\xi^{-1}_L \sim 0.0044$ $Å^{-1}$ as measured on the Bragg peak (4, 2, 4) at $T = 220$ K. The sample was found to be of good quality and the sample mosaic width was found to be ~ 0.05°, relatively low for a transition metal oxide single crystal. The crystal structure of $La_{5/3}Sr_{1/3}NiO_4$ is shown in Figure 5.3. All the measurements were performed by scans along the principal directions in reciprocal space. All peaks intensities are

integrated intensity that were collected by rocking the sample and were normalized with respect to beam monitor counts.

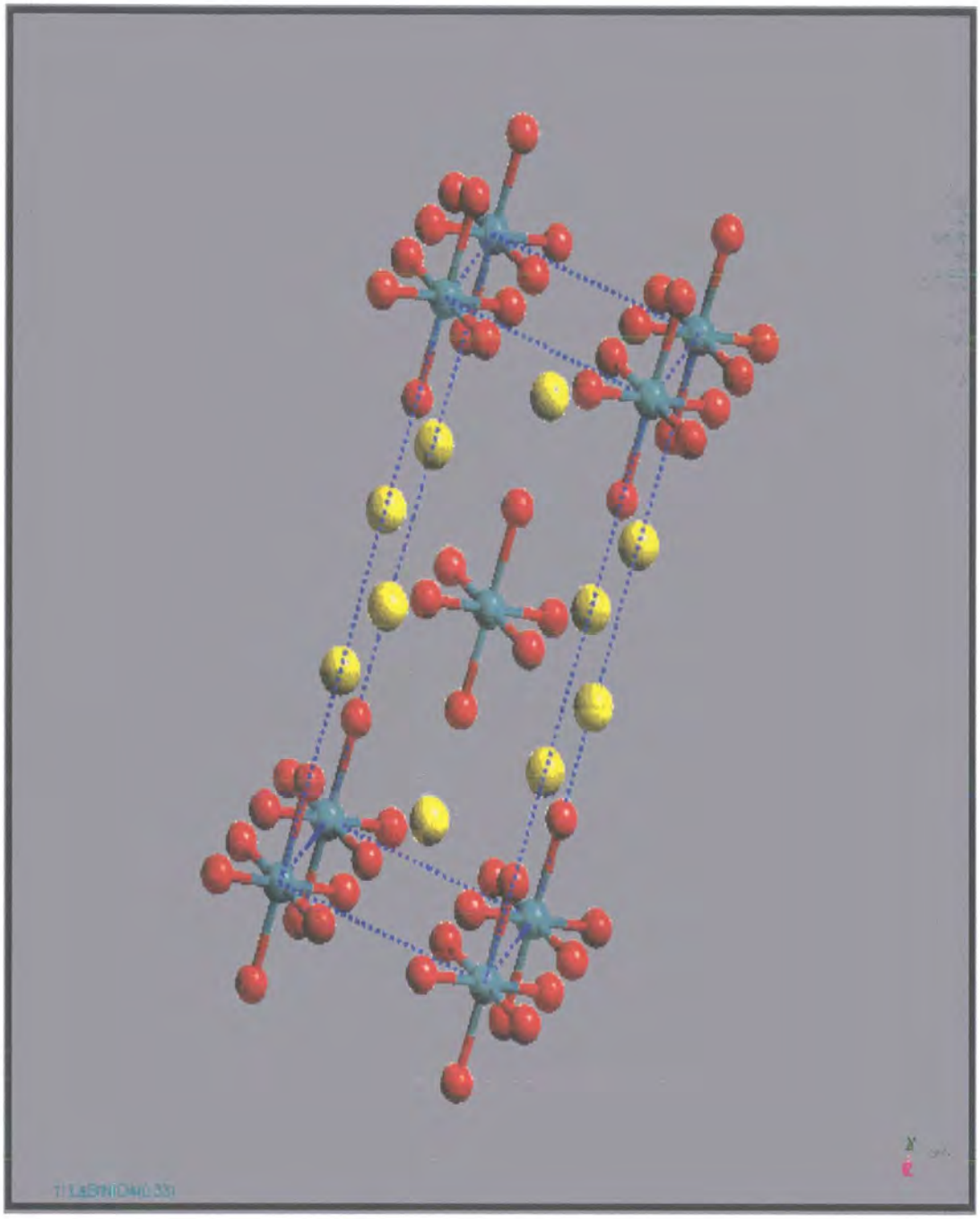

Figure 5.3 The crystal structure of $La_{2-x}Sr_xNiO_4$. Light blue, red, and yellow spheres are Ni, O, and La/Sr ions respectively.

5.2.3 Results and discussion

Upon cooling the sample, a number of charge ordered reflections were observed at non-integer positions. The intensity of these reflections was ~ 10^{-4} – 10^{-3} of the corresponding Bragg reflections. Representative charge ordering (CO) reflections at (4.66, 0, 5) (5.33, 0, 7) and (2.66, 0, 5) were measured. These peaks are separated from the neighbouring Bragg reflections (4, 0, 4), (6, 0, 6) and (2, 0, 4) by the charge ordering wavevector (2ε, 0, 1), $\varepsilon \approx 1/3$ in accord with neutron scattering studies [3, 7]. These peaks disappeared above $T_{CO} \approx 240$ K indicated that these are indeed associated with the formation of charge stripes.

Each peak at every individual temperature was measured, and they were fitted with Gaussian line shape in *H*- and *K*-directions and Lorentzian line shape in the *L*-direction. It will be clear that the charge-ordering peaks are very broad in this direction. Typical scans of the charge ordering reflection (4.66, 0, 5) along the *H*-, *K*-, and *L*-directions are shown in Figure 5.4. The solid lines represent the results of the fitting.

The resultant intensity of the charge ordering satellites (4.66, 0, 5) and (5.33, 0, 7) along the *H*-, *K*- and *L*-directions in reciprocal space as a function of temperature is shown in Figure 5.5 (graphs (a) and (b), respectively). The charge ordering peaks appear at around $T_{CO} \approx 240$ K and the intensity of these peaks grows as the sample is cooled down, with a big enhancement below T_{CO}. The anomalies associated with charge ordering in this temperature have been observed in resistivity, magnetic susceptibility, sound velocity and specific heat [8, 9].

In this system the spin ordering temperature T_{SO} is lower than the charge ordering temperature, an indication that the charge ordering is the deriving force for the spins to order antiferromagnetically. Polarized neutron diffraction has revealed that the spins in the ordered phase are canted away from the stripe direction, and below 50 K the canted angle increases [7]. The intensity of the peaks is a maximum at around 200 K, probably due to the spin ordering. The intensity profiles displayed in Figure 5.5 show that the intensity decreases as the sample is cooled down further. The reason for this reduction of the intensity at low temperature is not yet clear.

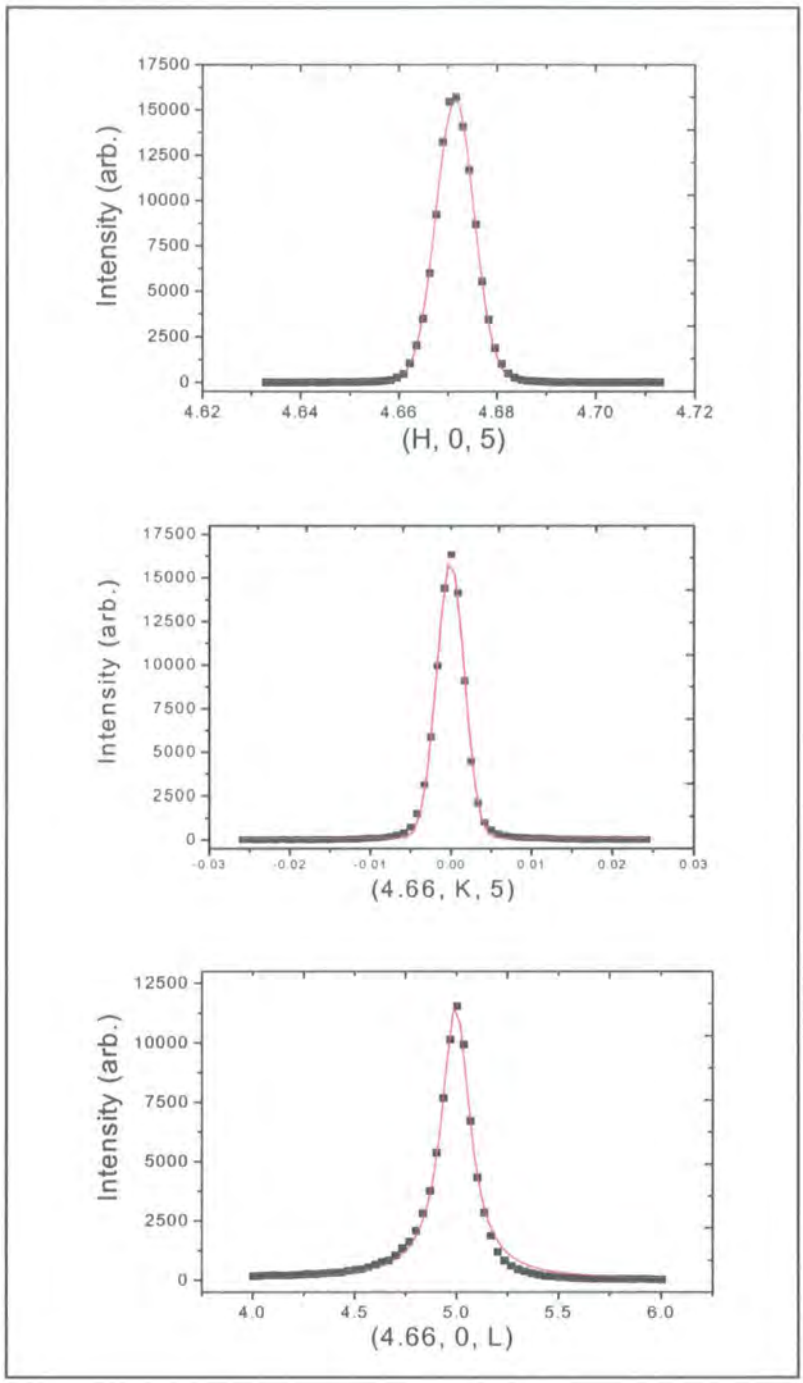

Figure 5.4 Typical scans of the charge ordering reflection (4.66, 0, 5) along the *H*-, *K*-, and *L*-directions. The solid lines represent the results of fitting of the intensity profiles with Gaussian line shapes (*H*- and *K*-directions) and Lorentzian line shape (*L*-direction).

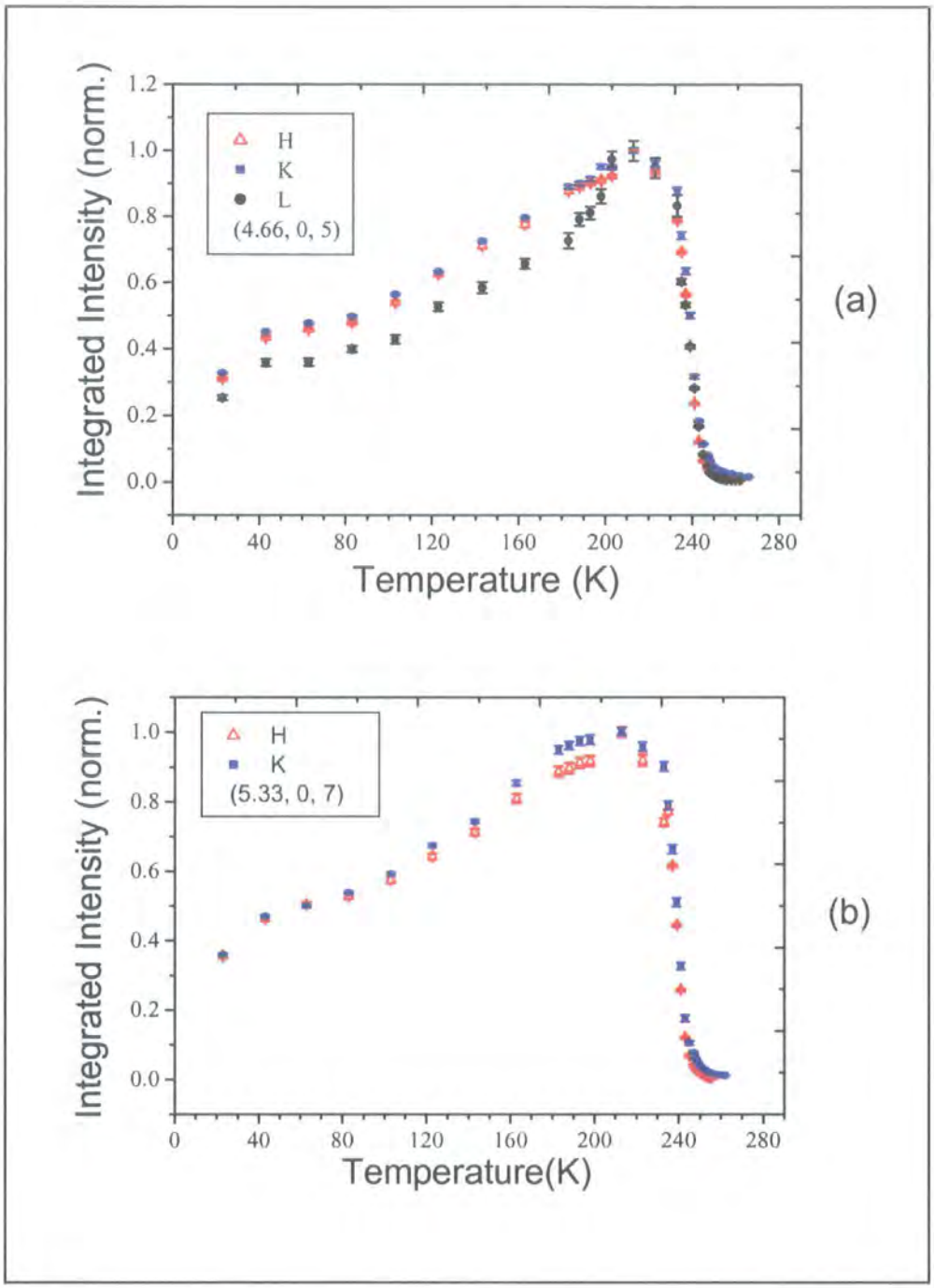

Figure 5.5 The temperature dependence of the integrated intensity of the charge-ordering peaks (a) (4.66, 0, 5) and (b) (5.33, 0, 7) along the *H*-, *K*- and *L*-directions.

However, the intensity behaviour is not correlated with the charge stripes because, as we will see later, the correlation length of the charge stripes does not show any change at low temperature. This implies that the decrease in intensity of the charge stripes is not related to the disorder in the charge stripes. One possible reason may be that is due to the movement of the holes from bond centred to site-centred stripes, causing lattice distortions, which affects the peak intensity.

From variable magnetic field studies on striped phases, it has been suggested that the stripe phase is O centred when the stripes form around T_{CO} (higher temperature phase), while the Ni centred stripe phase is favoured at lower temperatures [8]. The results obtained from these studies and neutron scattering show the charge and spin ordering temperatures are maximum at $n_h = 1/3$, and they decrease on both sides away from $n_h = 1/3$ [9].

Figures 5.6 and 5.7 show the width (FWHM) of the charge ordering reflections (4.66, 0, 5) and (5.33, 0, 7) along each of the reciprocal space directions respectively. The width in the L-direction of the (4.66, 0, 5) peak, is added to Figure 5.6 with a reduced scale for easier comparison. In Figure 5.7 the width of the Bragg reflection (4, 0, 6) has also been added to the graph. Some data points taken in a cooling run are also added to Figure 5.6, which behave exactly similar to those taken on a warming run, and does not show any hysteresis, a property of a second-order transition. The width profiles for both peaks are similar. The width in the L-direction shows a small anomaly, especially near to the charge ordering melting temperature, and may be related to the fitting process, because the peak profile in this direction is very broad and has a shoulder. The width is nearly constant from low temperature until $T = 225$ K from which it starts to increase with a divergence at T_{CO}. The profiles in the H- and K-directions are approximately identical, but it is much wider in the L-direction (note the scale). This indicates that the charge-correlated state occurs mainly in the ab planes (stripes form) and only a very short-range charge ordering forms normal to these planes. Further evidence will be given in section 5.2.4. Above the charge ordering transition temperature T_{CO} there is still some scattering from charge stripes (see also Figure 5.5). This means that when the sample is cooled from high temperature phase, clusters of charge ordered material form well above the transition

temperature, and with further cooling the sample the size of these charge stripes clusters grows and forms long-range correlated regions below T_{CO}.

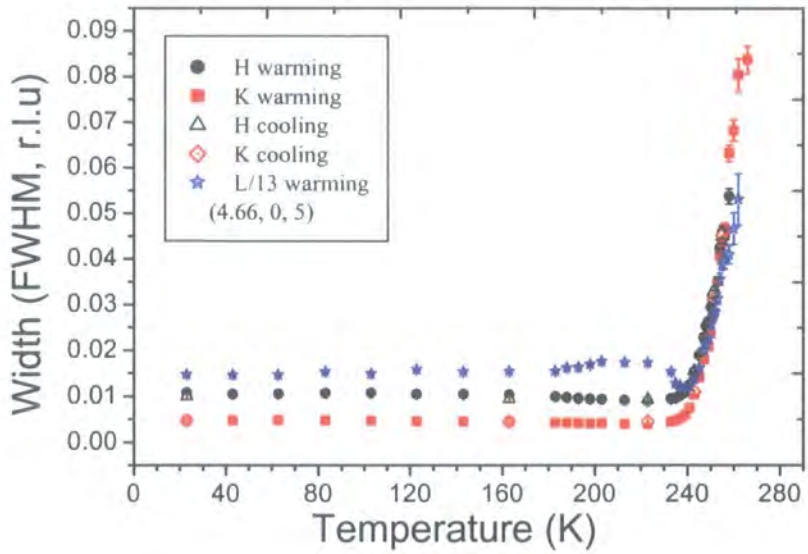

Figure 5.6 The evolution of the width of the charge ordering reflection (4.66, 0, 5) as a function of temperature. The width along the *L*-direction is added with reduced scale for comparison.

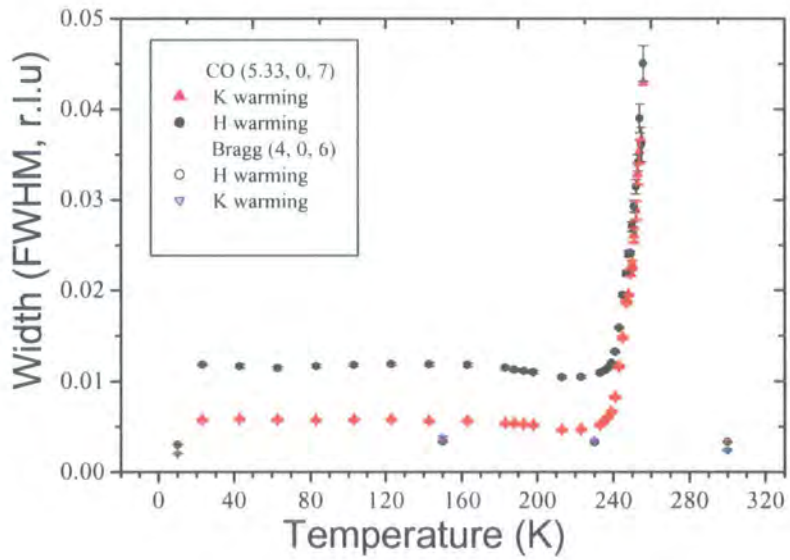

Figure 5.7 The evolution of the width of the charge ordering reflection (5.33, 0, 7) as a function of temperature. The width of the Bragg (4, 0, 6) is also added to the graph.

The correlation lengths of the charge stripes have been calculated from the measured width of the peaks in the principal directions in reciprocal space and are displayed in Figure 5.8 *. In graph (a) some data points from a cooling run are also included the graph. In the temperature range 20 K < T < 225 K, the correlation lengths are independent of temperature, in all three directions, and the charge stripes do not show any improvement in correlation with reduction of temperature. Their correlation lengths never approach the Bragg peak correlation length in any direction (see Figure 5.7) implying that the charge stripes are quenched and disordered even at very low temperatures. Figure 5.8 (graphs (a) and (b)) clearly show that there is a huge difference between the correlation lengths in the *ab* planes (*H*- and *K*-directions) and that normal to these planes (long-axis direction). In the *ab* planes, the correlation length in the stripe direction *K*, is about twice that of the correlation length along the modulation direction *H*. But the correlation length ratio between these two to the corresponding length in the *L*-direction is very large and there is a very short-range form of the charge ordering in the *L*-direction (only ~ 130 Å). For example, the ratios of correlation length at two different temperatures below and above the T_{CO} are as follows:

$$\xi_H^{183} / \xi_L^{183} \approx 10$$

$$\xi_K^{183} / \xi_L^{183} \approx 20$$

$$\xi_{H,K}^{255} / \xi_L^{255} \approx 5$$

These ratios show that even above the charge ordering melting temperature the residual charge stripes remain more correlated in the *ab* planes. In other words the charge stripes in this sample are truly 2-dimensional (see next section) in contrast to suggestion of quasi-3D ordering for n_h ~ 1/3 [9]. It has a quasi-long-range order in the NiO_2 planes, with very short-range correlated stripes normal to these layers direction.

* The equation $\xi = [\mathrm{HWHM} \times (1/d)]^{-1}$ has been used to calculate correlation length, where d is the lattice parameter in *H*-, *K*- or *L*-directions.

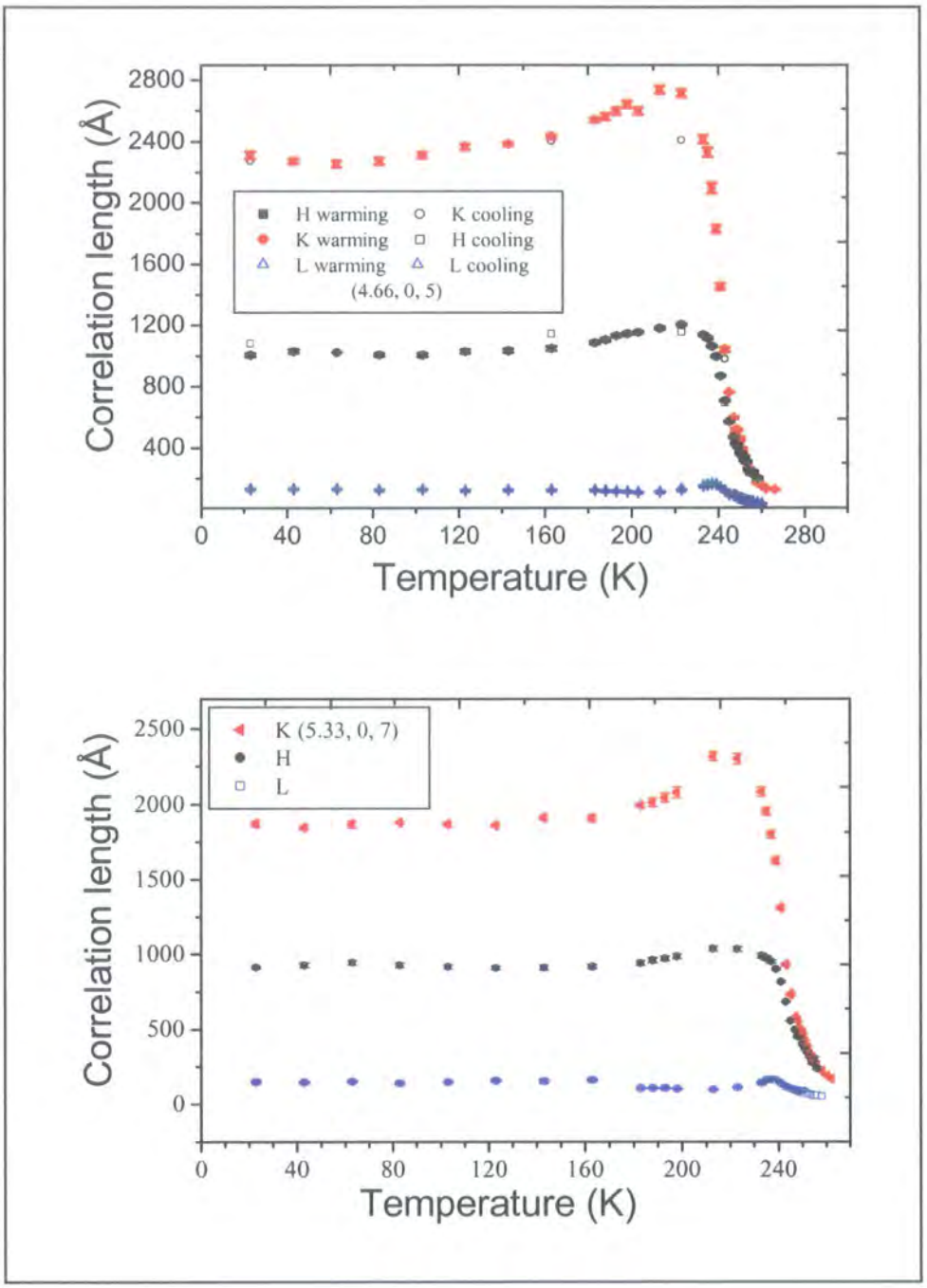

Figure 5.8 Measured correlation lengths of charge stripes versus temperature, (a) of the charge ordering reflections (4.66, 0, 5) and (b) (5.33, 0, 7) in all three principal directions in reciprocal space.

These results are consistent with neutron scattering results for which Lee *et al.* found the charge stripes in-plane correlation length of ~ 350 Å and out of plane of ~ 30 Å [1]. Resistivity measurements have showed there is an anomaly between the ratio of the *ab* plane and *c*-axis resistivity [10].

Comparisons made to the changes in the correlation lengths of charge ordering below and above T_{CO} indicate an anisotropic increase between the *ab* plane and the *c*-axis, i.e.,

$$\xi^H_{223} / \xi^H_{255} \approx 5$$

$$\xi^K_{223} / \xi^K_{255} \approx 10$$

$$\xi^L_{223} / \xi^L_{255} \approx 3$$

These ratios below 220 K for all directions are independent of temperature, and do not show any anisotropy. So around, and above the charge-stripe ordering temperature, melting of the charge stripes and reduction of the correlation length is direction dependent.

5.2.4 Proof of the 2-dimensional nature of charge ordering

Now we will concentrate on the dimensionality of the charge ordering in the $n_h = 1/3$ system. The intensity profiles of the charge-ordering peak (4.66, 0, 5) in all three directions are similar and the result along the *H*-direction is shown in Figure 5.9 (a). The triangular data points include scattering from critical fluctuations because without critical scattering the intensity should vanish at the charge ordering transition temperature. The data points from subtracting this effect are shown as spheres with error bar. The intensity profile after subtracting the scattering from the critical fluctuations has been fitted to a power law equation:

$$I(T) \approx \left[\frac{T_{CO} - T}{T_{CO}}\right]^{2\beta}$$

The fitted parameters extracted from this fitting process on the integrated intensity are:

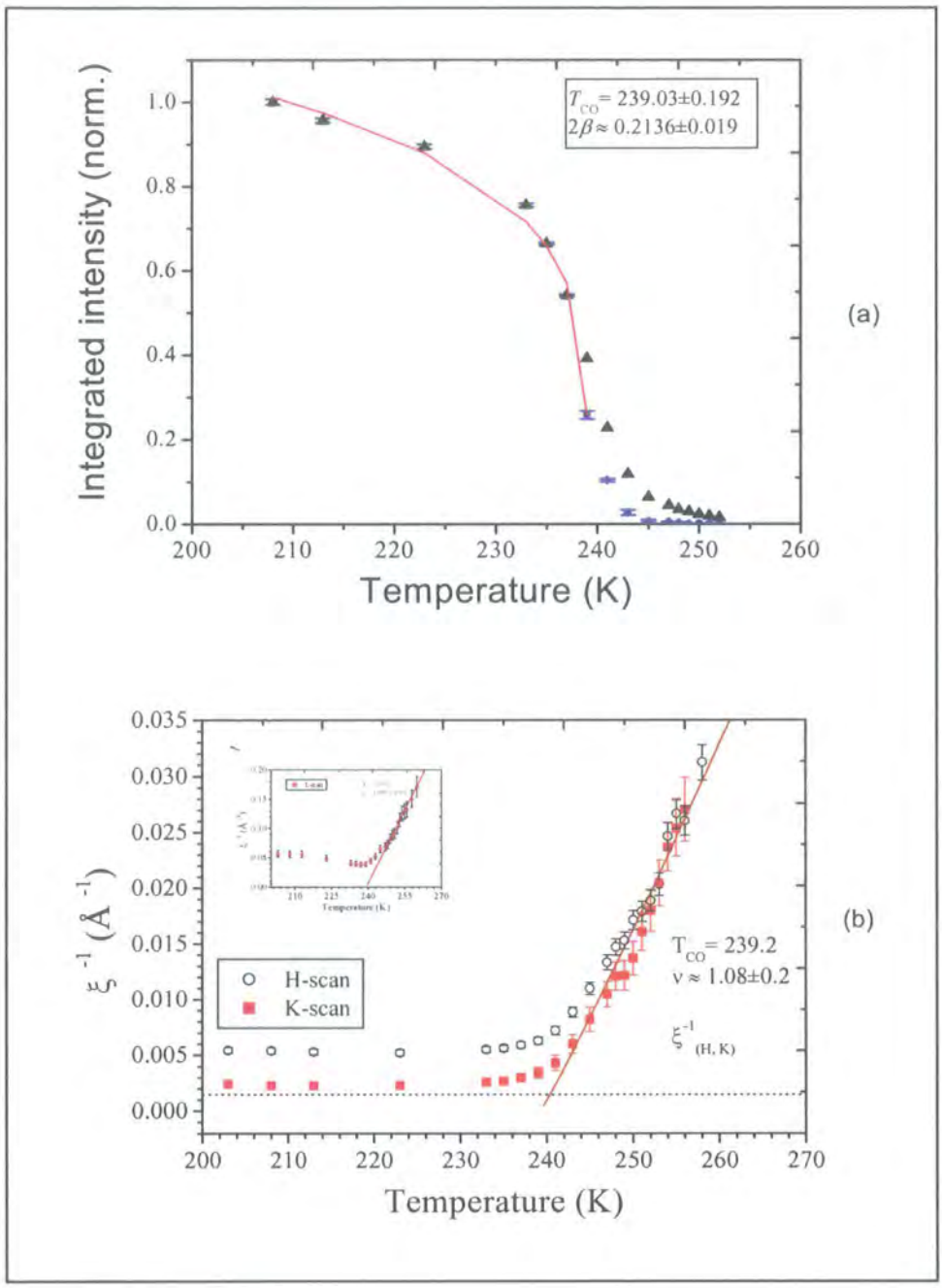

Figure 5.9 (a) The temperature dependence of the integrated intensity of the charge stripe peak (4.66, 0, 5) along the *H*-direction fitted with the power law equation explained in the text. (b) The evolution of the inverse correlation lengths of this peak, solid line shows the fitted result according to the equation (see text).

$$T_{CO} \approx 239.03 \pm 0.192 \text{ K}$$

$$2\beta \approx 0.2136 \pm 0.019$$

and they show the transition to be second order in nature. Table 5.1 lists the predicted exponents for 2D and 3D models [11]. The measured exponent of 2β clearly demonstrates that below T_{CO} the charge stripes in $La_{5/3}Sr_{1/3}NiO_4$ fall in the 2D universality class.

	2β	ν	ν_T
2D Heisenberg	0.3 [12]	≈0.95 [12]	0.9 [13]
2D Ising	0.25	1	1.32 [14]
3D Ising	0.624	0.64	0.85 [15]
3D Heisenberg	0.76	0.702	0.96 [14]
3D XY	0.692	0.669	

Table 5.1 Predicted exponents and the measured percolation exponents ν_T for 2D and 3D models.

The transition temperature of about 240 K is in accord with the susceptibility and resistivity measurements where the susceptibility decreases and resistivity increases, suggestive of a second-order phase transition due to the formation of charge stripes [4, 5].

The 2D character of charge stripes is also reflected in the anisotropic correlation lengths of the charge stripe satellites. Figure 5.10 displays linear scans through the charge ordering peak (4.66, 0, 5) along the *H*-, *K*-, and *L*-directions at temperatures well below and above $T_{CO} \approx 239.2$ K, respectively.

The dotted lines show the best fits convoluted with the resolution function. It is clear that the profile of the charge stripe satellite along the *H*- and *K*-directions are nearly identical, but it is much wider in the *L*-direction.

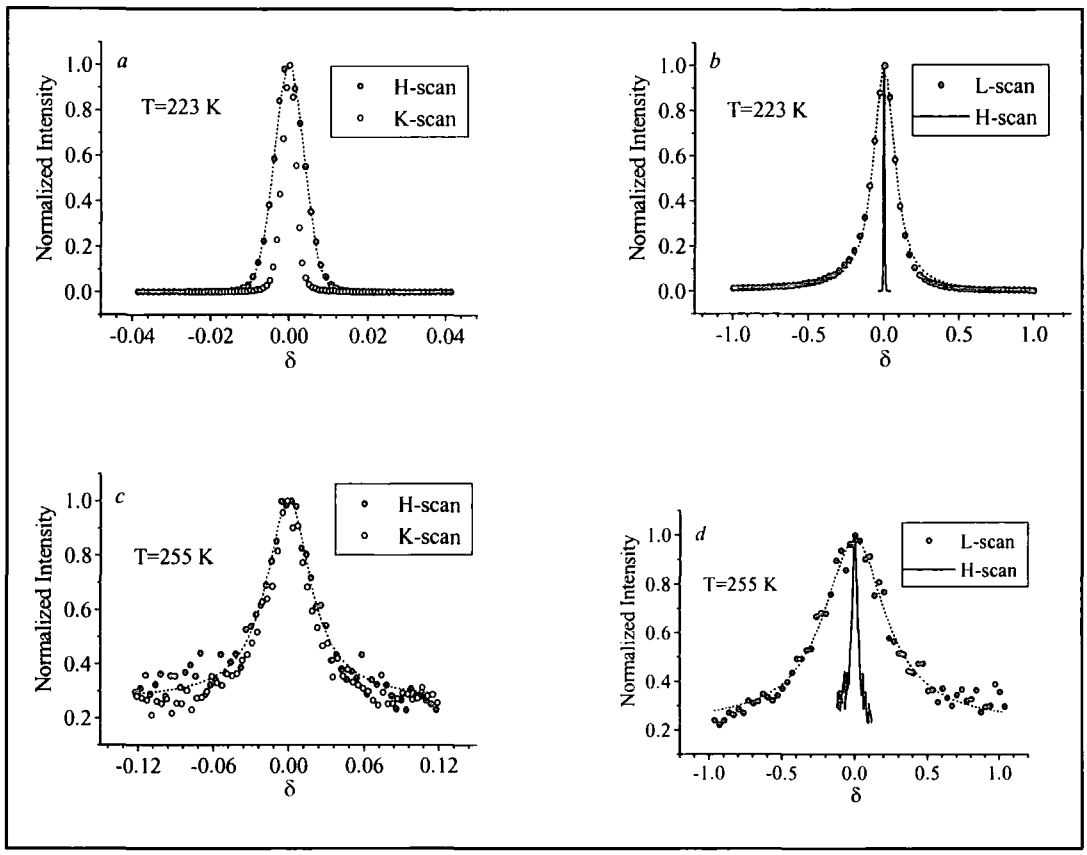

Figure 5.10 Linear scans through the charge-ordering peak (4.66, 0, 5) along the *H*-, *K*- and *L*-directions below and above the charge ordering temperature. The dotted lines show the best fit with a Lorentzian line shape.

Even in the high temperature range where the charge stripe shows critical fluctuations, the charge stripe also displays two-dimensional behaviour as shown in Figs. 5.10 (c) and 5.10 (d). This behaviour has also been observed on the charge stripe satellite (5.33, 0, 7).

La_2NiO_4 is a 2D-antiferromagnetic insulator, and transport and optical conductivity spectra have demonstrated an anisotropy ($> 10^2$) between the in-plane (*ab*) and *c*-axis components [10, 12], and this may limit the formation of 3D charge ordering. Scans along the *L*-direction at low temperatures exhibit extended wings on both sides of the charge stripe satellite as shown in Fig. 5.10 (b), resulting in a peak profile which was

fitted well by a Lorentzian line shape convoluted with the experimental resolution function. Diffuse streaks along the *L*-direction have been observed to be a common feature in Sr-doped La_2NiO_4 [13]. This short-range ordering along the *c*-axis, with a length scale of approximately ~ 130 Å along the *c*-axis, may be helpful to minimize the long-range part of the Coulomb interaction [3, 14].

Figure 5.9 (b) displays the evolution of the inverse correlation lengths with temperature. Above the transition temperature $T_{CO} \approx 240$ K, only very weak scattering is observed at the expected positions in reciprocal space. Such scattering is caused by critical scattering due to dynamic spatial fluctuations into the charge stripe phase. This is the first evidence and observation of charge stripe critical fluctuations existing above T_{CO} and up to T_{CO} + 20 K. The size of these clusters varies with temperature displaying a marked divergence close to T_{CO}. The curve over a temperature range T_{CO} to T_{CO} + 20 K has been fitted with a power law equation:

$$\xi^{-1}(T) \approx \left[\frac{T - T_{CO}}{T_{CO}}\right]^{\nu}$$

to allow the extraction of ν for the exponent of the correlation length of the charge ordering satellite. Such fitting gave a value of:

$$\nu = 1.08 \pm 0.2$$

in excellent agreement with the predicted value of ν = 1 expected for a two-dimensional system [11]. The critical scattering was observed at temperatures up to T_{CO} + 20 K, an abnormally high range, which gives an accurate determination of the exponent ν. The quantitative measurements of the correlation lengths and critical exponents demonstrate this reduced dimensionality. Measurements of the correlation lengths and critical exponents also demonstrate that within these fluctuations the stripes are still two-dimensional. The 2D nature of charge stripes was first observed by electron diffraction studies [2].

Measurements of the charge-ordering peak at every temperature, and fitting the data with a proper line shape can lead to the extraction of the commensurability, ε, when considering the *H*, *K* and *L* of the Bragg peak, as a base for comparison. For a more

clear understanding of behaviour of the commensurability, ε, it is displayed as a function of temperature in Figure 5.11.

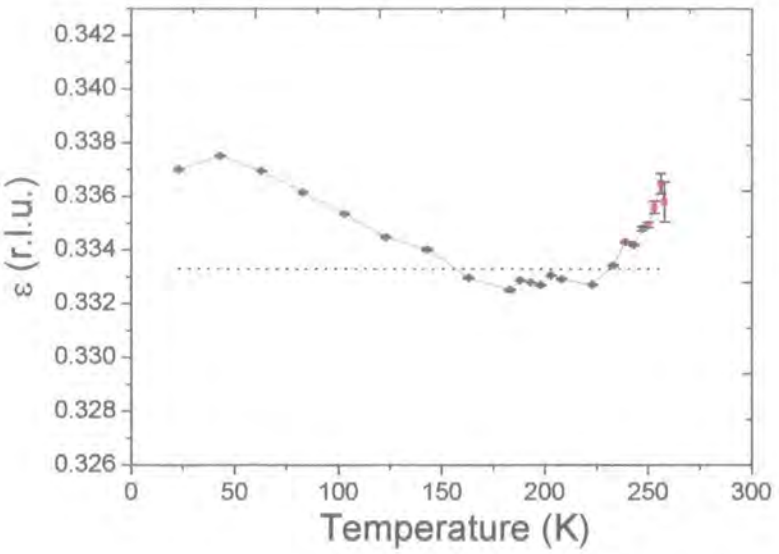

Figure 5.11 Commensurability, ε, as a function of temperature. The line $\varepsilon = 0.333$ is shown as a guide to the eye.

The commensurability, ε, is approximately constant and independent of temperature. The maximum deviation from $n_h = \varepsilon = 0.333$ is 0.0035, about 1% of the commensurability and mainly the deviation is much smaller than this amount. These fluctuations of ε maybe related to local chemical inhomogeneity in the sample which cab be probed with small movements of the sample with temperature. So the charge stripes in this compound are commensurate and ε is independent of temperature, in contrast with temperature dependence of ε when n_h differs from 1/3 (sections 5.3 and 5.4 and chapter 6) [3]. This commensurability effect is believed to be responsible for stabilizing the charge stripes [1].

5.3 Charge stripes in $La_{1.7}Sr_{0.3}NiO_{4.01}$

Whereas a large number of articles have been published on the properties of $La_{2-x}Sr_xNiO_4$ with $x = 1/3$, less is known about the properties of the strontium doped materials for $x \neq 1/3$. In this section the results obtained on an $x = 0.3$ sample will be

explained, this compound has smaller number of holes compared to the x = 0.33 sample. The aim is to find out what is the possible relationship between the charge stripes and the hole concentration.

5.3.1 Experimental details

The single crystal of $La_{2-x}Sr_xNiO_4$ with Sr concentration x = 0.3 used in this study was grown by the floating-zone method (see section 4.4) in Oxford University. To calculate the actual amount of oxygen, it had been analysed with the thermogravimetry analysis (TGA) technique and this showed that the excess oxygen from the stoichiometry is ~ 0.01±0.01. The sample was first studied using the D^3 diffractometer in the Durham by a rotating anode source and uses mirrors to focus the beam on to the sample with a small spot size (1×1 mm^2). The sample was cut and polished to have its (101) surface shiny. The experiments were performed on the beamline *XMaS* (BM28) at the European Synchrotron Radiation Facility (ESRF). A Ge (111) analyser crystal was used in triple crystal geometry to reduce the background and to achieve higher wavevector resolution. The crystal was mounted on the four-circle diffractometer, which was equipped with a closed cycle Displex cryostat, with its [101] direction in the vertical scattering plane.

The crystal has a tetragonal structure with the *I4/mmm* symmetry. For convenience and the same as others, we indexed reflections in orthorhombic lattice units with $a_o \sim b_o = \sqrt{2}\ a_t$ = 5.414 Å and c = 12.715 Å where o and t stand for orthorhombic and tetragonal respectively. The quality of this sample was better than the x = 0.33 sample with the mosaic width of ~ 0.02° (FWHM), which was measured on the Bragg peak (4, 0, -4). The experimental resolution function measured at this peak (4, 0, -4) was $\xi_H \sim 0.0024$ Å^{-1}, $\xi_K \sim 0.00117$ Å^{-1}, and $\xi_L \sim 0.0046$ Å^{-1} at low temperature. All the measurements were carried out in scans along the H-, K-, and L-directions. All the peaks intensities are the integrated intensity that were collected by rocking the sample, and have been normalized with a monitor located before the sample.

Refinements were made at room temperature after finding some Bragg reflections to calculate a UB matrix, and upon cooling down, extra reflections at expected

positions for charge modulation such as (3.37, 0, -3), (2.63, 0, -5), (3.37, 0, -5), and (2.63, 0, -3) were found that are separated from Bragg reflections (4, 0, 4) and (2, 0, 4) with the expected charge ordering wavevector (2ε, 0, *1*). The data were collected on the charge ordering reflection (3.37, 0, -3) on both warming and cooling runs and also on warming on the (2.63, 0, -5) peak as a function of temperature. The Bragg reflection (4, 0, -4) was also measured as a function of temperature to determine the commensurability ε. The crystal structure is exactly the same as the $x = 1/3$ sample (see Figure 5.3).

5.3.2 Results and discussion

Figure 5.12 shows the integrated intensity of the charge ordering satellites (3.37, 0, -3) and (2.63, 0, -5) upon warming (graphs (a) and (b), respectively). In the inset of graph (a), the cooling results of the intensity of the charge ordering reflection (3.37, 0, 5) are also shown. The intensity increases from base temperature, reaching a maximum at approximately 110 K and after that gradually decreases until 195 K the charge ordering transition temperature T_{CO}. Above this temperature, the peak had only a very weak intensity, but was still detectable and we were able to follow the peak until 220 K on warming. In this temperature range the charge stripes are likely to be due to critical fluctuations above T_{CO}. As the temperature decreases towards the transition temperature, the fluctuations increase in size and the charge stripes become more stable and static. At low temperatures, the intensity of the peaks is almost constant, gradually decreasing only below 50 K and the onset of this reduction is shifted to lower temperature in the cooling run (inset of graph (a)). The reason for this decrease of the intensity, again similar to that of the $x = 1/3$ crystal is not clear. The saturation temperature of the intensity at ~ 110 K is consistent with the saturation temperature of the incommensurability ε. The charge stripes transition temperature in this sample, which has a lower hole concentration (smaller x), is $T_{CO} \approx$ 195 K compared to $T_{CO} \approx 240$ K in the case of the $x = 1/3$ sample.

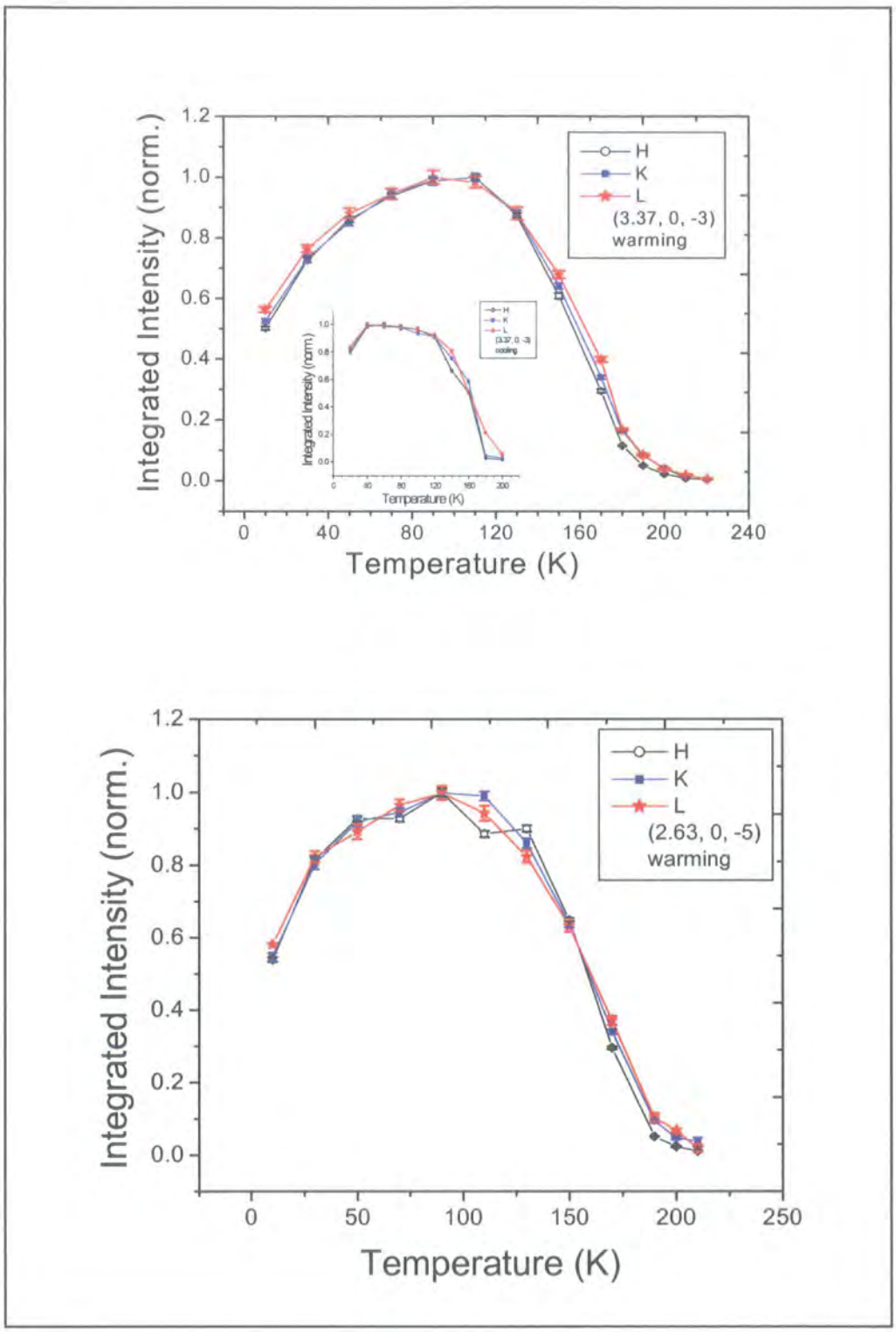

Figure 5.12 The intensity as a function of temperature of the charge ordering reflections (3.37, 0, -3) and (2.63, 0, -5) in *H*-, *K*- and *L*-directions upon warming from low temperature. Inset of graph (a) shows the intensity of the (3.37, 0, -3) peak in a cooling run.

The variation of the width (FWHM) of the charge ordering reflections (3.37, 0, -3) and (2.63, 0, -5) with temperature in all three directions is shown in Figure 5.13 and 5.14. The width has been rescaled to allow comparison between the different directions and the width of the Bragg peak (4, 0, -4) with the same scale as the charge ordering peaks is also included in the Figure 5.13.

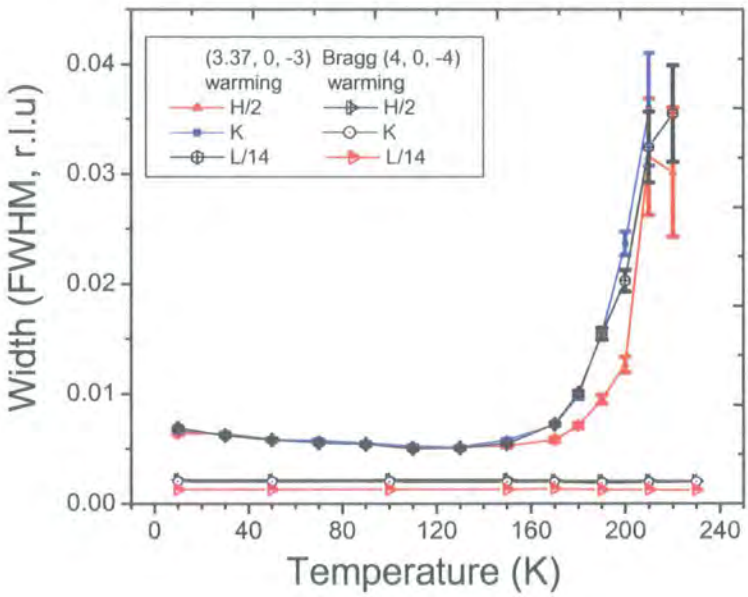

Figure 5.13 The temperature dependence of the width (FWHM) of the charge-ordering peak (3.37, 0, -3). The width of the Bragg reflection (4, 0, -4) is included on the same scale as the charge stripe peak.

While considering the width of the Bragg peak, it is worth noting that the width of the charge ordering reflections is far from the instrumental resolution or sample quality (Bragg width) limits. Unlike the intensity, the width of the peaks is nearly constant until 150 K and after that the width increases. This indicates that quasi-long range charge stripes grow below this temperature. As the spin ordering temperature is lower than the charge ordering transition temperature in the nickelate systems, the change in width at ~ 150 K can be attributed to the spin ordering transition temperature with the antiferromagnetic spin correlations affecting the peak intensity and incommensurability ε. The rate of the increase in the width enhances around the charge stripe melting temperature 195 K.

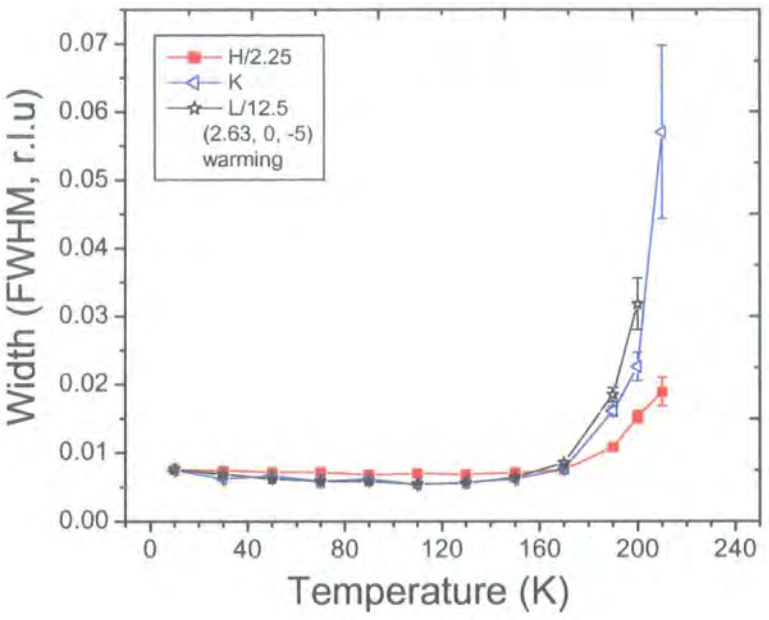

Figure 5.14 The temperature dependence of the width (FWHM) of the charge-ordering peak (2.63, 0, -5).

It seems that an essential property of the Sr-doped nickelate system is that the melting of the charge stripes in these two-dimensional systems happens in two stages [15]. The charge stripes system passes from the low temperature ordered phase to the high temperature disorder phase through an intermediate phase with a reduced order in the charge stripes correlation.

Displayed in Figure 5.15 is temperature dependence of the correlation lengths (in *H*-, *K*- and *L*-directions) of the charge-order satellite (3.37, 0, -3) in warming and cooling runs. The correlation lengths of the peak are nearly identical on cooling and warming runs. The correlation lengths along the *H*- and *K*-direction are ~ 1000 Å and ~ 1900 Å respectively, which show the charge stripes are quite long-range correlated in the *ab* plane. The correlation length along the stripes is much larger than the correlation length normal to this direction. It was also seen in $x = 0.33$ sample. The correlation length along the *L*-direction, which is normal to the NiO_2 layers, is ~ 300 Å. It shows the correlated charge stripes are ~ 25 unit cells wide in this direction. The correlation length is approximately constant until 150 K, the spin-ordering temperature in this compound.

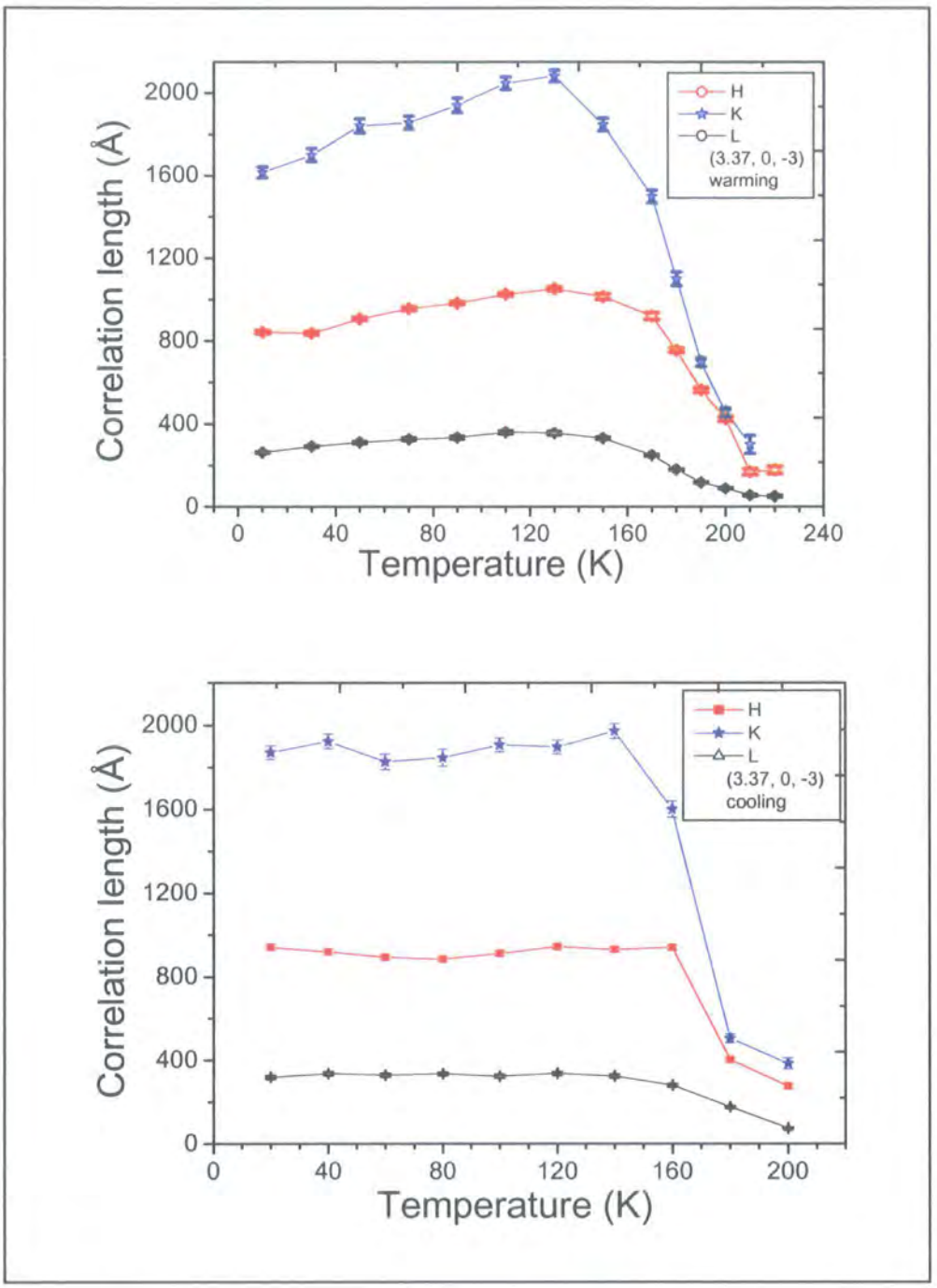

Figure 5.15 The correlation length against temperature of the charge ordering reflection (3.37, 0, -3) on warming and cooling runs.

The ratios of the correlation lengths at two different temperatures, one at low temperature and the other around the transition temperature are as follows:

$$\xi^H_{T<150} / \xi^L_{T<150} \approx 3,\ \xi^K_{T<150} / \xi^L_{T<150} \approx 5.5$$
$$\xi^H_{200} / \xi^L_{200} \approx 4.8,\ \xi^K_{200} / \xi^L_{200} \approx 5$$

From these ratios it is clear that even near to the transition temperature, the ratio of the in-planes to normal to these planes charge stripes correlation length is large. The charge stripes are again quasi 2-dimensional and the melting process falls in the 2D universality class, the same as the previous result on the x = 0.33 sample.

To determine the dimensionality of the charge stripe in this compound, the integrated intensity of the charge-ordering peak (3.37, 0, -3) along the H-direction versus temperature is shown in Figure 5.16.

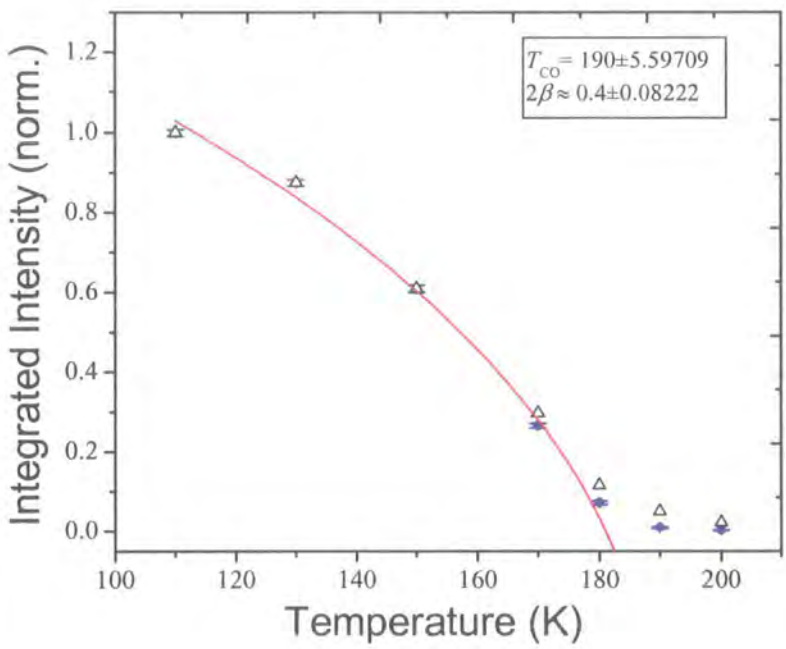

Figure 5.16 The integrated intensity of the charge stripe reflection (3.37, 0, -3) as a function of temperature along the H-direction. The solid line represents the result of fitting as explained in the text.

The triangular data points include scattering from the critical fluctuations and the data points from subtracting this effect are shown as spheres with error bars. The subtracted data points were fitted to a power law equation:

$$I(T) \approx \left[\frac{T_{CO} - T}{T_{CO}}\right]^{2\beta}$$

The fitted parameters extracted from this fitting process on intensity profile are:

$$T_{CO} \approx 190 \pm 5.59 \text{ K}$$

$$2\beta \approx 0.4 \pm 0.8$$

The 2β value is rather high for a 2D system, but is still far away from the three dimensional value (see Table 5.1). The measured exponent of 2β demonstrates that below T_{CO} the charge stripes in $La_{1.7}Sr_{0.3}NiO_{4.01}$ probably fall in the quasi-2D universality class.

The temperature dependence of the incommensurability, ε, is shown in Figure 5.17.

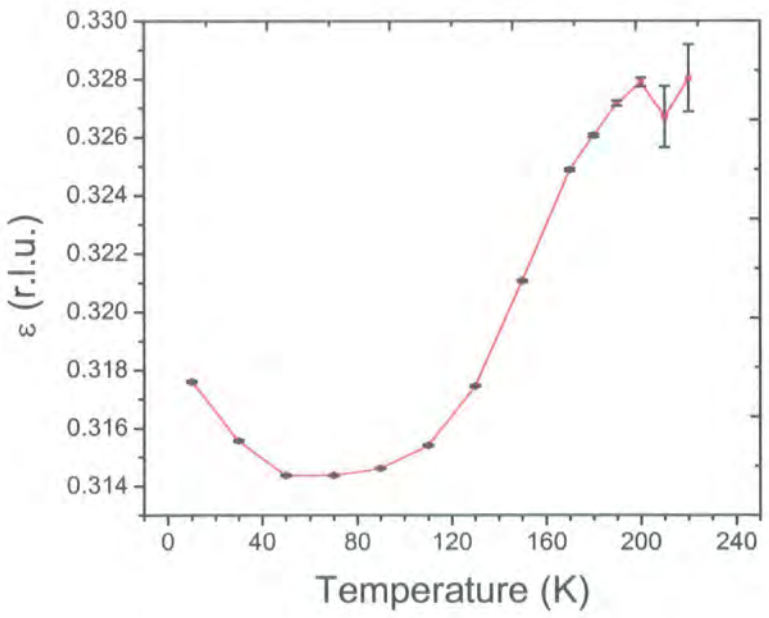

Figure 5.17 The temperature dependence of the incommensurability, ε, derived from the charge ordering peak (3.37, 0, -3) and the error bars from the fitting.

It clearly shows ε is nearly independent of temperature only in temperature range 40 K < T < 110 K (ε = 0.314), consistent with the change in peak intensity, and again before the corresponding peak width shows any change (Figures 5.13, 5.14). This implies the stability of the charge stripes in this temperature range. Above the 110 K, ε increases and becomes temperature dependent. The incommensurability, ε, is a bit higher than the hole concentration n_h in agreement with other published results [9, 14].

The interesting thing that can be seen from the graph is the behaviour of ε around, and above, the transition temperature. It seems that there is a trend for ε to move towards the commensurate value 1/3, that is the most stable situation for charge stripes. As ε is proportional to the hole concentration in the stripes, the increase in ε indicates that the hole density of stripes becomes smaller [8]. For T < 40 K, ε shows another different change with temperature. Tranquada *et al.* have argued about the temperature dependence of the ε. They concluded the carrier density within the charge stripes $n_{st} \equiv n_h / \varepsilon$ changes with ε and when the n_{st} differs from unity, the extra electrons or holes supplied to the antiferromagnetic domains causes local atomic displacements. These displacements disturb the lattice distortions induced by the charge stripes and reduce the charge stripes peak intensity. In the case of x = 1/3, ε is constant and so the carrier density in the charge stripes are constant. This is not consistent with the measured results on this sample (neutron results and present studies), in which the intensity of the charge stripes peak change with the temperature without any variation in ε.

5.4 Charge stripes in $La_{1.725}Sr_{0.275}NiO_{4.01}$

In the previous two sections the charge stripes in the x = 0.33 and 0.3 compounds and their dependence on the hole concentration have been studied. It was observed that upon moving away from n_h = 1/3, the charge stripes became incommensurate and their correlation lengths and ordering temperatures decreased. In this section the results obtained on an x = 0.275 crystal will be described.

5.4.1 Experimental details

The single crystal of $La_{2-x}Sr_xNiO_4$ with Sr concentration x = 0.275 used in this study was grown in Oxford University with an excess oxygen of 0.01±0.01, as indicated by the TGA technique. Preliminary alignments were performed using the D^3 diffractometer at Durham University, and further experiments were conducted on the beamline *XMaS* (BM28) at the European Synchrotron Radiation Facility (ESRF). A Ge (111) analyser crystal was used to reduce the background and to achieve higher wavevector resolution. The sample was mounted in a closed cycle Displex cryostat and the sample mosaic width was determined to be ~ 0.059° (FWHM). The experimental resolution function measured at the Bragg reflection (4, 0, 4) was ξ_H ~ 0.00189 Å^{-1}, ξ_K ~ 0.00118 Å^{-1}, and ξ_L ~ 0.00342 Å^{-1} at low temperature. All the measurements were in scans along the *H*-, *K*-, and *L*-directions. All intensities are integrated intensities that were collected by rocking the sample and have been normalized against monitor counts to compensate for variations in the synchrotron beam intensity.

The crystal structure of $La_{2-x}Sr_xNiO_4$ x = 0.275, the same as the other nickelate compositions, is tetragonal with the *I4/mmm* symmetry and for convenience we indexed reflections in orthorhombic lattice units with $a_o \sim b_o = \sqrt{2}\ a_t$ = 5.414 Å and c = 12.715 Å where o and t stand for orthorhombic and tetragonal respectively (see Figure 5.3).

Upon cooling down, extra reflections at expected positions for charge modulations such as (4.58, 0, 5), (3.42, 0, 5), (3.42, 0, 3), (2,58, 0, 5) and (2.58, 0, 1) were found which can all be indexed as q = (h±2ε, 0, l) with h = even and l = odd integer. Some of these charge ordering peaks and the Bragg reflection (4, 0, 4) were measured as a function of temperature from 10 K to above the charge ordering transition temperature and some were also measured in a cooling run.

5.4.2 Results and discussion

Alignment matrices were constructed by finding some Bragg peaks especially (4, 0, 4) and (2, 0, 2) reflections, which are near to these charge-ordering satellites. The

stronger charge ordering satellites (4.58, 0, 5) and (2.58, 0, 1) were measured as a function of temperature in all three directions H, K, and L in reciprocal space.

The peak profiles at every temperature were fitted with Lorentzian (K- and L-directions) and Gaussian (H-direction) line shapes and the results for integrated intensity (normalized) for charge ordering peaks (4.58, 0, 5) and (2.58, 0, 1) are shown in Figures 5.18. The intensities are approximately constant in the interval 30 K to 80 K and then gradually decrease until ~150 K, the charge ordering transition temperature from our measurements. Above this temperature there was still some very weak scattering detectable until 190 K (we were able to follow the strongest peak (4.58, 0, 5)) due to critical charge scattering. The intensity shows a small anomaly at low temperature.

Lee *et al.* using polarized neutron diffraction technique found the spin and charge order at $T_{SO} \sim 150$ K and $T_{CO} \sim 190$ K [7]. Their neutron data does not show any decrease in intensity at low temperatures. Their transition temperature $T_{CO} \sim 190$ K is a bit higher than our result and this may be is due to the difference in the amount of excess oxygen between the two samples.

In graph (a) of the Figures 5.19 and 5.20 is displayed the variation of the width (FWHM) of the charge ordering satellites (4.58, 0, 5) and (2.58, 0, 1) as a function of temperature. The width was rescaled so as to easily compare in different directions and the width of the Bragg reflection (4, 0, 4) have also been added to the Figure 5.19 (a). The widths of the charge ordering reflections still are far from the sample and instrumental resolution limits, implying the charge stripes have not very long-range correlation lengths. The width of the charge ordering peaks is approximately independent of temperature until 110 K and after that increases with increasing temperature, indicating the charge stripes are stable below this temperature and disorder affects the charge stripes above this temperature. The intensity of the peaks gets enhanced below this temperature $T \sim 110$ K and probably this is the spin ordering temperature T_{SO}. This implies that although the charge stripes can exist in the temperature range above the spin ordering transition temperature, long-range ordered charge stripes can only be formed in the coexistent temperature range, i.e., $T < T_{SO}$.

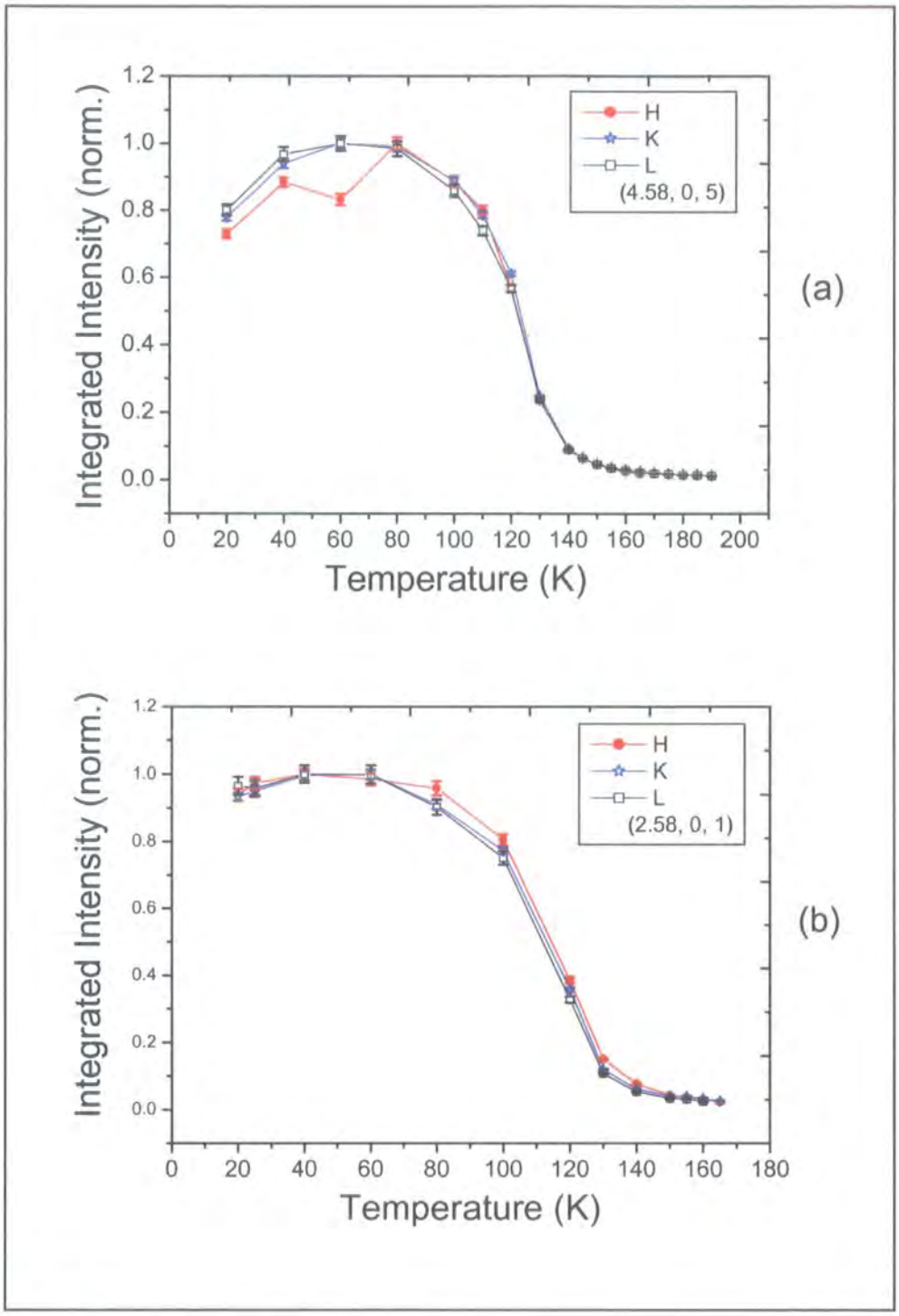

Figure 5.18 The temperature dependence of the integrated intensity of charge-ordering peaks (a) (4.58, 0, 5) and (b) (2.58, 0,1) along the *H*-, *K*- and *L*-directions.

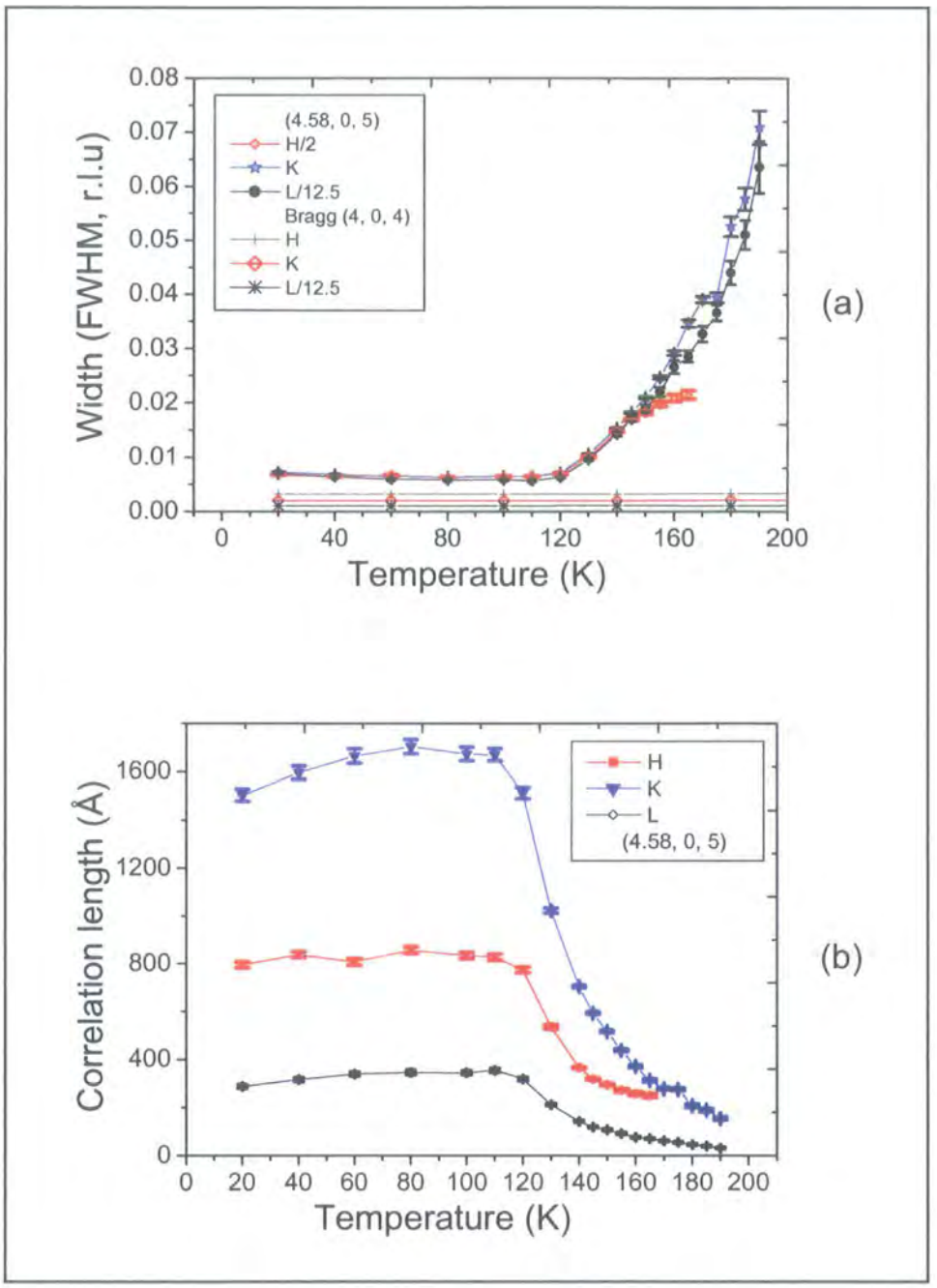

Figure 5.19 (a) Width and (b) correlation lengths of the charge ordering reflection (4.58, 0, 5) as a function of temperature. Values of the width of the neighbouring Bragg reflection (4, 0, 4) are included in (a) so as to give an indication of the sample quality and the instrumental resolution.

Displayed in graphs (b) of these Figures is the temperature dependence of the correlation length (in *H*-, *K*- and *L*-directions) of the charge order satellites (4.58, 0, 5) and (2.58, 0, 1) in the warming run. The correlation lengths along the *H*- and *K*-direction are ~ 800 Å and ~ 1600 Å compared with the in-plane correlation length measured by neutron diffraction ~ 100 Å [7], which shows the charge stripes are quite correlated in the *ab* plane and that synchrotron X-ray scattering is a proper and more appropriate technique for the study of these charge stripes. The correlation length along the *L*-direction, which is normal to the NiO_2 layers, is ~ 300 Å. It shows the correlated charge stripes are ~ 25 lattice parameters wide in this direction. The correlation length is approximately constant until 110 K. From these measurements it is clear that the charge stripes are quasi 2-dimensional in this compound the same as previous results on x = 0.3 and in contrast with the x = 0.33 sample in which the charge stripes are truly 2-dimensional [16].

Zachar has argued that the main source of disorder in stripes is non- topological elastic deformation along the stripes and not purely topological defects [17]. The present results strongly suggest that the hole concentration is a major factor in the charge stripe correlations.

The dimensionality of the charge stripes was also investigated by fitting of the integrated intensity of the charge-ordering peak (4.58, 0, 5) along the *H*-direction versus temperature with a power law equation and the result is shown in Figure 5.21. The triangular data points include scattering from the critical fluctuations and the data points from subtracting this effect are shown as spheres with error bars. The subtracted data points has been fitted to a power law equation:

$$I(T) \approx \left[\frac{T_{CO} - T}{T_{CO}}\right]^{2\beta}$$

The fitted parameters extracted from this fitting process on intensity profile are:

$$T_{CO} \approx 130.37 \pm 0.62 \text{ K}$$

$$2\beta \approx 0.296 \pm 0.056$$

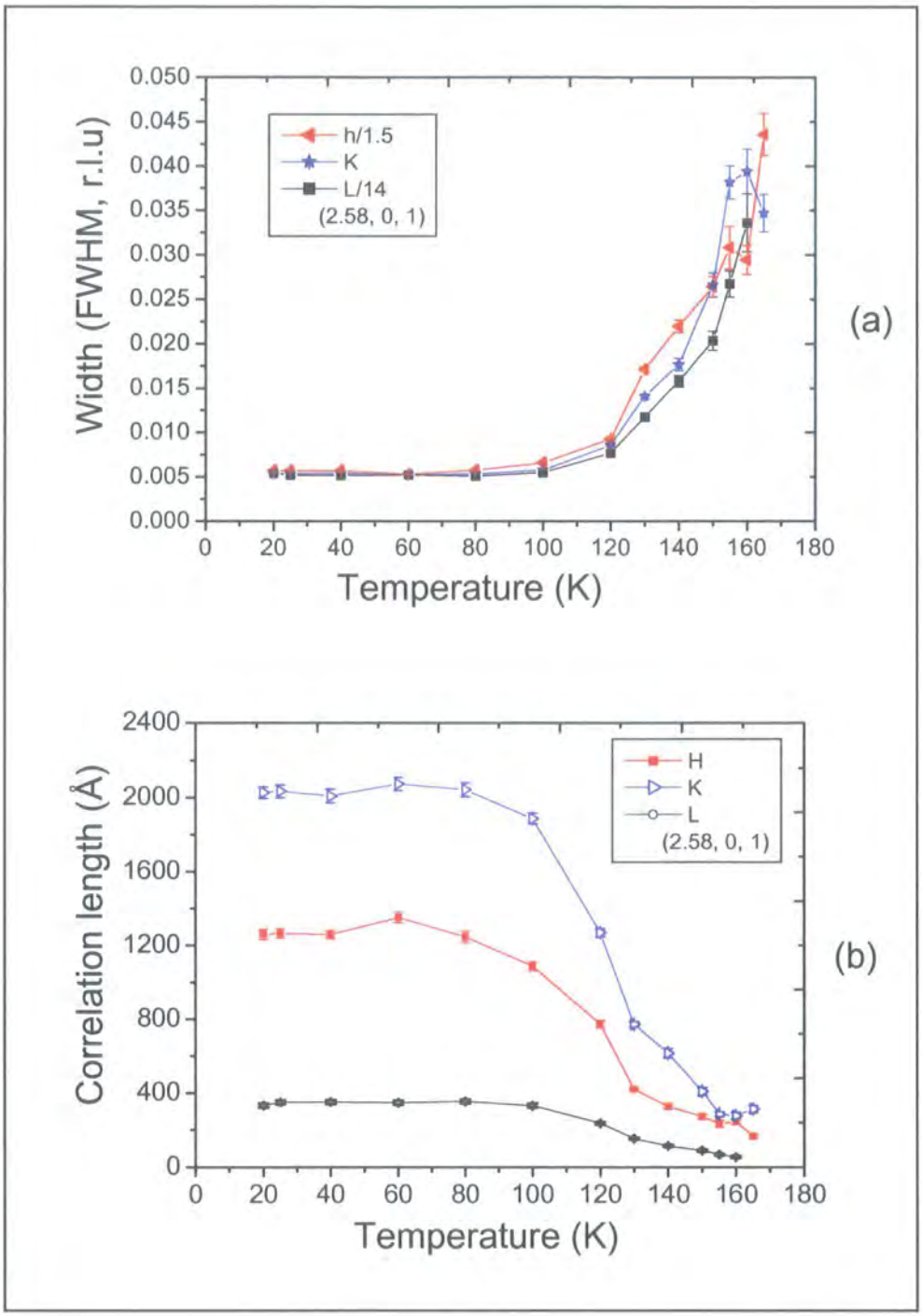

Figure 5.20 (a) Width and (b) correlation lengths of the charge ordering reflection (2.58, 0, 1) as a function of temperature.

Comparing the 2β value with the predicted value in Table 5.1, shows the transition to be second order in nature. The measured exponent of 2β clearly demonstrates that below T_{CO} the charge stripes in $La_{1.725}Sr_{0.275}NiO_{4.01}$ fall in the 2D universality class.

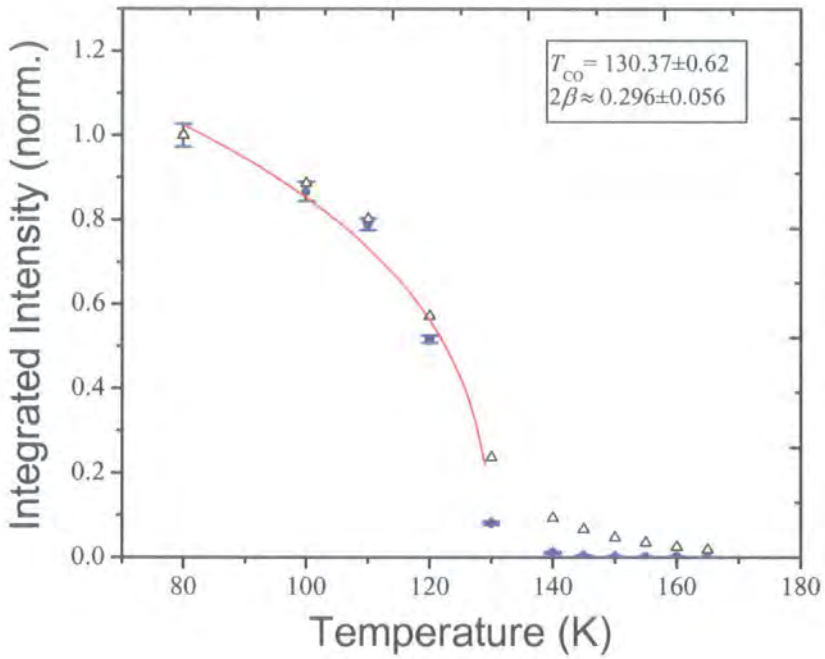

Figure 5.21 The integrated intensity of the charge stripe reflection (4.58, 0, 5) as a function of temperature along the *H*-direction. The solid line represents the result of fitting as explained in the text.

The temperature dependence of the incommensurability, ε, is shown in Figure 5.22. The incommensurability, ε, is independent of temperature until ~ 80 K and it increases with further increase in temperature before the width starts to change. The low temperature measured value $\varepsilon \sim 0.295$ is consistent with the ε from the neutron result for $\varepsilon = 0.3$ [7]. The incommensurability is a bit higher than the hole concentration x in agreement with known results [9, 14]. The interesting thing that can be seen from the graph is the behaviour of ε around, and above, the transition temperature range. It seems that, as with $x = 0.3$, there is a trend to move ε towards the commensurate value 1/3 that is the stable situation for charge stripes. As ε is related to the hole concentration within the stripes, the increase in ε indicates that the hole density of stripes becomes smaller as the temperature increases [8].

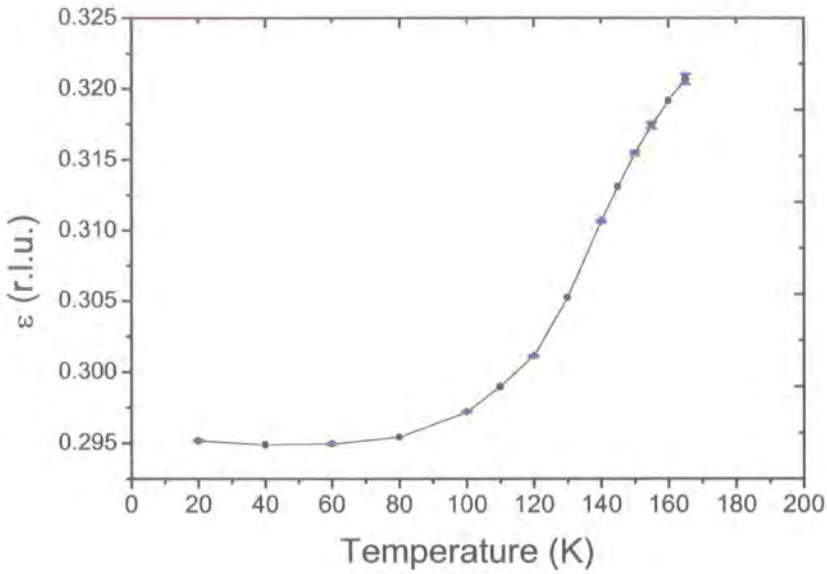

Figure 5.22 The temperature dependence of the incommensurability ε (the error has been calculated from the fitting of the charge ordering satellite at every temperature).

Since ε is weakly temperature dependent, the measured ε (at low temperature) from all three samples shows, that ε is approximately linear in n_h with only a small deviation from the $n_h = \varepsilon$ law for $n_h < 1/3$. We have to consider that the exact amount of the hole concentration is $x + 2\delta$, where δ is excess oxygen from stoichiometry. Neutron scattering results have showed that this deviation from the $n_h = \varepsilon$ law is also held for $n_h > 1/3$ [9]. Katsufuji *et al.* by measuring Hall coefficients, thermoelectric power and optical conductivity spectra have concluded that the deviation from 1/3 can be regarded as electron or hole doping into the commensurate charge-ordered state $n_h = 1/3$ [18].

5.4.3 Comparison of the correlation lengths for x = 0.33, 0.3 and 0.275 compounds

To answer the question how the hole concentration affects the charge stripes, in Table 5.2 is shown the correlation lengths measured from x = 0.33, 0.3 and 0.275 compounds. The data shown are for two selected temperatures in different regions of the intensity curves. The first point (labelled as (1)) is in the low temperature region

and the second point was chosen near to the transition region in which the peak intensity drops about 70% of its maximum value. The correlation length is directly related to the hole concentration in *ab* plane, and as can clearly be seen the correlation length decreases compared to x = 1/3 sample with decreasing x from 1/3 to 0.275. So there is a general trend that the charge stripes change from a well correlated state in the case of x = 1/3 stable state to a state with smaller correlation length.

Correlation length	**x = 0.33**		**x = 0.3**		**x = 0.275**	
	(1)	(2)	(1)	(2)	(1)	(2)
H	1030±11	816±5	986±8	753±12	848±14	534±9
K	2362±25	1451±21	1941±35	1099±33	1696±30	1017±11
L	119±2	138±3	333±7	176±4	327±8	207±4

Table 5.2 Correlation length in two selected temperatures, (1) at low temperature and (2) at a point in which the peak intensity is about 30% of the low temperature value for samples with x = 0.33, 0.3, and 0.275.

The correlation length along the *L*-direction in systems x = 0.3 and 0.275 is very short and nearly the same but is different from x = 1/3 sample. Maybe it can be classified as follows: the charge stripes in the x = 1/3 sample is truly 2-dimensional and with decreasing the hole concentration from x = 1/3, the charge stripes become quasi 2-dimensional. Therefore, these results imply that the correlation length in *L*-direction is independent of the hole concentration and normal to the layers the dimensionality of the compound, rather then other interactions, has a dominant effect. It has been argued that the strain field resulting from the radius mismatch of La and Sr ions affects the stripes. However, these results are in contrast with this idea, because as the Sr concentration increases the strain field should get stronger. This stronger field should cause more disorder. In contrast, the Sr ions have a pinning effect on charge stripes and doping more Sr more stabilizes the charge stripes (at least until x = 1/3).

In conclusion, by use of synchrotron X-ray scattering, the formation of the charge stripes in single crystals of $La_{2-x}Sr_xNiO_4$ (x = 0.33, 0.3, and 0.275) systems has been studied and it has been found that the charge stripes are formed below the charge

ordering transition temperature T_{CO}. The value of T_{CO} strongly depends on the hole concentration with the maximum temperature found for the x = 0.33 compound. As the hole concentrations reduce from 1/3, the charge ordering transition temperature shifts to lower temperatures. Measurements of the correlation lengths demonstrate that the charge stripes in these systems are two-dimensional and also for the first time, critical fluctuations well above T_{CO} have been observed in all three compounds.

It was found that the intensity of the charge-ordering peak also strongly depends on the hole concentration. To make a comparison between the charge-ordering peak intensities in all three samples, the ratio of the intensities of the charge-ordering peak and the corresponding Bragg peak were calculated. The results are as follows:

$$x = 0.33 \quad \frac{I_{CO}}{I_{Br}} \approx 5.07\times10^{-3}$$

$$x = 0.3 \quad \frac{I_{CO}}{I_{Br}} \approx 2.88\times10^{-3}$$

$$x = 0.275 \quad \frac{I_{CO}}{I_{Br}} \approx 2.6\times10^{-3}$$

Because the temperature dependence of the charge stripe peak intensity for these three samples are different, so these ratios have been calculated in the temperature range in which the intensity of the charge-ordering peaks are maximum. These ratios clearly show that the charge ordering peak intensity is maximum in the x = 0.33 sample and as the hole concentration reduces, the intensity of the peak decreases.

5.5 Polarised resonant scattering at the Ni *K*-edge from $La_{5/3}Sr_{1/3}NiO_4$

5.5.1 Introduction

The tuneability of synchrotron radiation has provided an opportunity to study the dependence of the charge, orbital and spin ordering satellites upon the incoming photon energy. Gibbs *et al.* observed a large resonance of the magnetic scattering in holmium metal at the *L*-absorption edge [19]. Hannon *et al.* explained that the

enhancement originated from electric multiple transitions [20]. When the incident photon energy is in the vicinity of the absorption edge of an element in the crystal, the dispersion parameters in the atomic form factor of the relevant atoms are modified and subsequently so is the structure factor. This can occur when the energy of the incident beam approaches the value required to excite a core electron into an empty state of a valence shell. In spin- and orbital ordering satellites tuning the beam energy to an absorption edge of the relevant element will always produce significant change in the scattering cross-section and enhancement in scattering intensity. This enhancement has been seen by different studies in spin and orbital ordering peaks in manganites [21-24].

At the *K*-edge of 3d transition metals two processes can be take place: a dipolar resonance (E1) involving the weakly polarized 4p levels and the quadrupolar resonance (E2) which involves the strongly polarized 3d bands. In both processes there are transitions from the initial core states to exited states, which are vacant and allowed transitions. These transitions are related to the chemical bonding of the relevant atom. In contrast with the E1 process (first order magnetic peak), the scattering amplitude of the E2 process is non-zero in both polarization channels. The presence of the enhancement in both polarization channels at the pre-edge in the absorption measurement identifies this resonance clearly as an E2 (1s –3d) type resonance. If the enhancement is not observed in the σ-σ channel, it is identified as an E1 transition (1s – 4p) [20]. Hill *et al.* have observed a twofold increase in x-ray magnetic scattering study of antiferromagnet NiO at an energy corresponding to a quadrupole transition in the absorption spectrum, and no enhancement was observed at the dipolar transition [25].

5.5.2 Experimental Details

The single crystalline sample of $La_{5/3}Sr_{1/3}NiO_4$ was grown at Bell Laboratories using the floating zone method, and had been previously studied by normal X-ray scattering. The synchrotron experiment was performed at beam line *XMaS* (BM28) at the ESRF. The wavelength of the incident X-rays was first selected to be 1.2715(1) Å using a Si(111) monochromator and most of high-order contamination was

rejected by the use of a focusing mirror. The incoming photon beam was polarized perpendicular to the vertical scattering plane (σ polarization). Polarization analysis of the scattered X-ray beam has been performed using Bragg scattering from a Ge (111) analyser crystal. In this geometry the incident beam polarization is σ-polarized. The sample was mounted on a Displex closed-circle cryostat, with the normal direction of the scattering plane along the [1 0 1] zone.

5.5.3 Results and discussion

First by cooling the sample below the charge ordering temperature T_{CO}, a number of charge ordering satellites at the expected positions were found with wave vector q_{CO} = (2ε, 0, 1) in reciprocal space. The characteristic wave vector for any spin satellite is q_{SO} = ($1+\varepsilon$, 0, 0). The stronger charge/spin satellites (3.33, 0, 3), (3.33, 0, 4) and (2.67, 0, 5) were chosen and the intensities of these peaks were measured in both polarization channels, σ - σ and σ - π as a function of energy between 8.32 keV and 8.38 keV (Ni edge at 8.349 keV). Their intensities were normalized to the monitor counts to correct for variation in beam current. The incident photons had σ-polarization, that means their electric field vector lies along the normal to the vertical scattering plane. A schematic view of the scattering geometry is displayed in Figure 5.23.

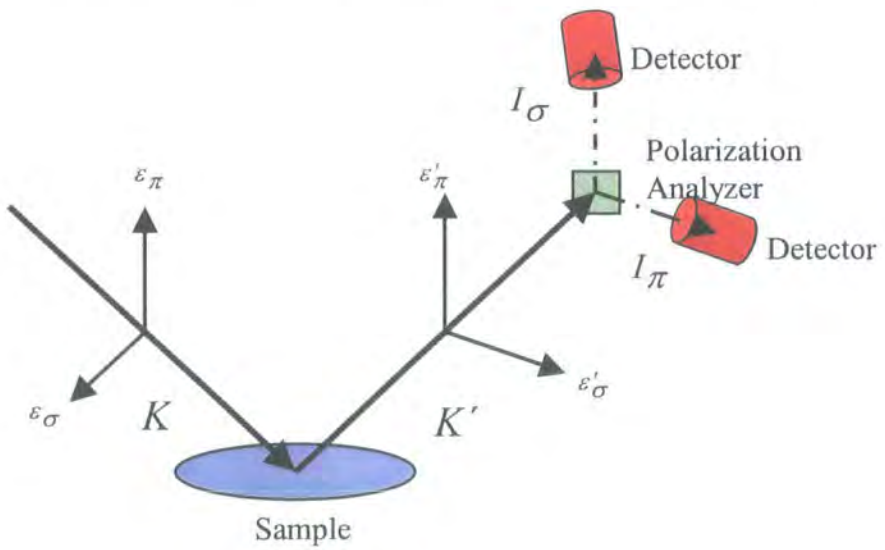

Figure 5.23 A schematic view of the resonance scattering geometry.

The incident photons with wave vector K and polarization components of ε_σ and ε_π hit the sample and the scattered photons emerge with wave vector K' and polarization components of ε'_σ and ε'_π. By a combination of rotating the detector and polarization analyser, the intensity of the scattered photons can be detected in both polarization channels.

Figure 5.24 (graphs a, b, and c) shows typical scans along the H-, K-, and L-directions through the charge ordering satellite (3.33, 0, 3) in both σ - σ and σ - π channels at 100 K respectively. The intensities in the σ - π channel have been rescaled for comparison. The main peak intensity is in the un-rotated channel σ - σ, with a very weak intensity in the σ - π channel.

By tuning the beam energy to the Ni K-edge energy, energy scans were performed through some selected charge/spin satellites. The main result is shown in Figure 5.25. The intensity of the charge stripe peaks (2.66, 0, 5), graph (a) and (3.33, 0, 3), graph (b) are plotted as a function of incident photon energy in both polarization channels, which were taken at 200 K. The data from fluorescence measurements is also added to the graphs.

As the graphs show there are a clear enhancement of the peak intensities in the σ - π channel at the Ni K-absorption edge without any resonance effect in the σ - σ channel. The enhancement occurs at the energy corresponding to the peak in absorption measurements. A resonant enhancement of approximately a factor 4 is observed at the Ni main absorption edge. The σ - σ scattering shows only a dip at the absorption edge, a characteristic of the normal charge scattering. Resonant effects can arise in the diffraction of X-rays when the transition element exists in an anisotropic crystalline environment. The influence of an electronic transition at the absorption edge atom results in the effect and depends on the spatial distribution of empty electronic levels of the atom.

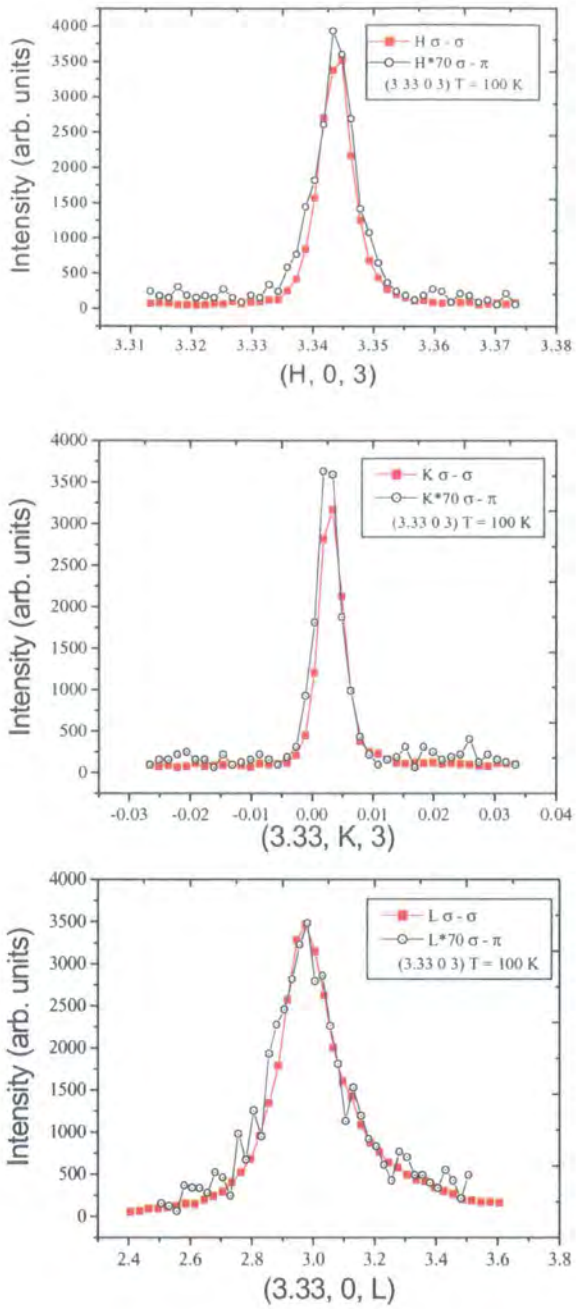

Figure 5.24 Typical scans along the three principal axes *H*, *K*, *L* in reciprocal space in σ - σ and σ - π channels (at Ni *K*-edge) at 100 K.

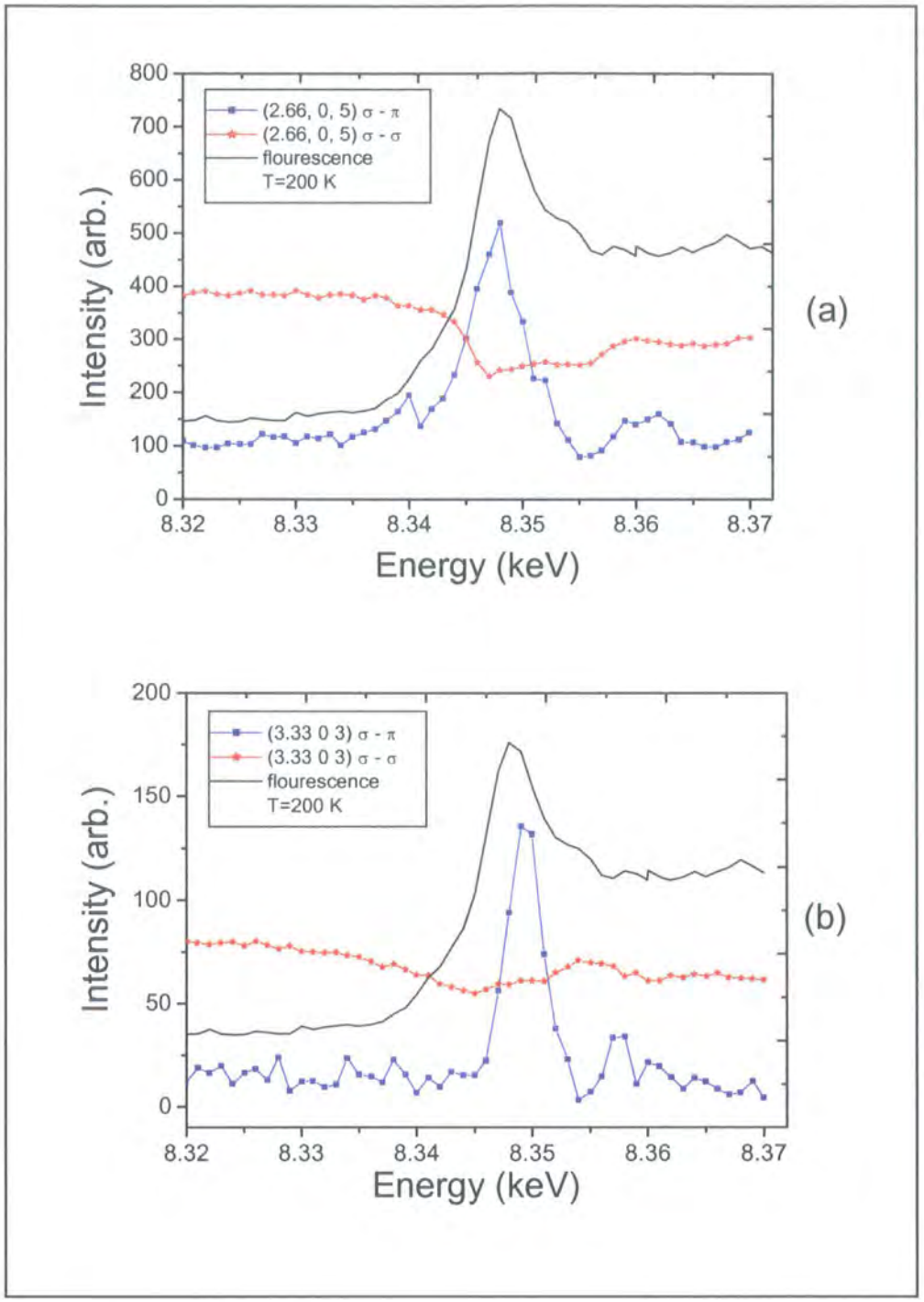

Figure 5.25 Energy scans through the charge ordering reflections (a) (2.66, 0, 5) and (b) (3.33, 0, 3) in the σ - σ and σ - π channels. The data from fluorescence measurements has also been included in the graphs.

X-ray absorption measurements on various Ni compounds revealed that the edge energy depends on the Ni electronic structure and its local environment in these materials [6]. The edge energy is higher for more positively charged species or if the atom is poorly screened. Tan *et al.* proposed that this dependence arises from the Coulomb interaction between the core-hole and the valence electrons, and between the core-hole and the surrounding electrons. Polarized Ni *K*-edge X-ray-absorption spectroscopy results on $La_{2-x}Sr_xNiO_4$ (x = 0.2 – 1.3) also showed splitting of the 4p state energy when the polarizations of the incident photons are parallel, or normal to, the *c*-axis [26]. Sahiner *et al.* also observed collapse of the energy splitting between $4p_\pi$ and $4p_\sigma$ spectral states by increasing the Sr substitution. As in the charge ordered state, the Ni valence is Ni^{3+} in hole rich regions and Ni^{2+} in hole-poor regions, their transition energies associated with 1s to 4p states are different and this causes an enhancement of the charge stripes peak intensity at the edge.

Referring to Figure 5.25, the intensity is enhanced by approximately a factor of 4 compared to the non-resonant signal seen at lower energy in the σ - π channel. This factor is unusually large (compare to magnetic resonance) for the *K*-edge of the transition metal elements [27]. The underlying non-resonant scattering is constant below and above the edge. The appearance of the resonance effect only in the σ - π channel at the main peak position in the fluorescence measurements indicates that the transition at the edge only involves a dipole transition [28]. A dipole transition is a transition from a 1s state to an empty 4p state of the Ni atom.

Typical energy scans through the (2.66, 0, 5) and (3.33, 0, 3) reflections in the σ - π channel which have been fitted with a Lorentzian line shape are displayed in graphs (a) and (b) of Figure 5.26. These are not good fits but are suitable for the purpose of finding the peaks centres and the widths at half the maximum of the peaks. The enhancements occur at $E \sim 8.349$ keV and the peak width is about 5 eV. The measured width is comparable with the 4p band, that is wider in energy than the narrow 3d band.

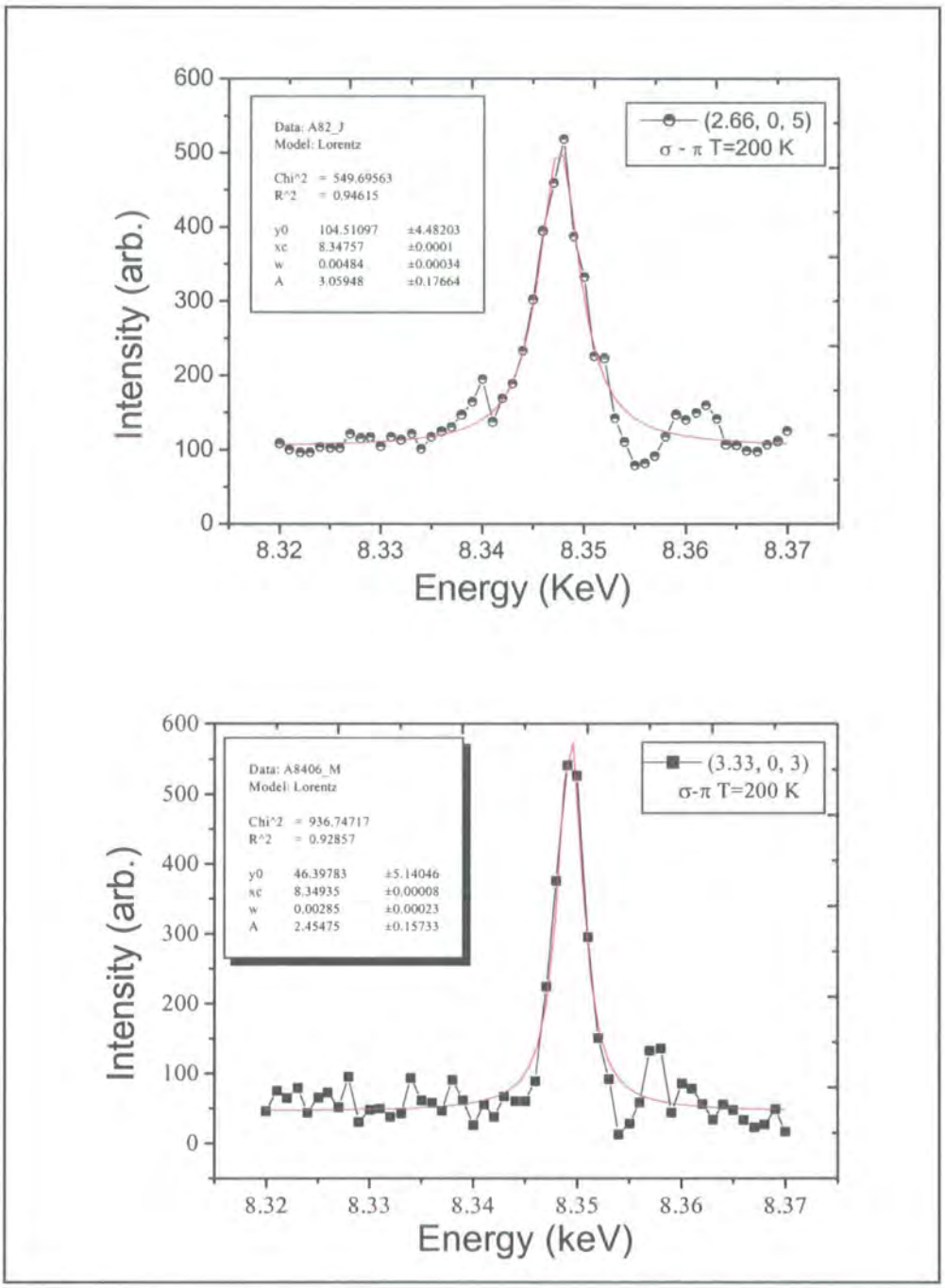

Figure 5.26 Energy scans through the charge-ordering satellites (2.66, 0, 5) and (3.33, 0, 3) in the σ- π channel fitted with a Lorentzian line shape.

The data from the fluorescence measurements is plotted in Figure 5.27. It does not show any clear pre-edge feature, or if it exists it is clearly very weak. Polarized Ni *K*-edge X-ray absorption spectroscopy results on $La_{2-x}Sr_xNiO_4$ showed a large increase in the integrated area of the 1s → 3d quadrupole transition with Sr content x and this was interpreted as a possible 4p-3d orbital mixing, besides the increase in the Ni 3d hole count [26]. So the absence of a clear pre-edge feature in the fluorescence measurements presumably shows that any p-d hybridisation is too weak to open a dipole-allowed transition at this energy.

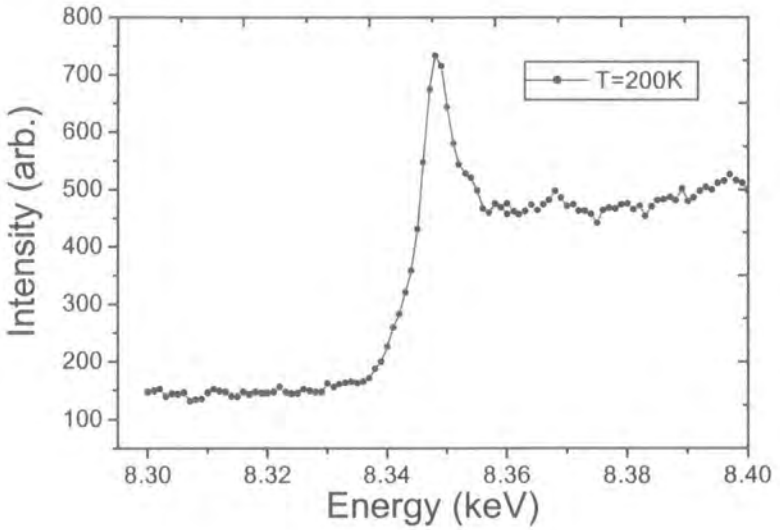

Figure 5.27 Fluorescence measurement at the Ni *K*-edge

To clearly demonstrate that the enhancement of the charge satellites is really from the resonance effect, the intensity of the (2.66, 0, 5) and (3.33, 0, 3) satellites obtained in the σ - π channel at some selected temperatures is displayed in Figure 5.28 (graphs (a) and (b) respectively). There is an increase in intensity, with increasing temperature, around the spin ordering transition temperature. The enhancement of the intensity around the spin ordering transition temperature has also been seen in neutron scattering measurements [7].

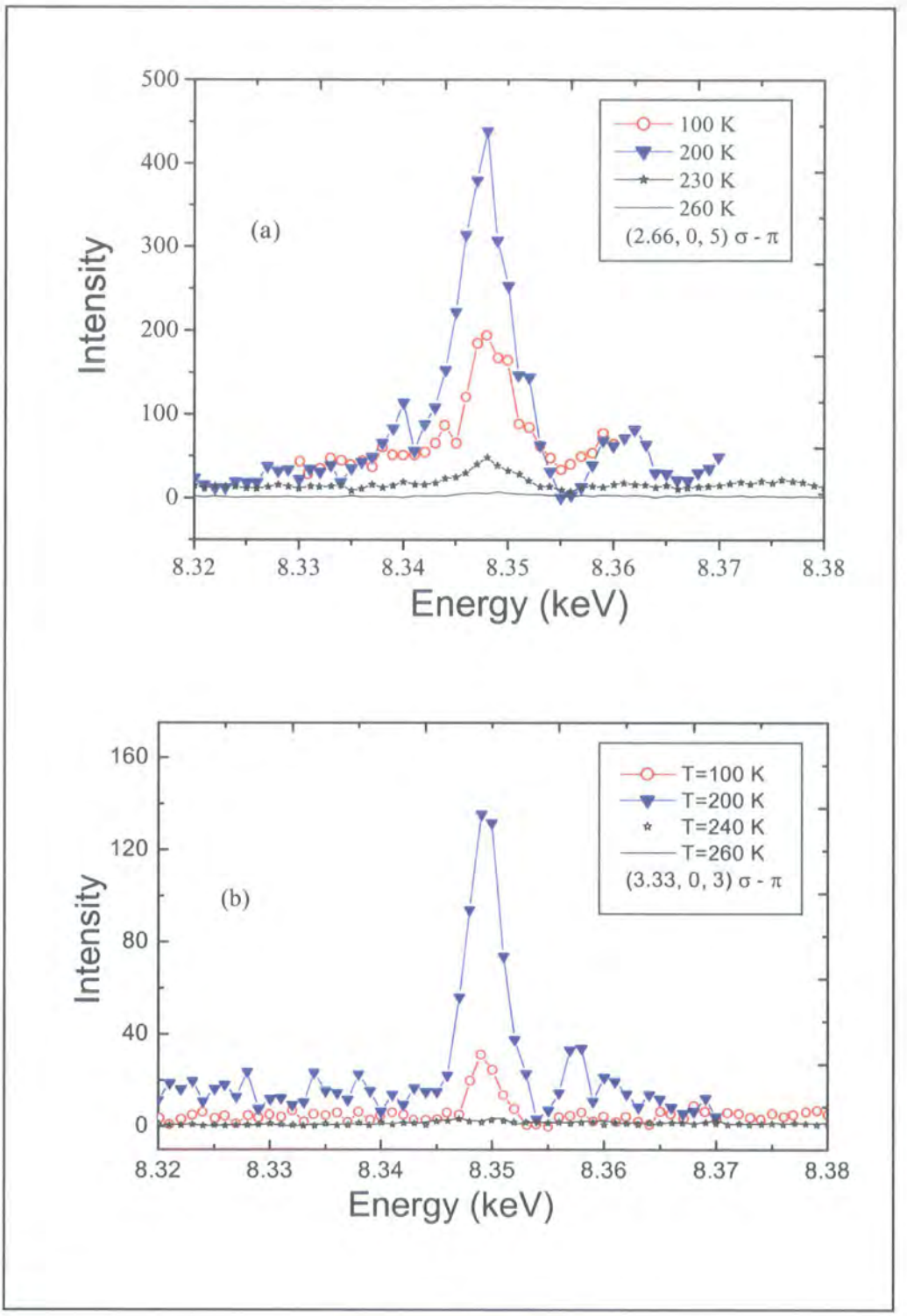

Figure 5.28 The intensity of (a) the (2.66, 0, 5) satellite and (b) the (3.33, 0, 3) satellite at various temperatures in the σ - π channel.

By further increase of the temperature of the (2.66, 0, 5) peak (graph (a)), at 230 K, which is near to the charge stripe melting transition temperature T_{CO} = 240 K, the peak intensity has fallen to 10% of the peak intensity at 200 K. Above the charge ordering melting temperature at 260 K, the peak intensity completely vanishes. The (3.33, 0, 3) satellite (graph (b)) behaves similarly to the (2.66, 0, 5) peak. Its intensity at T = 240 K is also plotted, and shows the peak disappears at this temperature. These two graphs show the intensity of these peaks demonstrates a clear temperature dependence. The results show the enhancement observed in intensity of these peaks at the Ni *K*-edge is truly from the resonance effect in the electronic transition from the Ni 1s state to the 4p state.

The energy scan through the expected spin position (3.33, 0, 4) in the σ - π channel is displayed in Figure 5.29 at various temperatures.

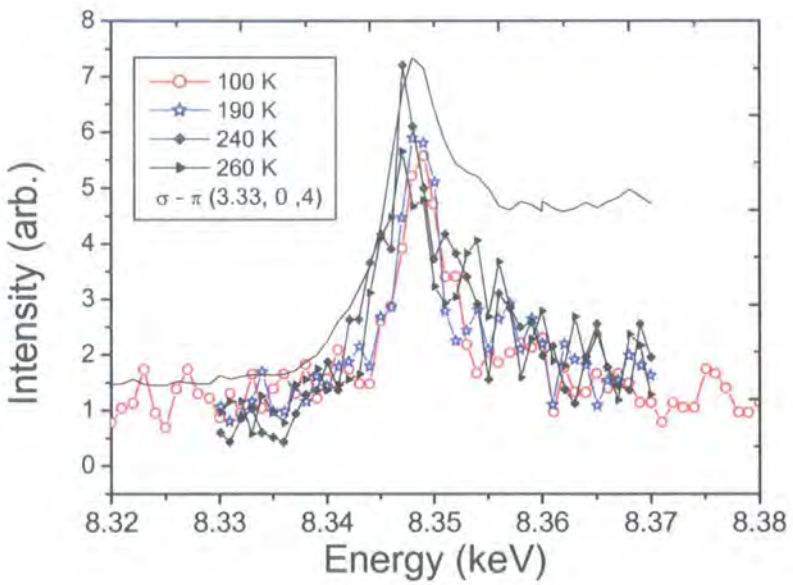

Figure 5.29 An energy scan through the (3.33, 0, 4) position at various temperatures.

The fluorescence measurements have also been added to the graph for comparison. The peak profiles at different temperatures are similar and clearly different from the (2.66, 0, 5) and (3.33, 0, 3) satellite intensity profiles. The scattering at the (3.33, 0, 4) position exactly follows the fluorescence profile. As can be seen the profile does not show any temperature dependence. The scattering exists even at 260 K, which is

above the charge ordering transition temperature. So, at this position the scattering is just from fluorescence and this peak does not show resonance by changing the photon energy.

Finally it should be mentioned that from these measurements resonant behaviour was observed in energy scans through the satellites with wavevector (2ε, 0, 1). The existence of scattering in only the σ - π channel shows that the resonant scattering factor is tensorial, as occur in so-called orbital reflections in $Nd_{0.5}Sr_{0.5}MnO_3$ and $LaMnO_3$. More experiments are needed, preferably on other samples having the [101] direction normal to crystal surface, to explore details of this behaviour.

5.6 References

[1] S. H. Lee and S. W. Cheong, Physical Review Letters **79**, 2514 (1997).

[2] C. H. Chen, S. W. Cheong, and A. S. Cooper, Physical Review Letters **71**, 2461 (1993).

[3] J. M. Tranquada, D. J. Buttrey, V. Sachan, *et al.*, Physical Review Letters **73**, 1003 (1994).

[4] S. W. Cheong, H. Y. Hwang, C. H. Chen, *et al.*, Physical Review B-Condensed Matter **49**, 7088 (1994).

[5] S. H. Han, M. B. Maple, Z. Fisk, *et al.*, Physical Review B-Condensed Matter **52**, 1347 (1995).

[6] Z. Q. Tan, S. M. Heald, S. W. Cheong, *et al.*, Physical Review B-Condensed Matter **47**, 12365 (1993).

[7] S. H. Lee, S. W. Cheong, K. Yamada, *et al.*, Physical Review B **6306**, 0405 (2001).

[8] J. M. Tranquada, P. Wochner, A. R. Moodenbaugh, *et al.*, Physical Review B **55**, R6113 (1997).

[9] H. Yoshizawa, T. Kakeshita, R. Kajimoto, *et al.*, Physical Review B **61**, R854 (2000).

[10] T. Katsufuji, T. Tanabe, T. Ishikawa, *et al.*, Physical Review B-Condensed Matter **54**, 14230 (1996).

[11] M. F. Collins, *Magnetic Critical Scattering* (Oxford University Press, New York, 1989).

[12] T. Ido, K. Magoshi, H. Eisaki, *et al.*, Physical Review B-Condensed Matter **44**, 12094 (1991).

[13] E. D. Isaacs, G. Aeppli, P. Zschack, *et al.*, Physical Review Letters **72**, 3421 (1994).

[14] J. M. Tranquada, D. J. Buttrey, and V. Sachan, Physical Review B-Condensed Matter **54**, 12318 (1996).

[15] M. E. Ghazi, C.-H. Du, P. D. Hatton, *et al.*, in *Magnetic and Superconducting Materials*, edited by M. Akhavan, J. Jensen and K. Kitazawa (World Scientific Press, Iran, 1999).

[16] C. H. Du, M. E. Ghazi, Y. Su, *et al.*, Physical Review Letters **84**, 3911 (2000).

[17] O. Zachar, Physical Review B **62**, 13836 (2000).

[18] T. Katsufuji, T. Tanabe, T. Ishikawa, *et al.*, Physical Review B-Condensed Matter **60**, R5097 (1999).

[19] D. Gibbs, D. R. Harshman, E. D. Isaacs, *et al.*, Physical Review Letters **61**, 1241 (1988).

[20] P. Hannon, G. T. Trammel, M. Blume, *et al.*, Physical Review Letters **61**, 1254 (1988).

[21] J. P. H. Zimmermann M. v, Doon Gibbs, M.Blume, D. casa, B. Kimer, Y. Murakami, Y. tomioka, and Y. Tokura, Rev. Lett. **83**, 4872 (1999).

[22] Y. Murakami, J. P. Hill, D. Gibbs, *et al.*, Physical Review Letters **81**, 582 (1998).

[23] Y. Murakami, J. P. Hill, D. Gibbs, *et al.*, Japanese Journal of Applied Physics Part 1-Regular Papers Short Notes & Review Papers **38**, 360 (1999).

[24] Y. Murakami, H. Kawada, H. Kawata, *et al.*, Physical Review Letters **80**, 1932 (1998).

[25] J. P. Hill, C. C. Kao, and D. F. McMorrow, Physical Review B **55**, R8662 (1997).

[26] A. Sahiner, M. Croft, S. Guha, *et al.*, Physical Review B **51**, 5879 (1995).

[27] M. J. Cooper and W. G. Stirling, Radiation Physics and Chemistry **56**, 85 (1999).

[28] W. Neubeck, C. Vettier, K. B. Lee, *et al.*, Physical Review B **60**, R9912 (1999).

Chapter 6

Observations on charge stripe glass phases in $La_{2-x}Sr_xNiO_4$ (x = 0.25 and 0.2)

6.1 Introduction

In the previous chapter, the results obtained from measurements on charge ordering in $La_{2-x}Sr_xNiO_4$ with x = 1/3, 0.3, and 0.275 have been explained. We saw how the charge stripes in the x = 1/3 compound are more stable, and the charge stripes have a longer correlation length compared to the two other compounds. The commensurability, ε, shows virtually no temperature dependence in the 1/3 compound, while in two other compounds it is incommensurate and varies with temperature particularly at high temperature. As the hole concentration decreases from the 1/3 value, the charge ordering peaks become broader, and the charge stripe ordering temperature decreases. It has also been shown that the charge stripes are 2-dimensional in nature in all three samples. In this chapter the results obtained from synchrotron X-ray scattering measurements on two other samples with x = 0.25 and 0.2 will be reviewed. The charge-ordered correlation lengths for x = 0.2 – 0.33 will be compared and the behaviour of the correlation lengths in this series of compounds will be discussed.

6.2 Charge stripes in x = 0.25 compound

6.2.1 Introduction

The $La_{2-x}Sr_xNiO_4$ system with various Sr concentrations has been studied by neutron, electron and X-ray diffraction, as well as other techniques which have measured the electrical and magnetic properties of the samples [1-5]. Among the published results so far, no study has been published on the x = 0.25 compound and the nature of the charge stripes for this hole concentration is therefore unknown in detail. This is the

first effort to study the charge stripes in this compound especially by high-resolution synchrotron X-ray scattering, which has the advantage over many other techniques of directly observing any variations of correlated electron charge density. We found this compound undergoes one phase transition to a charge ordered state at low temperature with the appearance of extra reflections due to the charge ordering. The characteristic wave vector for the charge ordering satellites is $q = (2\varepsilon, 0, 1)$, corresponding to a real space modulation of $a/2\varepsilon$. The charge stripes line up along the diagonal direction in the Ni-O planes and the period of these charge stripes varies with the hole concentration [6].

The charge stripes in this compound have unusual correlation lengths compared with previously reported results on other compounds in chapter 5. The correlation lengths in a and c directions are very short range (~ 300 Å) and along the stripe (b) direction is ~ 1450 Å. So it seems the stripes display quasi 1D long-range order.

6.2.2 Experimental details

Charge ordering in $La_{1.75}Sr_{0.25}NiO_4$ was studied by using synchrotron X-ray scattering. The experiment was performed at the European Synchrotron Research Facility (ESRF) at Grenoble in France. The single crystal of $La_{2-x}Sr_xNiO_4$ with x = 0.25 and an oxygen content of δ = 0.02(0.01) used in this experiment was grown by the floating-zone method in Oxford University. The crystal was first studied using the D^3 diffractometer in Durham to find the orientation and for alignment and cutting of a crystal face for studying the charge ordering. The sample is of good quality with narrow mosaic width, which was determined to be ~ 0.02° (FWHM). The crystal was mounted having its [101] axis vertical and [010] axis in the sample surface directed along the incident beam. A Ge (111) single crystal analyser was used in triple-crystal geometry to obtain higher wavevector resolution and lower the background. The sample was mounted in a closed-cycle Displex cryostat and the measurements were performed in the range of temperatures from 10 K to 270 K. With the other nickelate samples, the crystal has a body-centred tetragonal Bravais lattice and the *I4/mmm* space group in high temperature. As usual the crystal was indexed in orthorhombic

lattice units with $a_o \sim b_o = \sqrt{2}a_t = 5.4145$ Å and $c = 12.715$ Å, where o and t stand for orthorhombic and tetragonal respectively.

The experimental resolution function along H-, K-, and L-directions measured at the Bragg reflection (4, 0, 4) was $\xi_H \sim 0.0014$ Å^{-1}, $\xi_K \sim 0.00089$ Å^{-1}, and $\xi_L \sim 0.0028$ Å^{-1} at low temperatures. All the measurements were performed in reciprocal space and the data were collected in scans along the H-, K-, and L-directions. All the data have been normalized with the monitor counts of incident beam to account for variations in the beam current. All intensities mentions hereafter are integrated intensities, which were measured by rocking the sample.

6.2.3 Results and discussion

Upon cooling, extra reflections were found at the expected positions for charge modulations such as (3.42, 0, 3), (2.58, 0, 1), (4.58, 0, 3) and (4.58, 0, 5), which are separated from the Bragg reflections (4, 0, 4) and (2, 0, 2) with the charge ordering wavevector (2ε, 0, 1) with $\varepsilon = 0.29$. In addition scattering at twin position (4, 0.58, 5) was observed. In Figure 6.1 the observed charge ordering satellites around the (4, 0, 4) Bragg peak are shown. These peaks are distributed symmetrically around the (4, 0, 4) Bragg reflection.

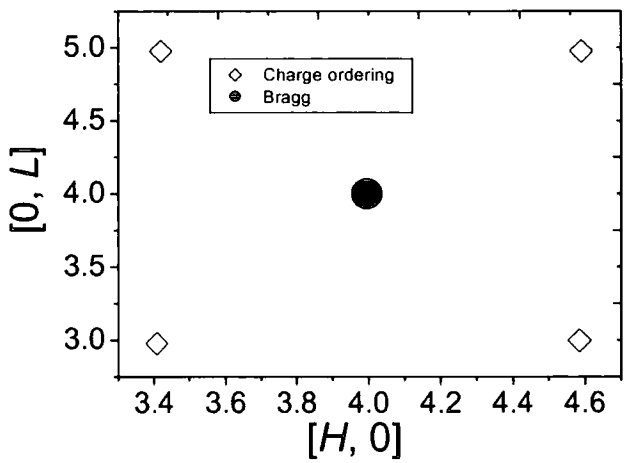

Figure 6.1 A schematic view of the observed charge ordering peaks in the [H, 0, L] plane around the (4, 0, 4) Bragg reflection.

The temperature dependence of the intensity of the peaks was measured on the (3.42, 0, 3), (2.58, 0, 1) and (4, 0.58, 5) charge-ordering reflections in the temperature range 10 to 240 K. The charge ordering reflection (3.42, 0, 3) was also measured on a cooling run to see if there was any hysteresis or temperature effects in the phase transition region. The charge ordering peaks and Bragg reflections have been fitted with appropriate Gausian or Lorentzian line shapes for every temperature, and in the rest of this section the results are those obtained from this fitting.

Figures 6.2 and 6.3 show the integrated intensity (normalized) of the charge ordering reflection (3.42, 0, 3) against temperature in both warming and cooling runs respectively. The intensity of the charge ordering satellite (2.58, 0, 1) is also shown in Figure 6.4 for comparison. This peak was very weak and also at low temperature in the *H*-direction the peak profile was not symmetrical, so the data in this direction is shown just for that fitted in the higher temperature range versus temperature. The other charge ordering peaks behave similarly.

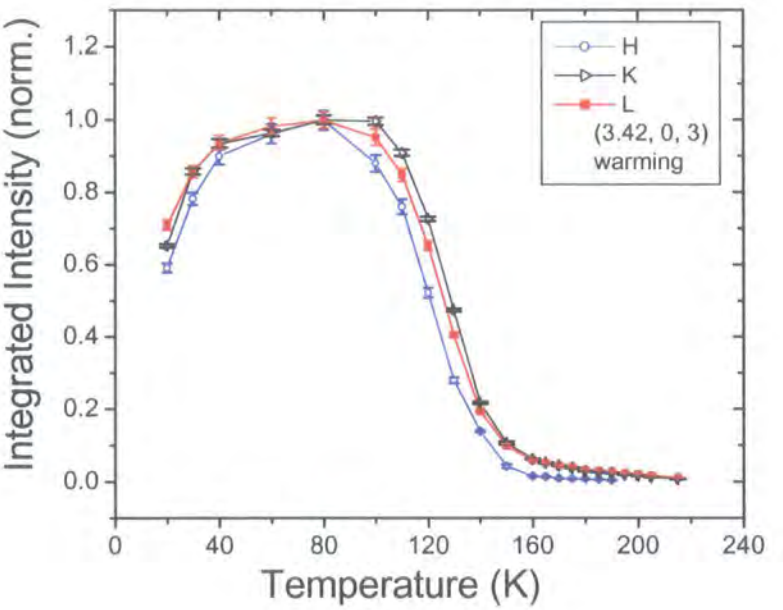

Figure 6.2 The temperature dependence of the intensity of the charge ordering satellite (3.4, 0, 3) along the *H*-, *K*-, and *L*-directions upon warming.

The shape of the integrated intensity of all three peaks is similar, and in following we will concentrate on the stronger charge-order peak (3.42, 0, 3). In the cooling run it

was difficult to find the peak at high temperatures near to the charge stripes melting temperature (~ 145 K) because even at 60 K, where the intensity of the peak is at a maximum, the strongest peak (3.42, 0, 3) has an intensity of only 3400 counts per second.

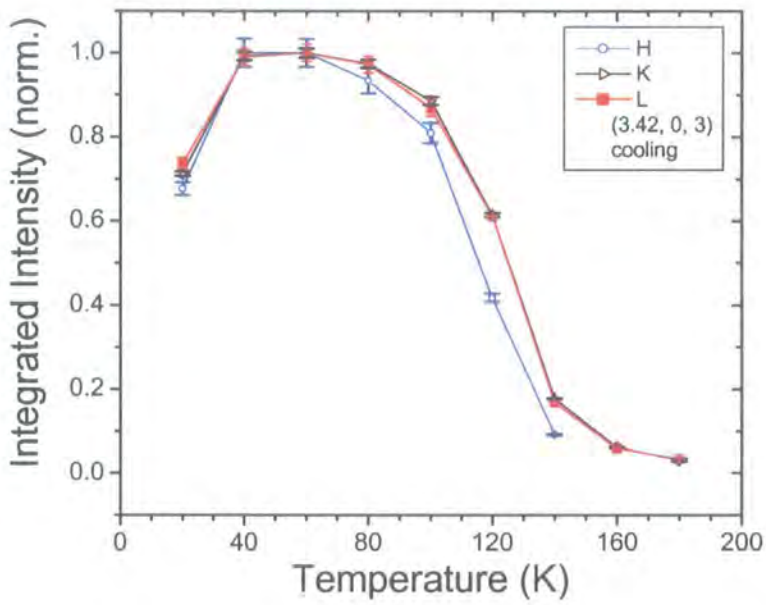

Figure 6.3 The temperature dependence of the intensity of the charge ordering satellite (3.42, 0, 3) along the *H*-, *K*-, and *L*-directions upon cooling.

The peak intensity is approximately constant in the temperature range 40 K to 110 K and it gradually decreases after 110 K upon warming until the transition temperature around 145 K. However, the peak stays with very weak intensity at higher temperature and it was possible to follow the peak until ~ 210 K. The scattering is due to the critical scattering above the charge ordering transition temperature T_{CO}, where the charge stripes exist in the form of fluctuations. Because resistivity and magnetization measurements in this compound, in contrast with the 1/3 compound, do not show a clear change in this temperature range, it is difficult to determine the exact charge-ordering transition temperature. The temperature range, in which the charge stripes have a fluctuating form, is large. The peak intensity decreases below 40 K and this decrease in intensity of the charge ordering peaks has also been seen in cooling runs (Figure 6.3) as well as (2.58, 0, 1) peaks (Figure 6.4). This may rule out

temperature or sample movement effects. The reason for this decrease is not clear and one possible candidate is the segregation of the hole carriers from the charge stripes.

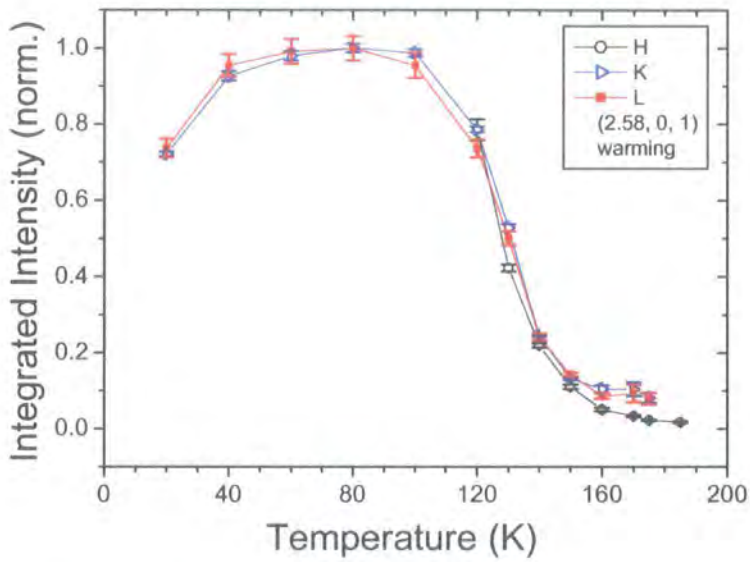

Figure 6.4 The temperature dependence of the intensity of the charge ordering satellite (2.58, 0, 1) along the *H*-, *K*-, and *L*-directions upon warming.

A neutron scattering study of $La_{1.775}Sr_{0.225}NiO_4$ crystal indicated the spin and charge ordering transition temperatures to be ~ 100 K and ~ 150 K [1] and in the $x = 0.275$ compound the spin and charge ordering peak's intensities vanish at 155 K and 200 K respectively [2]. These studies suggest that the charge ordering temperature of $La_{1.75}Sr_{0.25}NiO_4$ should be at approximately 175 K.

To compare the intensity behaviour of the charge stripes near to the stripes melting temperature, the temperature dependence of the intensity of the charge ordering reflection (3.42, 0, 3) in the *K*-direction, on warming and cooling runs, is displayed in Figure 6.5. The two intensities versus temperature lines behave similarly and do not show any hysteresis in the region that the charge-ordered state melts. This implies the transition associated with the change from the low temperature charge ordered state to the high temperature charge disordered state is a second order like transition. Naturally, X-ray scattering cannot distinguish between the high

temperature phase having no charge separation and that of a dynamically disordered charge separated phase. Only average long-range correlations are observed.

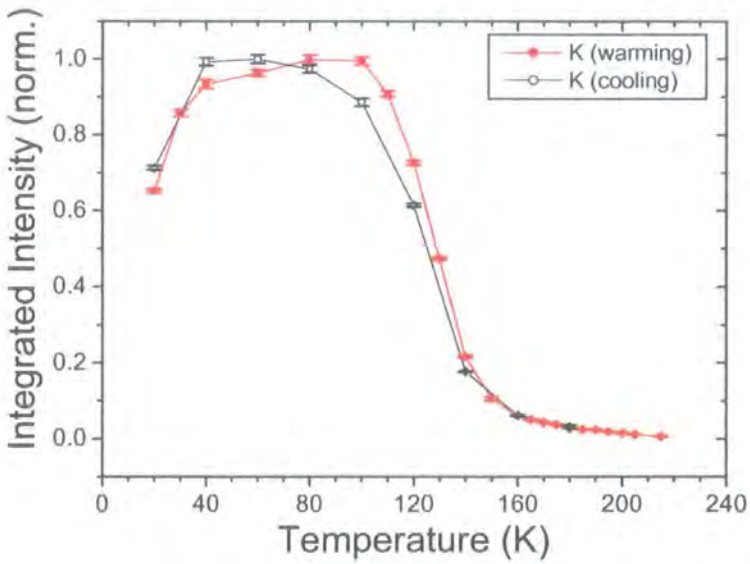

Figure 6.5 Intensity against temperature of the charge ordering satellite (3.42, 0, 3) in the *K*-direction on warming and cooling runs.

The full width at half maximum (FWHM) of the charge ordering reflection (3.42, 0, 3) as a function of temperature on warming and cooling runs is shown in Figure 6.6 and 6.7 respectively. In the graphs the widths in all three directions in reciprocal space are shown. The error bars from the fitting results along the *H*-, *K*-, and *L*-directions are included in the graph. Also shown is the width of the Bragg reflection (4, 0, 4), this gives an indication of the experimental resolution. As can be seen, the charge stripes peak width is much broader than the width of the Bragg peak in all three directions, indicating that the charge stripes do not have a long-range correlation length (at least as long as the Bragg peaks). The width of the peak, apart from a small increase below $T \sim 40$ K, is nearly constant until $T \sim 110$ K and increases with further raising of the temperature. In the temperature range between 110 K and the charge-ordering transition temperature ~ 145 K, the width increases and the correlated length scale decreases. This behaviour was also observed in the cooling run, which is displayed in Figure 6.7.

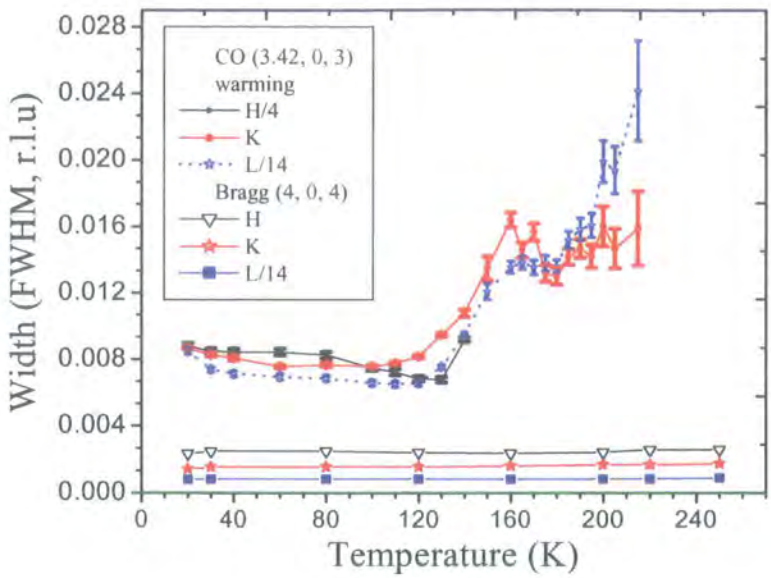

Figure 6.6 The width of the charge-ordering satellite (3.42, 0, 3) and Bragg reflection (4, 0, 4) in each three directions *H*, *K*, and *L* on a warming run. Note the width in some directions is reduced to aid comparison. The error bars are also included in the graph.

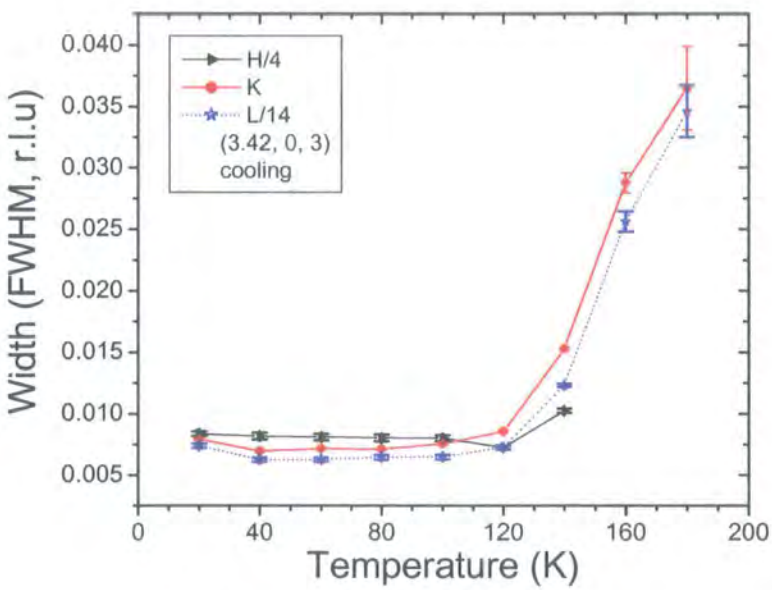

Figure 6.7 The width of the charge ordering satellite (3.42, 0, 3) in each of the three directions *H*, *K*, and *L* upon cooling.

The onset of increase at 110 K can be attributed to the spin-ordering transition temperature, that in nickelates is always lower than the charge-ordering transition

temperature. The width also changes above 145 K corresponding to dynamic critical fluctuations of the charge stripes. But the increase in width is not continuous within the transition region, and it seems between the low temperature ordered phase and the high temperature disordered phase, there is an intermediate phase with a reduced correlation length.

The correlation length has been calculated from the measured widths and is displayed in Figure 6.8 and 6.9 for warming and cooling runs respectively. The error bars are also added to the graph in all three directions. The temperature dependence of the correlation length above 40 K can be divided to three regions the same as the width and intensity variation. The first region is between 40 K and 110 K, in which the charge stripes correlation lengths, in all three directions, are constant and the stripes are in a stable state. In this temperature range the spin stripes as well as charge stripes are ordered and this antiferromagnetic ordering stabilizes the charge stripes.

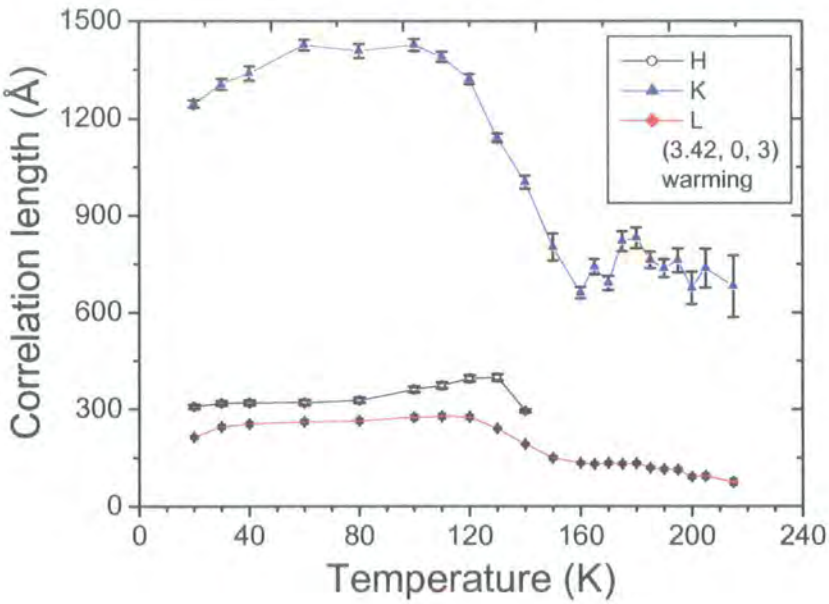

Figure 6.8 Correlation lengths versus temperature of the charge ordering satellite (3.42, 0, 3) on a warming run in each of the three *H*-, *K*-, and *L*-directions. The error bars are also included in the graph.

The measured correlation lengths along the *H*-, *K*-, and *L*-directions are ~ 310 Å, ~ 1380 Å, and ~ 250 Å respectively. Neutron measurements taken on a crystal with x =

0.225 indicated that the in-plane correlation length of the magnetic satellites is much larger then the charge ordering satellites. In the *L*-direction, the magnetic peaks are sharper for *l* odd and the charge ordering reflection correlation length is half that of the spin [1] and the in-plane correlation length measured by neutron diffraction on x = 0.275 was ~ 100 Å [2]. The correlation lengths gradually decrease in the second temperature range from 110 K to 145 K, until the charge stripes melting temperature ~ 145 K. Finally in the third temperature range above the ~ 145 K the charge stripes exist in a fluctuating dynamic form with a very short-range correlation length. These charge ordered clusters are due to critical scattering in the charge stripes phase, and with decreasing the temperature toward the charge ordering transition temperature the size of these clusters grow and the correlation length increases. An interesting result is a large anisotropy in the correlation length along the stripe (*K*) direction compared to the two other directions. The correlation length in this direction is more than 4 times larger than other two directions. The correlation lengths in x = 1/3, 0.3, and 0.275 compounds (previous chapter) along the *H*- and *K*-directions are quite large but with a very short-range correlation length along the *L*-direction that shows the 2D nature of the charge stripes.

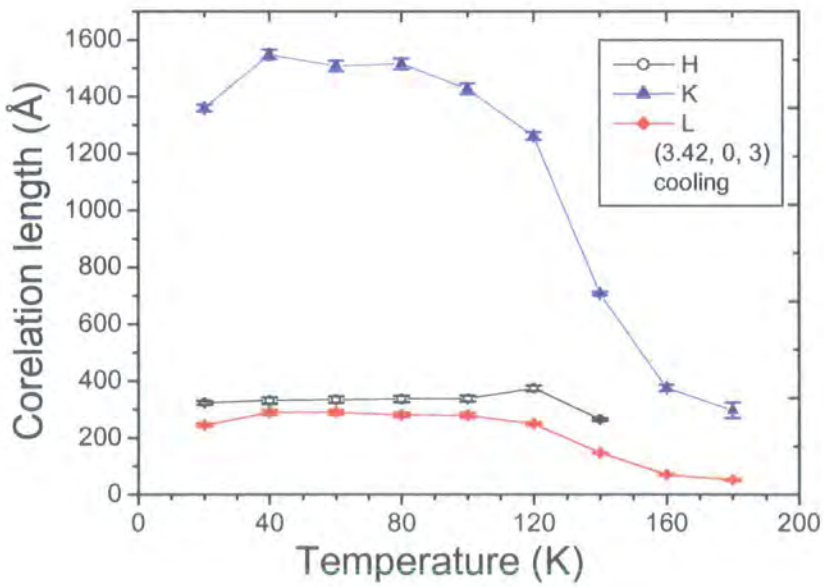

Figure 6.9 Correlation lengths versus temperature of the charge ordering satellite (3.4, 0, 3) on a cooling run in each of the three *H*-, *K*-, and *L*-directions.

As we saw in Table 5.2 the correlation length decreases in both the *H*- and *K*-directions when the hole concentrations decrease. However, this decrease keeps the correlation length ratio in the *H*- and *K*-directions nearly identical. In the present compound the correlation length along the *K*-direction is quite large, but the *H*-direction is approximately the same as the *L*-direction both with a much reduced correlation length. Therefore, when the hole concentration decreases from $x = 1/3$, the correlation length also decreases, but this decrease in stripe modulation direction is more sensitive to the hole concentration. It will be seen in section 6.4 that around $x = 0.25$ is a transition point between long-range stripe order and a glassy stripe phase characterised by only short-range order. This behaviour can be probably attributed to the spin ground state, because in $x = 0.25$ the stripe period should be 4 Ni atoms wide and this breaks the AFM ground state.

The incommensurability, ε, extracted from fitting the peak of the (3.42, 0, 3) satellite with a Gaussian line shape at every temperature is shown in Figure 6.10.

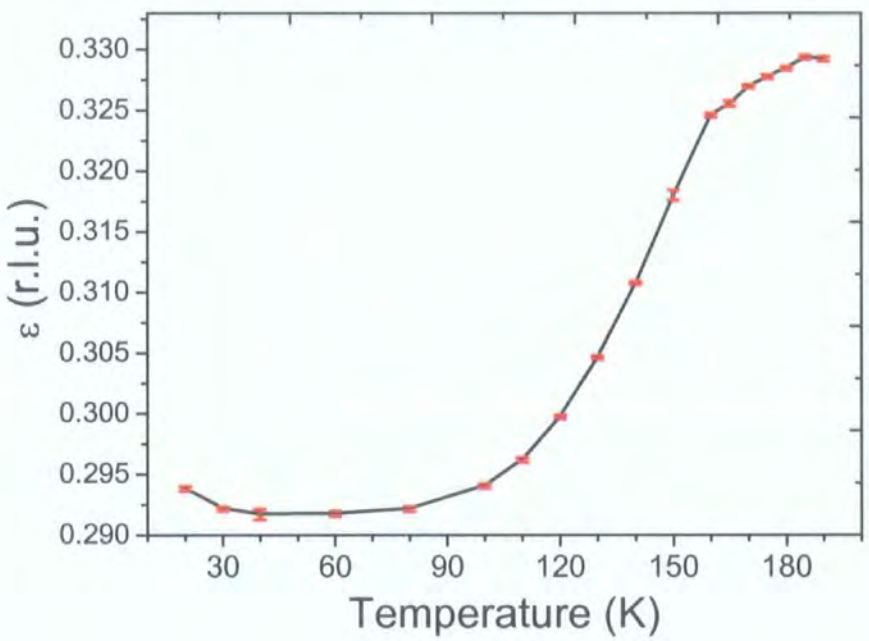

Figure 6. 10 Incommensurability, ε, versus temperature extracted from the charge-ordering satellite (3.4, 0, 3) on a warming run.

The ε at low temperatures is nearly constant with $\varepsilon \approx 0.293$ that is consistent with the $\varepsilon = n_h = x+2\delta$ law (in this sample $\delta = 0.02$) with a small deviation. This small

deviation from the $\varepsilon = n_h$ law on both sides of the $n_h = 1/3$ has been observed by others [3]. The incommensurability, ε, gradually increases above 90 K, ~ 20 K below the temperature at which the width of the charge stripes starts to increase. The measured value of ε in the $x = 0.225$ compound is ≈ 0.275 at low temperature and it gradually changes at higher temperature [1]. As proposed by Tranquada *et al.* the density of the charge carriers per Ni site within a stripe is n_h / ε [4], so any change in ε is associated with the movement of the carriers from/to the stripes. An increase in ε indicates a decrease in the density of holes within the stripes, and this causes a decrease in the intensity of the charge ordering satellite.

The very interesting behaviour of ε, in the temperature range around, and above, the transition temperature, is its variation with temperature. There is a general trend to lock the ε into the commensurate value 1/3. This behaviour has been seen in other compounds with $x = 0.3$ and 0.275. It seems that 1/3 commensurate charge stripes is the ideal low energy stable structure, probably due to the numbers of the Ni sites that can be accommodated between the stripes. At low temperatures the charge stripes are tightly correlated with the underlying lattice and hence they follow the $n_h = \varepsilon$ law. When the charge stripes become disordered at higher temperatures and are likely to be fluctuating they prefer to lock closer to the 1/3 commensurate state. This scenario is further supported by recent neutron scattering results on samples with a hole concentration higher than 1/3 [5]. The commensurability ε, for $n_h > 1/3$ samples, near and above, the charge ordering transition temperature decreases in contrast with the samples in which for them $n_h < 1/3$. By neutron scattering they could not follow the peak higher than the charge ordering transition temperature.

Further confirmation of the commensurability versus temperature line shape, was found by the charge-ordering reflection (4, 0.58, 5) which comes from twining, and also the charge-ordering satellite (2.58, 0, 1). These are plotted in Figure 6.11. The general behaviour of the line shapes is very similar.

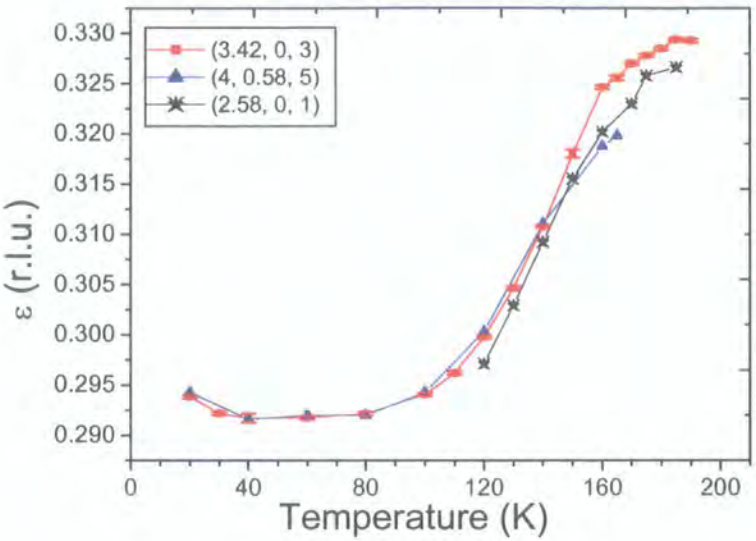

Figure 6. 11 The temperature dependence of the commensurability, ε, extracted from the charge stripes satellites (4, 0.58, 5) and (2.58, 0, 1) as well as (3.42, 0, 3) peak.

6.3 Charge stripes in the $x = 0.2$ compound

6.3.1 Experimental details

The single crystal of $La_{2-x}Sr_xNiO_4$ with $x = 0.2$ used in this experiment was grown at Oxford University. Thermo-gravimetric data on the crystal indicated that the crystal has an oxygen content of $\delta = 0.01(1)$ and magnetic susceptibility measurements also showed a peak at 30 K. The crystal was mounted having its [100] axis vertical and [010] axis in the sample surface directed to the incident beam. A Ge (111) single crystal analyser was used in triple-crystal geometry to obtain higher wavevector resolution and lower background. The sample was mounted in a closed-cycle Displex cryostat and the sample mosaic width was determined to be ~ 0.03° (FWHM). All the measurements were performed in reciprocal space. The use of the multi-circle diffractometer allows measurement of the scattering to be performed along the principal axes H, K, and L in reciprocal space. The experimental resolution function measured at the Bragg reflection (4, 0, –4) was $\xi_H \sim 0.00173$ Å^{-1}, $\xi_K \sim 0.00133$ Å^{-1}, and $\xi_L \sim 0.00346$ Å^{-1} at the low temperature. To find the orientation of the crystal,

primary studies were made by finding some Bragg reflections on the D^3 diffractometer situated at Durham University. Detailed measurements were performed at BM28 at the European Synchrotron Research Facility (ESRF) at Grenoble in France. The scattered intensity was normalised with the monitor counts, to correct for beam current variations.

6.3.2 Results and discussion

Primary alignments were made by finding some Bragg reflections and constructing the orientation matrix. The characteristic wave vector for the charge stripe modulation is q_{CO} = (2ε, 0, 1). Upon cooling down, the studies were made of satellites at positions $q_{CO} \pm G$, where G is a Bragg peak in reciprocal space. A number of reflections at expected positions for charge modulations such as (4.5, 0, –5), (4.5, 0, -3) and (3.5, 0 –3) were found that are separated from the Bragg reflection (4, 0, –4) with the charge-ordering wavevector (2ε, 0, 1). The charge ordering satellite (4, 4.5, –5) was also observed due to twining of the crystal. The strongest charge satellite (4.5, 0, -5) has only ~ 200 counts per second (c/s) at low temperatures which is very weak compared to the ~ 23000 in the x = 1/3 compound. The characteristic wave vector for the spin density modulation is q_{SO} = ($1+\varepsilon$, 0, 0) and in this compound they are well separated from the charge satellites. An attempt was made to detect the spin modulation reflections, but due to the weakness of the charge satellites this made it impossible to detect spin stripe satellites, expected to be ~ 100 times weaker than the charge stripe reflections. Measurements on (4.5, 0, -3), (4.5, 0, -5), and (4, 0.5, –5) charge-ordering reflections were made in the temperature range 10 - 250 K.

The integrated intensity (normalized) of the charge-ordering reflections (4.5, 0, -5) and (4.5, 0, -3) as a function of temperature along the H-, K-, and L-directions in reciprocal space are displayed in Figures 6.12 and 6.13, the other peaks behaving similarly. These graphs have been obtained by fitting the data at each temperature with a Lorentzian line shape. Upon warming from low temperature, the intensity increases with temperature until it reaches a maximum at T ~ 60 K, and after that the intensity gradually decreases with increasing temperature. The melting of the charge

stripes occurs around 125 K, but the stripes in a very weakly correlated form persist until 160 K. Critical scattering due to spatial fluctuations into the charge stripe phase causes such a scattering; the intensity profiles of the two peaks are similar.

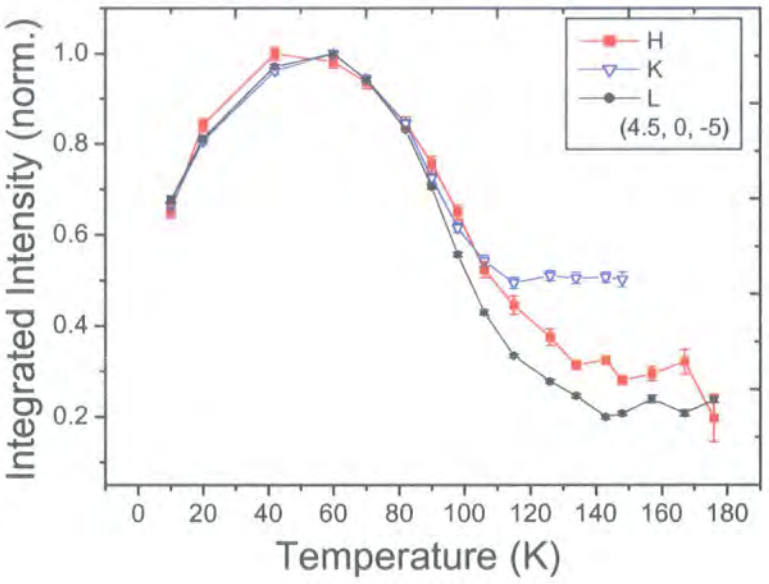

Figure 6.12 The temperature dependence of the integrated intensity of the charge-ordering satellite (4.5, 0, -5) along the *H*-, *K*-, and *L*-directions.

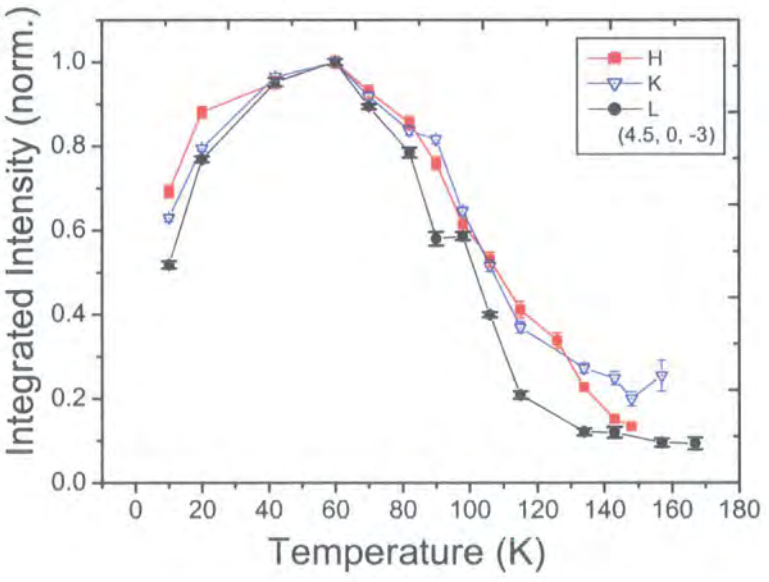

Figure 6.13 The temperature dependence of the integrated intensity of the charge-ordering satellite (4.5, 0, -3) along the *H*-, *K*-, and *L*-directions.

Critical fluctuations of the charge stripes have also been observed in a x = 0.33 crystal but in a narrower temperature range [6] and in other nickelate compounds studied in this thesis. The reason for the decrease of the intensity below 60 K is not yet clear, but it may indicate a decrease in the amplitude (electron density difference) between the stripes. Decrease of the intensity of the charge ordering peaks below 50 K has also been reported in x = 1/3 sample by polarized neutron scattering and they interpreted this as a result of the further localization of charge and spin reorientation [2]. However, our results show that this decrease is accompanied with an increase in the peak width and hence a decrease in the correlation of the stripes.

Neutron diffraction measurements results on an x = 0.2 sample showed that the intensity of the spin-ordering satellite is not constant even at low temperature and it gradually decreases from ~ 20 K and vanishes at ~ 100 K [7]. The neutron results showed that the charge peak survives to higher temperature and vanishes at ~ 130 K. Figures 6.12 and 6.13 show the charge-ordering peak intensity profile is consistent with the neutron result apart from the low temperature decrease, which has not been seen by neutron and the intensity gradually decreases starting at ~ 40 K.

Figures 6.14 and 6.15 show the width (FWHM) of the charge satellites (4.5, 0, -5) and (4.5, 0, -3) as a function of temperature. The width in the L-direction has been added to the graph with a reduced scale to allow comparison with the width in the *ab* planes, and also shown is the width of the Bragg reflection (4, 0, -4). The width of the charge stripes reflections is much wider than that of the Bragg reflection implying that the charge stripes order never approaches the long-range crystallographic order even at low temperatures. The minimum width (longest correlation length) is found in the temperature range ~ 30 - 90 K, corresponding to the greatest intensity of Figures 6.12 and 6.13. The width starts to increase at around ~ 90 K, well below the temperature at which the peak intensity approaches zero. Above this temperature the width increases, probably due to spin disorder, which frustrates the charge stripe order. The general feature of the width profiles (apart from the small increase at low temperature) is in agreement with the neutron results but in their results the width first starts to increase at ~ 70 K [7]. This neutron diffraction indicated the magnetic ordering peaks disappear at ~ 100 K.

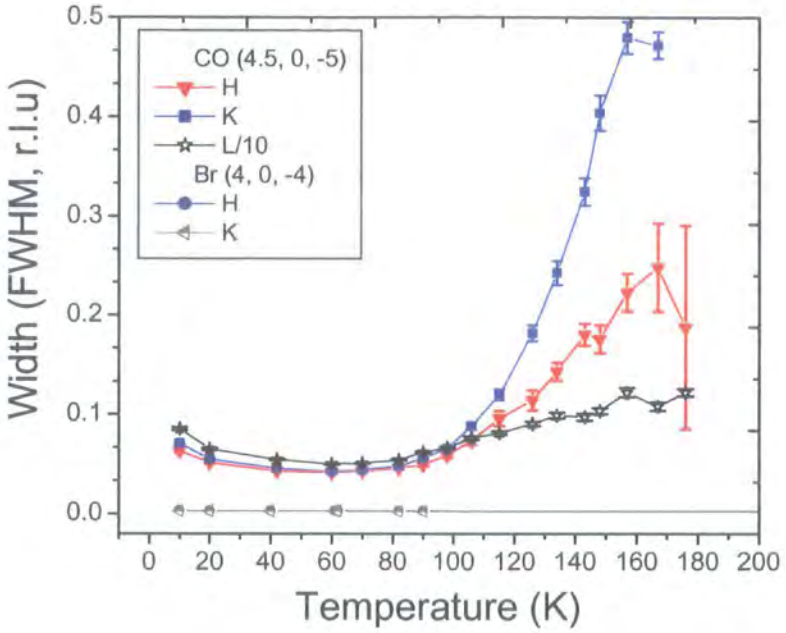

Figure 6.14 The width of the charge-ordering satellite (4.5, 0, -5) as a function of temperature along the *H*-, *K*-, and *L*-directions (note the reduced scale along *L*). The width of the Bragg reflection (4, 0, -4) also added to the graph to aid comparison.

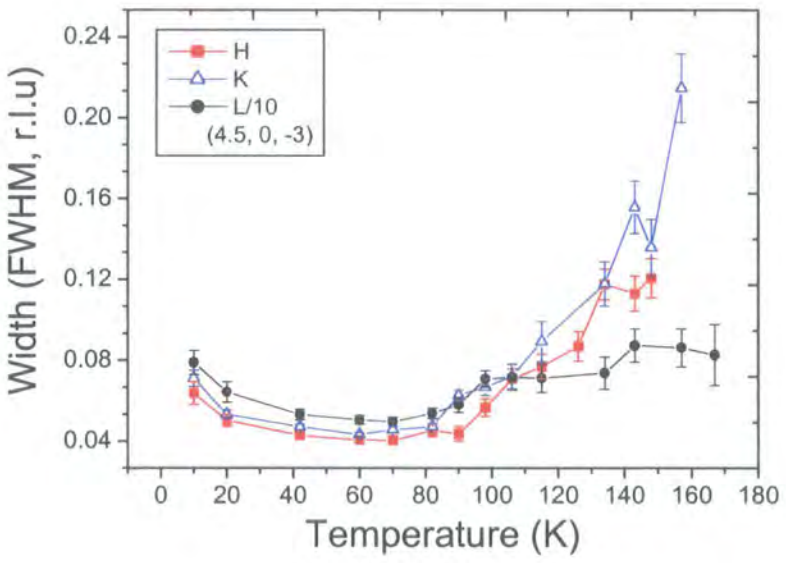

Figure 6.15 The width of the charge-ordering satellite (4.5, 0, -3) as a function of temperature along the *H*-, *K*-, and *L*-directions (note the reduced scale along *L*).

Figure 6.16 shows the evolution of the width of the (4.5, 0, -5) peak at selected temperatures. The centres of the peak at different temperatures have been moved to 4.5 and the intensities have been normalized for easily comparison. As the temperature increases from 10 K, the width becomes narrower at 42 K, and after that becomes broader and finally at 134 K there is a very broad peak with an intensity that is just a little above the background.

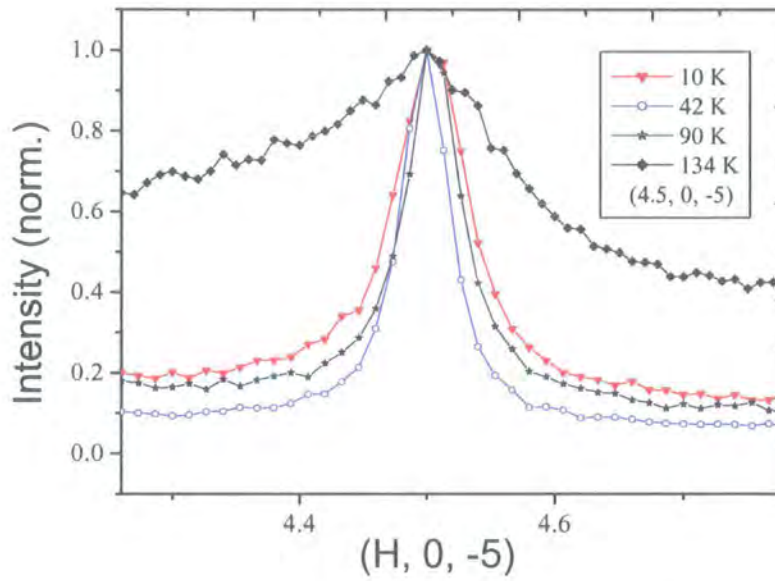

Figure 6.16 Typical *H*-scans of the charge-stripe peak (4.5, 0, -5) at some selected temperatures.

Returning to Figure 6.14, the first increase in the width of the charge-ordering peak and consequently decrease in the correlation length occurs at around the 90 K. There is a correlation between the magnetic ordering melting temperature and an increase in width, suggesting that this change of the width is related to the disordering of the Ni spins in domains. This re-arrangement of the spins affects the ordering of the charges. The graph also shows the disorder in the charge stripes is more effective along the stripes at high temperatures.

To see clearly how the correlation lengths vary with the temperature, they have been calculated from the measured (4.5, 0, -5) charge-ordering satellite widths in each of the three principal directions in reciprocal space, and are plotted in Figure 6.17. The correlation length along the *L*-direction is multiplied by factor 5 for comparison. The correlation lengths in all three directions are very short (less than 250 Å) even around

60 K at which the peak has it maximum intensity. The correlation length along the *L*-direction is less than 4 unit cells indicating a charge stripe glass. The charge stripes are still two-dimensional but they have very short-range correlation length. The correlation length follows the intensity indicating that the decrease at low temperatures is not an experimental artifact but is related to the charge stripes. These results are significantly different to those of the commensurate (x = 0.33) material, suggesting a complex behaviour with stoichiometry.

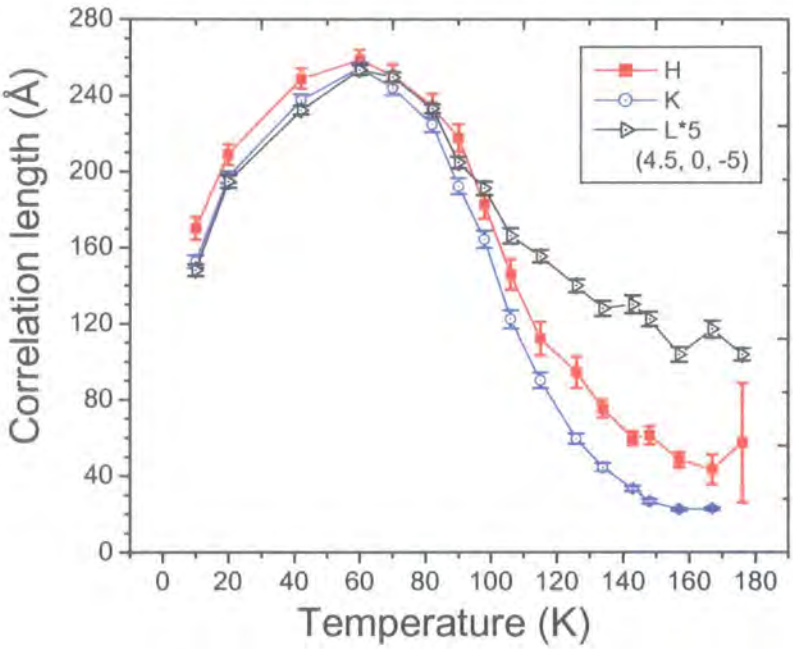

Figure 6.17 Correlation length against temperature of the charge ordering reflection (4.5, 0, -5) in the *H*-, *K*-, and *L*-directions (note: the correlation length along the *L*-direction is multiplied by a factor 5 to aid comparison).

The intensity profile of the charge stripe reflection (4.5, 0, -5) versus temperature along the *H*-direction is fitted with the following power law equation and is shown in Figure 6.18.

$$I(T) \approx \left[\frac{T_{CO} - T}{T_{CO}}\right]^{2\beta}$$

The data points shown as triangles in Figure 6.18 are the intensity of the peak without subtracting scattering from critical fluctuations around the transition temperature.

Table 5.1 shows that the 2β value for the 2D universality class is between 0.25 and 0.3. The extracted values from this fitting are:

$$T_{CO} \approx 108.003 \pm 1.32 \text{ K}$$

$$2\beta \approx 0.298 \pm 0.047$$

This 2β value indicates that the charge stripes are still two dimensional in this compound, similar to the other crystals investigated in this thesis.

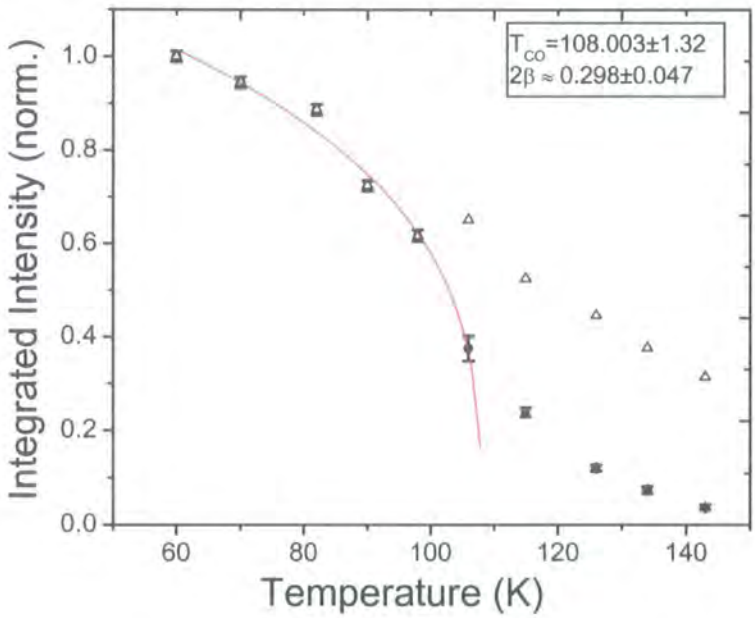

Figure 6.18 The temperature dependence of the integrated intensity of the charge stripe peak (4.5, 0, -5) fitted with the power law equation explained in the text.

The commensurability, ε, against temperature is displayed in Figure 6.19. It has a very complicated behaviour. Its line shape exactly follows the intensity and width. It is nearly constant only in a very short temperature range, indicating stability of the charge stripes in this range. The deviation from 0.2 is due to the small amount of the excess oxygen from the stoichiometry. Sachan *et al.* by neutron measurements mentioned that the value of ε is almost exactly 1/4 below 100 K when the magnetic and charge ordering peaks appear [7]. However, the present results show the commensurate value 0.25 is only approached in the temperature range ~ 30 – 65 K. Above and below this temperature range there is a general trend to be

incommensurate with a wavevector greater than 0.25. These results, especially at low temperatures, are different from the published neutron results on this sample. Hayden *et al.* by neutron scattering found the magnetic correlations in this compound is also incommensurate [8].

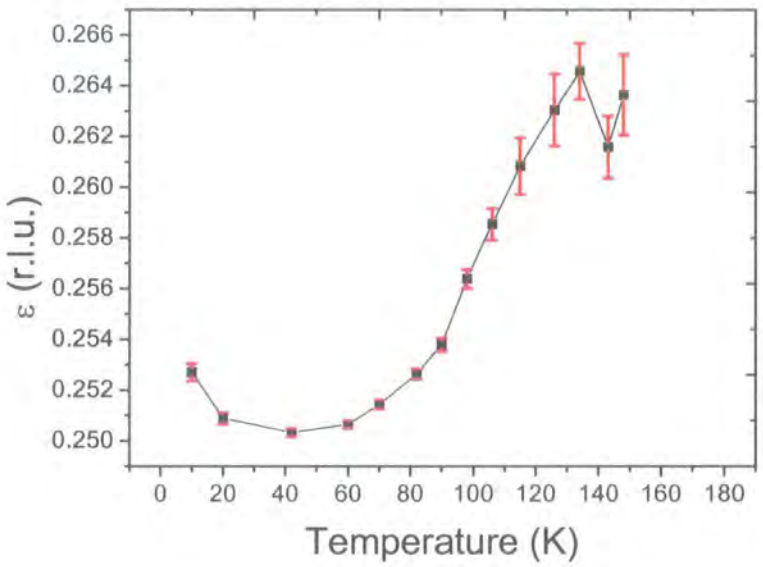

Figure 6.19 The commensurability, ε, as a function of temperature.

In the temperature range between ~ 30 K and 90 K in which the width of the charge-stripes satellites is nearly constant, the commensurability shows variation with temperature. An increase in ε indicates the density of the charge carriers within the charge stripes is decreased. So this implies that the change in the density of the carriers does not affect the stripe correlation length in this temperature range ~ 70 K – 90 K. These graphs show that the charge stripes in this compound is not stable and shows very strong temperature dependence.

6.4 Concluding remarks on the nickelates, $x = 0.33$ - 0.2

For a clearer understanding of the relation between hole concentration and the charge stripes correlation length, the measured correlation length of the charge stripes in *H*-, *K*-, and *L*-directions for samples with $x = 0.2$, 0.25, 0.275, 0.3, and 0.33 is displayed in Figure 6.20.

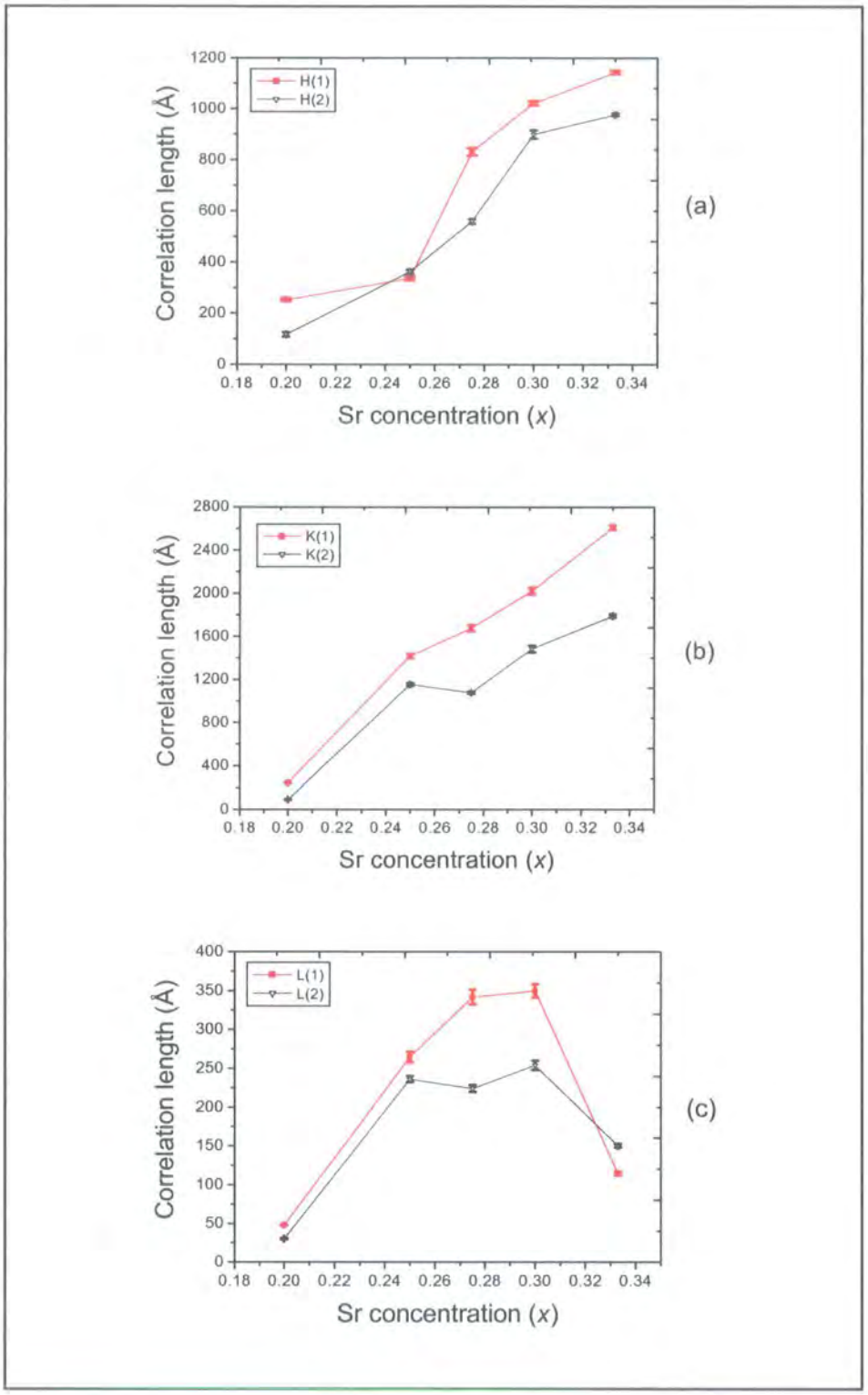

Figure 6. 20 The correlation length as a function of Sr concentrations for two selected temperatures, as explained in the text along (a) *H*-, (b) *K*-, and (c) *L*-directions.

Two different points were selected within the temperature range that the stripes form. The graphs labelled (1) are the measured correlation lengths at low temperatures, where the charge stripes are stable. The temperature in which the intensity of the charge satellite in each sample falls to ~ 30 % of its initial value, is labelled (2). In fact these two temperatures were selected within two different regions of the charge and spin ordered phases, (1) in a region with both charge and spin ordered states, (2) near to the charge stripe melting temperature, a region without spin ordering.

One point to note is the behaviour of the correlation length along the *L*-direction that is different to the other directions. The correlation lengths along the *H*- and *K*-directions are maximised for the $x = 0.33$ sample, that is the composition for which the ordering temperature is also a maximum and the transition into the charge ordered phase has the greatest effects on the electrical and magnetic properties.

By decreasing the hole concentration, the correlation lengths along the *H*- and *K*-directions decrease with a constant slope until $x \sim 0.25$. Below this concentration, there is a sudden decrease in correlation lengths with a larger slope. For example, the correlation length along the *K*-direction from $x = 0.33$ to 0.25 decreases from ~ 2615 Å to ~ 1420 Å at low temperature, and ~ 1790 Å to ~ 1150 Å at temperature (2). While for $x = 0.2$, it drops from ~ 1420 Å to ~ 250 Å for (1) and from ~ 1150 Å to ~ 90 Å for (2). So there may be a threshold number of holes which are necessary to form ordered charge stripes and stabilise them. The correlation length along the *L*-direction (graph c) has a completely different behaviour. The correlation length is small for both sides of the hole concentration range and it has a larger value in the intermediate range.

Considering all three graphs, the charge stripes in these samples can be classified as follows:

1- In the upper range of the hole concentration ($x = 0.33$), the charge stripes have a truly two-dimensional long-range correlation length. This is in contrast with quasi-3D long-range order for n_h =1/3 which has been proposed by Yoshizawa *et al.* from neutron scattering [3].

2- On the lower side of this range ($x = 0.2$), the charge stripes have a truly two-dimensional short-range correlation length. The proposed feature from neutron measurements is three-dimensional short-range order.

3- In the intermediate range of the hole concentration, the stripes have a quasi-two-dimensional correlation length.

The commensurability, ε, extracted from these studies in a range of hole concentration from x = 0.2 to 0.33 is displayed in Figure 6.21. The error bars were smaller than the symbol size and the $n_h = \varepsilon$ line is also added to the graph. Almost all the published results on the $La_{2-x}Sr_xNiO_4$ system come from the neutron scattering measurements and the results represented in this thesis in a wide range of samples with different carriers concentration are the first attempt to study the charge stripes in this system by using synchrotron X-ray scattering techniques. In addition to points labelled (1) and (2), points (3) were measured at temperature above the transition temperature, in the temperature range that the charge stripes exist within critical fluctuations. The commensurability shown in Figure 6.21 was measured in these three different regions of the charge stripe phase. These results are in general agreement with the neutron results (see also Figure 2.16) [3].

Starting from the low temperature data, there is a deviation from the $n_h = \varepsilon$ law below the critical hole concentration x = 0.33. This deviation increases with a decrease in x, but again there is a jump in deviation around the point x = 0.25, approximately consistent with the results obtained from the correlation lengths measurements. The density of the holes within the stripes is n_h/ε, so any variation in ε is inversely related to the hole density [3].

The behaviour of the commensurability, ε, at the point where the charge stripe intensity has fallen to 30% of its low temperature value is labelled (2) in the graph, which is near to the charge stripe melting temperature but is still in the ordered phase, is exactly the same as in the low temperature phase but with a shift to higher values of ε. The interesting part of these measurements comes from the results from the points labelled as (3), the data measured from above the charge stripe melting temperature. There is a general trend to attempt lock the commensurability to ε = 1/3 above the $n_h \geq 0.25$. This means the charge stripes in this temperature range re-arrange themselves in an attempt to form the stable state 1/3. In $n_h > 1/3$, the recent neutron measurements results show the commensurability decrease at high temperature but they could not follow the peak at higher temperatures to make a clear conclusion about the trend to the 1/3 value [5].

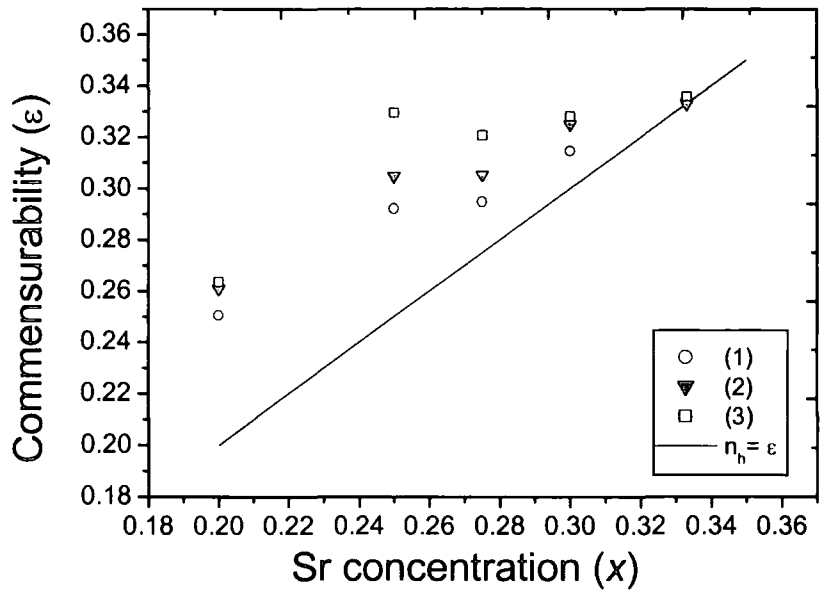

Figure 6.21 The commensurability, ε, as a function of hole concentration. Labels (1), (2), and (3) have been defined in the text.

6.5 References

[1] J. M. Tranquada, D. J. Buttrey, and V. Sachan, Physical Review B-Condensed Matter **54**, 12318 (1996).

[2] S. H. Lee, S. W. Cheong, K. Yamada, *et al.*, Physical Review B **6306**, 0405 (2001).

[3] H. Yoshizawa, T. Kakeshita, R. Kajimoto, *et al.*, Physical Review B **61**, R854 (2000).

[4] J. M. Tranquada, P. Wochner, A. R. Moodenbaugh, *et al.*, Physical Review B **55**, R6113 (1997).

[5] R. Kajimoto, T. Kakeshita, H. Yoshizawa, *et al.*, Physical Review B **64**, 144432 (2001).

[6] C. H. Du, M. E. Ghazi, Y. Su, *et al.*, Physical Review Letters **84**, 3911 (2000).

[7] V. Sachan, D. J. Buttrey, J. M. Tranquada, *et al.*, Physical Review B **51**, 12742 (1995).

[8] S. M. Hayden, G. H. Lander, J. Zarestky, *et al.*, Physical Review Letters **68**, 1061 (1992).

Chapter 7

An X-ray scattering study of ordering in $Nd_{0.5}Sr_{0.5}MnO_3$

7.1 Introduction

Charge, orbital and spin ordering in direct space has very recently attracted considerable attention due to their probable role in the observed colossal magnetoresistance (CMR) in manganites. In this chapter the results obtained by a very high-resolution X-ray scattering study of magnetic domain structures on a single crystal of $Nd_{0.5}Sr_{0.5}MnO_3$ will be explored. Then the results obtained from the study of Jahn-Teller (J-T) distortion ordering (associated with the charge and orbital ordering) and spin ordering will be introduced. Finally the behaviour of the J-T distortion and spin satellites at the Mn *K*-edge (resonance scattering) will be reviewed.

7.2 Observation of magnetic domain structure and phase segregation

7.2.1 Introduction

$Nd_{0.5}Sr_{0.5}MnO_3$ undergoes a phase transition from a paramagnetic insulator state at high temperatures to a ferromagnetic metallic state at the Curie temperature ($T_C \approx$ 255 K). This transition is followed by another transition to an antiferromagnetic insulator state at $T_{CO} \approx 160$ K (section 7.3). As a generic feature of hole-doped perovskites of manganese oxides, the crystal undergoes a second-order transition from the ferromagnetic state at Curie temperature (T_C) via the double-exchange mechanism, and a first-order transition at T_{CO} ($= T_N$) from a metallic to an insulating state. This metal-insulator transition has been ascribed to be due mainly to the disproportional distortion of the Mn^{3+} and Mn^{4+} ions, to produce a charge-ordered

antiferromagnetic state. A *CE*-type antiferromagnetic structure with charge ordering has been observed below T_{CO} using neutron powder diffraction [1, 2]. More recently, using neutron powder diffraction on $Nd_{1/2}Sr_{1/2}MnO_3$, Ritter *et al.* observed the phase segregation at low temperature, in which are contained two different crystallographic structures and three magnetic phases: orthorhombic *(Imma)* ferromagnetic, orthorhombic *(Imma) A*-type antiferromagnetic, and monoclinic *($P2_1/m$) CE*-type antiferromagnetic phases [3]. Also for certain compounds of CMR materials, such as $La_{1/2}Ca_{1/2}MnO_3$ and $Nd_{1/2}Sr_{1/2}MnO_3$, a spatially inhomogeneous distribution of domain structures has also been observed by Mori *et al.* [4] and Fukumoto *et al.* [5] using electron microscopy, indicating a mixture of micro domain structures. In this section the results obtained using high-resolution X-ray scattering on a single crystal of $Nd_{1/2}Sr_{1/2}MnO_3$ will be explored, which is the first experimental evidence, to support these features of the phase segregation in CMR materials. A major distinction between this study and that of previous reports is that these observations of domain structures were obtained in a single crystal rather than powdered material. This has allowed determination of the anisotropies in the domain sizes and in the correlation lengths.

7.2.2 Experimental details

The single crystal of $Nd_{0.5}Sr_{0.5}MnO_3$ was grown using the floating zone method at Bell Laboratories and then polished to get a shiny and even surface with an area of ~ 2×1 mm^2 using 1 μm diamond paste. The crystal was indexed in the orthorhombic structure with $a_o \approx b_o \approx \sqrt{2}a_c$ and $c_o = 2a_c$, where subscripts c and o represent the cubic and orthorhombic perovskite structure respectively. The lattice parameters a = 5.431 Å, b = 7.625 Å, and c = 5.477 Å with the space group of *Imma* were used for indexing of the reflections. A schematic view of the crystal structure is shown in Figure 7.1. Preliminary measurements were carried out at the University of Durham using a four-circle triple-axis diffractometer on a rotating anode X-ray generator with a Cu target operated at 2.8 kW and a displex closed-cycle cryostat. The longitudinal direction in the scattering plane was determined to be the ⟨1 0 1⟩ direction. The

alignment was completed by scanning many Bragg peaks, both in the scattering plane and out of the plane.

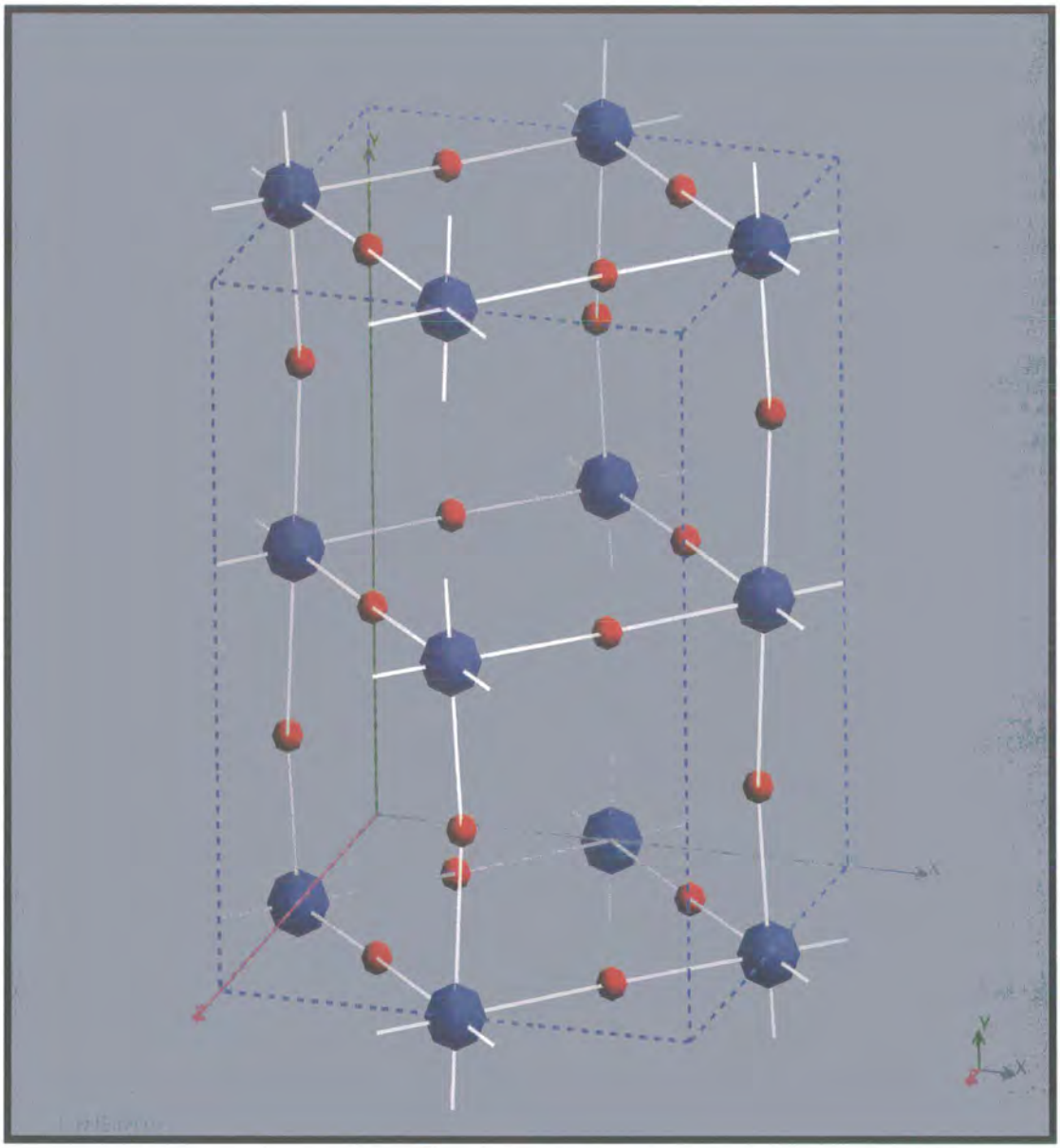

Figure 7. 1 A schematic representation of the unit cell of $Nd_{0.5}Sr_{0.5}MnO_3$. Only Mn (large blue spheres) and O (red spheres) atoms are shown.

The detailed studies utilising synchrotron radiation were performed at station 16.3 at Daresbury Synchrotron Radiation Source. A double bounce Si (111) monochromator

was used to select the incident X-ray beam of 1.000 Å. A second Si (111) single crystal was used as an analyser to achieve high-resolution measurements. A solid state Ge detector with a narrow energy window was used to decrease the background scattering, including fluorescence and higher-order contamination.

A common feature of this crystal and many manganites with a high doping level is that of twinning. Typically the crystals are twinned in all three cubic directions of the underlying cubic perovskite structure. However such twins are macroscopic in size. In order to avoid probing the twin structure of the sample, a small beam size of 0.2 x 0.1 mm^2 was used to search around the crystal until the Bragg reflections were found to be singlet. This technique ensures that although the sample may contain macroscopic twins, the probed volume of the crystal is overwhelmingly single domain. The mosaic width of the sample was determined to be ~ 0.05° (FWHM) as measured on the Bragg reflection (5, –2, 3) at room temperature. Such an experimental arrangement provides extremely high instrumental resolution and ensures that the widths of the Bragg reflections are entirely due to the size of coherent domains within the sample. The use of such a high-resolution analyser ensures that even if more than one domain is illuminated by the X-ray beam the scattered radiation is only collected by the analyser/detector from one domain. Others being slightly misaligned will not fulfil the Bragg condition of the analyser. The relatively small rocking curve width of the crystal demonstrates the high quality of at least the part of the sample from which measurements were taken.

7.2.3 Results and discussion

The evolution of the normalised integrated intensities of the Bragg reflection (5, –2, 3) as a function of temperature is displayed in Figure 7.2. The intensity of the Jahn-Teller distortion superlattice reflection (2.5, 0, 2) is also included in the Figure to compare it intensity profile with that of the Bragg peak in the charge ordering transition temperature region. Upon cooling, a large drop of the intensity of the Bragg peak happens at $T \approx 200$ K, and then a sharp and abrupt change takes place at $T_{CO} \approx 152$ K. Similar behaviour was also observed on a warming run with the transition observed at 162 K. The superlattice satellite intensity vanishes exactly as

the same temperatures of the Bragg peak on cooling and warming runs. Both peaks show a clear hysteresis width of about 10 K due to the first order phase transition. The intensity of the high-temperature Bragg reflection did not reach a maximum until 200 K. The transition happened at $T \approx 200$ K, upon cooling and warming runs respectively, is a second-order transition as the data shows no hysteresis in this temperature region.

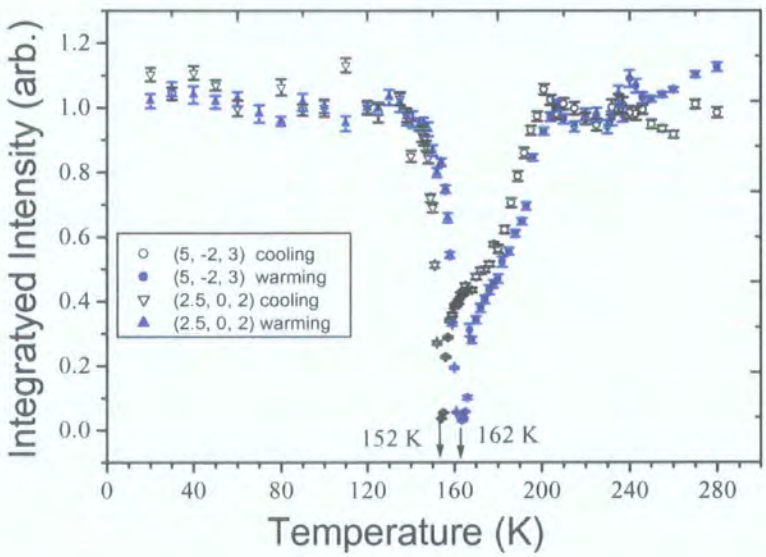

Figure 7.2 The evolution of the integrated intensities of the Bragg reflection (5, -2, 3) and the superlattice reflection (2.5, 0, 2) as a function of temperature.

In Figure 7.2, it is also noteworthy that both curves measured in cooling and warming runs split at $T \approx 180$ K, which suggests the existence of a non-equilibrium state between domains in the temperature range 180 to 160 K due to the first-order phase transition at T_{CO}. Using neutron powder diffraction, Kajimoto *et al.* reported that $Nd_{1-x}Sr_xMnO_3$, $x \approx 0.5$, undergoes a structural phase transition from a ferromagnetic phase to an *A*-type antiferromagnetic phase at $T \approx 200$ K [1]. As X-rays are not sensitive to changes of magnetic phases but to the changes of domain sizes in a crystal, the decrease in the integrated intensities of Bragg peak as shown in Figure suggests that the ferromagnetic domains break into smaller domains at $T = 200$ K due to the formation of *A*-type antiferromagnetic domains.

This suggestion of a change in the size of the domains is also supported by measurements of the Bragg peak width (FWHM) along the longitudinal direction as displayed in Figure 7.3. It is clear that both curves, measured upon cooling and warming runs, split at $T \approx 180$ K. Below 180 K the peak widths diverge as the temperature approaches T_{CO}, indicating a decrease of the length scale of the long-range ordered structure. A structural phase transition occurs at $T_{CO} \approx 152$ K due to the disproportional distortion of the Mn ions, resulting in the formation of the charge ordered state.

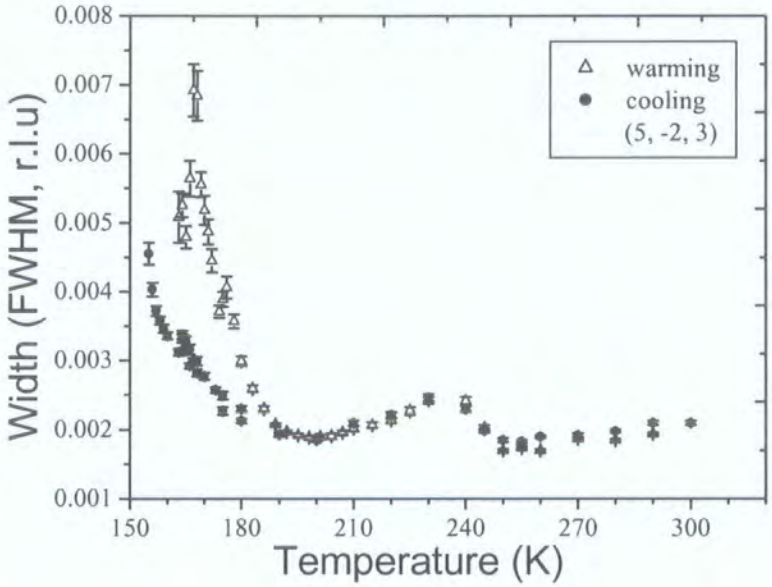

Figure 7.3 The evolution of the width (FWHM) of the Bragg reflection (5, -2, 3) as a function of temperature upon cooling and warming runs along the longitudinal direction in reciprocal space.

$Nd_{1/2}Sr_{1/2}MnO_3$ was reported to be a paramagnetic insulator at room temperature and undergo a transition to a ferromagnetic metallic state at $T \approx 248$ K [1, 2]. By measuring the evolution of the peak width with temperature, these results are in agreement with the studies of the transport and neutron powder diffraction measurements. As shown in Figure 7.3, the width of the Bragg reflection shows unusual peak broadening around the transitions from PM to FM and FM to AFM charge-ordered phases. Such a peak broadening of the Bragg peak have been observed by Radaelli *et al.* on $La_{1/2}Ca_{1/2}MnO_3$ in contrast to $Nd_{1/2}Sr_{1/2}MnO_3$ in whole range of the FM phase [6]. The

peak width increases at $T \approx 252$ K and then decreased at $T \approx 234$ K, indicating a transition starting at 252 K, which is completed at 234 K. In the paramagnetic state, magnetic moments distribute randomly, but align ferromagnetically in the ferromagnetic state. Such a picture is consistent with this measured data. Starting from high temperature, the peak profile became sharp as the temperature was lowered, indicating that the randomly distributed domains tended to become ordered and correlated over a longer distance. At 252 K, the domains start to break up into smaller domains due to the formation of the ferromagnetic phase, as demonstrated by an abrupt change in both resistivity and magnetization [7]. This change is continuous, and it suggests the existence of a mixture of both domains, paramagnetic and ferromagnetic domains, in the temperature range 252 - 234 K. The paramagnetic state disappeared below 234 K. Such a transition has been reported by both transport and neutron powder diffraction measurements [1-3].

In order to further study the evolution of the domain structures with temperature, the scans along the 3 crystallographic axes, *H*, *K*, and *L* were performed individually. The width of the Bragg reflection (5, -2, 3) as a function of temperature along these three axes is shown in Figure 7.4, in which the width profiles are exactly the same as in Figure 7.3.

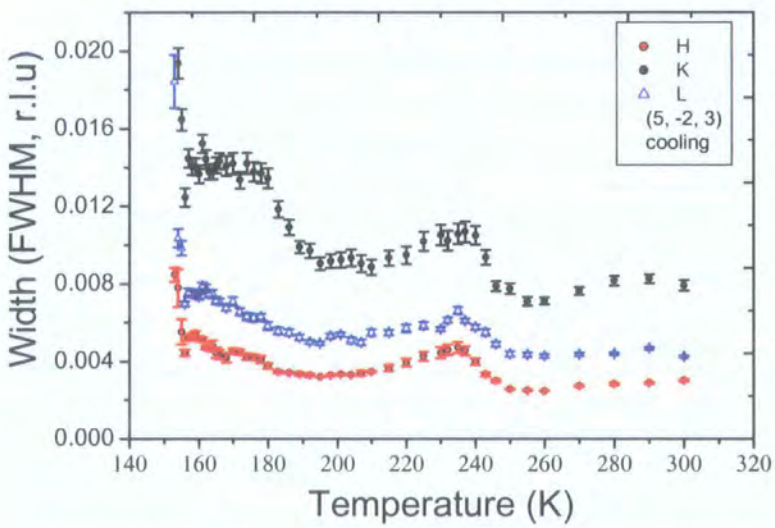

Figure 7.4 The temperature dependence of the width (FWHM) of the Bragg reflection (5, -2, 3) along the *H*-, *K*-, and *L*-directions.

Figure 7.5 shows the result of such measurements displaying the normalised integrated intensity of the (5, -2, 3) Bragg reflection in each crystallographic direction. In this Figure the abbreviations are P (paramagnetic), P-F (mixture of paramagnetic and ferromagnetic), F (Ferromagnetic), and AF-F (mixture of antiferromagnetic and ferromagnetic).

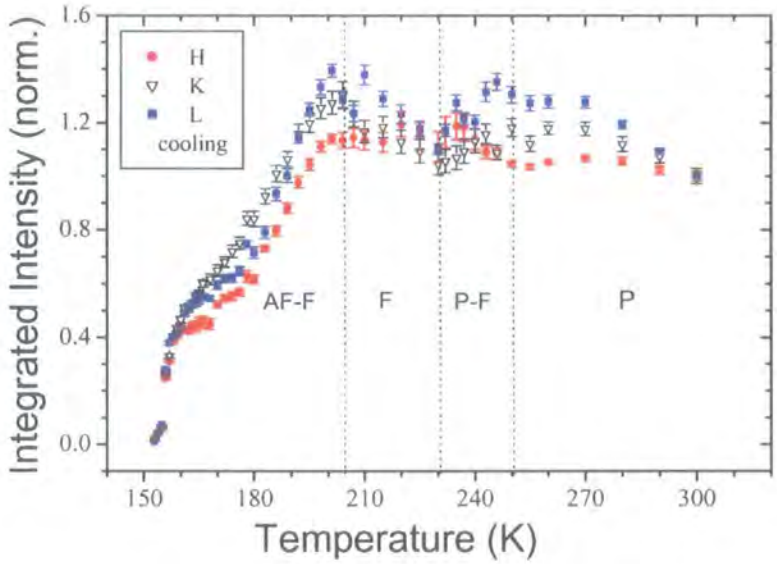

Figure 7.5 The normalised integrated intensity of the Bragg peak (5, -2, 3) as a function of temperature along the *H*-, *K*-, and *L*-directions. P, P-F, F, and AF-F represent paramagnetic, mixture of paramagnetic and ferromagnetic, ferromagnetic and mixture of antiferromagnetic and ferromagnetic respectively.

The correlated domain volume was determined from the product of the 3 correlation lengths that were calculated from the measured widths (HWHM's) of the Bragg peak (5, –2, 3) along the *H*-, *K*-, and *L*-directions and is displayed in Figure 7.6. We realise that this determined domain size might not be the actual size of the domains, but rather the size of long-range correlations within a crystallite. However, it will reflect the domain structure, size and dislocation density and the effect of magnetic and crystallographic transitions. The actual correlated domain size can be obtained by deconvolution of the peak profiles from the resolution function. However, in this experiment, the resolution function was very narrow compared to the measured Bragg peak and deconvolution was neglected.

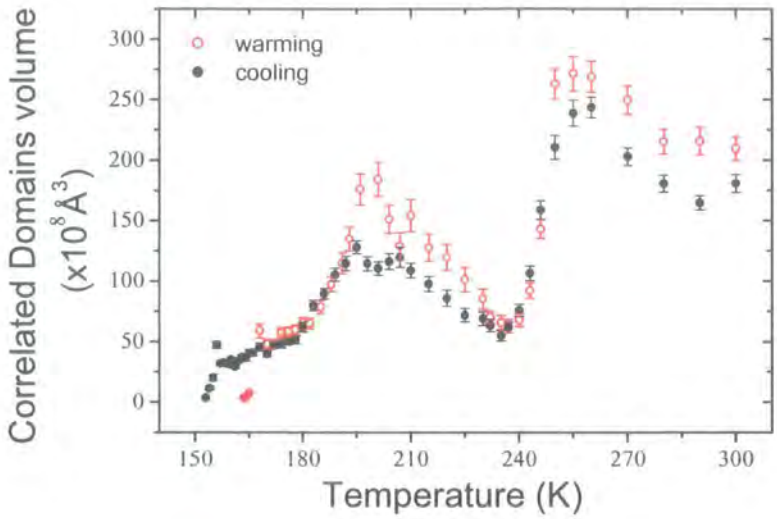

Figure 7.6 The temperature dependence of the domain size on warming and cooling runs.

For temperatures above 252 K, (the region marked by P in Figure 7.5), the paramagnetic domains were observed to grow as the temperature was lowered, indicating long-range order was forming. Upon cooling, a drop of about 70 % in the volume of the correlated domains was observed in the temperature range 252 K to 234 K as shown in Figure 7.6. This corresponds to the region marked P-F in Figure 7.5. As was mentioned, this is due to the transition of the paramagnetic state to the ferromagnetic state. In the interval 234 - 200 K, the size of the domains increases with decreasing temperature, and the integrated intensities increase as well. The development of a long-range order of the ferromagnetic state stops at about 200 K, where the integrated intensity starts to drop and the peaks profiles became increasingly broad upon cooling. An *A*-type antiferromagnetic phase in which the spins of Mn ions antiferromagnetically order along the *b*-axis with a $d_{x^2-y^2}$ orbital ordering has been demonstrated to co-exist with a ferromagnetic phase below 200 K on neutron powder diffraction patterns [1, 3]. Using transmission electron microscopy, Fukumoto *et al.* also observed the transformation of microstructures relating to the microscopic-scale electronic phase separation [5]. On further cooling, a turning point on the transition curves of Figure 7.5 was observed at $T \approx 182$ K. Such a discontinuous change is more pronounced on the curves along the *H*- and *L*-

directions than that along the *K*-direction (long-axis). The origin of this is not exactly known yet, but it might be the precursor of orbital ordering. It has been demonstrated that orbital ordering results from a Jahn-Teller effect distorting the $M^{3+}O_6$ octahedra, associated with long Mn^{+3}-O bonds along the *a*- and *c*-axes, which could suppress the domains formed at high temperatures and change the distribution of domains. Kajimoto *et al.* proposed that orbital ordering could cause the observed phase segregation, and therefore it could explain the coexistence of the *CE*- and *A*-type antiferromagnetic phases at low temperatures [1]. Kajimoto *et al.* observed a two-component feature at around the ferromagnetic transition temperature $T \approx 250$ K in a single crystal of $Nd_{1/2}Sr_{1/2}MnO_3$ using inelastic neutron scattering [8, 9]. Between two components, the central component was observed to be the quasielastic scattering originated from the paramagnetic phase and persists even in the ferromagnetic state, suggesting the coexistence of paramagnetic and ferromagnetic phases below 250 K. Their finding supports this explanation for the changes of the peak profiles in the temperature range from about 230 to 250 K. The coexistence of multiple phases ascribed to micro-domain structures in the temperature range of $T_N < T < T_C$ has also been observed in $Pr_{1/2}Ca_{1/2}MnO_3$, $Nd_{1/2}Sr_{1/2}MnO_3$ and $La_{1/2}Ca_{1/2}MnO_3$ using electron microscopy and neutron diffraction on powder samples [3-5, 10]. On further cooling, a transition occurred at $T_{CO} \approx 152$ K, which is in accord with the formation of the *CE*-type charge/spin ordering. Measurements were also taken on the warming run, showing the identical behaviour except for the different transition temperature ($\approx$ 162 K) for the disappearance of the charge ordering due to the first order phase transition.

7.3 Charge ordering

7.3.1 Introduction

$Nd_{0.5}Sr_{0.5}MnO_3$ is a paramagnetic (PM) insulator with *Imma* orthorhombic symmetry at room temperature [11-13]. Upon cooling it becomes a ferromagnetic metal (FMM) below $T_C \sim 250$ K and at $\sim$ 160 K undergoes a first-order phase transition to a *CE*-type antiferromagnetic (AFM) insulator state [2]. The measurements of the lattice parameters showed an abrupt change at this temperature ($\sim$ 160 K) [14]. Neutron and

electron diffraction have demonstrated the presence of charge, spin and orbital ordering in this phase [1]. Upon cooling the crystal from the FM state, and before transition to this ordered state, the system undergoes to another transition, which is a mixed domain state of *A*-type AFM and *CE*-type AFM [2]. The charge, spin, and orbital ordering satellites appear at the same temperature in this compound. The orbital ordering is believed to possess the $d_{3x^2-r^2/3y^2-r^2}$ type orbital ordering [1]. In this half-doped system, the charge ordering is believed to be the ordering of Mn^{3+} and Mn^{4+} ions in *CE*-type antiferromagnetic phase.

7.3.2 Experimental details

The single crystal of $Nd_{0.5}Sr_{0.5}MnO_3$ used in these experiments was the same as mentioned in the previous section. The crystal was again indexed in the orthorhombic structure. The crystal was first aligned and studied at the University of Durham using a four-circle triple-axis diffractometer on a rotating anode x-ray generator with a Cu target operated at 2.8 kW and a closed-cycle displex cryostat, which confirmed the charge ordering at low temperatures, and confirmed the orientation of the sample crystal. Further experiments were conducted using synchrotron radiation at the *XMaS* diffractometer situated on BM28 at the European Synchrotron Research Facility in Grenoble (ESRF) and at beamline 16.3 at the SRS in Daresbury. At Daresbury, a double bounce Si (111) monochromator was used to select the incident X-ray beam wavelength of 1.000 Å, whilst at the ESRF a focusing mirror was used to focus the beam to a small spot. Single crystals were used as analysers to provide a good wavevector resolution and decrease the background at the SRS and ESRF. The alignment was completed by scanning many Bragg peaks on the scattering plane and the off-scattering planes within the setting of the space group. The mosaic width of the sample was determined to be ~ 0.05° (FWHM) as measured on the Bragg reflection (5, –2, 3) at room temperature. Measurements at the SRS were performed along the longitudinal and transverse directions with a Si (111) single crystal as an analyser, while at the ESRF they were performed along the *H*-, *K*-, and *L*-directions in reciprocal space by using a single crystal Cu (220) as an analyser.

7.3.3 Results and discussion

Upon cooling the crystal below 160 K additional peaks were observed at non-integer positions in reciprocal space. These peaks had a wavevector (1/2, 0, 0) and are due to the structural modulation arising from the Jahn-Teller distortion associated with charge ordering of Mn^{3+} and Mn^{4+} ions and orbital ordering in the sample. This causes the neighbouring undistorted $Mn^{4+}O_6$ octahedra to displace in opposite directions (see Figure 7.7) [6, 15]. This causes a doubling of the unit cell along the *a*-axis.

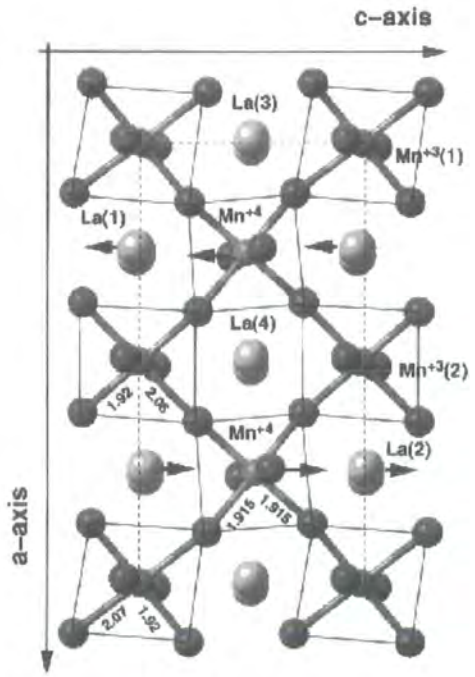

Figure 7. 7 The projection of $Nd_{0.5}Sr_{0.5}MnO_3$ superstructure in the *ac*-plane at low temperature. Arrows show the displacements of the $Mn^{4+}O_6$ octahedra. (taken from Radaelli *et al.* [6])

Between 200 K and 160 K no superlattice reflections were observed, indicating that charge ordering does not occur in the *A*-type AFM state. The peaks observed below 160 K have an intensity of approximately 10^{-3} that of the Bragg reflections. The search for superlattice reflections with wavevector (0, 2K+1, 0), which directly probes the charge ordering, was not successful probably due to the crystal orientation and the peak intensity. A schematic representation of the *CE*-type charge, spin, and orbital ordering is shown in Figure 7.8.

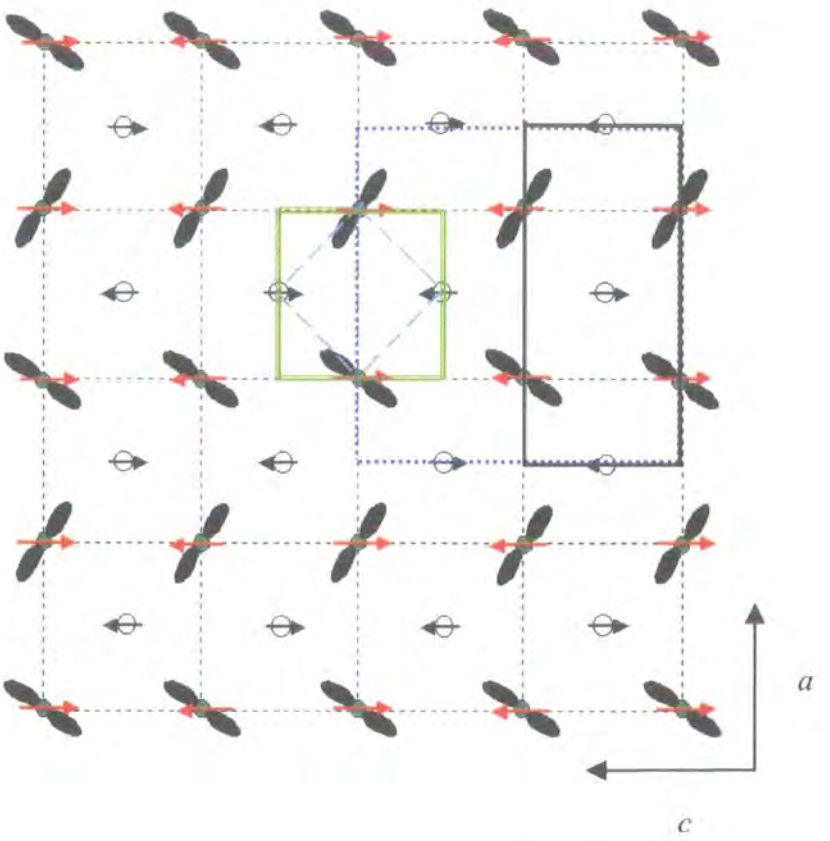

Figure 7.8 A schematic view of *CE*-type charge, spin, and orbital ordering.

Figure 7.9 shows the integrated intensity (normalised) of the superlattice reflection (2.5, 0, 2) as a function of temperature in the *H*-, *K*-, and *L*-directions in reciprocal space. As the Figure indicates, the intensity of the peak increased as the temperature decreased from T_{CO} ~ 160 K and the variation with temperature is in accord with a

first-order phase transition. The transition temperature is in accord with other measurements [14]. The peak had a noticeably different peak shape to the Bragg reflections and could be indexed using the wavevectors ($h/2$, k, l) and (h, k, $l/2$). These wavevectors are associated to the structural modulation due to the charge ordering and the presence of two wavevectors 90° apart is due to twinning. The peak intensity is approximately constant over the whole temperature range, except near to the transition temperature, where the intensity vanishes suddenly as expected for a first order transition.

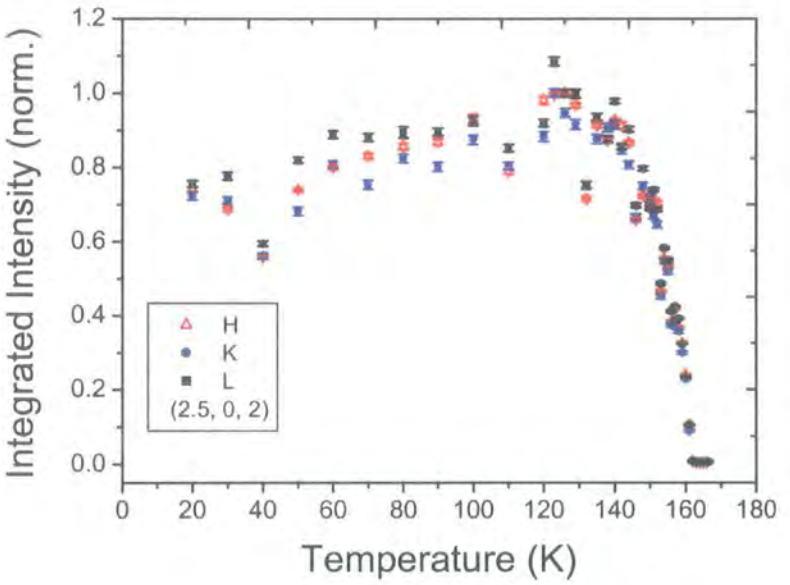

Figure 7.9 The integrated intensity (normalised) of the superlattice reflection (2.5, 0, 2) as a function of temperature in the *H*-, *K*-, and *L*- directions in reciprocal space.

A property of a first-order phase transition is the presence of a hysteresis loop upon reversing the temperature in the transition region. The intensity profile of the superlattice reflection (2.5, 0, 2) and Bragg reflection (5, -2, 3) on cooling and warming runs is displayed in Figure 7.10. When the sample was warmed from low temperature, the superlattice satellite (2.5, 0, 2) disappeared at ~ 162 K, the same temperature as the high-temperature Bragg peak appeared, and on the cooling run this peak appeared at ~ 152 K, the temperature at which the Bragg peak disappeared. Figure 7.10 clearly shows that the transition has a marked hysteresis of ~ 10 K on cooling and warming runs in agreement with the resistivity measurements [5].

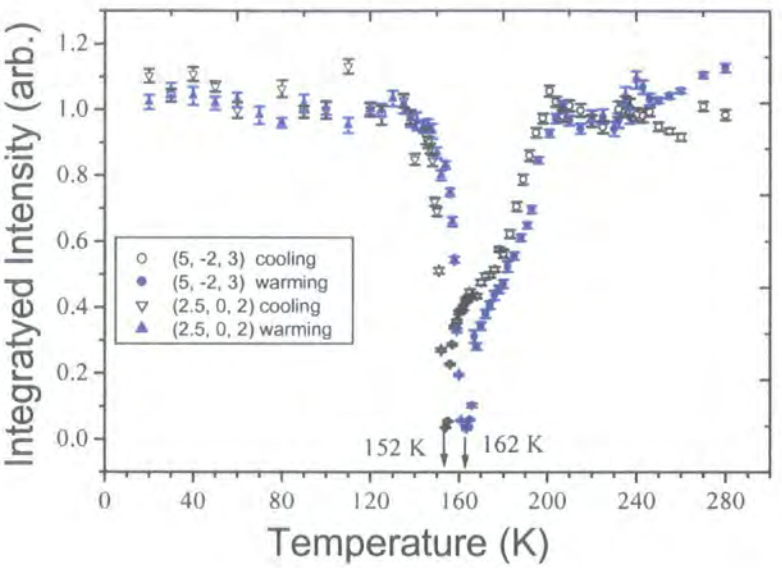

Figure 7.10 Integrated intensity (normalised) of the superlattice reflection (2.5, 0, 2) and Bragg peak (5, -2, 3) as a function of temperature in cooling and warming runs along the longitudinal direction in reciprocal space.

Scans along the *H*-, *K*-, and *L*-directions in reciprocal space were performed for the Jahn-Teller distortion ordering peak (2.5, 0, 2) at every temperature and the results have been fitted with a Gaussian line shape. Figure 7.11 shows the width (FWHM) of this peak in reciprocal lattice units obtained from the fitting.

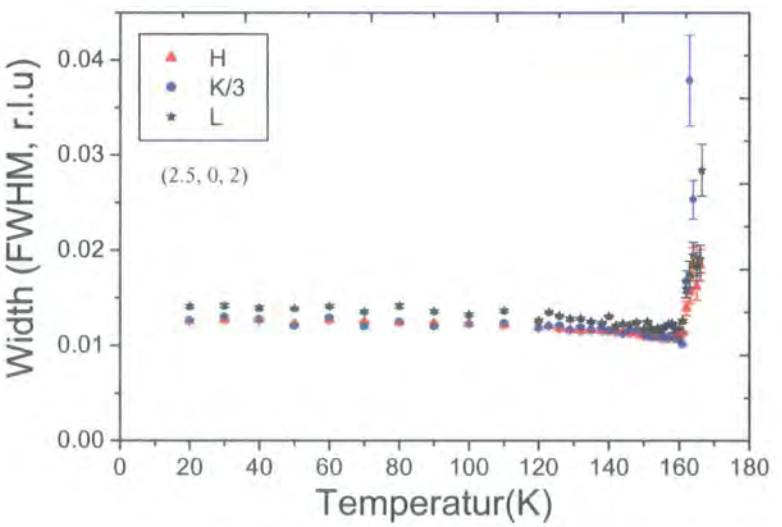

Figure 7.11 The width (FWHM) of the superlattice reflection (2.5, 0, 2) as a function of temperature in the *H*-, *K*-, and *L*-directions in reciprocal space.

The error bars resulted from this fitting are also included in the graph. The width in the *K*-direction is added to the Figure with a reduced scale to ease comparison with the other directions. The width along the *K*-direction, which is the long-axis direction in this setting, is much wider than the other directions, probably due to the structural anisotropy e.g. anisotropy in the Mn-O-Mn bond angles and Mn-O bond lengths in the *ac* plane and *b*-direction [1, 11]. The width is approximately constant and independent of temperature unlike the charge stripes in nickelate crystals, indicating the charge ordering in this crystal is stable. The width abruptly increases at the charge ordering transition temperature.

Figure 7.12 shows typical scans along the *H*-, *K*-, and *L*-directions in reciprocal space for the superlattice reflection (2.5, 0, 2) and Bragg peak (2, 0, 2) at 100 K. In this experiment Cu (220) was used as an analyser crystal that has a lower resolution. The width of the (2.5, 0, 2) reflection along the *H*-direction is nearly the same as the Bragg peak and measurement in this direction is limited by the instrumental resolution, because measurements of the Bragg peak width with Si (111) single crystal showed also a very narrow peak in this direction. However, in Figure 7.12 the width of the superlattice reflection along the other two directions is much broader than the Bragg peak. Again the Figure shows the widths in the *K*-scan (long-axis) are wider for both Bragg and charge ordering satellite compared with the width along the *H*- and *L*-directions.

Figure 7.13 displays the correlation length (proportional to the inverse of the width) of the superlattice reflection (2.5, 0, 2), which was measured in a warming run along the *H*-, *K*-, and *L*-directions in reciprocal space. The correlation lengths are not the same in all three directions and show the anisotropy between the *ac* planes and normal to these planes (long-axis). The ordered regions are correlated over much longer distances in the *ac* planes, ~ 800 Å, compared to those in normal to these planes, ~ 400 Å. The correlation lengths are nearly constant with decreasing temperature. The ratio of the correlation lengths, in the *ac* planes to normal to these planes, $\xi_{H,L}/\xi_K$ is about 2.

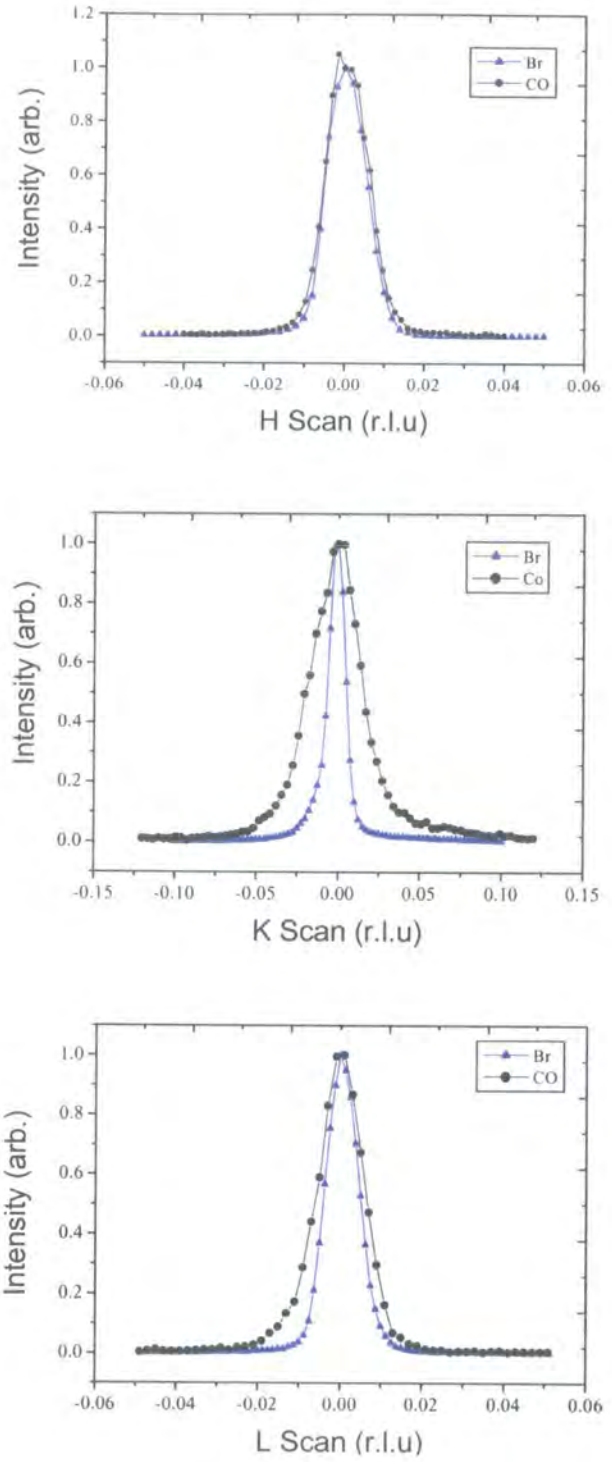

Figure 7.12 Typical *H*-, *K*-, and *L*-scans of the superlattice reflection (2.5, 0, 2) and Bragg reflection (2, 0, 2) at 100 K.

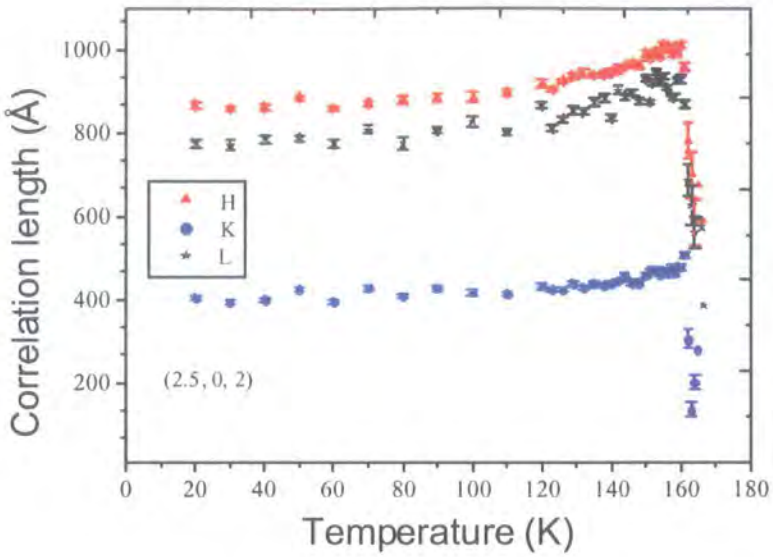

Figure 7.13 The measured correlation length of the superlattice reflection (2.5, 0, 2) versus temperature along each three directions *H*, *K*, and *L*.

These results show the transition into the charge-ordered phases is strongly first-order as it was seen in the superlattice peak intensity profile and the presence of the hysteresis loop in cycling of the temperature.

7.4 Spin ordering

7.4.1 Experimental details

$Nd_{0.5}Sr_{0.5}MnO_3$ undergoes a first-order phase transition from a ferromagnetic state to a *CE*-type antiferromagnetic state at ~ 160 K. According to the magnetic X-ray scattering theory (see chapter 3), the dominant scattering from spins is in the rotated channel σ - π. In this experiment a Cu (220) analyser crystal was used for analysing the polarisation dependence of scattered photons. The Cu (220) crystal has a Bragg scattering angle ~ 45° at the Mn *K*-edge energy. The experimental geometry is similar to that used for the study of the nickelate $x = 0.33$ crystal as is shown in Figure 5.23. By rotating the analyser crystal around the scattered beam, the linearly polarised σ (perpendicular to the diffraction plane) and π (parallel to the diffraction

plane) components can be studied separately. All the measurements were performed in the σ - π channel around the Mn *K*-edge energy to enhance the peak intensity.

7.4.2 Results and discussion

Upon cooling down, in addition to the satellites associated with the J-T distortion, other very weak satellites (only 10^{-5} that of Bragg reflections) were observed. These peaks can be indexed as (*h*/2, *k*, *l*/2) with *h*, *k*, and *l* = odd integer. The wavevector of these peaks is in accord with the spin-ordering superstructure, as reported by neutron powder diffraction. From this neutron study, Kajimoto *et al.* reported that the characteristic reflections for the Mn^{3+} sublattice are (*h*/2, *k*, *l*) with *k* = integer and *h*, *l* = odd integer and those for Mn^{4+} sublattice reflections are (*h*/2, *k*/2, *l*) with *h*, *k*, and *l* = odd integer [1]. Figure 7.14 shows the variation of the integrated intensity (normalised) of the spin ordering reflection (1.5, 1, 1.5) as a function of temperature in the *H*-, *K*-, and *L*-directions.

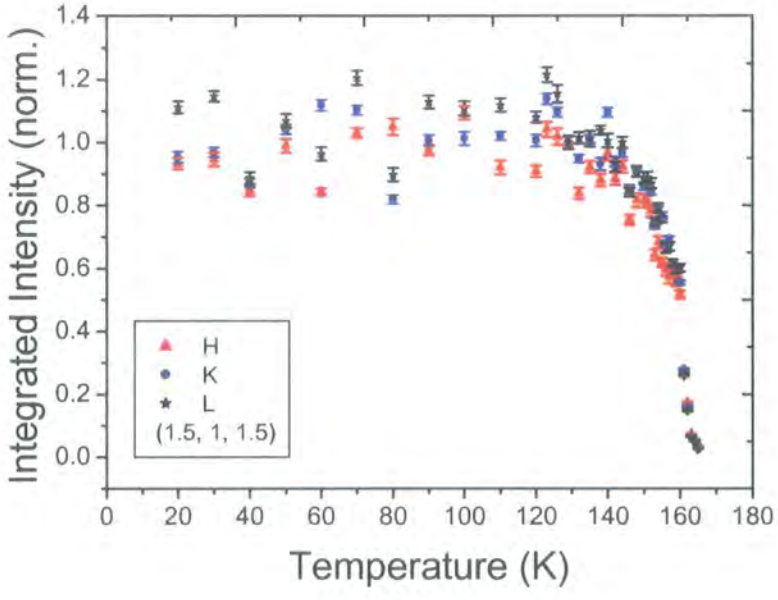

Figure 7.14 The integrated intensity (normalised) of the spin-ordering reflection (1.5, 1, 1.5) as a function of temperature along the *H*-, *K*-, and *L*-directions.

The Figure clearly shows that the spin ordering transition temperature is the same as the charge ordering transition temperature, $T_{SO} = T_{CO} = 160$ K, and that the transition

is strongly first-order. The intensity of the peak is approximately constant upon increasing the temperature and it suddenly drops at around 160 K, the transition temperature, as expected for a first-order transition.

To get a clear picture of the behaviour of the Jahn-Teller (J-T) distortion ordering (2.5, 0, 2) and spin ordering (1.5, 1, 1.5) satellites, their intensity profiles as a function of temperature along the *H*-direction are plotted in Figure 7.15. The Figure shows that the both satellites behave similarly over the whole temperature range. Both peaks disappear at the same temperature with a first-order transition. This behaviour implies that the J-T distortion and the *CE*-type antiferromagnetic spin ordering are intimately coupled to each other.

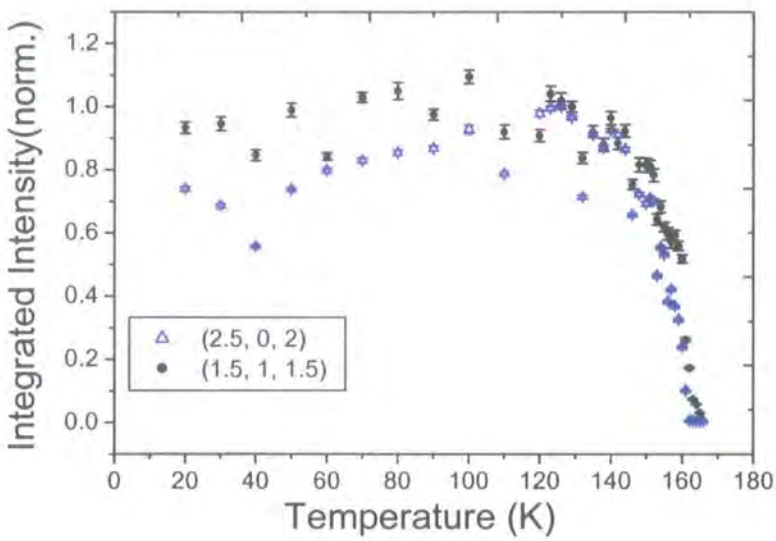

Figure 7.15 The integrated intensity of the superlattice reflections (2.5, 0, 2) and (1.5, 1, 1.5) versus temperature along the *H*-direction.

The measured width of the spin ordering reflection (1.5, 1, 1.5) against temperature along the *H*- and *K*-directions is shown in Figure 7.16. The error bars extracted from the fitting of the peak profile with a Gaussian function at each temperature are also included in the Figure. It should be noticed that these data were collected using the Cu (220) polarization analyser and this limits the wavevector resolution. Within the experimental error the width is nearly constant, apart from a small anomaly just

before the transition temperature, and it abruptly increases at the transition temperature.

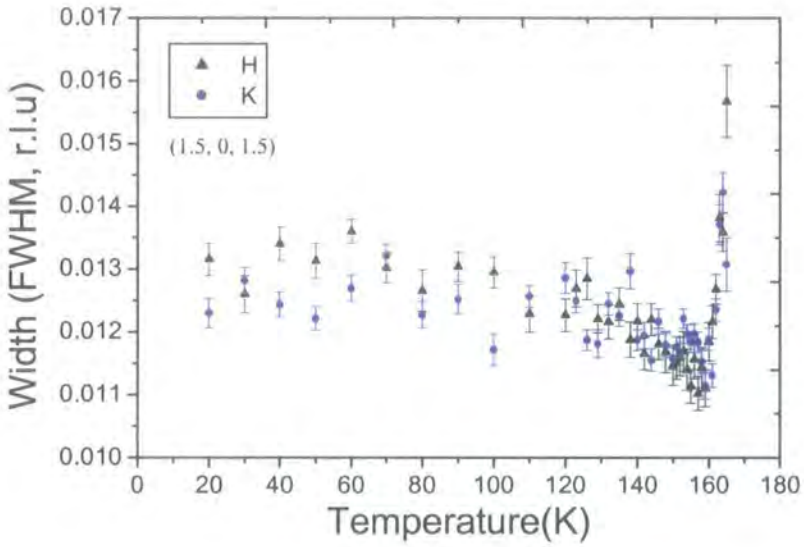

Figure 7.16 The variation of the width of the spin ordering satellite (1.5, 1, 1.5) as a function of temperature along the *H*- and *K*-directions.

The correlation length of the spin satellite (1.5, 1, 1.5) along the *H*- (in-plane) and *K*- (out of plane) directions is displayed in Figure 7.17. The correlation length of the spin-ordering peak shows an anisotropy between different directions, different to that of the peak associated with the Jahn-Teller distortion. The correlation length along the *H*-direction is ~ 850 Å, and that along the *K*-direction is ~ 1250 Å, indicating that the spin ordering has a larger correlated length scale in this direction. This is in contrast with the J-T distortion peak which was shorter in this direction (long-axis direction). The spin-correlated distance in this direction is ~ 1250 Å, whereas the corresponding distance for the (2.5, 0, 2) reflection is only ~ 400 Å (Figure 7.13). The ratio of the spin correlation length, ξ_{SO}, to the distortion peak correlation length, ξ_{CO}, in this direction is $\xi_{SO}/\xi_{CO} \approx 3$. The correlation lengths along the *H*-direction for both peaks are identical.

The ratio of the spin correlation length along the *H*- and *K*-directions at two temperatures below and around the transition is:

$$\xi_{50}^{H} / \xi_{50}^{K} \approx \xi_{160}^{H} / \xi_{160}^{K} \approx 0.7$$

These ratios show that the anisotropy is independent of temperature and melting and that the reduction of the correlation length is identical in both directions, in contrast with the melting of the charge stripes in nickelate systems.

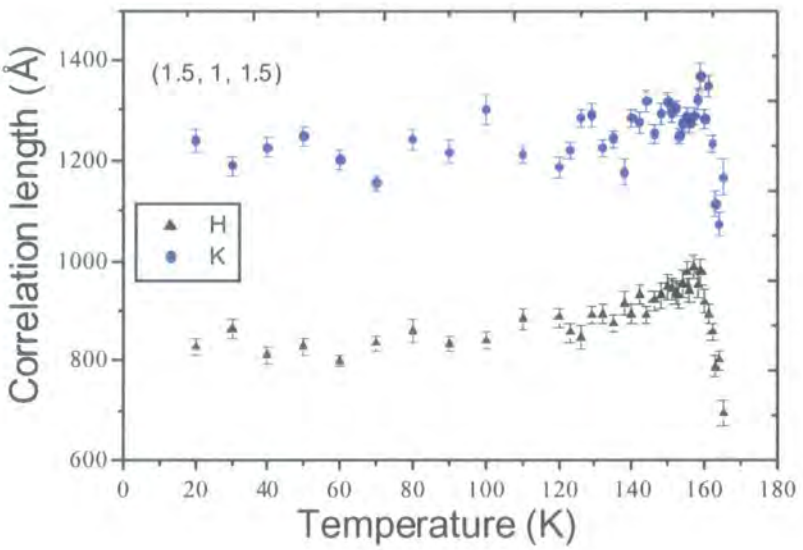

Figure 7.17 The temperature dependence of the in-plane (*H*) and out-of-plane (*K*) correlation length of the superlattice reflection (1.5, 1, 1.5).

Oron Zachar when considering the effects of topological defects and elastic deformations on disordering the charge and spin stripes in the cuprate systems has concluded that predominantly topological defect disorder always leads to $\xi_{SO}/\xi_{CO} < 1$ [16]. If disorder arises by pure elastic deformations, it is expected that $\xi_{SO}/\xi_{CO} = 4$ and any observation of $1 < \xi_{SO}/\xi_{CO} < 4$ implies that there is a relatively dilute concentration of topological defects. Assuming that this suggestion is applicable to the manganite systems, these results indicate disorder in the distortion- and spin ordering in this compound has a different contribution from topological defects in different directions. Whereas, this contribution is very small in the *K*- direction (out of plane), the in-plane correlations are mainly affected by it.

7.5 Resonance scattering

7.5.1 Experimental details

Polarisation measurement of the scattered beam from spin ordering reflections was undertaken using a Cu (220) single crystal as the analyser, giving a scattering angle of 95.6° when the incident photon energy was set to the Mn *K*-edge. It was found that the polarisation of the incident beam is 98 % σ (perpendicular to the scattering plane). By rotating the analyser crystal around the scattered beam, the linearly polarised σ and π (in the scattering plane) components can be studied separately. In the following the data have not been corrected for the absorption of photon by the crystal.

In order to clarify the origin of weak satellite reflections found at (h/2, k, l/2) with h, k, and l = odd integer and distortion superlattice peaks at (h/2, *0*, l) with h = odd integer and l = even integer, resonant X-ray scattering and polarisation analysis were carried out at the *XMaS* beamline at ESRF. By tuning the incident beam energy to the Mn *K*-edge and scattering into the π channel to suppress the charge scattering, it was possible to observe resonant enhancement of the spin ordering wavevector.

7.5.2 Results and discussion

Before moving to a discussion of the resonant scattering results, the result obtained from fluorescence measurement is shown in Figure 7.18. The increase of the intensity around 6.556 keV is due to the Mn *K*-edge, which corresponds to the transition of an electron from the 1s core state to the empty 4p state, an intra-atomic dipole transition. The small peak at the pre-edge energy near 6.543 keV is a dipole forbidden transition corresponding to the transition of an electron from the 1s to the 3d state, which is a quadruple transition.

Energy scan through the superlattice satellites (2. 0, 2.5), (2, 0, 1.5), and (1.5, 0, 2) in the σ - σ channel are shown in Figure 7.19. These were taken at 100 K. Comparing these with the fluorescence spectrum in Figure 7.18 indicates that the peak intensities are approximately independent of the photon energy and only show a big dip due to

big dip due to the absorption at the Mn *K*-edge. The intensity in the high-energy side is lower than low-energy side due to the higher absorption.

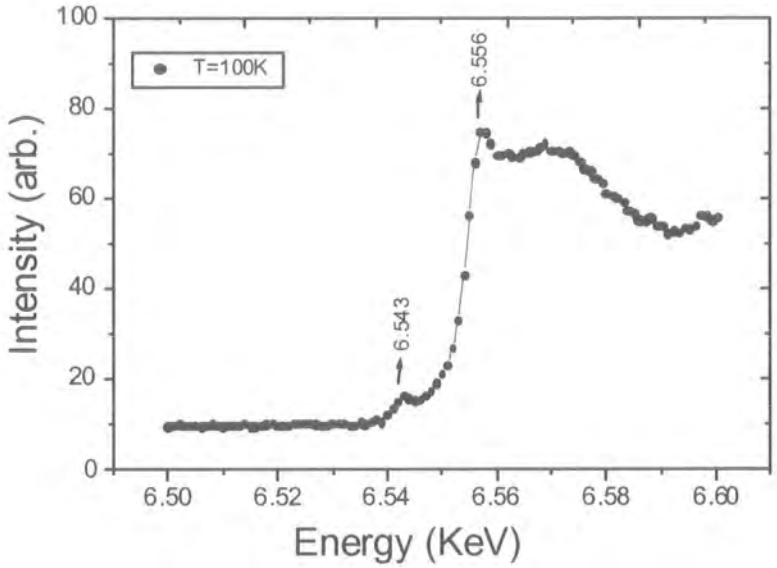

Figure 7.18 Fluorescence measurements of the sample at the Mn *K*-edge taken at 100 K.

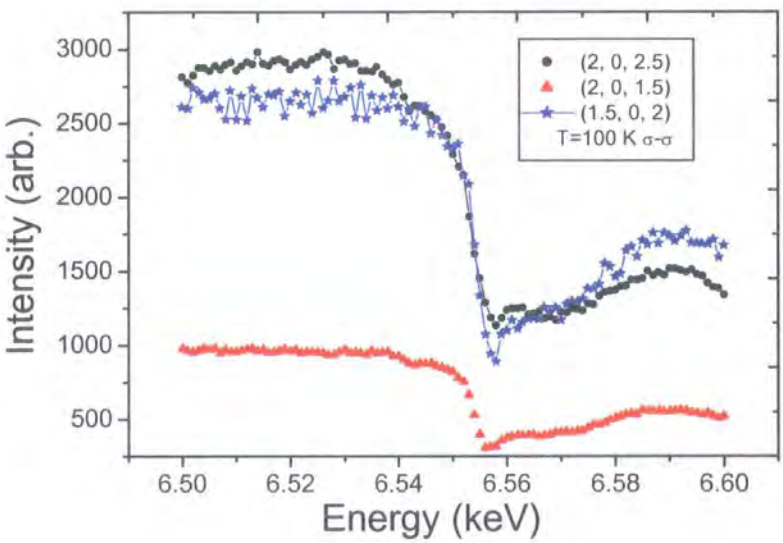

Figure 7.19 Energy scan through the superlattice reflections (2, 0, 2.5), (2, 0, 1.5), and (1.5, 0, 2) in the σ - σ channel at 100 K.

In Figure 7.20 the energy scan of the (1.5, 2, 0) peak in both polarisation channels is displayed. The energy scan profiles in both channels are similar and do not show any resonance behaviour, a characteristic of normal charge scattering. Nakamura *et al.* observed resonance at the real charge-ordering peak (0, 3, 0) at 6.555 keV [17].

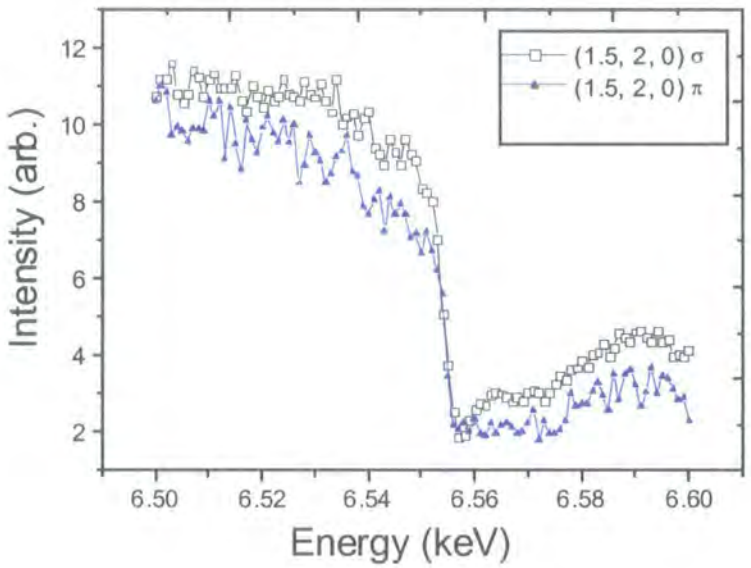

Figure 7.20 Energy scan through the reflection (1.5, 2, 0) in the σ - σ and σ - π channels at 100 K.

Figure 7.21 shows the normalised intensity of the spin-ordering reflection (1.5, 1, 1.5) as a function of energy in both polarisation channels, σ - σ and σ - π, at 100 K. As can be seen there is scattering in both polarisation channels and the widths of the peaks are nearly identical in both channels. The peak enhancement is at energy of ~ 6556 eV, which is ~ 4 eV above the Mn^{3+} *K*-absorption edge. The chemical shift between Mn^{3+} and Mn^{4+} edge is 4.2 eV [18]. From a neutron diffraction study, Kajimoto *et al.* reported that the characteristic reflections for the Mn^{4+} sublattice reflections are (h/2, k/2, l) with h, k, and l = odd integer [1].

These results show that the scattering at (1.5, 1, 1.5) is due to spin ordering from the Mn^{4+} sublattice. The non-resonant magnetic scattering on the low-energy side is high and above the edge it becomes weaker due to the higher absorption. The enhancement of the intensity at the edge compared with the non-resonance intensity

at lower energy is of order of 2. Fluorescence measurement data has also been included in Figure 7.21 for comparison. It demonstrates a pre-edge at 6543 eV. It can be clearly seen that the enhancement of intensity at spin satellite occurs at the energy of 6556 eV and not at the pre-edge energy. The very broad peak at low-energy side is probably due to the charge because it has been seen in energy scans through the charge and Bragg peaks with a dip at the edge energy.

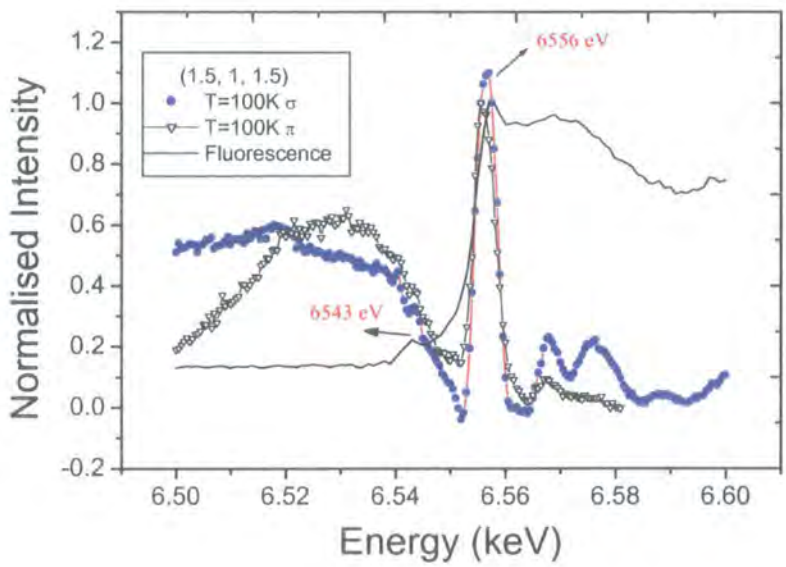

Figure 7.21 The energy scans through the spin-ordering satellite (1.5, 1, 1.5) in the σ- σ and σ- π channels. The data from fluorescence measurements is also shown in the graph.

Figure 7.22 shows the energy scans through the spin satellite (1.5, 1, 1.5) at 100 K and 162 K, in the spin ordered phase and at higher temperature around the spin ordering transition temperature respectively, which were measured in the σ - π channel. As the Figure shows, the intensity of the peak is near to zero at 162 K, a clear temperature dependence of the intensity of the peak at resonance, and indicates the peak is truly from spin ordering in the sample at low temperature.

To get a clear idea about the enhancement of the spin peak intensity at the Mn *K*-edge, the intensity of the peak along the *H*-direction in two different energies at 100 K is shown in Figure 7.23. One scan was taken at the Mn *K*-edge and the other below the edge. As this reflection is due to the antiferromagnetic ordering of the spins on

the Mn^{4+} sublattice, the peak intensity shows a big enhancement at the edge. The enhancement is of a factor of about three.

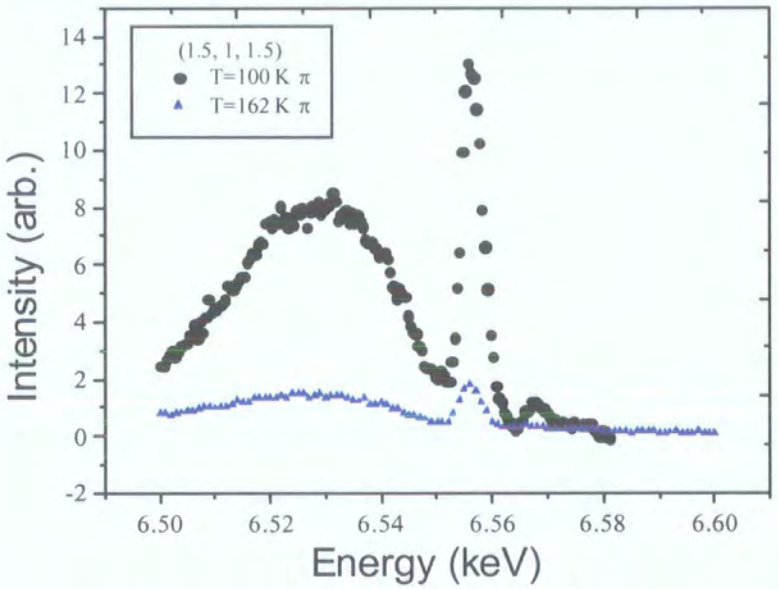

Figure 7.22 The energy scans of spin satellite (1.5, 1, 1.5) at 100 K and 162 K in the σ - π channel.

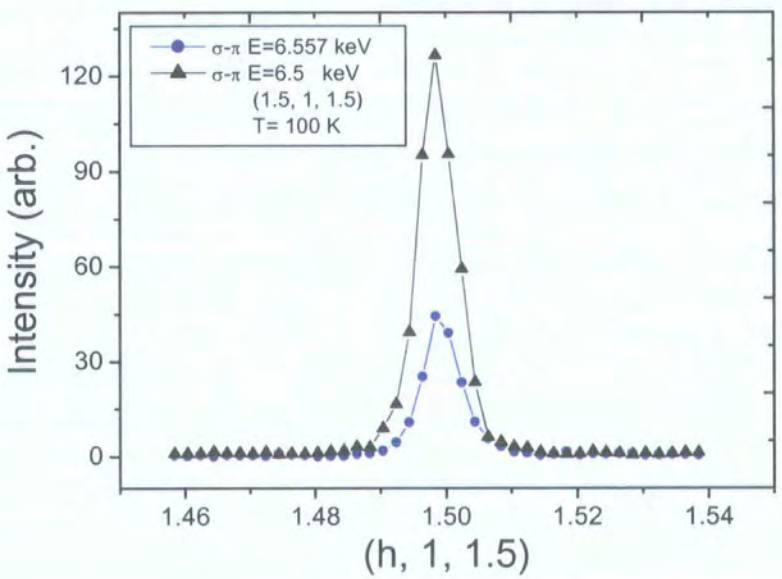

Figure 7.23 The intensity of the (1.5, 1, 1.5) satellite along the *H* direction at the Mn *K*-edge and below the edge energy at 100 K.

Figure 7.24 displays the energy scans through the spin-ordering satellite (2.5, 1, 2.5) in both polarisation channels σ - σ and σ - π. This peak clearly shows the enhancement of the intensity only in σ - π channel. The intensity profile in the σ - σ channel shows a dip at the Mn *K*-edge due to the absorption, and exactly follows the normal charge satellite profile. This is in contrast with the behaviour of the (1.5, 1, 1.5) peak, which shows resonance behaviour in both polarisation channels.

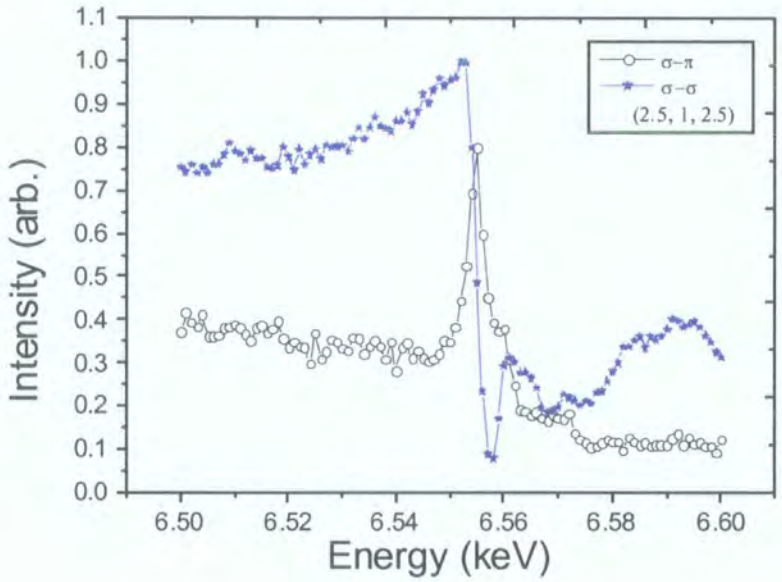

Figure 7.24 The energy scans through the spin satellite (2.5, 1, 2.5) in the σ - σ and σ - π channels.

Figure 7.25 shows the energy scans through the satellites (1.5, 1, 1.5) and (2.5, 1, 2.5) in the σ - π channel, where the intensities of the peaks have been normalised. The enhancement of the intensities of both peaks occurs at 6.556 keV, which is the energy required to excite an electron from the Mn 1s state to the empty 4p state, a dipole transition. From fluorescence measurements, Figure 7.18, a small peak was found at 6.543 keV due to the transition of an electron from Mn 1s state to the 3d state, an electric quadrupole transition. From Figure 7.25 it is clear that the enhancements of the intensities are only at the main Mn *K*-edge, 6.556 keV, and the resonance is due to a dipole transition.

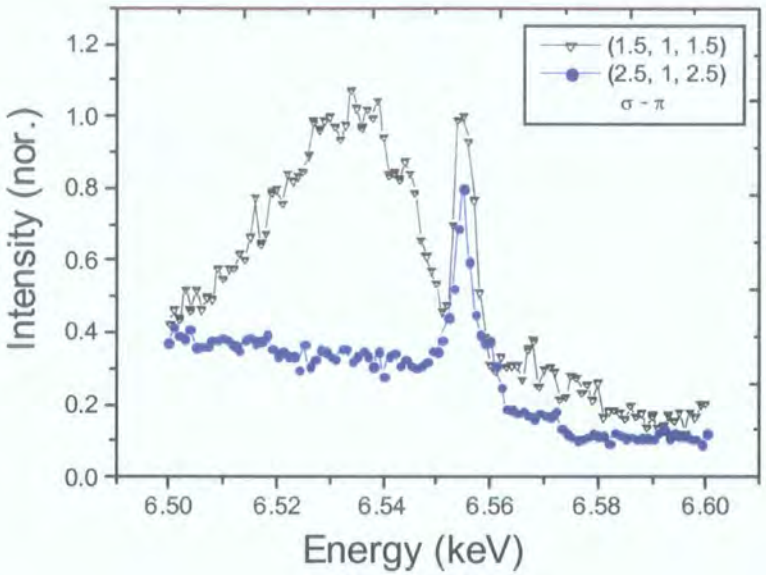

Figure 7.25 The energy scans through the spin ordering satellites (1.5, 1, 1.5) and (2.5, 1, 2.5) in σ- π channel.

In conclusion, transformation of domain structures and the formation of the charge- and spin-ordered phase in single crystal $Nd_{1/2}Sr_{1/2}MnO_3$ have been observed by using synchrotron X-ray scattering. $Nd_{1/2}Sr_{1/2}MnO_3$ is orthorhombic with a space group of *Imma* at room temperature and doesn't undergo a structural transition until T_{CO} where the charge ordered antiferromagnetic state forms. The phase transitions observed in the temperature interval, $T_{CO} < T < T_C$, are unlikely to be caused by the structural phase transition, instead, it is evidence for phase segregation due to the formation of different magnetic domains. Such a mixture of magnetic phases has previously been observed in powdered material. Below T_{CO} additional satellite reflections were observed with wavevectors q = (1/2, 0, 0) and q = (1/2, 1, 1/2) due to the Jahn-Teller distortion of the MnO_6 octahedra and antiferromagnetic spin ordering. The transition into this ordered phase is first-order with a marked hysteresis of ~ 10 K. The intensity of the spin ordering satellites shows a clear energy dependence by tuning the photon energy to the Mn K absorption edge. For spin ordering a scattered signal is predicted in the π channel in resonance scattering at the dipole transition (see chapter 3) as was observed at (2.5, 1, 2.5) peak. On the contrary, the (1.5, 1, 1.5) satellite shows scattered signal in both polarisation channels and clearly further investigation is required to explain this behaviour.

Unfortunately it was not possible to carry out an azimuthal scan because the experimental geometry requires the reflection wavevector to be normal to the crystal surface to carry out a large range azimuthal scan. Detailed measurements are required to examine these peaks on a crystal with a different orientation.

7.6 References

[1] R. Kajimoto, H. Yoshizawa, H. Kawano, *et al.*, Physical Review B-Condensed Matter **60**, 9506 (1999).

[2] H. Kawano, R. Kajimoto, H. Yoshizawa, *et al.*, Physical Review Letters **78**, 4253 (1997).

[3] C. Ritter, R. Mahendiran, M. R. Ibarra, *et al.*, Physical Review B **61**, R9229 (2000).

[4] S. Mori, C. H. Chen, and S. W. Cheong, Physical Review Letters **81**, 3972 (1998).

[5] N. Fukumoto, S. Mori, N. Yamamoto, *et al.*, Physical Review B-Condensed Matter **60**, 12963 (1999).

[6] P. G. Radaelli, D. E. Cox, M. Marezio, *et al.*, Physical Review B-Condensed Matter **55**, 3015 (1997).

[7] H. Kuwahara, Y. Tomioka, A. Asamitsu, *et al.*, Science **270**, 961 (1995).

[8] R. Kajimoto, H. Yoshizawa, H. Kawano, *et al.*, Journal of Physics and Chemistry of Solids **60**, 1177 (1999).

[9] R. Kajimoto, T. Kakeshita, Y. Oohara, *et al.*, Physical Review B-Condensed Matter **58**, R11837 (1998).

[10] C. H. Chen and S. W. Cheong, Physical Review Letters **76**, 4042 (1996).

[11] V. Caignaert, F. Millange, M. Hervieu, *et al.*, Solid State Communications **99**, 173 (1996).

[12] P. M. Woodward, T. Vogt, D. E. Cox, *et al.*, Chem. Mater. **10**, 3652 (1998).

[13] P. M. Woodward, D. E. Cox, T. Vogt, *et al.*, Chemistry of Materials **11**, 3528 (1999).

[14] S. Shimomura, K. Tajima, N. Wakabayashi, *et al.*, Journal of the Physical Society of Japan **68**, 1943 (1999).

[15] S. Shimomura, N. Wakabayashi, H. Kuwahara, *et al.*, Physical Review Letters **83**, 4389 (1999).

[16] O. Zachar, Physical Review B **62**, 13836 (2000).

[17] K. Nakamura, T. Arima, A. Nakazawa, *et al.*, Physical Review B-Condensed Matter **60**, 2425 (1999).

[18] G. Subias, J. Garcia, M. G. Proietti, *et al.*, Physical Review B **56**, 8183 (1997).

Chapter 8

Conclusions and further work

8.1 Conclusions

High-resolution X-ray scattering studies of the charge stripes in $La_{2-x}Sr_xNiO_4$ were conducted on crystals with various hole concentrations from $x = 0.33 - 0.2$. The intensity of the charge stripe reflections is hole concentration dependent and it decreases from $x = 0.33$ (~ 23000 counts per second (c/s)) toward the 0.2 sample (~ 200 c/s) as expected from the charge stripe picture that the stripes are ordered Ni^{3+} ions in the domain walls and Ni^{2+} ions in the hole-poor region and the amplitude of the charge stripe is proportional to this difference. The intensity profiles of the charge stripe reflections show the transition into the charge stripe phase is second order in all samples.

The charge ordering transition temperature, T_{CO}, is also strongly hole concentration dependent, defined as $n_h = x + 2\delta$, where δ is excess oxygen from stoichiometry. The T_{CO} decreases as the hole concentration decreases from $x = 0.33$ to $x = 0.2$ with the maximum transition temperature for 0.33 sample, ~ 240 K. The transition temperatures for $x = 0.3$, 0.275, 0.25 and 0.2 samples are ~ 195 K, ~ 150 K, ~ 145 K, and ~ 125 K respectively. The transition temperatures for $x = 0.275$ and 0.25 samples are nearly identical but the 0.25 sample has an excess oxygen as the T_{CO} is dependent on hole concentration and not on the Sr concentration. In addition, for the first time, critical fluctuations above T_{CO} were observed.

By measurement of the correlation lengths it was found that there is a huge anisotropy between the correlation length in the *ab* plane and along the *c*-axis direction. The stripes are well correlated in the *ab* planes and show only very short-range order along the *L*-direction. The measured correlation lengths and extracted critical exponents from the fitting of the intensity profiles revealed that the charge

stripes are 2-dimensional in all the series. In the $x = 0.25$ sample, which has an extra oxygen content of $\delta = 0.02(0.01)$, measurements of the correlation lengths along the *H*-, *K*-, and *L*-directions revealed that in contrast with other Sr concentrations mentioned above, the correlation length along the modulation direction, *H*, falls rapidly and is approximately identical with the correlation length along the *L*-direction. On the other hand, the correlation length along the stripe direction, *K*, is four times larger, indicating quasi-long range correlations in this direction. The correlation length is also hole concentration dependent and it decreases as the hole concentration decreases. The results show the correlation length along the *L*-direction is approximately constant and independent of hole concentration. It implies the structural properties of the crystal rather than the hole concentration have a dominant effect in this direction. The correlation length of these charge stripes does not increase as the temperature is lowered significantly below T_{CO}, indicating that the length scale of the disorder is quenched at low temperatures.

Measurements of the commensurability, ε, showed that it is constant and temperature independent for the $x = 0.33$ sample, indicating the stability of the charge stripes in this compound. It becomes incommensurate for other samples with $x < 0.33$ and also temperature dependent as the temperature increases towards the transition temperature indicating the stability of the charge stripes in the case of $x = 0.33$.

Detailed measurements of the peak intensity of the Bragg peaks as a function of temperature of a single-crystal of $Nd_{1/2}Sr_{1/2}MnO_3$ have allowed the determination of the onset temperatures and hysteresis associated with a series of structural and magnetic phase transitions. Measurement of the anisotropic peak profiles and widths show an increase in the width of the Bragg reflections, caused by a dramatic decrease in the correlated volume, at the Curie temperature (252 K) corresponding to the transition from a paramagnetic to a ferromagnetic state. Below approximately 200 K the formation of a mixture of antiferromagnetic and ferromagnetic phases is observed via a dramatic increase in the width of Bragg reflections and decrease in the integrated intensity of the peaks. This increasing width continues until the first-order structural phase transition at $T_{CO} = 152$ K upon cooling.

Below this temperature additional satellite reflections were observed with a wavevector q = (1/2, 0, 0) in the charge-ordered phase. These reflections are due to the Jahn-Teller distortion of the MnO_6 octahedra. The intensity profiles of these reflections show that the transition into the charge-ordered phase is strongly first-order. This structural phase transition was observed to display a large hysteresis width of 10 K upon warming, as evidenced by the rapid disappearance of the superlattice satellites and the reappearance, and sharpening, of the structural Bragg peaks upon warming. The measured correlation lengths of these peaks show that the charge modulation is correlated primarily in the *ac* plane rather than the *K*-direction (long-axis) probably due to the anisotropy in the structural properties.

In addition to these satellites, extra very weak reflections were observed with wavevector (1/2, 1, 1/2) possibly due to spin ordering in the sample. Upon cooling these reflections appear as the same temperature as the charge ordering peaks appear. Their intensity profiles are exactly similar to the charge ordering one. The spin ordering peak correlation length along the *K*-direction in contrast to the distortion peak, is not small, indicating a long-range spin correlation distance in this direction. Energy scan through these satellites also show a clear enhancement of intensity at the Mn *K*-edge energy, and the resonance is due to a dipole transition.

8.2 Further work

The low intensity of the charge ordering satellites and their short-range order nature, compared to the fundamental Bragg reflections, limits the use of laboratory based X-rays source and needs synchrotron radiation for the study of charge-ordering satellites. On the other hand the availability of beamtime at synchrotron radiation sources is limited as is the period of a Ph.D., two majors factors limiting the exploration of at least parts of the unknown questions.

In $La_{2-x}Sr_xNiO_4$ system, the studies should be extended to good quality single crystals up to x = 0.5 and smaller than x = 0.2 especially on crystals with stoichiometric oxygen content. The commensurability behaviour showed that it tends to move towards the commensurate value 1/3 at high temperatures. These experiments will find out the commensurability behaviour for the crystals with Sr concentration x >

0.33. For x = 0.25 and x = 0.2 crystals there is a need to repeat the experiments if single crystals with stoichiometric oxygen content are available. As these crystals have also commensurate Sr concentration, their commensurability behaviours will help to understand the role of antiferromagnetic spin background on the stability of the charge stripes and the effect of commensurability. It should also noticed that these studies will also explored the dependence of the charge stripe melting temperature and correlation length on Sr concentration and commensurability effect.

In $Nd_{0.5}Sr_{0.5}MnO_3$ crystal, the real charge ordering and also orbital ordering satellites, which have wave vectors (0, 1, 0) and (0, $2k$+1/2, 0) respectively, have not been found in this studies. These satellites are accessible on a new crystal with its [0, 1, 0] axis normal to the crystal surface and can also be studied from the variation of the peak intensities upon changing the energy of the incoming photons and rotation of the crystal around the scattering vectors (azimuthal angle ψ). The satellites with wavevector (1/2, 1, 1/2) also need to be re-examined to clarify their origin and behaviour.

In recent experiments, it has been found that replacing some of the Sr atoms with Nd atoms in the high-T_C cuprate superconductor, $La_{2-x}Sr_xCuO_4$, suppresses the superconductivity and leads to the formation of charge stripes. The suppression of superconductivity in the optimally doped system, x = 0.15, has been observed by addition of the Cu substituting Zn and Ni. A replacement of only 5% of Cu atoms by Ni atoms destroys superconductivity and causes a metal-insulator transition. The study of this insulating system, is likely to be helpful for understanding the role of the charge stripes and their effect on superconductivity.